

UNIVERSIDAD DE CANTABRIA



Departamento de Ingeniería Estructural y Mecánica

E.T.S. de Ingenieros Industriales y de Telecomunicación

**CONTRIBUCIÓN AL ESTUDIO DEL COMPORTAMIENTO
DINÁMICO DE TRANSMISIONES MECÁNICAS EN
RÉGIMEN NO ESTACIONARIO**

**CONTRIBUTION TO THE STUDY OF THE DYNAMIC
BEHAVIOR OF MECHANICAL TRANSMISSIONS UNDER
NON-STATIONARY CONDITIONS**

TESIS DOCTORAL

Autor: D. Ahmed Hammami

Directores: Dr. D. Fernando Viadero Rueda

Dr. D. Fakher Chaari

Dr. D. Alfonso Fernández Del Rincón

Dr. D. Mohamed Haddar

Santander, 2015



Doctoral thesis

Presented by

Ahmed HAMMAMI

(Electro-mechanics engineer)

CONTRIBUTION TO THE STUDY OF THE DYNAMIC BEHAVIOR OF MECHANICAL TRANSMISSIONS IN NON-STATIONARY CONDITIONS

Advisers:

- M. Fagher Chaari
- M. Fernando Viadero Rueda
- M. Alfonso Fernández Del Rincón
- M. Mohamed Haddar

Dedication

I dedicate this work to my family and my friends especially:

My wife “Ines”

My parents “Mohamed” and “Maymouna”

My son “Mohamed”

My sister “Olfa” and my brother “Anas”

Acknowledgments

In the research work, the personal effort must enlist the help of a group that supports individual activity, thus allowing collectively achieve objectives. In this sense, I have been fortunate to have the support of the Laboratory of Mechanics, Modeling and Production, of the National School of Engineers of Sfax-Tunisia and Group of Mechanical Engineering, University of Cantabria-Spain.

I want to express my deep appreciation to each and every one of members of this laboratory and this group for their help and support, starting with their headers Professor Mohamed Haddar and Professor Fernando Viadero Rueda.

I express my sincere gratitude to Professor Fakher Chaari director of this thesis and Professor Alfonso Fernández Del Rincon for their guidance and support throughout this research.

I am also thankful to Professor Pablo García Fernández, Professor Higinio Rubio Alonso and Professor Mnaouar Chouchane for serving on the dissertation committee.

In addition, I am grateful to the University of Cantabria cooperation project for doctoral training of University of Sfax's students and the Tunisian-Spanish Joint Project No. A1/037038/11.

I would like also to acknowledge project "Development of methodologies for the simulation and improvement of the dynamic behavior of planetary transmissions DPI2013-44860" funded by the Spanish Ministry of Science and Technology.

I want to sincerely thank my family for their continuous support and encouragement without which this work would not have been possible. Finally, I would like to thank my wife, Ines, for her patience and faith in me throughout this endeavor.

Abstract

Research developments devoted to dynamic behavior characterization of mechanical transmissions is always an interesting topic since there is a continuous need to decrease vibration and noise while keeping high compactness and efficiency. Most studies were focused on transmissions running under stationary condition where speed and load are assumed constant. However, repetitive run ups, time varying loading and speed conditions are very common in many industrial applications which imply non stationary operations.

The work presented through this thesis aims to a better understanding of the dynamic behavior of planetary gears running under non-stationary operating conditions. Typical use of such gear sets is in wind turbines, new generation aircraft engines, hybrid car transmissions... In order to fulfill the objectives, a planetary gear test bench with mechanical power recirculation which has been particularly analyzed through numerical simulations and experimental tests.

A modal analysis has been done on the available test bench in order to determine the natural frequencies, modal deflections and modal kinetic and strain distributions. A lumped parameters model of the corresponding test bench with three degree of freedom for each component was used for this purpose. Numerical results are compared with those obtained through experimental modal analysis done on the test bench.

The dynamic behavior is investigated firstly in stationary conditions with constant speed and load. The objective is to highlight the amplitude modulation in the time signals measured on ring gear induced by the individual influence of the passage of each planet near the measurement point. Asymmetric sidebands around meshing frequency and harmonic are observed in both simulations and experimental results

The next part of the thesis is dedicated to the study of the transmission in non-stationary operations. For this purpose, several operating conditions have been considered, such as time varying load and speed, as well as run-up and run down regimes using numerical simulation and experimental tests. The simultaneous amplitude and frequency modulation are emphasized using time frequency analysis based on Short Time Fourier Transform.

Moreover, studies on the Load Sharing between planets has been done taking into account the interaction between meshing gears, the gravity of the carrier and the planet position errors in stationary condition. In addition, the effect of speed on the load sharing behavior is studied during the run up regime.

Finally, a Transfer Path Analysis approach called Global Transmissibility Direct Transmissibility is used to study the propagation of vibration in planetary gears in the stationary and non-stationary conditions. The directed transmissibilities between the components of the planetary gear test bench are computed from the measured transfer functions.

Resumen

Los trabajos de investigación orientados a la caracterización del comportamiento dinámico de transmisiones constituyen una cuestión de gran interés teniendo en cuenta la necesidad permanente de reducir los niveles de vibración y ruido, manteniendo su elevada compacidad y eficiencia. La mayor parte de los estudios se han concentrado en transmisiones operando en condiciones de funcionamiento estacionarias, en donde la velocidad y la carga a transmitir se consideran constantes. No obstante, es muy común encontrarse, en multitud de aplicaciones en la industria, con condiciones de operación no estacionarias, tales como arranques y paradas repetitivas así como variaciones de la carga y de la velocidad.

El trabajo presentado a lo largo de esta tesis tiene como objeto fundamental conseguir una mejor comprensión del comportamiento dinámico de transmisiones planetarias operando en condiciones no-estacionarias. Este tipo de transmisiones se emplean habitualmente en los generadores eólicos, componentes aeronáuticos, transmisiones en vehículos convencionales e híbridos, etc. Con el fin de alcanzar los objetivos propuestos, se ha analizado un banco de ensayos de transmisiones planetarias con recirculación mecánica de potencia combinando simulaciones y ensayos experimentales.

Se ha llevado a cabo un análisis modal del citado banco con el objetivo de determinar las frecuencias naturales, los modos de vibración y la distribución de energía cinética y de deformación. Para conseguir este propósito, se ha desarrollado un modelo de parámetros concentrados del banco, considerando tres grados de libertad para cada uno de los componentes. Los resultados numéricos se han contrastado con los que se han obtenido de un análisis modal experimental realizado sobre el banco de ensayos.

En primer lugar, se ha investigado el comportamiento dinámico del banco de ensayos en condiciones de operación estacionarias, considerando carga y velocidad constante. El objetivo

de este análisis ha sido resaltar la modulación en amplitud de las señales temporales registradas en el anillo exterior, como consecuencia de la influencia de cada uno de los planetas al pasar por las proximidades del punto de medida. Esta modulación se ha manifestado en forma de bandas laterales asimétricas alrededor de la frecuencia de engrane y sus armónicos, tanto en los resultados numéricos como en los experimentales.

A continuación, el trabajo de tesis se ha orientado al estudio del comportamiento de transmisiones planetarias en condiciones no-estacionarias. En particular, se han analizado distintas situaciones, tales como carga y velocidad variable, arranques y paradas combinando simulaciones numéricas y registros experimentales. Los resultados obtenidos han sido analizados mediante la Transformada de Fourier de Tiempo Reducido (STFT), resaltando la modulación simultánea en fase y amplitud.

Además, se ha estudiado el reparto de carga entre planetas, teniendo en cuenta la interacción entre el contacto en los engranajes, el efecto de la gravedad sobre el porta-satélites y la existencia de errores de posición de los planetas operando en condiciones estacionarias. También se ha estudiado el efecto de la velocidad de operación en el reparto de carga durante el régimen de arranque.

Finalmente, se ha aplicado una técnica para el análisis de la trayectoria de transferencia, denominada Transmisibilidad Global Transmisibilidad Directa, con el fin de evaluar la propagación de la vibración en las transmisiones planetarias operando en condiciones estacionarias y no-estacionarias. Las transmisibilidades directas entre los distintos componentes se han obtenido a partir de la medida experimental de las funciones de transferencia.

Table of contents

Introduction	1
Chapter 1 : bibliographic study	4
1. Introduction.....	6
2. State of the art of the dynamics of gears.....	7
2.1. Models in the literature.....	7
2.2. Kinematic characteristics.....	10
2.3. Tooth deflection of spur gear.....	14
2.4. Mesh Stiffness	14
2.5. Damping	18
3. Modelling of Non Stationary Excitations for Transmission Systems.....	19
3.1. Variable load.....	19
3.2. Variable speed	20
3.3. Run up.....	22
3.4. Acyclism.....	26
4. Techniques for detection of the non stationary excitation	28
4.1. Time domain descriptors	29
4.1.1. The Root Mean Square (RMS).....	29
4.1.2. The crest factor F_c	30
4.1.3. Kurtosis	30
4.1.4. Time synchronous averaging (TSA)	31
4.2. Frequency domain descriptors.....	31

4.2.1. Spectral analysis	31
4.2.2. Envelope Analysis	32
4.3. Cepstrum analysis	34
4.4. Joint time-frequency analysis	35
4.4.1. Short Time Fourier Transform (STFT):	35
4.4.2. Wigner-Ville Distribution	36
4.4.3. Wavelet Transformation:	36
4.4.4. Continuous wavelet transformation:	36
5. Experimental test benches	37
6. Modal analysis of planetary gear	40
7. Load sharing behavior of planetary gear	42
8. Transfer path analysis (TPA)	44
8.1. Classical transfer path analysis	44
8.2. Approaches to TPA	45
9. Conclusion	46
Chapter 2 : Description of the test bench	48
1. Introduction	49
2. Test bench description	49
3. Instrumentation	55
3.1. Existent instrumentation	55
3.2. Developed instrumentation	57
4. Excitation method	62
5. Data analysis	63
5.1. Data acquisition system	63
5.2. Data Software	64
6. Conclusion	65

Chapter 3 : Modal analysis of back-to-back planetary gear	66
1. Introduction	67
2. Experimental setup	67
3. Numerical model	67
4. Results	71
4.1. Natural frequencies and vibration modes	71
4.1.1. Teeth modes	73
4.1.2. Bearing modes	77
4.2. Analysis of the distribution of modal kinetic energies and modal strain energies	79
4.2.1. Teeth modes	79
4.2.2. Bearing modes	82
5. Conclusion	84
Chapter 4 : Dynamic behavior of back-to back planetary gear in non-stationary conditions	86
1. Introduction	87
2. Numerical model	87
3. Stationary conditions	90
3.1. Frequency characterization of the planetary gear	95
3.2. Effect of loading variation on frequency content	101
4. Variable load	105
5. Run up regime	108
6. Run down regime	114
7. Variable speed	120
8. Conclusion	123

Chapter 5 : Load sharing and transfer path analysis	124
1. Introduction	125
2. Planet load sharing	125
2.1. Planet load sharing under stationary conditions	125
2.1.1. Effect of meshing phase	126
2.1.2. Effect of gravity of carrier.....	127
2.1.3. Effect of planet position error	130
2.1.4. Correlation with experimental results	131
2.2. Load sharing behavior under the run-up regime	132
3. Transfer Path Analysis	134
3.1. Calculation of the direct transmissibility matrix	134
3.2. Operational response decomposition.....	136
3.3. Experimental setup	137
3.4. Experimental results	139
3.4.1. Global and direct transmissibilities	139
3.4.2. Operational response reconstruction in the stationary conditions.....	142
3.4.3. Operational response reconstruction in the run-up regime	145
4. Conclusion	147
Contribution, conclusion and future work	149
Contribuciones, conclusiones y trabajo futuro	154
Scientific publications	159
References	161

Introduction

It is well known that mechanical transmissions produce vibration and noise induced by various excitations to which they are subjected. These excitations can be divided into internal and external ones. The internal excitations are mainly caused by changes in internal properties of the system like stiffness. External excitations can be associated to changes on the transmission operating conditions such as driving and loading torques and/or speed variation.

Gears are popular mechanical transmission used in several industrial applications.

The increasing demand on improving performance in terms torque, speed, compactness, and cost of production explains the multiplicity of research developments in this kind of power transmission system.

Among the variety of gear transmissions, planetary gears are widely used like in wind turbines, hybrid car transmissions and new generation aircraft engines. They are characterized by the ability to transmit significant amount of power with large speed reductions or multiplications. Different gear ratios can be achieved by changing the input, the output and the reaction components. In addition, their configuration is axi-symmetric and their planets are equally spaced. With these two characteristics, the radial forces created at the meshes of each gear set balance each other. So, the radial bearing forces is zero. Furthermore, the input load sharing in planets reduce the gear loads. Finally, the self-centering capability of planetary gear sets tends to reduce many effects of manufacturing errors.

Planetary gear sets are also known to exhibit several unique behaviors like planet load sharing as a function of manufacturing errors, planet mesh phasing for cancellation or neutralization of the gear mesh excitations. Modulation sidebands can be recognized as harmonic orders other than the pure tones defined by the gear mesh harmonics in vibration and noise spectra of geared systems have been studied extensively.

Planetary gears are used work in different operating conditions. The most critical conditions are those including variable speed and load, acyclism, repetitive run up and run downs called non-stationary operating conditions. This thesis will investigate through numerical and experimental studies the influence of non-stationary operating condition on a back to back planetary gear transmission.

This dissertation is presented in five chapters. Literature review is presented in the first chapter. State of the art of the dynamics of planetary gear is first presented. The internal excitation on gear and especially in the planetary gear is highlighted. In addition, an investigation on modulation sidebands in the stationary condition observed in different kind of planetary gear is presented. Techniques for detection of non-stationary excitations are detailed. Finally, state of art of load sharing behaviour of planetary gear and the transfer path analysis and its approaches are detailed.

The second chapter will be dedicated to the description of the test bench used for experiments. The back to back mechanical configuration of the planetary gear transmission setup is presented. Instrumentation layout and driving motor systems are then presented. A focus will be done on data processing methods and techniques.

In the third chapter, modal analysis of a back-to-back planetary gear is achieved. Natural frequencies are numerically computed following the development of a model of the transmission. Correlations with natural frequencies extracted from experimental impact tests are done. Classification of modes into bearing and gear modes is then detailed. The distribution of modal kinetic energies and modal strain energies is analysed.

The dynamic behavior of back-to-back planetary gear in stationary and non-stationary conditions is studied on the fourth chapter. A model of back-to-back planetary gear is defined. The effect of variable loading conditions on the dynamic behavior of the transmission is highlighted. Frequency characterization of the planetary gear and effect of loading variation on frequency content are studied numerically and correlated with experiments. In addition, the dynamic behavior of back-to-back planetary gear is studied in the cases of variable speed, run up and run down regimes. The numerical results are compared and correlated to experimental results.

In the last chapter, the effects of meshing phase, the gravity and the error position of the pin hole of planets on the load sharing behavior are studied numerically and validated experimentally in the stationary condition and in the run-up and the run-down regimes. Then, an approach to the classical transfer path analysis called “direct transmissibility global transmissibility” is used to study the propagation of vibration in the case of stationary condition and in the run up regime.

In the final part of this dissertation a conclusion and future work will be presented.

Chapter 1:

Bibliographic study

Sommaire

1. Introduction.....	6
2. State of the art of the dynamics of gears.....	7
2.1. Models in the literature.....	7
2.2. Kinematic characteristics.....	10
2.3. Tooth deflection of spur gear.....	14
2.4. Mesh Stiffness	14
2.5. Damping	18
3. Modelling of Non Stationary Excitations for Transmission Systems.....	19
3.1. Variable load.....	19
3.2. Variable speed	20
3.3. Run up.....	22
3.4. Acyclism.....	26
4. Techniques for detection of the non stationary excitation	28
4.1. Time domain descriptors	29
4.1.1. The Root Mean Square (RMS).....	29
4.1.2. The crest factor F_c	30
4.1.3. Kurtosis	30
4.1.4. Time synchronous averaging (TSA)	31
4.2. Frequency domain descriptors.....	31

4.2.1. Spectral analysis	31
4.2.2. Envelope Analysis	32
4.3. Cepstrum analysis	34
4.4. Joint time-frequency analysis	35
4.4.1. Short Time Fourier Transform (STFT):	35
4.4.2. Wigner-Ville Distribution	36
4.4.3. Wavelet Transformation:	36
4.4.4. Continuous wavelet transformation:	36
5. Experimental test benches	37
6. Modal analysis of planetary gear	40
7. Load sharing behavior of planetary gear	42
8. Transfer path analysis (TPA)	44
7.1. Classical transfer path analysis	44
7.2. Approaches to TPA	45
9. Conclusion	46

1. Introduction

This chapter will be dedicated in its first part to a state of art of the dynamics of gear. Models in literature, kinematic characteristics of planetary gear, tooth deflection and mesh stiffness are described in this part. Variable speed, variable load, run up and acyclism which are the main non stationary excitations for transmission systems are presented in the second part. The main techniques for detection and characterization, of non stationary excitations are also presented. Literature on load sharing behavior of planetary gears is discussed. Finally, the transfer path analysis and its approaches are detailed.

Gearboxes are powerful kind for power transmissions in various mechanisms and especially in rotating mechanisms. The planetary gears are one of the most used gears. A planetary gear set is a particular group of gears which ensure transmission of power between two coaxial shafts with multiple combinations corresponding to reduction or multiplication ratios.

It consists of four types of moving components (Fig 1.1):

- The sun (S): it is an external gear; it is generally the input component of the gear train and drives the planets.
- Planets (P): their number varies from 3 to 6. They rotate around their axes and around the sun.
- The carrier (C): includes the axes on which are mounted the planets, it is often the output component of the planetary gear transmission.
- The ring (R): It is an internal gear. It can also be the housing of the whole transmission (fixed ring).

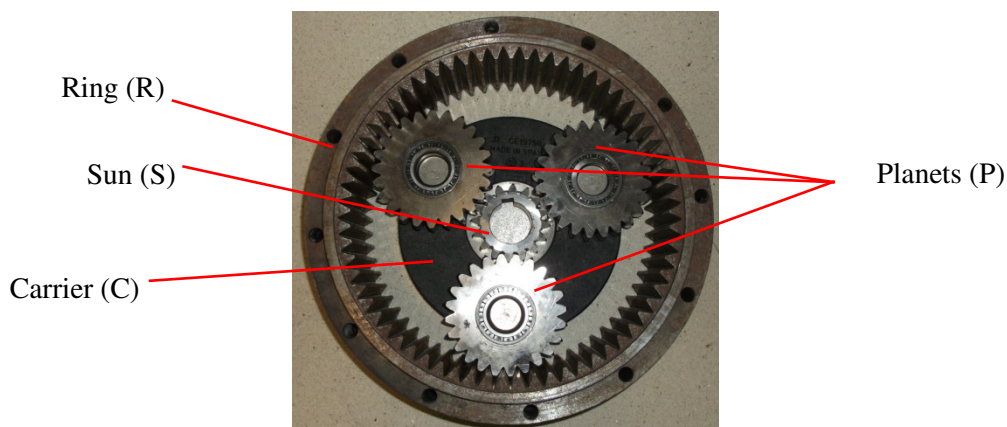


Fig 1.1: Planetary gear

Planetary gears are particularly useful due to their compactness and their ability to transmit a significant power with lower loads on the bearings and low level of vibration and noise.

In 1781, James Watt was the first scientist who submitted a patent for a system consisting of a sun and one planet (Dickinson and Jenkins, 1981).

The compact structure and arrangement in-line component of the planetary gear has found success with design engineers of the first automobiles. Lanchester (Lanchester, 1924) was the first who used two-stages planetary gear set in automotive industry. He used the ring of the first stage as a carrier on the second stage. Stoeckicht (Hidaka et al., 1976a) adapted the planetary gear set for aeronautics and marine engineering.

Nowadays, the planetary gear trains are frequently used as elements of reduction in gas turbines, rotors of helicopters, engines of agricultural machinery...

2. State of the art of the dynamics of gears

2.1. Models in the literature

It is well known that gears produce vibration and noise by excitations localized at the contact between teeth.

For reasons of simplicity, many researchers used lumped models (mass-springs) (Figure 1.2). The gears are considered as rigid cylinders connected by a stiffness modeled as an elastic connection between teeth (meshing stiffness) (Kohler 1989) (Özguven and Houser, 1988) (Maatar 1995). The dynamic study consists in solving the dynamic equation of motion of such models which can be written as:

$$M \ddot{q} + C \dot{q} + K(t)q = F(t) + E(t) \quad (1.1)$$

Where M is the mass matrix. $K(t)$ is the stiffness matrix, C is the damping matrix and $F(t)$ is the vector of the external torque vector applied on the system and $E(t)$ is the vector of geometric errors excitations.

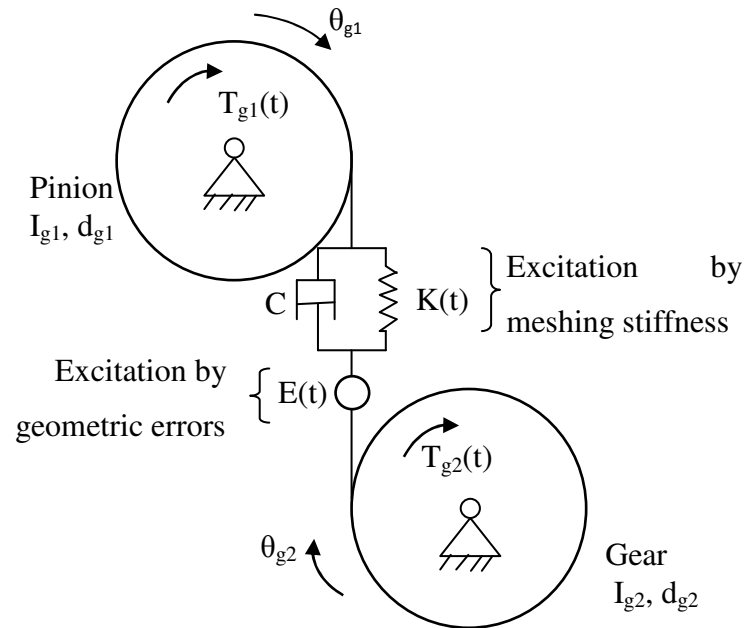


Fig 1.2: Dynamic model of one stage of spur gear with two degree of freedom (Özguven and Houser, 1988)

The studies of the dynamic behavior of gearboxes are based on the transmission error which was introduced by Harris (Harris 1958). The transmission error takes account of the instantaneous deflections on loaded teeth and the influence of variations of shape and mounting.

Depending on the objectives, the stiffness linking two gears, called mesh stiffness, is assumed as:

- Constant for global studies in order to determine natural modes. Contacts between teeth are then reduced to average mesh stiffness.
- Periodic, to take account of variations in the length of contact between mating teeth. These models describe the parametric excitations of the meshing.
- Non- linear to reflect the instantaneous contact areas fluctuations and especially transient loss of contact due to significant variations in the transmitted torque.

For planetary gear transmission, modeling the dynamic behavior was initiated by Cunliffe (Cunliffe et al 1974) who studied the vibration response for the case of fixed carrier. The model was with lumped parameters and the correlation "theory-experiment" was satisfactory. Botman (Botman et al 1976) proposed a model with three degrees of freedom for each component; gears are linked by constant stiffness. For lightweight structures (Aircraft),

Stockton (Stockton 1985) developed techniques for the study of axis-symmetric structures to characterize repetitive patterns of body gear.

August and Kasuba (August et al 1986) built a torsional model of a planetary gear set, translational degrees of freedom are introduced into the sun. The numerical results indicate that floated suns have a limited interest in the case of high speed.

Several analytical investigation and the finite element models of planetary gears were also developed in the last decades.

Saada and Vexex (Saada et al 1995) developed a finite element model of a planetary gear train the influence of some parameters (planets shafts, sun and ring supports) on the generation overloads at the contact zones.

Kahraman (Kahraman, 1994a) established an analytical model including a variable meshing stiffness. It was extended to a 3-dimensional model and he determined the influence of planets phase on the dynamic response (Kahraman, 1994b).

Kahraman and Blankenship (Kahraman et al., 1994) used the 3D model to determine the load sharing on planets. Kahraman (Kahraman, 1994c) has reduced its model to a purely torsional model to find the natural frequencies and the corresponding vibration modes.

Lin and Parker (Lin and Parker 1999a) developed a model of a planetary gear set which was used for modal analysis and in particular to study the gyroscopic effect on the system. Agashe (Agashe 1998) and Parker (Parker et al. , 2000a) used a finite element tool in order to determine the dynamic response and the influence of planets phasing by including fluctuating mesh stiffness and transmission error. Chaari et al (Chaari et al, 2009) used the finite element model in order to validate analytical model of meshing stiffness in the cases of healthy and cracked pinion.

Furthermore, Parker (Parker, 2000) has shown the efficiency of selecting the phase shift between planets to reduce the vibration of the planetary gear. Kahraman (Kahraman , 2001) developed a family of torsional dynamic models of compound gear sets to predict the free vibrations characteristics under different kinematic configurations resulting in different speed ratios.

Regarding experimental studies, a series of tests on the dynamic behavior of planetary gear set was conducted by Hidaka and his colleagues on a gearbox type Stoekicht (Hidaka et al 1976a) (Hidaka et al 1976b) (Hidaka et al 1977)(Hidaka et al. 1979a) (Hidaka et al. 1979b) (Hidaka et al. 1979c) (Hidaka et al. , 1979d) . They highlighted the distributions of the load and the effect of phase shift of tooth meshing.

Chiang and Badgley (Chiang et al 1973) observed spectra from the vibration of the ring of a planetary gearbox of two helicopters. Toda and Botman (Toda et al 1979) have shown experimentally on a planetary gear set of a turboprop airplane PT6 engine vibrations from the error of spacing of can be minimized by proper indexing of planets. Rakhit (Rakhit 1997) measured the asynchronous vibration of a gas turbine generator and proposed a new design of a planetary gear train to reduce vibration.

Kahraman (Kahraman, 1999) developed a generalized model to predict the load sharing on planets and validated the model with experimental tests.

Ligata (Ligata et al, 2008) and Inalpolat and Kahraman (Inalpolat and Kahraman 2009) used the same test bench which is a back-to-back planetary gear set configuration: the electric motor powers the suns of both gear set. Ligata used a 32 channel four strain bridge modules to compare the load sharing between planets for different kind of planetary gear (3-6 planets). Inalpolat (Inalpolat and Kahraman 2009) used accelerometers which are mounted radially on the outside surface of the ring and a photoelectric sensor measured the angular speed of the sun gear shaft in order to validate experimentally the investigation on modulation sidebands observed in planetary gear.

2.2. *Kinematic characteristics*

The variation of the mesh stiffness is the main source of excitation of the gear trains (Özguven and Houser, 1988). It occurs at mesh frequency f_m . For a single-stage gearbox, it can be expressed as a function of frequency of rotation of the pinion f_1 and frequency of rotation of wheel f_2 and their number of teeth Z_1 and Z_2 :

$$f_m = Z_1 f_1 = Z_2 f_2 \quad (1.2)$$

$$\text{With } f_1 = \frac{2\pi N_1}{60} \text{ and } f_2 = \frac{2\pi N_2}{60}$$

N_1 and N_2 are the rotation speeds of the pinion and the wheel expressed in “rpm”.

The meshing period T_m is defined by:

$$T_m = \frac{1}{f_m} \quad (1.3)$$

The planetary gear trains are considered as special case of the assembly of conventional gear trains. The multiplicity of meshing and the existence of internal and external meshes yield to very specific mounting schemes.

Henriot (Henriot 1985) classified planetary gear sets according to morphology. The four main types are presented in Figure 1.3.

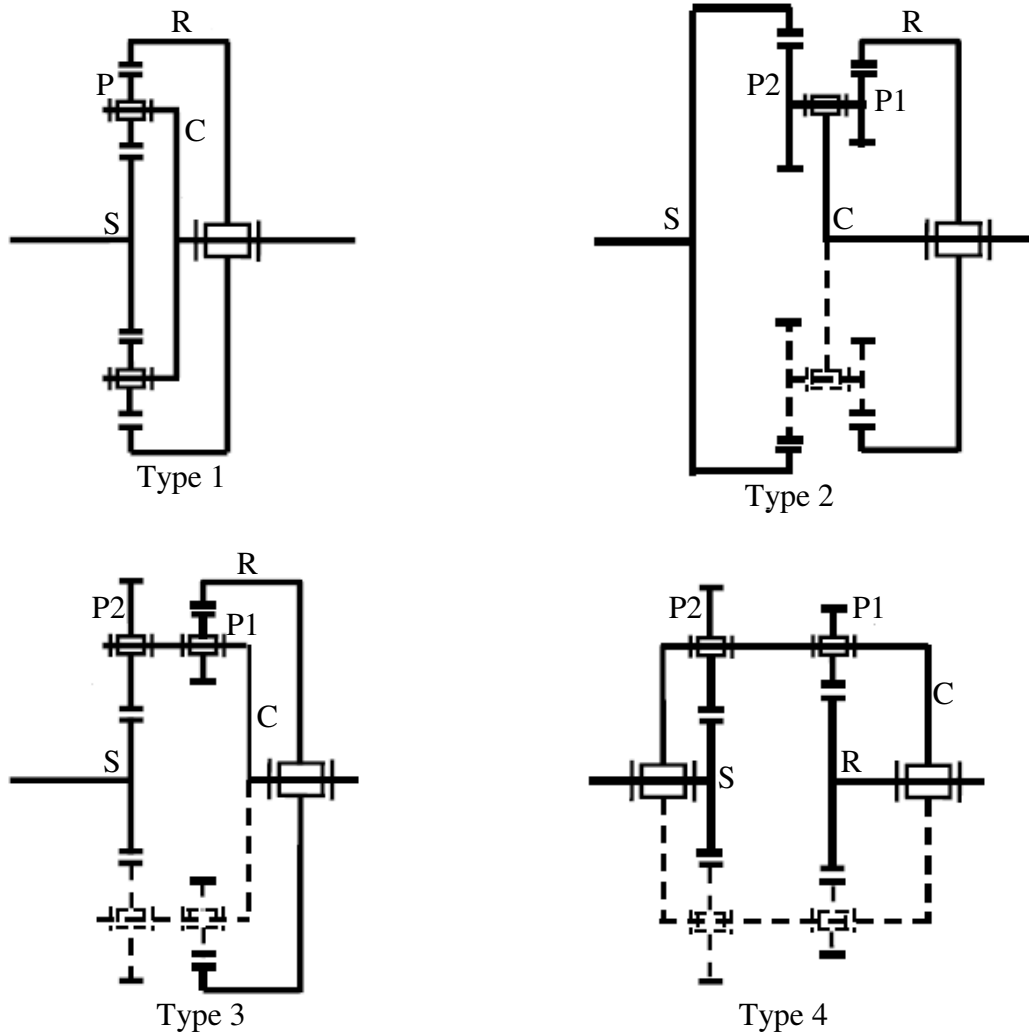


Fig 1.3: Different types of planetary gear sets

The basic transmission ratio K_W of a planetary gear set is given by the Willis formula:

$$K_W = \frac{\Omega_R - \Omega_C}{\Omega_S - \Omega_C} \tag{1.4}$$

With Ω_R , Ω_C and Ω_S are respectively the angular velocities of the ring, the carrier and the sun. The transmission ratio of the planetary gear R is the ratio of velocity of the input component by the velocity of the output component:

$$R = \frac{\Omega_{input}}{\Omega_{output}} \tag{1.5}$$

Each one of the three components (Sun, ring and carrier) can be input, output or blocked. There are six possible configurations of motion transmission, summarized in Table 1.1.

	1	2	3	4	5	6
Input	S	C	R	R	S	C
Blocked	C	R	S	C	R	S
Output	R	S	C	S	C	R
R	K_W	$(K_W - 1)/ K_W$	$1/(1 - K_W)$	$1/ K_W$	$K_W / (K_W - 1)$	$1 - K_W$

Table 1.1: Transmission configurations for planetary gear set

We note by Z_S , Z_R and Z_P the number of teeth respectively of the sun, the ring and planets. f_S and f_R the frequency of rotation of the sun and the ring, the meshing frequency f_m can be written in the case of blocked ring by:

$$f_m = \frac{Z_S Z_R}{Z_S + Z_R} f_S \quad (1.6)$$

For the case of a blocked sun, it is written by:

$$f_m = \frac{Z_S Z_R}{Z_S + Z_R} f_R \quad (1.7)$$

For the case of fixed carrier, the gearbox is reduced to a two-stage gear and the meshing frequency can be expressed by:

$$f_m = Z_S f_S \quad (1.8)$$

Some applications, like automotive transmission, need from three to six speed ratios. Three or four speed ratios can be obtained by connecting two single-stages planetary gear sets in certain kinematic configurations whereas five or six speed ratio are achieved by complicated planetary gear called “compound planetary gear set” (Kahraman, 2001). This kind of planetary gear allows significant reductions in transmission size and weight which made it very desirable for many applications. Figure 1.4 shows the two most common examples of compound planetary gear systems.

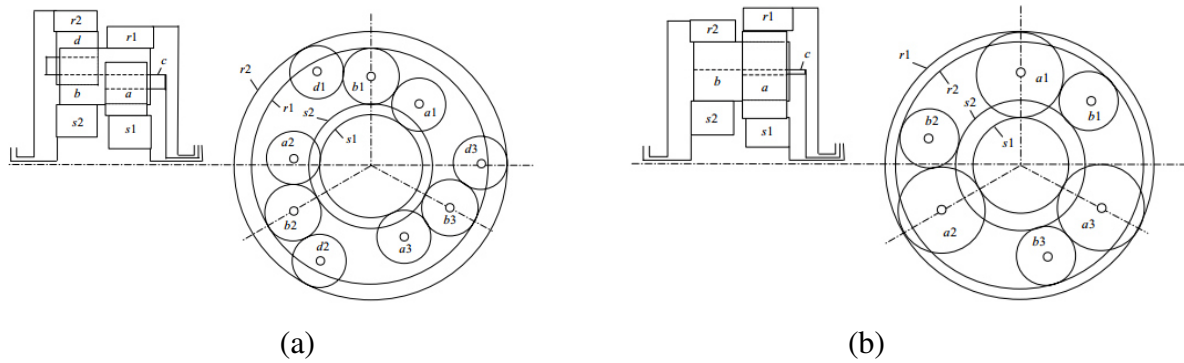


Fig 1.4: Two common types of compound planetary gear set (Kahraman, 2001)

The first type is known as “Ravigneaux” gear set (Fig 1.4. (a)): “b”, a long planet, connects two planes of gear sets (s1-a-b-r1 and s2-b-d-r2). “s1” and “s2” are the sun gears, “r1” and “r2” are the ring gears and “a” and “d” are the short planets. All planets are supported by a common carrier “c”. The second type is kinematically equivalent to the first one: two single planetary gear set (s1-a-r1 and s2-b-r2) are connected through the mesh of the long planet “a” and the short planet “b”. Planets “a” and “b” are supported through a common carrier “c”.

Five central components (s1, r1, s2, r2 and c) can be used as input, output or reaction components in both arrangements and only three of these five components will have assignments. So, 60 distinct power flow configurations can be founded (Permutation of 3 from 5: $P(5,3)=60$). Once assignments are determined, 6 ways as input, output and reaction members can be used ($P(3,3)=6$). Fig 1.5 shows 10 distinct configurations for consideration in dynamic analysis (Combination of 3 from 5: $C(5,3)=10$).

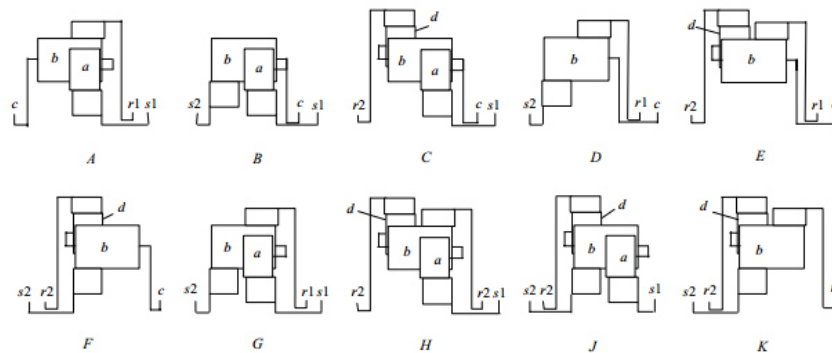


Fig 1.5: Ten distinct configurations of compound planetary gear set (Kahraman, 2001)

2.3. *Tooth deflection of spur gear*

The study of the loaded tooth deflection has been widely considered by designers to estimate the capacity of the load transmission of gear.

This study is of great importance for calculating the transmission errors of the spur gear, the stiffness of teeth as well as dynamic loads applied to the teeth and also for the study of the vibration of gear system.

The estimate of the stiffness of teeth at different points of contact on the flank and during different phases of meshing allows determining the mesh stiffness which is the main source of excitation of the system.

Several methods for calculating the deflection of teeth under load are used, the most recent being the finite element method (FEM). Analytical methods have also proven effective. Various analytical approaches have been used in the literature.

Timoshenko and Baud (Timoshenko and Baud 1924) considered gear tooth as embedded beam and divided the deflection of teeth in a hertzian local deflection and a bending deflection.

Nakada and Utagawa (Nakada and Utagawa 1956) considered a tooth as a variable section beam. The tooth deflection is induced by bending, shear and compression as well as hertzian contact. Weber (Weber, 1949) took into account the particular form of involute circle to calculate the deflection due to bending and expressed deflection of foundation. Based on the work of Weber, Cornell (Cornell, 1981) determined the compliance (flexibility) of a pair of teeth in contact as well as the variation constraints.

Shing (Shing, 1994) and Maatar (Maatar, 1995) considers that during meshing, the deflection of tooth consists of a deflection of the bending and shearing of the tooth " δ_f ", a deflection of the fillet-foundation of the tooth gear " δ_v " and hertzian deflection " δ_h ".

2.4. *Mesh Stiffness*

The computation of the mesh stiffness results from calculating the tooth deflection. Indeed, since the total tooth deflection is the sum of different deflections mentioned, the equivalent mesh stiffness k_m is calculated, for a given position of the loading, by putting in series bending- shearing stiffness k_f and fillet-foundation stiffness k_v .

$$\frac{1}{k_m} = \frac{1}{k_f} + \frac{1}{k_v} \quad (1.9)$$

To obtain the equivalent mesh stiffness k_{12} of a pair of teeth in contact, the stiffness of the pinion tooth (1) and the wheel tooth (2) and the stiffness of contact k_h are placed in series so that:

$$\frac{1}{k_{12}} = \frac{1}{k_1} + \frac{1}{k_2} + \frac{1}{k_h} \quad (1.10)$$

In the case of spur gear, the number of teeth in contact depends to the contact ratio. If the contact ratio is between 1 and 2, the meshing stiffness is sometimes maximal corresponding to two pairs of teeth on contact (Fig 1.6) and sometimes minimal corresponding to a pair of teeth on contact (Velex, 1988).

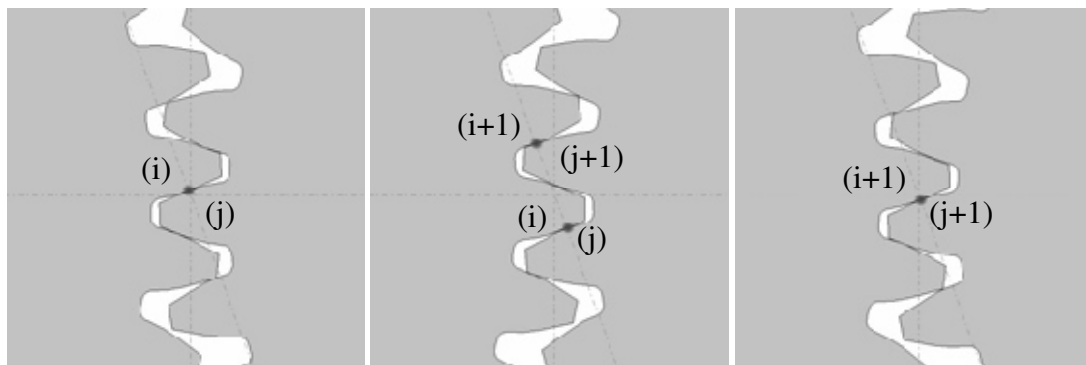


Fig 1.6: Succession 1 pair of teeth - 2 pairs of teeth in contact

This variation can be approximated as square function (Lin and Parker, 2002) (Lin and Parker, 2000a) (Maatar, 1995). Figure 1.7 shows the time evolution of the mesh stiffness.

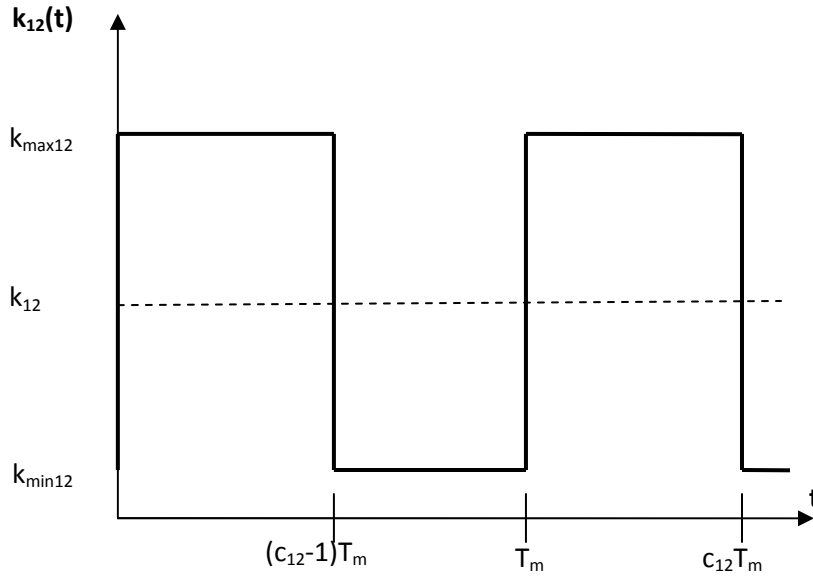


Fig 1.7: Evolution of the mesh stiffness $k_{12}(t)$

c_{12} is the contact ratio of the transmission. T_m is the meshing period. $k_{\max 12}$, $k_{\min 12}$ and k_{12} represent respectively the values of the maximum, the minimum and the average values of the mesh stiffness.

The Fourier series expansion of $k_{12}(t)$ gives:

$$k_{12}(t) = k_{12} + \frac{\Delta k}{\pi} \sum_{i=1}^{\infty} \frac{1}{i} \left[\sin((2i\pi(c_{12}-1)) \cos(\frac{2i\pi t}{T_m}) + (1 - \cos((2i\pi(c_{12}-1))) \sin(\frac{2i\pi t}{T_m}) \right] \quad (1.11)$$

where:

$$k_{12} = k_{\max 12} (c_{12} - 1) + (2 - c_{12}) k_{\min 12} \quad (1.12)$$

$$\Delta k = k_{\max 12} - k_{\min 12} \quad (1.13)$$

Henriot (Henriot, 1985) provided an empirical formula for the calculation of the average stiffness of a pair of teeth in contact. It is expressed in N/microns/m by:

$$k_{12} = \frac{b}{A_1 + \frac{A_2}{z_1} + \frac{A_3}{z_2}} \quad (1.14)$$

With $A_1 = 0.04723$, $A_2 = 0.15551$, $A_3 = 0.25791$ and b is the tooth width.

Chari et al (Chari et al, 2008) computed the meshing stiffness as:

$$\frac{1}{k_m} = \frac{1}{k_{b1}} + \frac{1}{k_{f1}} + \frac{1}{k_{b2}} + \frac{1}{k_{f2}} + \frac{1}{k_h} \quad (1.15)$$

Where k_{b1} and k_{b2} are the bending stiffness of pinion and wheel teeth which are considered as a non-uniform cantilever beams (Weber, 1949). k_{f1} and k_{f2} are the corresponding fillet-foundation stiffness which are computed by using the theory of Muskhelishvili (1975) applied to circular elastic rings (Sainsot et al., 2004) which assumes linear and constant stress variations at root circle. k_h is the stiffness of Hertzian contact of two meshing teeth which is considered as constant along the entire line of action (Yang and sun, 1985). Chaari et al (Chaari et al, 2009) confirmed his analytical model using a finite element model.

Fig 1.8 shows the time varying gear mesh stiffness using the two methods.

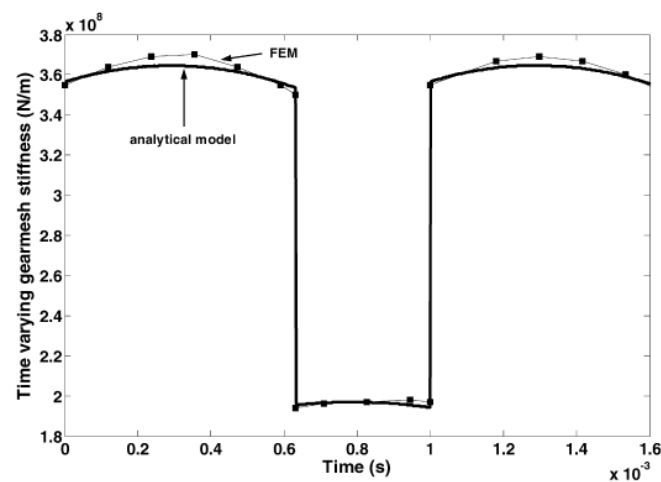


Fig 1.8: Time varying gear mesh stiffness using the two methods (Chaari et al, 2009)

Fernandez et al (Fernandez et al, 2013) computed the meshing stiffness using the finite element model. They decomposed gear deflection into local and global deflections. The local deflection is non linear whereas the global deflection is linear. They considered the interaction between different pairs of teeth in contact and the effect of the load variation on the contact ratio.

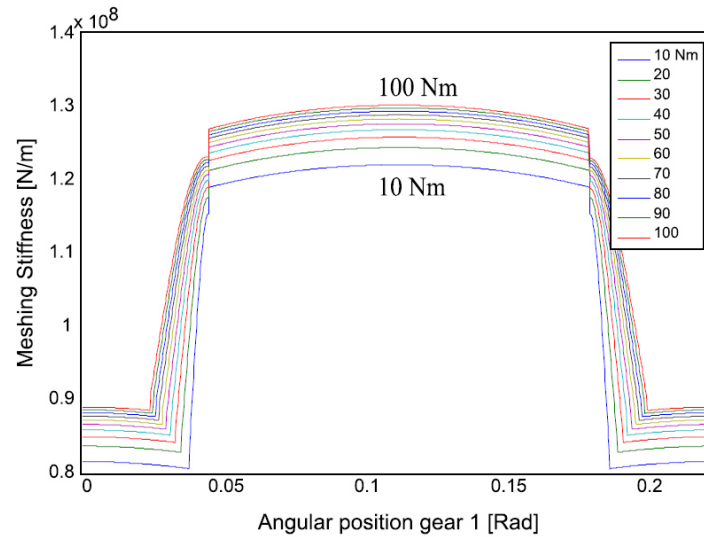


Fig 1.9: Meshing stiffness for several torques throughout a meshing period (Fernandez et al, 2013)

Figure 1.9 shows the meshing stiffness obtained for several transmitted torques (from 10 to 100 Nm with step of 10Nm) in a meshing period. The number of pairs in contact alternates between 1 and 2. The period of double contact and therefore the contact ratio increase clearly as the torque is increased. The magnitude of the meshing stiffness increases with load. In addition, it is evident that local contact model is non linear when the torque is increased.

2.5. Damping

Characterization of energy dissipation in gear transmissions is still a complicate issue. It seems acquired that:

- For elasto-hydrodynamic (EHD) operation with full fluid film, friction forces are neglected overlooked those normal efforts.
- A significant part of the dissipation due to the lubricant comes from effects of crushing, these effects being more important in case of shocks like teeth engagement.

For a gear set in a complex mechanical system, the sources of dissipation are various imperfect (connections and structural damping). Most authors introduce an equivalent viscous modal damping (Al-shyyab and Kahraman, 2007) (Viadero et al, 2014). For models with one or more degrees of freedom, the damping coefficient is:

$$c_i = 2m_i\omega_i\zeta_i \quad (1.16)$$

Where ζ_i is the modal damping ratio varying between 0.01 and 0.2, m_i is modal mass and ω_i is the natural pulsation.

The introduction of damping in the equations of motion is required to obtain a solution around critical areas of operation and to describe dissipative processes in the system.

The viscous damping can be assumed as a proportional damping called ‘‘Rayleigh damping’’. This damping is mass-proportional and stiffness-proportional and can be written as (Rayleigh, 1877):

$$[C] = \alpha [M] + \beta [K] \quad (1.16)$$

Where α is the mass-proportional coefficient and β is the stiffness-proportional coefficient.

The form of Rayleigh damping is orthogonal and respects the system eigen-vectors.

The modal damping ratio can be written for the i^{th} mode (Chopra, 1995):

$$\zeta_i = \frac{\alpha}{2\omega_i} + \frac{\beta\omega_i}{2} \quad (1.17)$$

3. Modelling of Non Stationary Excitations for Transmission Systems

Rotating machinery operates in stationary conditions when the spin speed and the torque exerted are maintained constant by a driving device (Genta, 2005).

In several industrial case, rotating machinery like wind turbines, helicopters, mining machines work in non stationary condition where the speed or/and load are variable. As examples of the non stationary condition, we can cite the run up, the run down, variable speed, variable load and acyclism.

3.1. Variable load

Many researchers have noticed that machines work in non-stationary loading conditions: Bartelmus (Bartelmus et al, 2010) noticed that this will lead to a smearing effect in the spectra of two stage gearbox and planetary gearbox.

Chaari et al (Chaari et al, 2013) presented a bi-dimensional model of a planetary gear running under a periodic load (Fig 1.10) which is applied on the carrier giving rise to variability in the speed of motor and thereafter a variation of the period of the meshing stiffness.

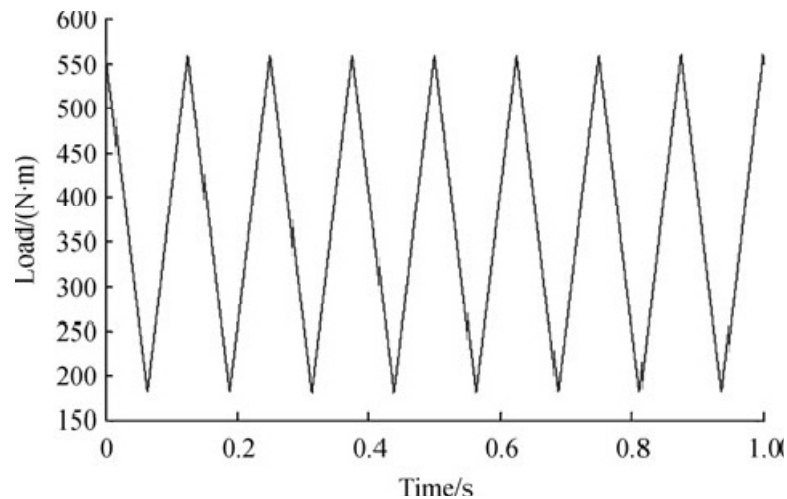


Fig 1.10: Load applied to the carrier (Chaari et al, 2013)

This variation of load modulates in amplitude the time response of the sun (Fig 1.11a). In addition, the STFT (Fig 1.11b) showed sawtooth shapes evolution of mesh frequency and its harmonics.

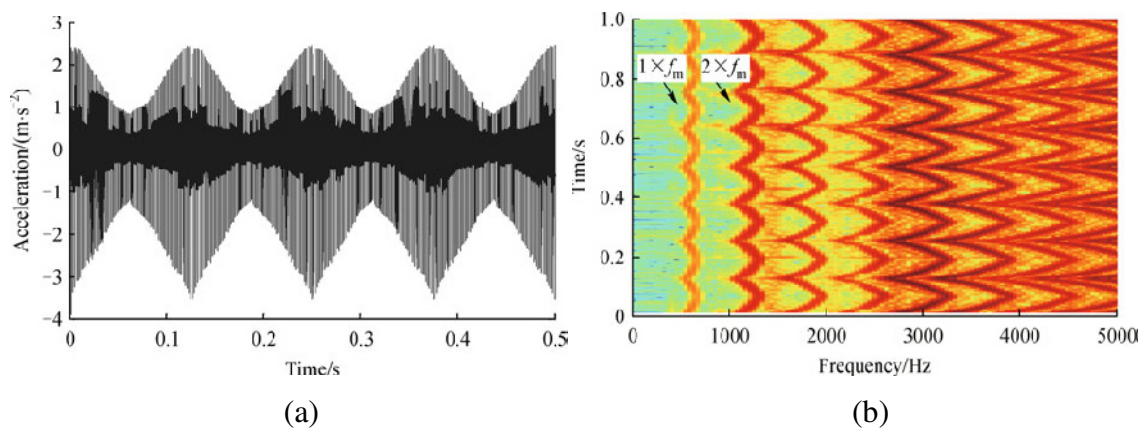


Fig 1.11: Acceleration on the sun: (a) Time response and (b) STFT (Chaari et al, 2013)

3.2 Variable speed

Planetary gears are used under variable speed in many fields of application. The most popular application is that of wind turbines. Zimroz et al (Zimroz et al, 2011) measured the shaft speed and the vibration of wind turbine gearbox. He highlighted the variability in this speed induced by the fluctuation of wind speed (Fig 1.12).

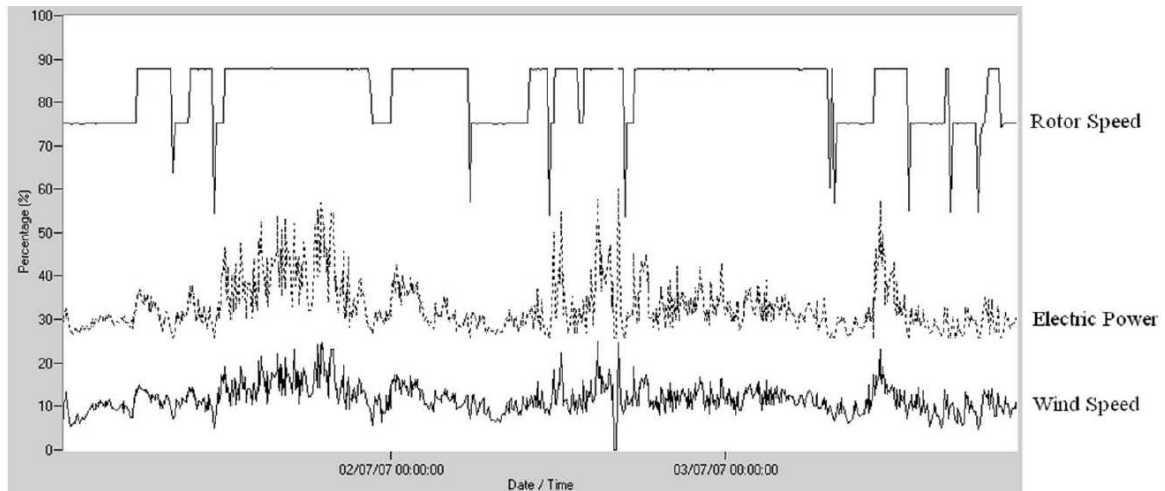


Fig 1.12: Conditions of the wind turbine (Zimroz et al, 2011)

The measured vibration signal is modulated by the variation of speed: when the speed increase, the amplitude of the signal decrease (Fig 1.13a).

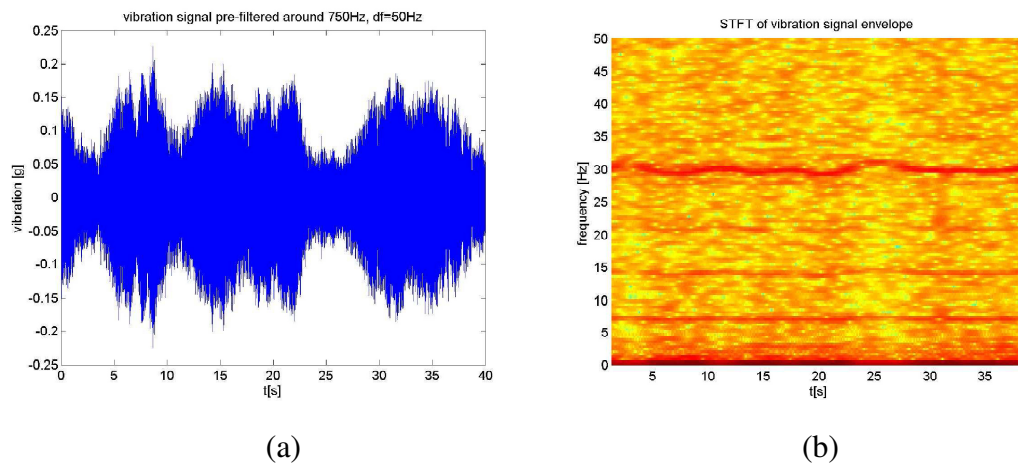


Fig 1.13: Vibration signal: (a) Time response and (b) STFT of the envelope (Zimroz et al, 2011)

The input shaft of the wind turbine is rotating with a time-varying instantaneous speed depending on operating conditions and it causes smearing in the envelope spectra and the STFT of the envelope with time varying mesh frequency and its harmonics (Fig 1.13b).

3.3 Run up

Several systems are subjected to such repetitive run up and run down regimes during their exploitation. The run up regime is very critical especially when the system is overloaded (Drago 2009).

For an electrical motor driving a gearbox, the rotational velocity Ω can be obtained by solving the following equation:

$$J \frac{d\Omega}{dt} = C_m - G_r C_r \quad (1.17)$$

Where J is the equivalent inertia moment of the system, C_m is the motor's driving torque and C_r is the loading torque. G_r is the gear ratio of the system. In the run up regime, the system accelerates ($\frac{d\Omega}{dt} > 0$). So, the motor's torque must be higher than the loading torque.

For an asynchronous motor, C_m can be expressed by (Wright, 2005):

$$C_m = \frac{T_b}{(1 + (s_b - s)^2) \left(\frac{a}{s} - bs^2\right)} \quad (1.18)$$

Where a and b are constants of motor. T_b and s_b are the torque and the slip at breakdown and s is the proportional drop in speed given by:

$$s = 1 - \frac{N}{N_s} \quad (1.19)$$

N and N_s are the instantaneous speed and the synchronous speed of the motor.

Figure 1.14 presents the evolution of driving motor and load torques for a motor connected to a load.

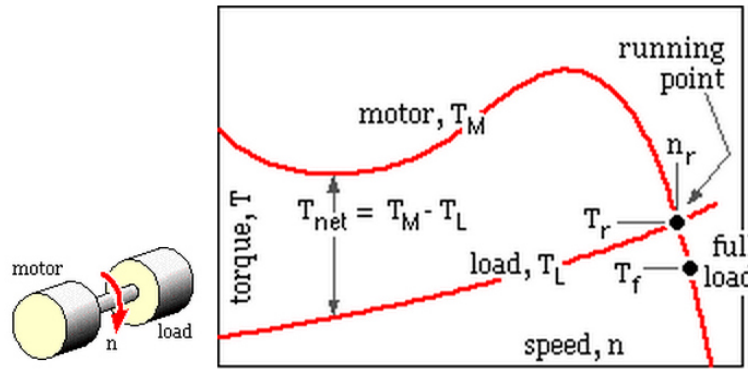


Fig 1.14: Mechanical characteristic of the driving and the driven system (Wright, 2005)

In the run up, the motor torque T_M must always exceed the torque absorbed by the load T_L . The excess torque defined as $T_{net} = T_M - T_L$ is necessary to accelerate the system of motor-load until the system settles at a steady running speed n_r where torque equilibrium obtains ($T_M = T_L = T_r$) and the two characteristics intersect.

During run up regime, the meshing stiffness evolution of a spur gear was modeled by Khabou (Khabou et al, 2011) as square function with decreasing periodicity with respect to time. (Fig 1.15)

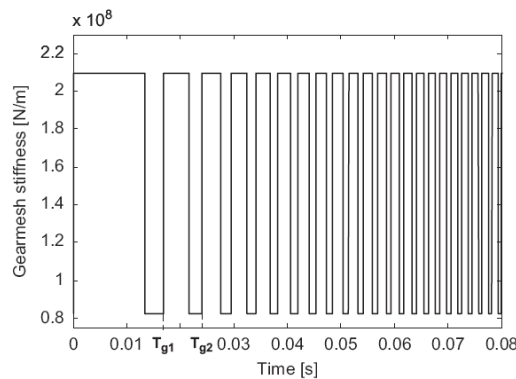


Fig 1.15: Gear mesh stiffness of spur gear under the run up (Khabou et al, 2011)

He showed that the displacement on the bearing of the driven gear is non periodic. (Fig 1.16a)

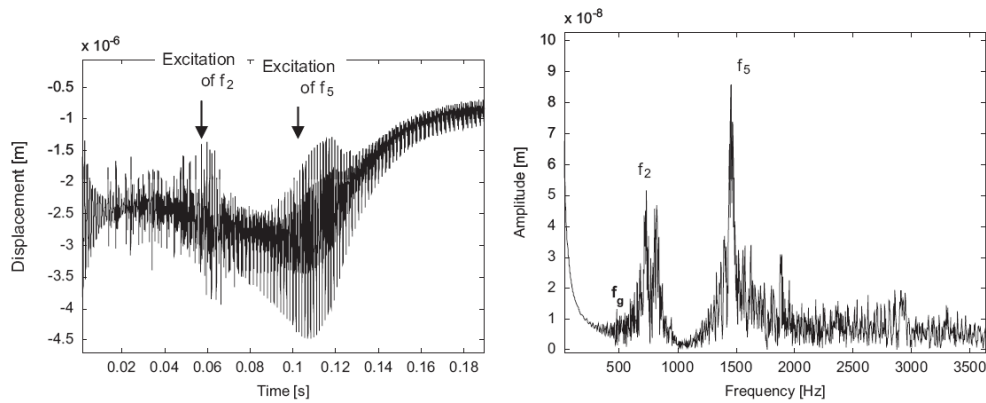


Fig 1.16: Displacement of the bearing of the driven gear and its spectrum (Khabou et al, 2011)

The spectrum (Fig 1.16b) showed a lot of frequency components. High amplitudes are explained by the fact that the system is excited at its natural frequencies.

Recently, Viadero (Viadero et al, 2014) analyzed the dynamic behavior of wind turbine which includes a gearbox composed by a planetary gear and two stage of parallel gears sets. The rotor hub is connected to the carrier of the planetary gear. The planet carrier transmits the power to the low speed shaft via the sun. He used the Cai's approach (Cai, 1995) to present the evolution of the planet-ring meshing stiffness in the run up (Fig 1.17).

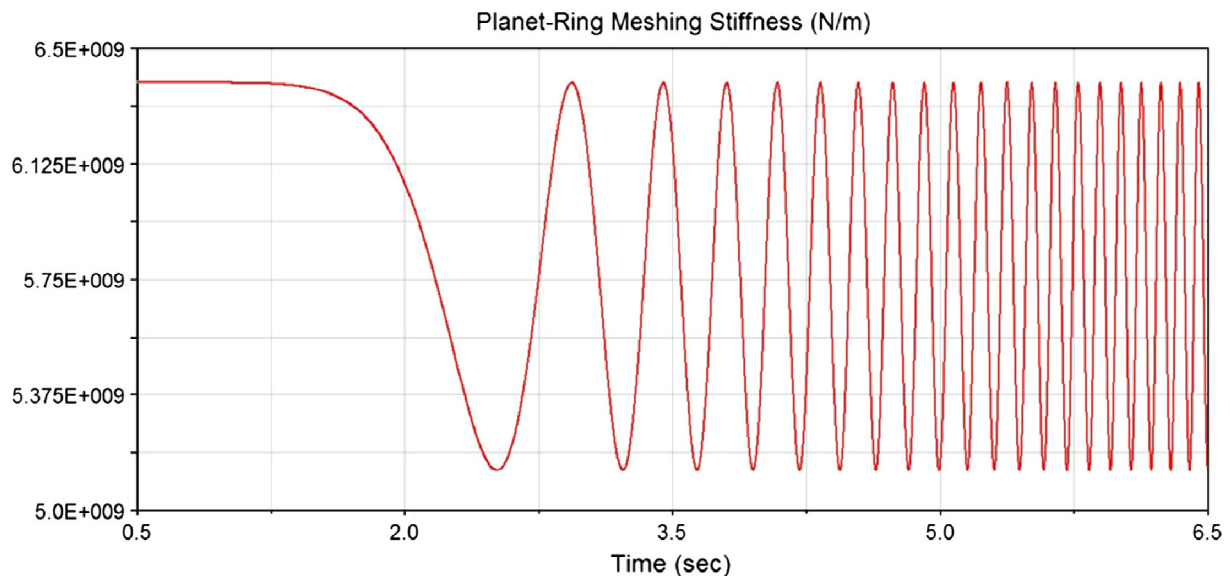


Fig 1.17: Evolution of the mesh stiffness during the run up (Viadero et al, 2014)

Figure 1.18(a) shows the time evolution of the load produced by wind. The effect of thrust and torque of wind are clearly observed during run up and during aerodynamic brake. The

thrust and the torque are increased during run up and decreased in the aerodynamic brake. The loads on the generator and its angular velocity are presented in figure 1.18(b) during run up and during an aerodynamic brake.

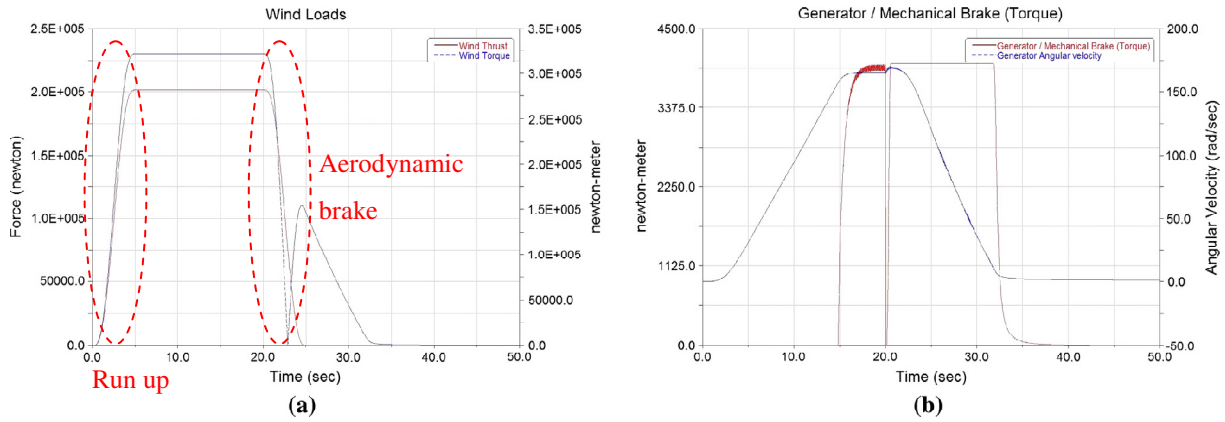


Fig 1.18: In put load (a) and receiver load (b) (Viadero et al, 2014)

Figure 1.19 shows a waterfall spectrum of the high-speed gear stage deflection derivative. Inclined directions are observed representing the evolution of the meshing stiffness during start up (0-15s) and the emergency brake (22s-40s). In addition, the spectrum reveals resonance at low frequencies (approximately 10 Hz).

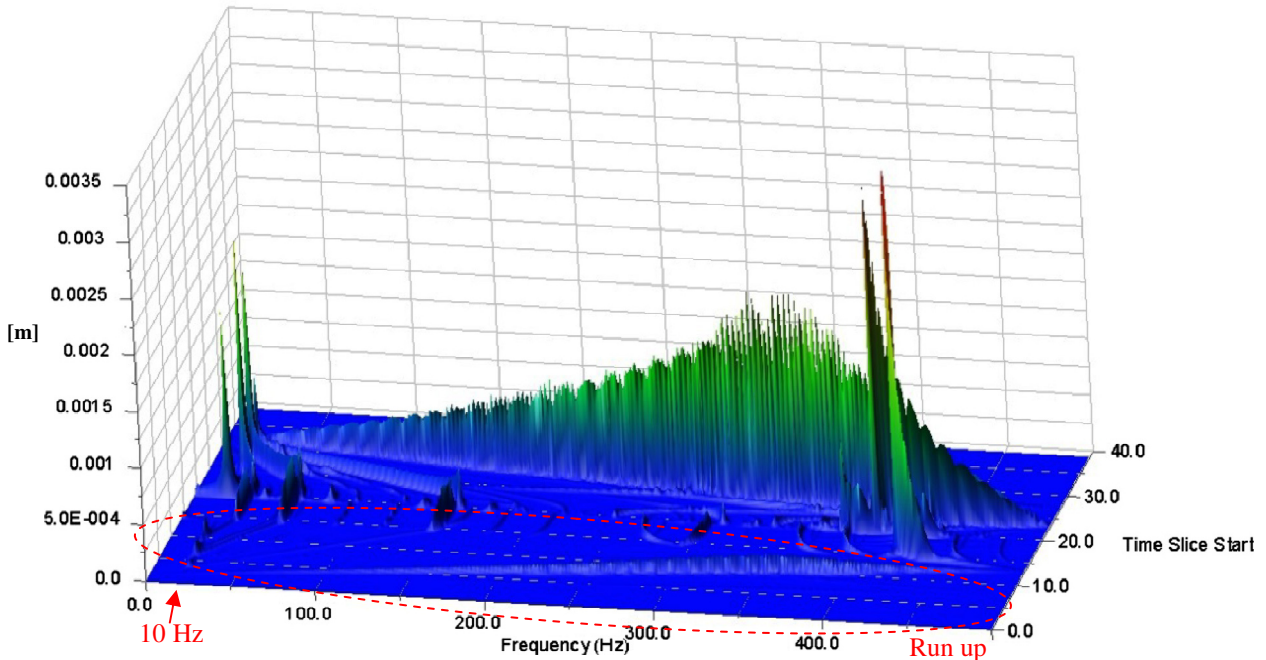


Fig 1.19: Waterfall spectra of high speed gear stage deflection (Viadero et al, 2014)

3.4 Acyclism

The acyclism is a transient regime characterized by the fluctuation of a combustion engine torque. Barthod (Barthod et al, 2007) studied the effect of acyclism inside different configurations of gearboxes (unloaded gear with different inertia and backlash) in the rattle threshold. The input speed is a sinusoidal function. When the inertia decreased, the input speed will be composed of several harmonics with relative amplitudes and phases (Fig 1.20).

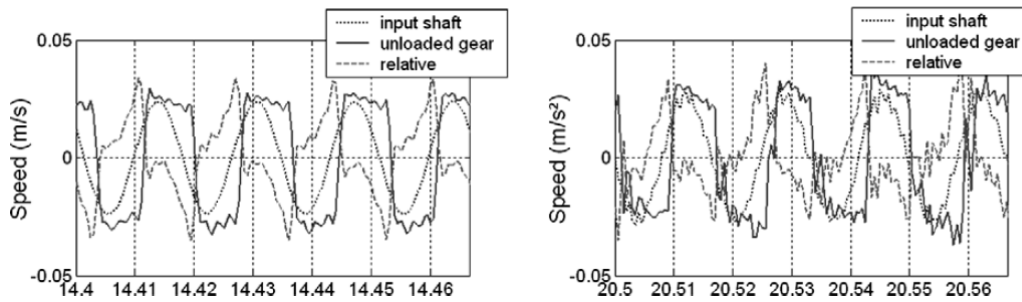


Fig 1.20: Temporal signal under acyclism with initial inertia and decreased inertia (Barthod et al, 2007)

Barthod (Barthod et al, 2007) proved that threshold is linked to the kinetic energy and threshold increases when backlash increases and decreases when the unloaded gear increases. Sika and Vex (Sika and Vex, 2008) studied the effect of the meshing stiffness and the engine speed fluctuations on a torsional gear model. In fact, they modeled the engine speed fluctuations as sinusoidal and multi-harmonic function (Fig 1.21).

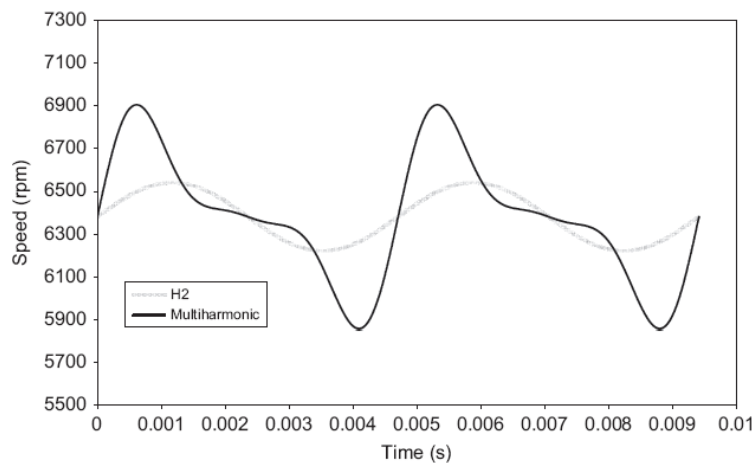


Fig 1.21: Engine speed fluctuations (Sika and Vex, 2008)

They modeled also the meshing stiffness with variable load as shown on Figure 1.22:

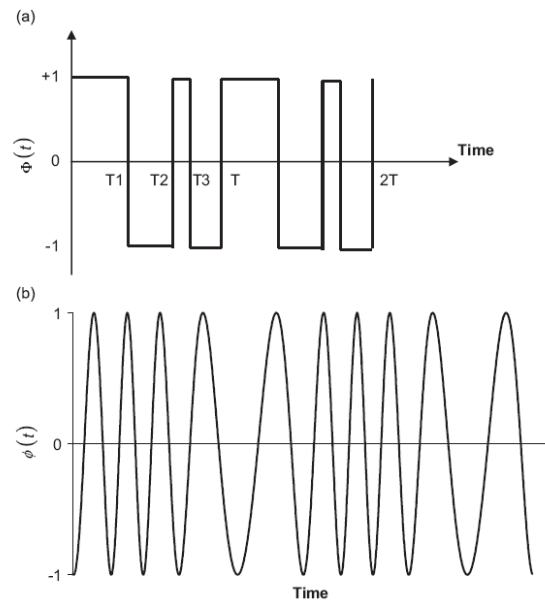


Fig 1.22: Modulation of meshing stiffness: (a) square mesh stiffness and (b) sinusoidal mesh stiffness function (Sika and Vexlex, 2008)

Engine speed fluctuations are found to generate additional secondary instabilities equally spaced around the main area probably caused by modulation side-bands. Multi-harmonic engine speed fluctuations generate more instability side-bands than mono-harmonic ones because of their wide ranging spectral contents.

Khabou et al (Khabou et al, 2011) modeled the applied torque to a spur gear as multi-harmonic function with a period of acyclism T_{acy} . (Fig 1.23)

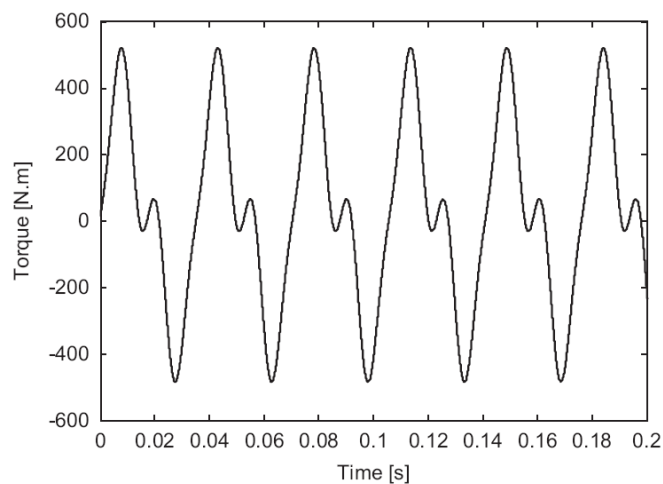


Fig 1.23: Evolution of the applied torque (Khabou et al, 2011)

He found that the transmission error is periodic and its fluctuation is proportional to the loading conditions (Fig 1.24)

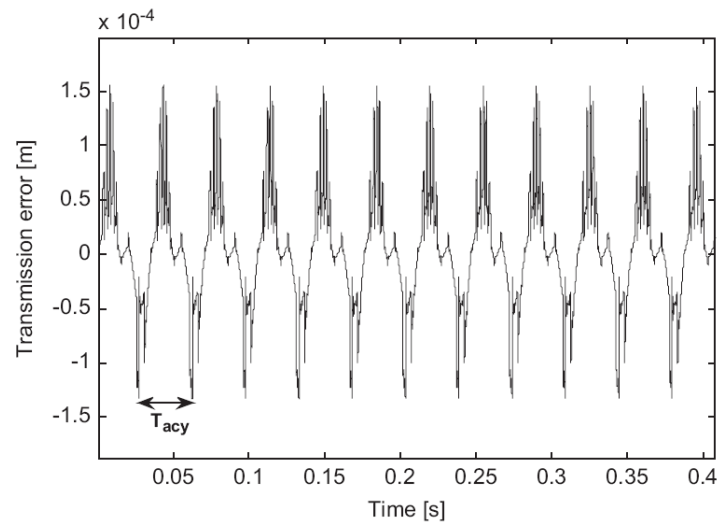


Fig 1.24: Transmission error due to acyclism (Khabou et al, 2011)

4. Techniques for detection of the non stationary excitation

Mechanical transmissions, working in several conditions, produce specific vibration signals that characterize them. Some signals, like gears working under constant speed and load, are characterized with repetitive frequencies and apparition of sidebands which characterize the modulating effects. These signals are called “stationary signals” and their statistical properties are invariant with time. Another kind of signals characterized by their repetitive statistical properties is called “cyclostationary signal”. One of the most fundamental ways of evaluating stationary and cyclostationary signals is in terms of their “frequency spectrum”. Some signals have frequency content which varies with time and are called “non-stationary signals”.

Randall (Randall, 2011) classified signals according to their statistical properties. He divided signals into “stationary signal” characterized by their invariant statistical properties and “non-stationary signal” characterized by their variant statistical properties. Figure 1.25 resumes this classification.

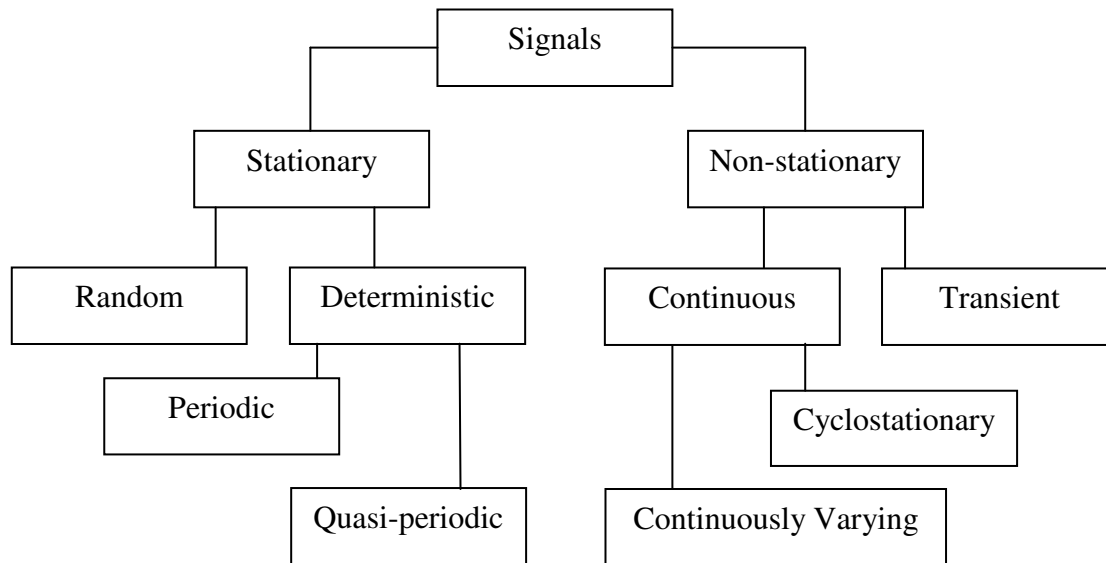


Fig 1.25: Classification of signals (Randall, 2011)

Deterministic signals are composed entirely of discrete frequency sinusoids and their frequency spectrum consists of discrete lines at the frequencies of those sinusoids and the value of the signal can be predicted at any time whereas the value of a random signal cannot be predicted despite their statistical properties are unchanging with time.

“Non-stationary signals” can be divided into two main classes: “continuously varying signal” and “transient signal” which only exist for a finite length of time and are analyzed as an entity. Run-up and run-down are two examples of transient signal.

In next sections, some vibration analysis techniques are presented for both “stationary signals” and “non-stationary signals”.

4.1. Time domain descriptors

These descriptors include:

4.1.1. The Root Mean Square (RMS)

This is the square root of the time signal $q(t)$ having a period T . It is also equal to the mean square of the RMS values of each of the harmonic component (Parseval's Theorem) (Bigret et al, 1995.)

In continuous form:

$$RMS = \sqrt{\frac{1}{T} \int_{t_0}^{t_0+T} q^2(t) dt} \quad (1.20)$$

In discretized form:

$$RMS = \sqrt{\frac{1}{M_d} \sum_{m=0}^{M_d-1} q^2(m\Delta t)} \quad (1.21)$$

With M_d is the number of discrete elements and $\Delta t = \frac{T}{M_d}$ is the discretization step.

The RMS measure the power content of the vibration signature. It identifies a comprehensive disturbance signal but does not give specific information on the cause of the failure and doesn't show significant changes in the early stages of its appearance.

Nevertheless, it remains effective when detecting major imbalances of a rotating system.

4.1.2. The crest factor F_c

it is the ratio of the peak value A_c to the RMS value. The peak value may be the upper peak or lower peak.

$$F_c = \frac{A_c}{RMS} \quad (1.22)$$

This technique is widely used to detect changes in the shape of signals due vibration impulses, induced for example by breaking of a gear tooth.

4.1.3. Kurtosis

Kurtosis is the degree of peakedness of a distribution, defined as a normalized form of the fourth central moment of a distribution. It characterizes the enlargement or flattening of the distribution of signal levels compared to the Gaussian distribution (which corresponds to a random signal).

In continuous form:

$$Kr = \frac{1}{\sigma^4 T} \int_{t_0}^{t_0+T} (q(t) - \mu_q)^4 dt \quad (1.23)$$

In discrete form:

$$Kr = \frac{1}{M_d \sigma^4} \sum_{n=0}^{M_d-1} (q(n\Delta t) - \mu_q)^4 \quad (1.24)$$

With: σ^2 variance of the signal; μ_q : average value of $q(t)$. M_d : The number of discrete elements.

For a Gaussian distribution, the value of kurtosis is equal to 3. The increase of kurtosis is a sign of initiation of a fault on one or more teeth (Lebold et al. 2000).

4.1.4. Time synchronous averaging (TSA)

It is defined by Wang et al. (Wang et al, 2001) as a signal averaging process over a large number of cycles, synchronous with the running speed of a specific shaft.

In practice, TSA is done by averaging together a series of signal segments each corresponding to one period of a synchronizing signal. TSA can be written as (Miller, 1999):

$$TSA = \frac{1}{N_b} \sum_{n=0}^{N_b-1} (q(t + nT)) \quad (1.25)$$

Where TSA is the time synchronous average signal $q(t)$, T is the period of rotation and N_b is the number of averages.

This technique allows the separation of periodic signals from background noise which is not periodic with a particular fundamental frequency.

4.2. Frequency domain descriptors

These descriptors include:

4.2.1. Spectral analysis

It is the most widespread techniques. In fact, monitoring of gear vibration spectra can provide information on their state.

For a periodic signal $q(t)$, the spectrum denoted by $Q(f)$ is given by the Fourier transform of $q(t)$:

$$Q(f) = \int_{-\infty}^{+\infty} q(t) e^{-j2\pi ft} dt \quad (1.26)$$

Figure 1.24(a) shows measured acceleration time histories $a(t)$ in the ring gear of planetary gear set with 3 planets by Inalpolat (Inalpolat and Kahraman, 2009) at the load 800 N.m and the speed 3200 rpm. The time axis of this figure is normalized by the mesh cycle period T_c/Z_r .

Figure 1.26(b) shows the spectra $A(\omega)$ corresponding to the time history presented in Figure 1.14(a). The data presented on figure 1.26(a) covered one period of carrier rotation. An apparent amplitude modulation repeated three times corresponds to the passage of each planet near to the fixed accelerometer. As a result of this amplitude modulation, significant number

of sidebands around the fundamental gear mesh harmonic order H_m and its harmonic orders ($2H_m$, $3H_m$, and so on) appears on the spectra $A(\omega)$.

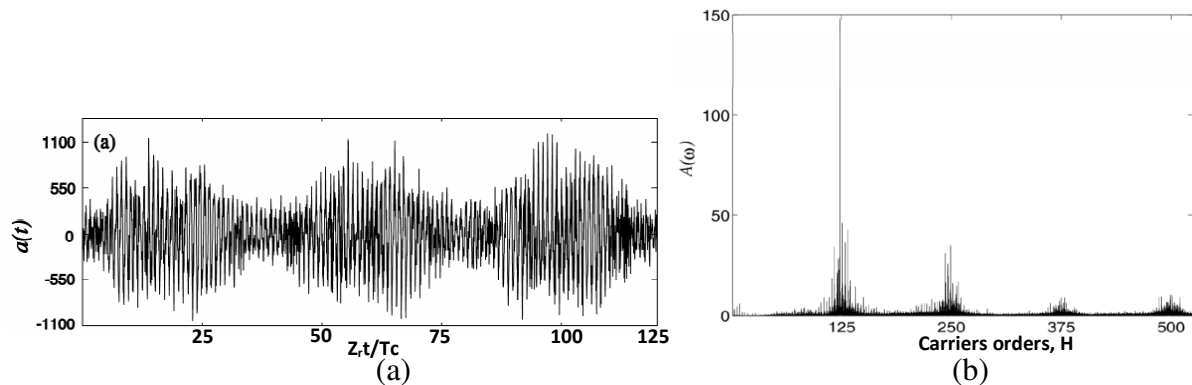


Figure 1.26: (a) measured time histories and (b) measured acceleration frequency spectrum

The example in Figure 1.27 shows two spectra of a gear pair, one before repair and the other after repair of a gear failure (replacement of the defective wheel) (Randall, 1980).

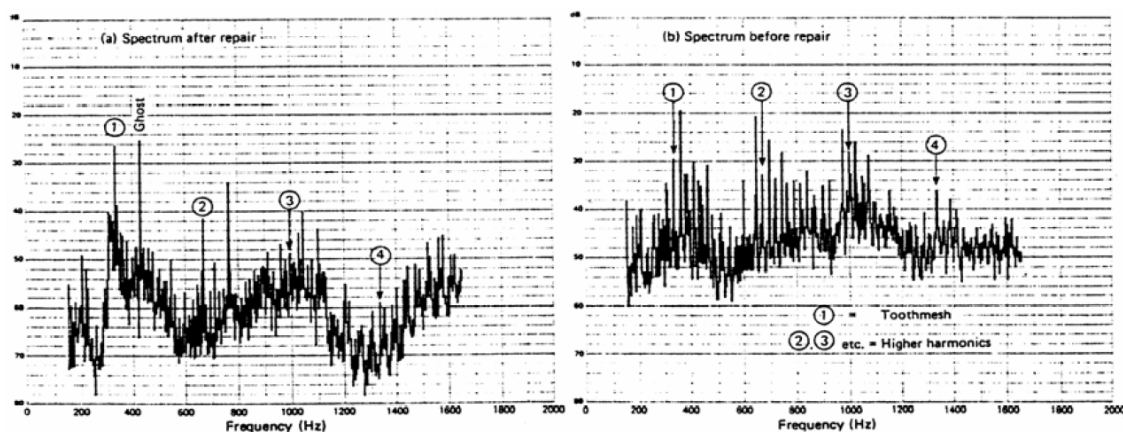


Fig 1.27: Spectrum after and before repair

We see clearly that after repair, general vibration level decreased activity including sidebands and meshing rays.

4.2.2. Envelope Analysis

The envelope analysis is an amplitude demodulation process. It is a technique used to monitor the high-frequency response of periodic mechanical impacts to remove the low-frequency noise (Ho and Randall, 2000). The envelope spectrum allows the determination of the defect frequency of components (Bigret et al , 1995) (Lebold et al , 2000) (Maynard , 1999).

In order to be more efficient, the envelope analysis can be made by digitizing and band-pass filtering of the signal in a frequency region, for example around a resonance or around meshing frequency. Then, the envelope spectrum can be obtained using the Hilbert transform technique.

Also, the envelope of a complex signal can be obtained by taking the amplitude of the signal as the real part and its Hilbert transform as the imaginary part. The Hilbert transform can be obtained in two steps: shifting the phase of the original spectrum is the first step and inverse Fourier transforming back to the time domain is the second step.

As an example, Zimroz et al (Zimroz et al, 2011) used the envelope method to analyze the vibration signal of wind turbine gearbox working under non-stationary condition (Fig. 1.28). The pre-filtered signal of the input shaft around the 1st harmonic of the meshing frequency shows the relationship between the speed and the amplitude of the signal which is modulated. The signal envelope shows clearly the effect of the time varying instantaneous speed which causes smearing in the spectra of the envelope signal.

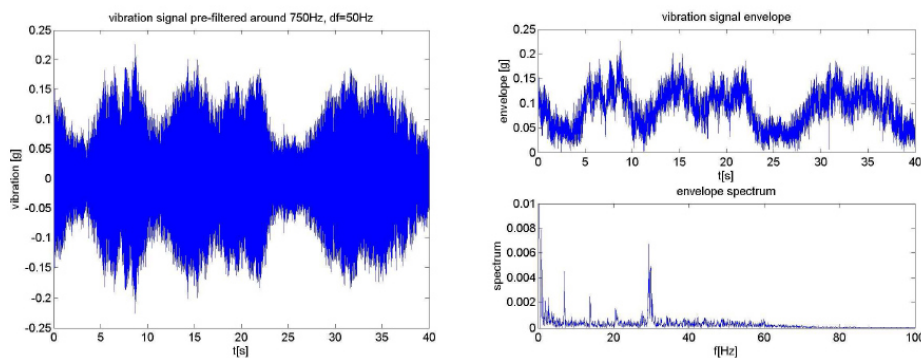


Fig 1.28: Pre-filtered signal of the input shaft around f_{mesh} , envelope and envelope spectrum (Zimroz et al, 2011)

The advantage of this method is reducing of the size of the record and the flexibility in choosing cut-off frequencies of the filter.

In addition, an approach to this method called “analysis of the squared envelope” can be used to characterize a (quasi) cyclo-stationary signal (Randall et al, 2001).

4.3. Cepstrum analysis

Bogert was the first who defined the cepstrum as " the power spectrum of the logarithm of the power spectrum " (Bogert et al, 1963) and its application was to detect echoes in seismic signal.

The original definition of the cepstrum (Randall, 2013) :

$$Ce(t) = |TF^{-1}\{\log S(f)\}|^2 \quad (1.27)$$

Currently, the complex cepstrum is often expressed (El Badaoui et al, 1999.)" As the inverse transform of the logarithm of the Fourier power spectrum ":

$$Ce(t) = TF^{-1}\{\log S(f)\} \quad (1.28)$$

With $S(f)$: power spectral density (PSD) of a signal $s(t)$. The portion of the frequency domain to time domain is achieved by the inverse Fourier transform (FT^{-1}).

Figure 1.29 shows the passage from spectrum to cepstrum.

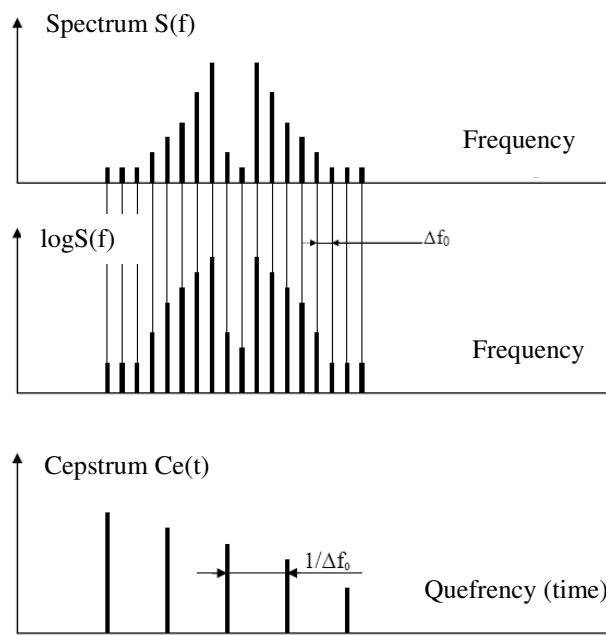


Fig 1.29: spectrum and cepstrum (Randall, 1977)

This technique allows diagnosis of which component developed a defect.

4.4. Joint time-frequency analysis

The Fourier transform carries valuable information about the analyzed signal. We know for example that if it has only low values for high values of the variable frequency, this means that the signal varies slowly. Conversely, if it takes significant values for high frequencies, the signal contains a significant amount of high frequencies, and hence varies rapidly, at least in some areas.

Fourier analysis is conducive to a comprehensive study of the signal with spectral characteristics do not change over time but is unable to locate the portions of the signal in which the variations occur quickly or those where they are slow.

Several alternative techniques have been used including the following insight:

4.4.1. Short Time Fourier Transform (STFT):

This technique allows visualizing the spectrum by moving the observation time window (Shin et al. 1993):.

For a time signal $q(t)$, it is defined by:

$$STFT(t, w) = \int q(\tau) \gamma_{t,w}^*(\tau) d\tau = \int q(\tau) \gamma(\tau - t) e^{-jw\tau} d\tau \quad (1.29)$$

(*) Represents the complex conjugate.

This is a product that reflects the similarity of $q(t)$ and $\gamma(\tau - t)e^{-jw\tau}$. The window $\gamma(t)$ is a very short in time, which gives us an idea about the local frequency content (Figure 1.30)

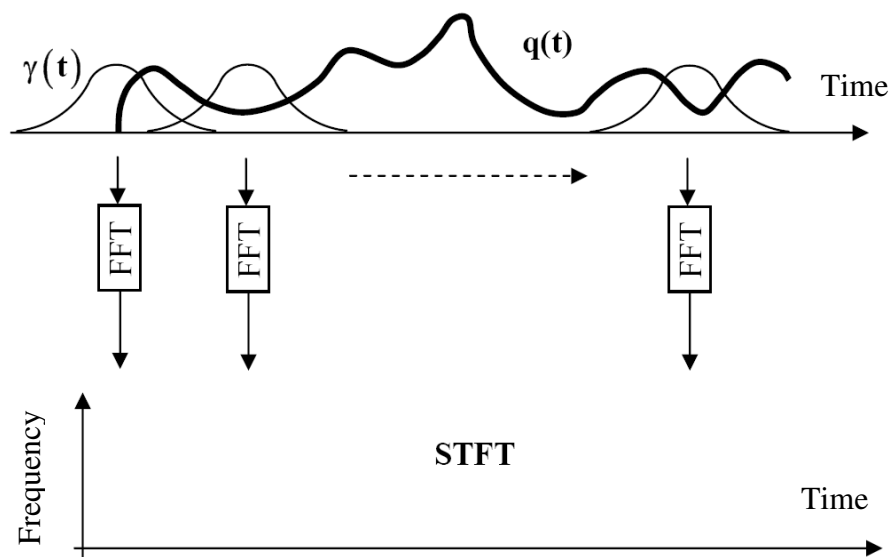


Fig 1.30: Calculating the Short Time Fourier Transform

The squared modulus of the STFT leads to a quadratic representation commonly known as spectrogram. This representation distributes the signal energy in the time-frequency plane. It is defined by:

$$SP(t, w, \gamma) = \left| \int q(\tau) \gamma^* (\tau - t) e^{-jw\tau} d\tau \right|^2 \quad (1.30)$$

The disadvantage of this method is that the observation window remains constant over time, which means that the time resolution will be constant.

4.4.2. Wigner-Ville Distribution

It can be defined from the temporal representation of the signal $q(t)$ as (Shin et al, 1993.):

$$WV(t, w) = \int q\left(t + \frac{\tau}{2}\right) q^*\left(t - \frac{\tau}{2}\right) e^{-jw\tau} d\tau \quad (1.31)$$

Or, from its Fourier transform:

$$WV(t, w) = \int Q\left(w + \frac{w'}{2}\right) Q^*\left(w - \frac{w'}{2}\right) e^{-jw't} d\tau \quad (1.32)$$

4.4.3. Wavelet Transformation:

It allows to promptly locating the different frequencies of the spectrum of the signal analysis. In practice, the wavelet signals are used for analysis of other signals. A signal well-known and the analyzing wavelet are selected and we seek the similarity between the studied signal and the wavelet. The time signal $q(t)$ will be decomposed on a family of translated and dilated functions from a single function $g(t)$ called mother wavelet. The family put in the form (Miller, 1999):

$$\Psi_{a,b} = \frac{1}{\sqrt{a}} \Psi\left(\frac{t-b}{a}\right) \quad (1.33)$$

The parameter "a" represents the expansion or scale defining the width of the analysis window parameter. The parameter "b" is the translation parameter locating the analyzing wavelet in the time domain. Note that $\frac{1}{\sqrt{a}}$ is a coefficient used to have the same energy in each wavelet. We can obtain the wavelet in the desired frequency and the desired time By changing the two parameters a and b.

4.4.4. Continuous wavelet transformation:

The wavelet transform of a continuous signal $q(t)$ is defined by (Miller, 1999):

$$d\Psi(a,b) = \frac{1}{\sqrt{a}} \int_{-\infty}^{+\infty} q(t) \Psi\left(\frac{t-b}{a}\right) dt \quad (1.34)$$

This parameter is important for the signal $q(t)$ in the frequency $1/a$ and the time domain b .

Figure 1.31 shows the steps of continuous wavelet transform.

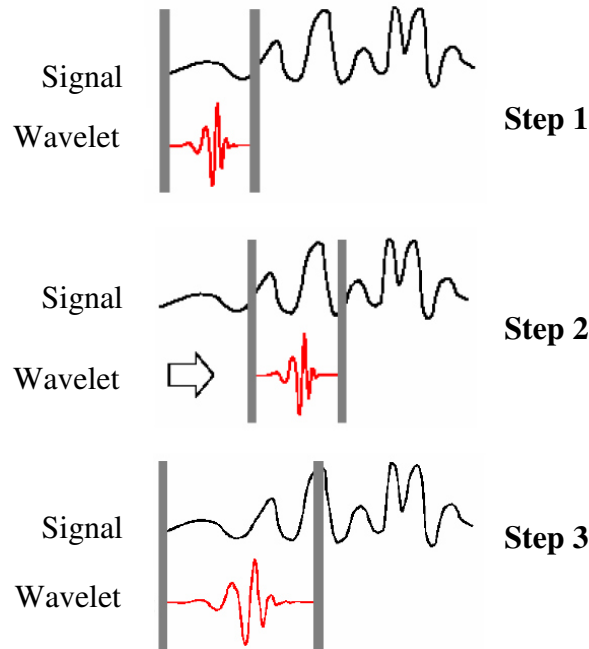


Fig 1.31: Continuous wavelets transform

- Step 1: We consider a wavelet we will look at a section of the signal seeking how it correlates to the signal and calculates a coefficient for this purpose "Cor". More "Cor" is bigger, more general similarity is important. Note that the result depends on the chosen wavelet.
- Step 2: translate the wavelet and repeat step 1 to cover the entire signal.
- Step 3: The wavelet is now expanded. Operations performed in steps 1 and 2 are repeated.

5. Experimental test benches

Different developed models tried to investigate the dynamic behaviour of gear transmissions. These models required a detailed experimental validation which can provide this field of knowledge with valuable and reproducible data about the dynamic behavior of the transmissions. Test benches can be suitable tools to achieve experimental investigation on planetary gear.

The first criterion of test bench design is the type of layout. It is possible to find direct configuration and power circulating configuration (Fernández et al 2013). The first configuration is with Gears Under Test (GUT) placed between a driving motor and a loading device. In this configuration, the power loop is open and the energy consumed in the tests is lost by heat dissipation in the load.

(Schon 2005) used two kind of test bench in the direct configuration: a conventional helical gearbox test bench and an epicyclic gearbox test bench. Measurement hardware was composed of four ICP accelerometer and “Siglab” data acquisition connected to the computer.

(Boguski 2010) used a planetary test machine driven by a motor in order to avoid the dynamic effects of planetary gear under quasi-static condition (Fig 1.32). The motor is connected to a torque meter. A torque sensor is connected to the sun gear. Two optical encoders (Heidenhain IBV600) controlled the speed of the sun and the carrier and are connected to the software application Transmission Error Measurement System (TEMS).

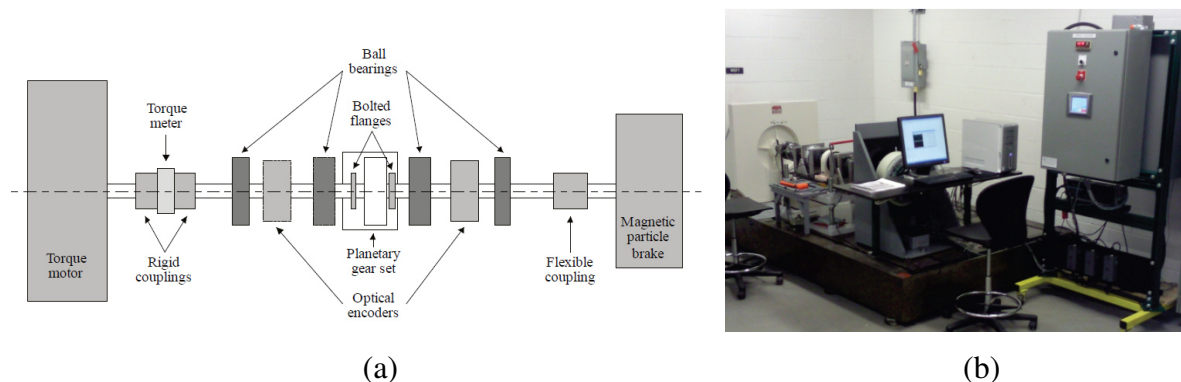


Fig 1.32: Schematic view (a) and real view (b) of the planetary gear test setup (Boguski 2010)

For the high power tests like wind turbine gearboxes, the directed configuration is characterized by high energy consumption.

This fundamental drawback motivates the appearance and usage of power circulating test benches. In these kinds of test benches, the energy received by the load from the gear train can be transformed (if necessary) and re-injected at an initial point. This point can be before the actuator for electric or hydraulic power circulation (Sweeney, 1994) and it can be after actuator for mechanical power circulation (Ligata 2007).

Test bench with electrical power circulation needs a generator who transforms mechanical energy to electrical energy and feeds the electrical motor. This configuration makes their cost higher despite their efficiency. In the case of planetary gear, the high gear ratio makes

necessary the installation of an auxiliary planetary gear box in order to force the generator works in his nominal speed range.

According to energetic criterion, the test bench with purely mechanical circulation is the best solution because the power follows a closed loop inside the bench. The Gears Under Test and auxiliary gear train are parallel and with the same gear ratio. The motor is the only non-pure mechanical component and it supplies only the internal losses.

As an example of test bench with mechanical circulation, (Ligata 2007) and (Inalpolat 2009) used the same test bench which is a back-to-back planetary gear set configuration: the electric motor powers the suns of both gear set (Fig 1.33).

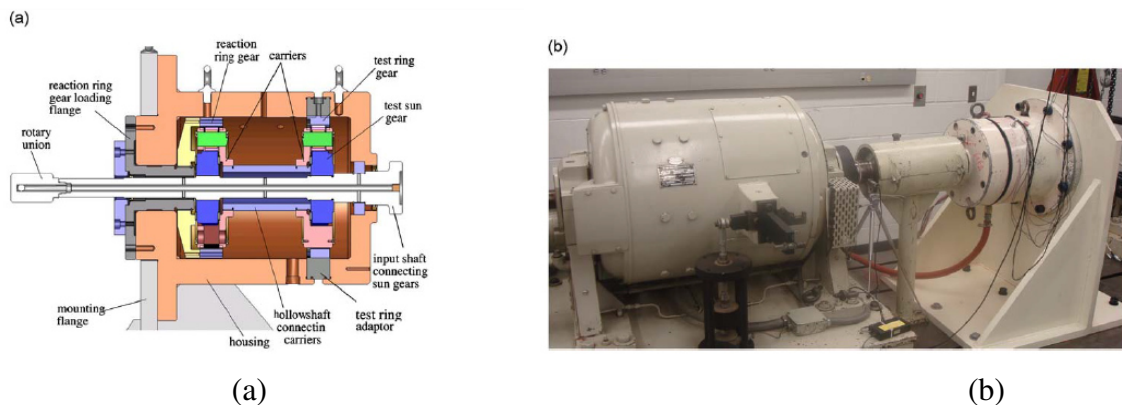


Fig 1.33: Cross section (a) and real view (b) of the back-to-back planetary gear test setup

(Ligata 2007) used a 32 channel strain gauge conditioner unit (four NI SCXI-1520 strain bridge modules mounted NI SCXI-1000 chassis), a PC with suitable data acquisition boards (NI PCI-6052E multifunction I/O board), and a magnetic pick-up for identification of a particular planet as it passes through a given gauge location (Fig 1.34).

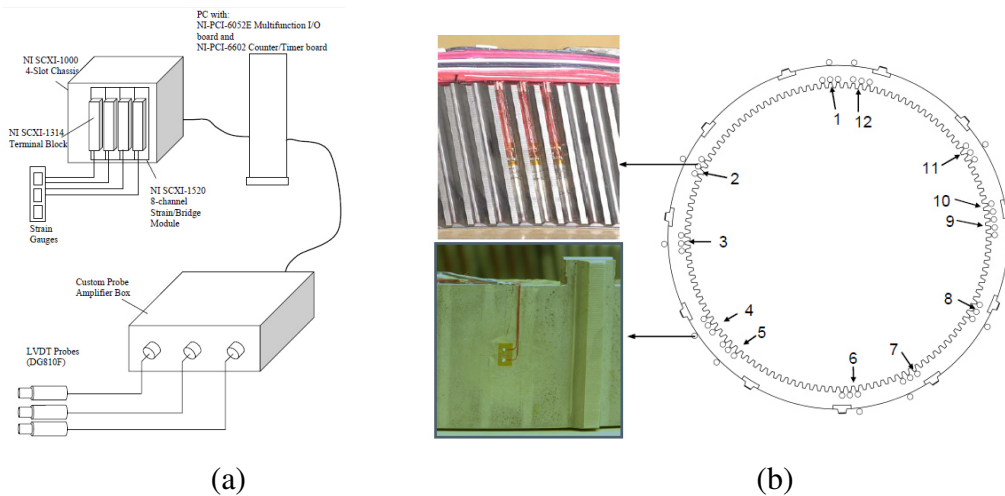


Fig 1.34: Data acquisition systems (a) and position of train gauges (b) (Ligata 2007)

Inalpolat (Inalpolat 2009) used eleven accelerometers (PCB-353B15) mounted radially on the outside surface of the ring and photoelectric sensor measured the angular speed of the sun gear shaft (Fig 1.35).

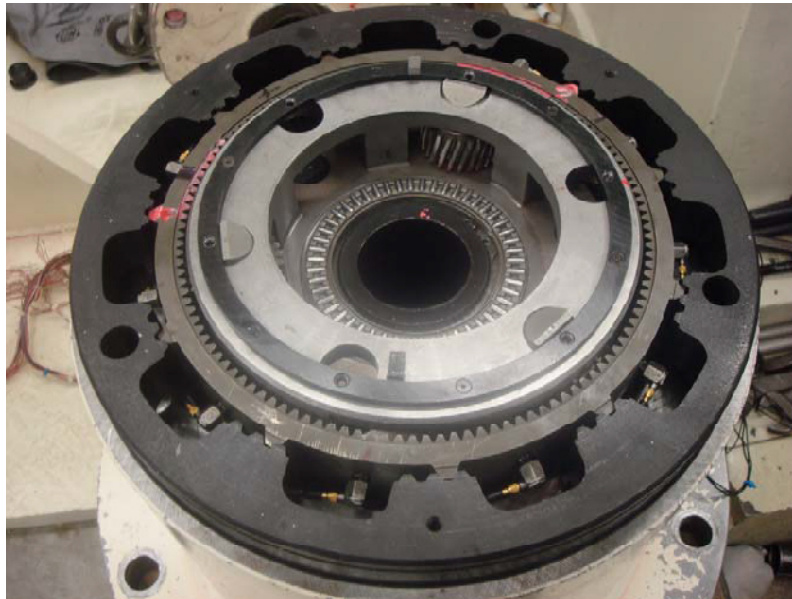


Fig 1.35: Accelerometers mounted on the outside surface of the test ring (Inalpolat 2009)

6. Modal analysis of planetary gear

Many researchers studied the modal properties of planetary gears highlighting the relationship between natural frequencies and parameters of the system. Cunliffe (Cunliffe et al 1974) focused on analytical model of planetary gear with a fixed carrier and characterised the vibration modes. Botman (Botman, 1976) studied the effects of planet pin loads on the Eigen-frequencies using an eighteen degree of freedom system. August (August and Kasuba, 1986) used a torsional model with nine degree of freedom to determine torsional vibrations and dynamic loads in a basic planetary gear system. Kahraman (Kahraman, 1993) and Sondkar (Sondkar and Kahraman, 2013) analyzed respectively the three dimensional modal deflection of a helical planetary gear and double-helical planetary gear. Kahraman (Kahraman, 1994) provided expressions for natural frequencies by using rotational lumped parameter model. Lin and Parker categorized rotational, translational, and planet modes and explained the unique modal properties of planetary gear with equal planet spacing (Lin and Parker, 1999b) and unequal planet spacing (Lin and Parker, 2000b). Tanna (Tanna and Lim, 2004) compared the modal frequencies of ring gears and idealized smooth rings. They quantified the frequency

deviations in applying the simpler smooth ring solutions to represent the primary modal behaviors of ring gear structures.

Wu and Parker considered the elastic deformation of the ring on the modal properties of planetary gear with equal planet spacing (Wu and Parker, 2008) and unequal planet spacing (Parker and Wu 2010). Eritenel (Eritenel and Parker, 2009) presented the modal properties of three-dimensional helical planetary gears. Bu (Bu et al, 2012) developed a generalized dynamic model for herringbone planetary gear train in order to investigate its modal properties. Vibration modes of compound planetary gears were studied by Kiracofe (Kiracofe and Parker, 2007) and Guo (Guo and Parker 2010). Cooley and Parker (Cooley and Parker, 2012), (Cooley and Parker, 2013) modeled the gyroscopic effects and studied the vibration properties of high-speed planetary gears.

There were few experimental studies to correlate the numerical model with vibration experiments.

Singh (Singh et al, 2008) presented results of a comprehensive experimental and theoretical study under static condition to determine the influence of manufacturing tolerance on gear stresses and planetary load sharing. Kahraman (Kahraman and Vijayakar, 2001) investigated the effect of internal gear flexibility under the quasi-static condition behavior of planetary gear set. Toda and Botman (Toda and Botman, 1979) showed experimentally that planetary gear vibration resulting from planet position error can be minimized by proper indexing planet.

Velex (Velex et al 1994) compared experimental results of a double helical epicyclic gear in its natural environment to a mathematical model. But some natural frequencies do not agreed between their model and experiments. Ericson (Ericson and Parker, 2013) applied experimental modal analysis techniques to characterize the planar dynamic behavior of spur planetary gears and correlated these results against lumped parameter and finite element model. Few works were dedicated to modal analysis of multistage or compound planetary gears; we can cite the works of Kahraman (Kahraman, 2001) who developed a torsional dynamic model of compound planetary gear sets in order to predict the vibration characteristics under different kinematic configurations.

7. Load sharing behavior of planetary gear

Planetary gear can transmit higher power density levels because they use multiple power paths formed by each planet branches. This allows the input torque to be divided between n planet paths, reducing the force transmitted by each gear mesh.

Under ideal conditions, each planet path carries an equal load. Nevertheless, planetary gears have inevitable manufacturing and assembly errors. So, the load is not equally shared amongst the different sun-planet and planet-ring paths, which can be a problem in terms of both dynamic behavior and durability.

Many researchers have done significant works on the subject of planetary gear load sharing. Their works were based on transmission modeling and assessed by experimental tests. In fact, Kahraman (Kahraman, 1994a) used a discrete model to study the influence of carrier pin hole and planet run-out errors on planet load-sharing characteristics of a four-planet system under dynamic conditions. He (Kahraman, 1999) employed later a planet load-sharing model to determine the static planet load sharing of four-planet systems and presented experimental data for validation of the model predictions. Iglesias (Iglesias et al, 2013) studied the effect of planet position error on the load sharing and transmission error. Singh (Singh, 2005) found that the tangential pin position error has a greater effect on the load sharing than the radial pin position error. Ligata (Ligata et al, 2008) proved experimentally that for the same amount of error, the degree of inequality in the planet load-sharing behavior increases with the number of planets in the system. Guo and Keller (Guo and Keller 2012) presented a three-dimensional dynamic model which take into account to the addressing gravity, bending moments, fluctuating mesh stiffness, nonlinear tooth contact, and bearing clearance. They validated this model against the experimental data.

Bodas and Kahraman (Bodas and Kahraman, 2004) defined the load sharing factor of given planet i as the ratio of the load carried by this planet to the total load. First of all, the planet load sharing ratio (LSR) is defined as the ratio of the meshing torque due to sun-planet(i) and ring-planet(i) meshes of planet (i) by the meshing torque of all planets.

$$L_{Pi} = \frac{T_{mesh}(Pi)}{\sum_{i=1}^n T_{mesh}(Pi)} \quad (1.33)$$

They studied the effect of manufacturing errors causing change of the positions of profile on the load sharing behaviour. Figure 1.36 shows the change of the positions of profile due to

three types of manufacturing errors: tooth thickness error “ e_t ”, carrier pinhole position error “ e_c ” and planet run-out error “ e_r ”.

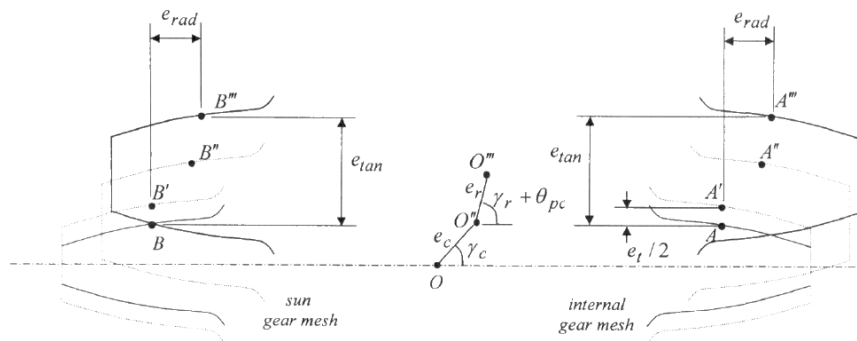


Fig 1.36: Influence of errors on the position of planet tooth contact surfaces (Bodas and Kahraman, 2004)

As result, the variation of the load sharing ratio with the rotation angle of planets relative to the carrier is shown in figure 1.37. In the initial position, an equal load sharing is observed and $L_i=25\%$. At the position corresponding to the high point of the run-out of planet 1 ($\theta_{p/c} = \frac{\pi}{2}$), planet 1 and 3 reach the maximum of share of load and $L_i=32\%$ whereas at the position corresponding to the low point of the run-out of planet 1 ($\theta_{p/c} = \frac{3\pi}{2}$), planet 1 and planet 3 reach the minimum of load sharing and $L_i=18\%$. At $\theta_{p/c} = \pi$ and $\theta_{p/c} = 2\pi$, the error is zero and $L_i=25\%$.

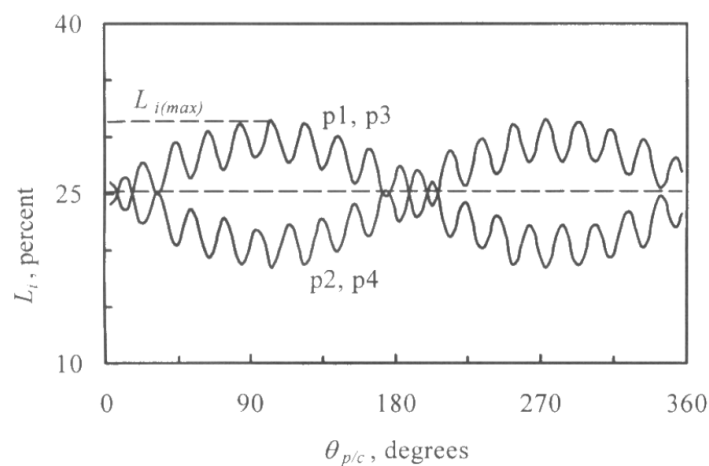


Fig 1.37: Effect of planet run-out error on the variation of the load sharing ratio (Bodas and Kahraman, 2004)

Guo and Keller (Guo and Keller 2012) presented a three-dimensional dynamic model which take into account to the addressing gravity, bending moments, fluctuating mesh stiffness, nonlinear tooth contact, and bearing clearance. They modeled these effects by additional forces to the meshes load. They validated this model against the experimental data (Fig 1.38).

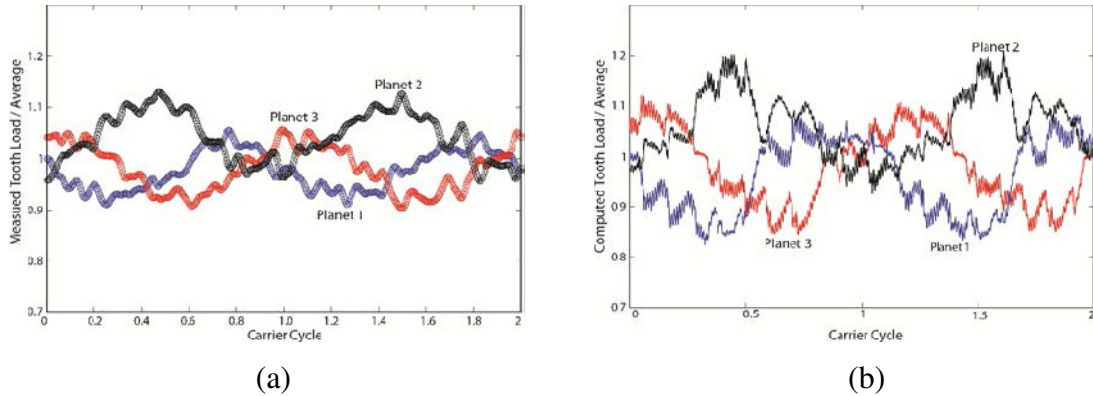


Fig 1.38: Measured (a) and calculated (b) planet load sharing with different effects (Guo and Keller 2012)

8. Transfer path analysis (TPA)

Research developments in transfer path analysis (TPA) are required in order to improve noise and vibration control. The most celebrated technique is the classical TPA which is used particularly in the automotive industry for the analysis of the different contributions of noise and vibration at a particular receiver position (the driver and passenger positions in a vehicle) (Plunt, 2005).

The two main limits of the classical TPA which are decoupling of the active part and the measurement of the operational forces obliged many researchers to propose approaches to the classical TPA.

7.1. Classical transfer path analysis

The classical transfer path analysis (TPA) is a two steps method. The first step is the measurements of the Frequency Response Functions (FRFs) of source-receiver paths using an artificial excitation like impact hammer, shaker or loudspeaker whereas the second step is the measurement of the operational forces or volume velocities acting on the system.

For a classical TPA model, the global system is divided into an active part which contains the sources and a passive part which contains the transfer path and receiver points.

For example in Fig 1.39, forces (F_i) and volume velocities (Q_j) excite the passive part and propagate through the transfer paths corresponding to their Frequency Response Functions (FRF) and also called noise transfer functions (NTF's).

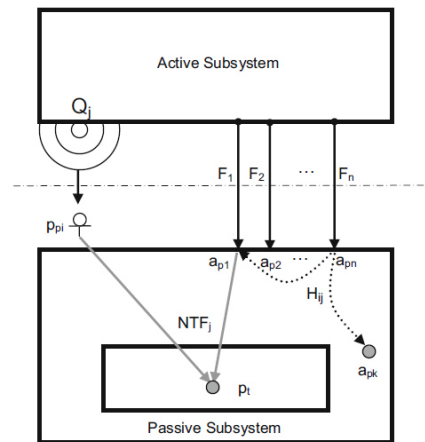


Fig 1.39: Classical Transfer path analysis model (Gajdatsy et al, 2010)

The response at the receiver point p_t can be written as:

$$p_t(\omega) = \sum_{i=1}^n NTF_i(\omega)F_i(\omega) + \sum_{j=1}^r NTF_j(\omega)Q_j(\omega) \quad (1.34)$$

A second group of FRFs called “local FRFs” H_{ij} express the relationship between responses at the input of degree-of-freedom. The response at a passive side can be expressed by:

$$a_{pi} = \sum_{j=1}^n H_{ij}F_j \quad (1.35)$$

This method has two limits: the first one is decoupling the active part of the system in the measurements of FRFs. The second one is the difficulties to measure the operational forces.

7.2. Approaches to TPA

Many approaches are proposed to avoid the drawbacks of the classical TPA. The Operational Transfer Path Analysis OTPA method, based on a response-response relationship model, requires measurement data of the operating vehicle in order to perform the analysis. The OPTA, a one step method, allows the identification of the transfer paths without disassembling the system and facilitates the measure of the operational forces (De Sitter et al, 2010) (De Klerk, 2010). OPTA which uses matrix of transmissibility as introduced Rebeiro et al (Ribeiro et al, 2000) has technical drawbacks. In fact, Transmissibilities are different from

transfer functions like mobility transfer functions. Also, the transmissibility matrix concept should carefully be used because the input measurement points are inherently coupled (Gajdatsy, 2010).

Roozen and Leclère (Roozen and Leclère, 2013) ameliorate OPTA method by using a non instrumented excitation in two steps and they applied this method on small gearbox. The first step is to determine transmissibility matrix: the system is excited by hammer strokes which are independent. The second step is to determine the operational forces through force transducers integrated in the pins which supported the gearbox. An other approach so-called OPAX combines the measurements of the transfer path with operational measurements (Janssens et al, 2011). In this method, force sensors are mounted on the connection between the source and the receiver. The drawback of the last two approaches is the difficulty of the measurement of the operational forces in some cases.

In order to avoid these drawbacks, an other two steps strategy was developed by Magrans (Margans, 1981): the first step is the measurements of transmissibility which requires no demounting tests and the second step is the measurements of the operational responses. In contrast, the so-called direct transmissibilities obtained from the measured transmissibilities are used for the operational response contribution. The direct transmissibilities approach is used also by Guash and Magrans (Guasch and Magrans, 2004) (Guasch, 2009) and termed Global Transmissibility Direct Transmissibility (GTDT).

9. Conclusion

In this chapter, we reviewed the various models describing the dynamic behavior of single-stage gear units and planetary. Non stationary excitations for gear transmission systems were detailed. Techniques used to describe time signals issued from gear sets were described. The main test rigs used to validate numerical works were also discussed. The final part was dedicated to the transfer path analysis techniques.

The main points that can be drawn are:

- The modeling of the dynamic behavior of gear trains encountered in the literature are based on lumped parameters (springs or masses) or on finite element method.
- The periodic variation of the mesh stiffness is the main excitation source gear trains.
- Non stationary conditions can excite transmission systems and especially gears and change the dynamic behaviors of transmission systems.

- Manufacturing errors, gravity, fluctuating mesh stiffness have an important effects on Planet load sharing behavior.

- The transfer path analysis and its approaches allow the study of propagation of vibration.

Based on this literature review, we are interested in following our research to the dynamic behavior of gear trains and planetary under non stationary condition. Numerical model is proposed and is validated through a back-to-back planetary gear test bench which will be presented in the next chapter.

Chapter 2:

Description of the test bench

Sommaire

1. Introduction.....	49
2. Test bench description	49
3. Instrumentation	55
3.1. Existent instrumentation	55
3.2. Developed instrumentation.....	57
4. Excitation method	62
5. Data analysis	63
5.1. Data acquisition system	63
5.2. Data Software	64
6. Conclusion	65

1. Introduction

Planetary gears are excellent mechanisms for power transmission due to their high efficiency and their significant transmitting power with large speed reductions or multiplications. So, many works are devoted to these kinds of gears.

Different developed models tried to investigate the dynamic behaviour of the gear transmissions as described in the first chapter. These models required a detailed experimental validation which can provide this field of knowledge with valuable and reproducible data about the dynamic behavior of the transmissions. Test benches can be suitable tools to achieve experimental investigation on planetary gear.

In this chapter, a back-to-back planetary gear test bench is used to validate the numerical model. First-of-all, the mechanical part of this test bench is described. Then, instrumentation layout is presented and the developed alternatives for measurement are detailed. In addition, “LMS SCADAS 3163 data acquisition system and “LMS Test.Lab” data software are described.

2. Test bench description

A test bench was developed at the Department of Structural and Mechanical Engineering of the University of Cantabria in Spain (Fig.2.1).



Fig.2.1: Picture of the test bench

For economic and energy efficiency criteria, the configuration of the test bench is compact with purely mechanical power circulation (Fernández 2013). So, test bench include two identical planetary gear sets with the same gear ratio. Gear under test set is a test gear set and auxiliary gear train is a reaction gear set. The test gear set and the reaction gear set are connected in a back-to-back configuration: the sun gears of both planetary gear sets are connected through a common shaft and the carriers of both planetary gear sets are connected to each other through a rigid hollow shaft (Fig.2.2 and Fig.2.3).

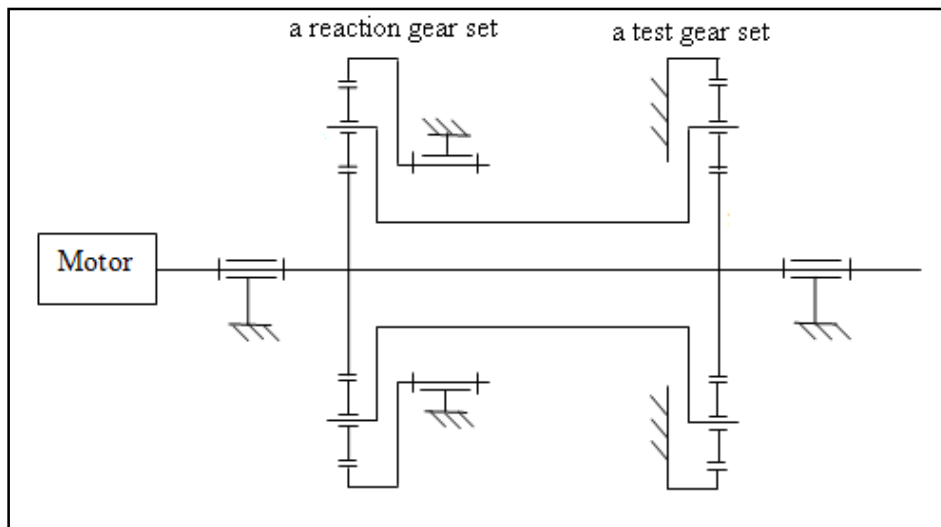


Fig.2.2: Back-to-back layout as assembled in the bench

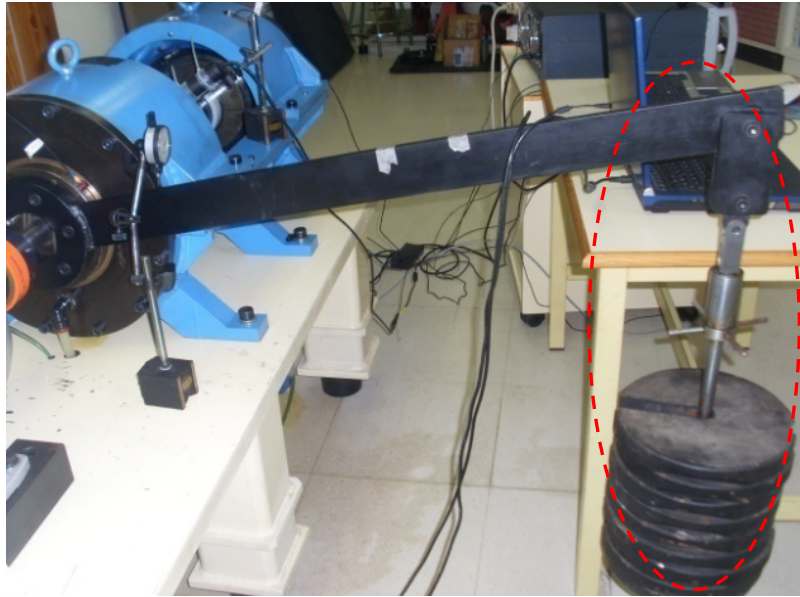


Fig.2.4: Application of the external torque by adding mass

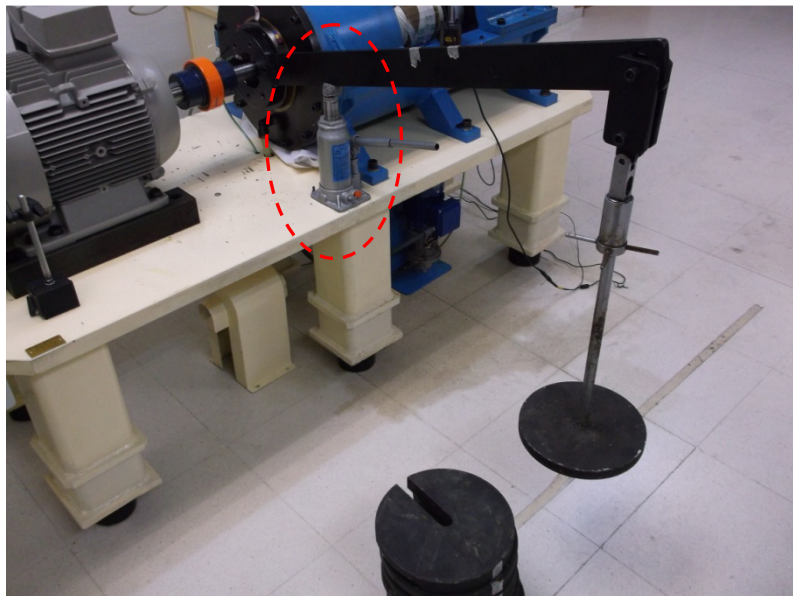


Fig.2.5: Application of the external torque with jack

The maximum torque applied by the mass is 900 N.m while the torque with jack can reach 4000 N.m.

Based on the international standard “ISO 6336: Calculation of load capacity of spur and helical gears” (ISO 6336, 2006), an estimation of the minimum tangential torque on the

reaction ring that will produce the mechanical failure in case of tooth bending and pitting for the sun, planets and ring gears is summarized in the table 2.2.

Contact	Component	Torque producing Bending (N.m)	Torque producing Pitting (N.m)
Sun-Planet	Sun	2644	1100
	Planet	3630	1100
Ring-Planet	Planet	2411	1650
	Ring	47587	9446

Table 2.2.External torque required in order to achieve the failure

In order to avoid bending defect and pitting defect, the value 1100 Nm was chosen. This will be the maximum torque value that the bench must be able to supply.

Motor drive selection

A “SIEMENS” electric motor is connected to the shaft of the sun gear to rotate both gear sets.

The characteristics of the electric motor are on the table 2.3.

V	Hz	A	Kw	Cos	Nom.Eff	1/min	V	A
400 Δ	50	29.5	15	0.82	89.4	1460	380-400	30-30.2
690 Y	50	17.1	15	0.82	89.4	1460	660-725	17.4-17.5

Table 2.3.Characteristics of the electric motor

Control of the electric motor “SIEMENS” is made by a frequency inverter “MICROMASTER 440” which is located on the electric cabinet (Fig.2.6).

	V	A	Hz
Input	380-480	37	47-63
Output	0-Input	32	0-650Hz
Motor		15 KW	

Table 2.4.Characteristics of the frequency inverter



Fig.2.6: Electric cabinet

This inverter can be configured with the help of the software “STARTER”. This software, developed by “SIEMENS” can be started directly through the frequency converter integrated into PCS 7. With this software, we can control the speed under the stationary condition and command the run up and the run down (Fig.2.7).

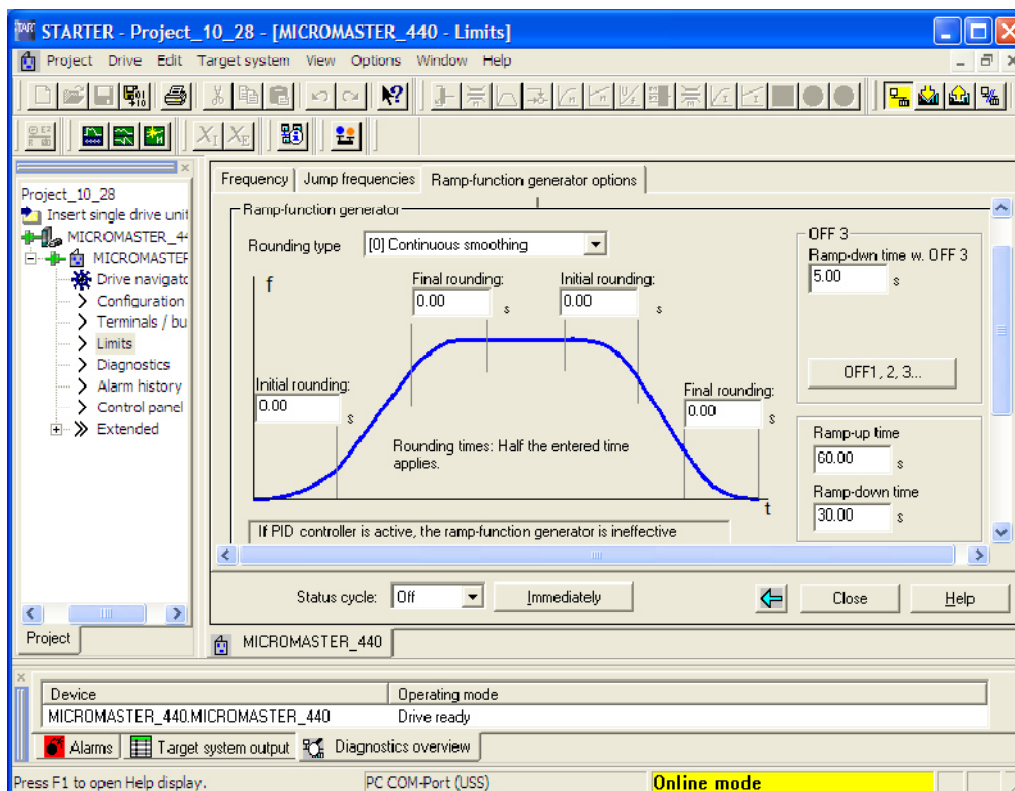


Fig.2.7: Window of ramp function generator function of “Starter” software

3. Instrumentation

3.1. Existent instrumentation

Four tri axial accelerometers are mounted on the test bench: two on each ring (Fig.2.8 and Fig.2.9).

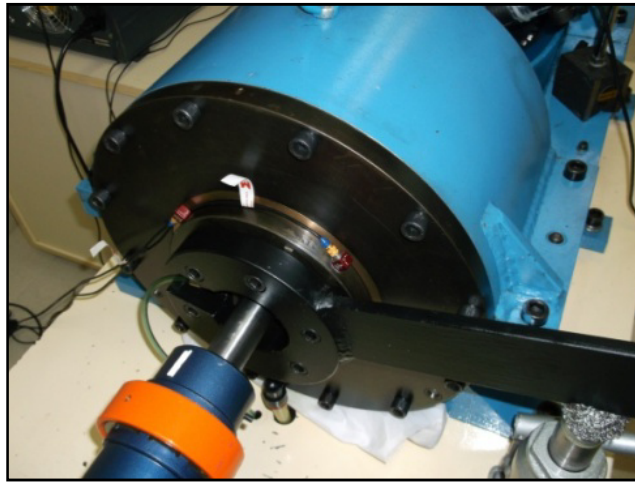


Fig.2.8: Tri axial accelerometers on the reaction ring



Fig.2.9: Tri axial accelerometers on the test ring

The table 2.5 characterise each ISOTRON accelerometer.

Place	Free ring	Fix ring	Free ring	Fix ring
Serial number	10020	10021	10022	10023
X-Sensitivity (mV/g)	102.6	103.5	100.4	101.6
Y-Sensitivity (mV/g)	101.3	98.68	99.67	103.0
Z-Sensitivity (mV/g)	101.1	104.3	102.6	101.9
Manufacturer	ENDEVCO			
Model number	65M-100			

Table 2.5: Accelerometer's characteristics

These accelerometers are calibrated regularly in all used direction: X and Z directions (Fig.2.10 and Fig.2.11). A “Brüel & Kjær” calibration exciter is used. The frequency of calibration is 159.2Hz for $\omega=1000$ rad/s. Its level of acceleration is 3.16m/s^2 .



Fig.2.10: Calibration of accelerometer in the X direction

Additionally, an optic tachometer (Compact VLS7) is combined with pulse tapes along the hollow shaft connecting carriers in order to measure its instantaneous angular velocity. It was placed along the hollow shaft (Fig.2.12).



Fig.2.11: Optic tachometer

3.2.Developed instrumentation

In order to transmit signals from the rotating carriers to the data acquisition system “LMS SCADAS 316”, a slip ring (HBM SK5/95) with 5 wires is installed with the hollow shaft that connects the carriers and, therefore, it allows the installation of accelerometers on these elements (Fig.2.12).

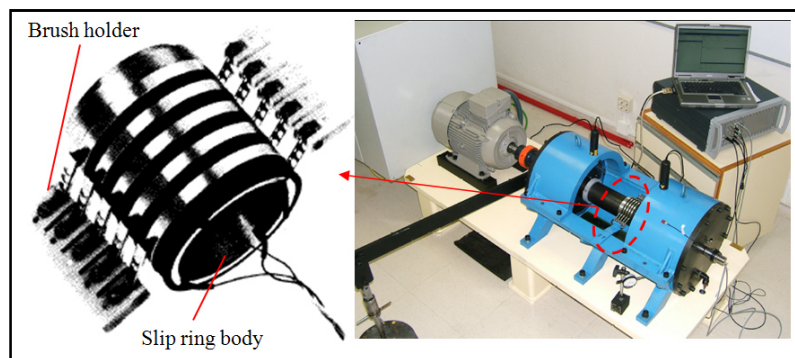


Fig.2.12: Slip ring assembly SK5

The slip ring body comprises a hollow cylinder with five hard silver slip rings.

Two brush holders SK5/ZB with five brushes each complete the slip ring body to form the assembly. The five brushes are arranged for signal transmission on the holder. They can move about a common bolt and springs will provide the necessary mechanical pressure. Two holes with M3 thread are for the mounting of the brush holder.

The instrumentation layout with the extended slip ring is on fig.2.13.

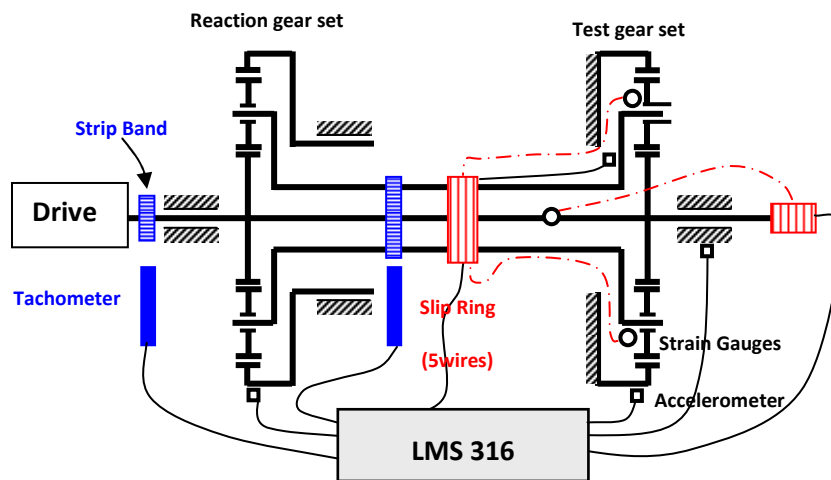


Fig.2.13: Schematic representation of the instrumentation layout

To connect the accelerometers to the acquisition system “LMS SCADAS 316”, we should connect accelerometers to the slip ring body on the one hand and then connect the brushes of slip ring to the acquisition system.

The used connections are BNC connector male and female and port RS232 male and female.

The first four wires of the slip ring are for signal channel whereas the fifth wire which is connected to the hollow shaft is used as common mass.

Fig.2.14 shows the connection between accelerometers and the slip ring body.

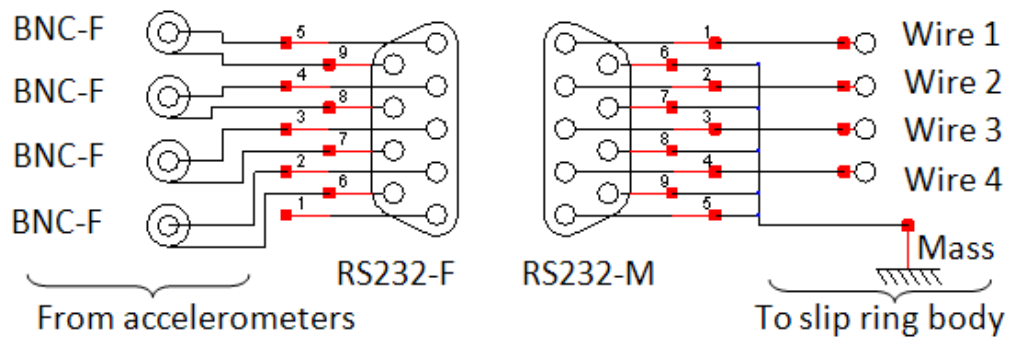


Fig.2.14: Connection between accelerometers and the slip ring body

Every brushes of the slip ring have a colour. The white, the black, the blue and the red brushes are for signal channel whereas the yellow brush is used as common mass.

Fig.2.15 shows the connection between the brushes of the slip ring and the acquisition system “SCADAS LMS 316”

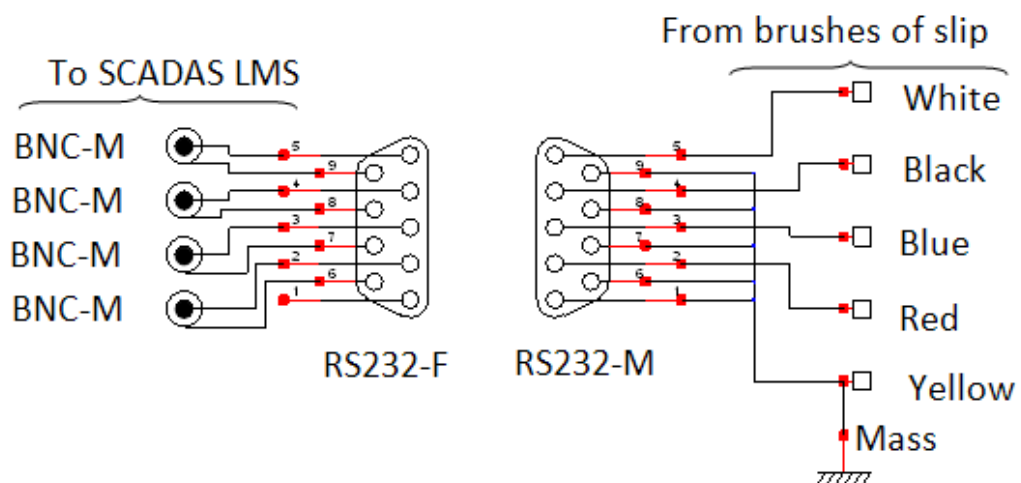


Fig.2.15: Connection between brushes of the slip ring and the acquisition system

In order to measure the input torque, four strain gages are mounted on the suns shaft (Fig.2.16)

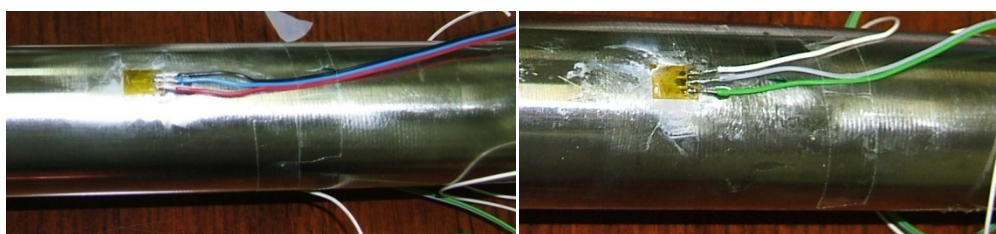
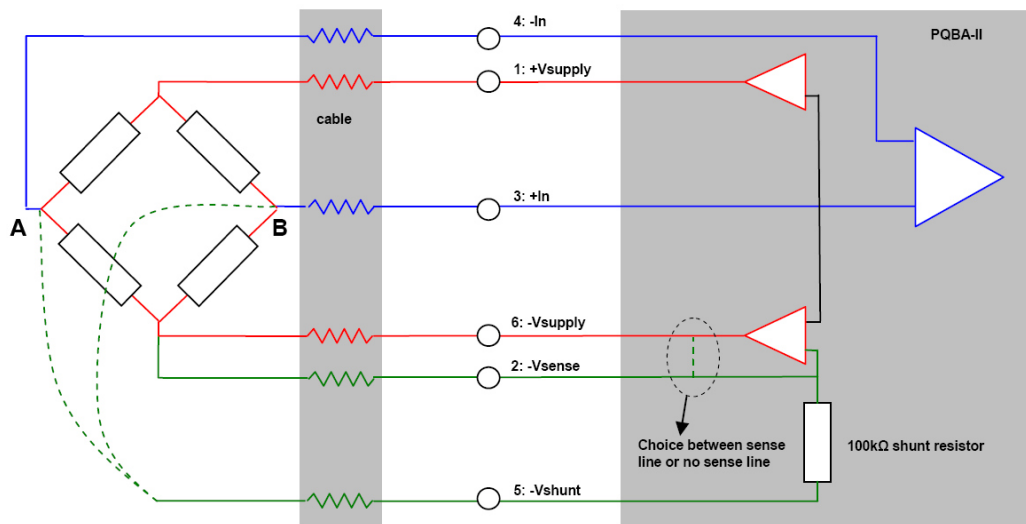


Fig.2.16: Strain gauges mounted on the shaft of suns

Those strain gauges are characterized by their resistance ($R=120\Omega$) and their gage factor ($K=2.02$). They are used in a full bridge configuration as shown in Fig.2.17 (Doebelin, 2004). This configuration compensates for cable wire resistance and temperature difference (Hoffman, 1989).

**Fig.2.17:** Schematic diagram of strain gauge mounting in full bridge mode with shunt resistor (LMS SCADAS, 2009)

A slip ring with 8 wires has been used (model: Michigan Scientific S8). It was mounted in the extremity of the shaft of suns allowing the connection to input module of the data acquisition system (Fig.2.18).

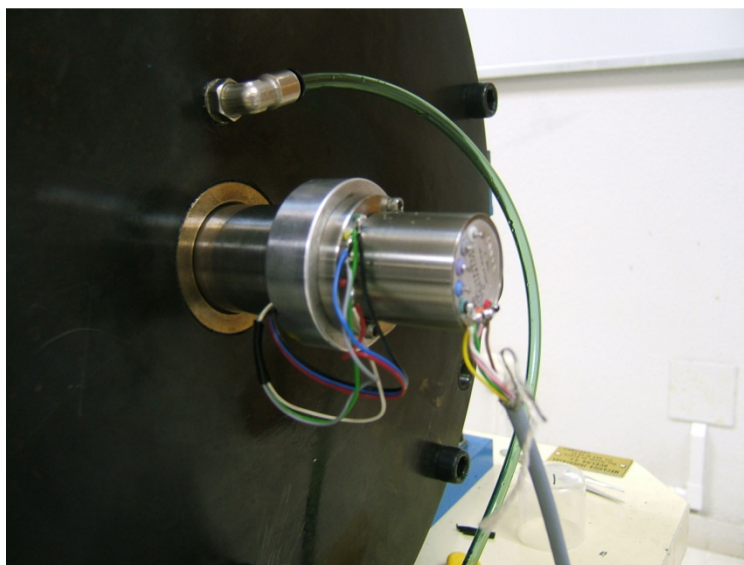
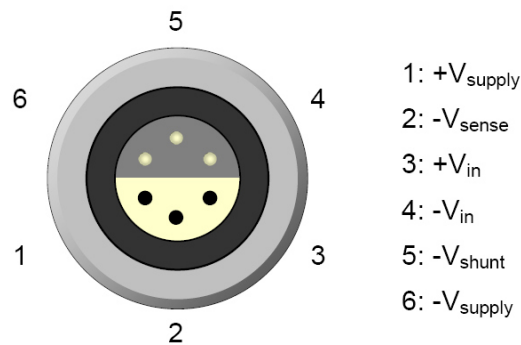
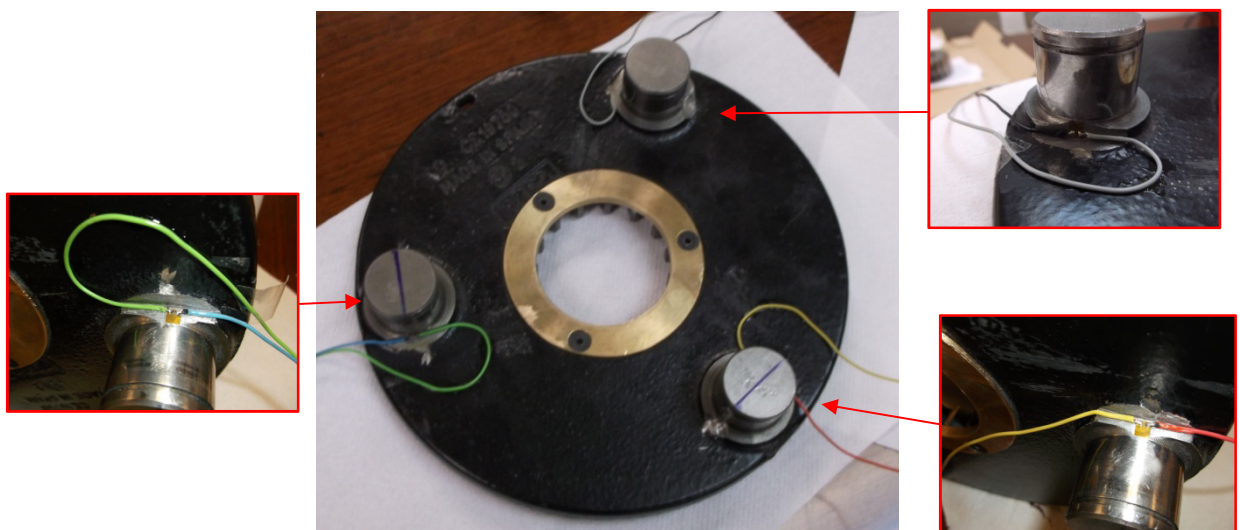


Fig.2.18: Slip ring mounted on the shaft of suns

Those sensors are connected to the acquisition system by 6pole LEMO connector (Fig.2.19).

**Fig.2.19:** Connector layout

In order to compare the load sharing between planets, a strain gauge is mounted in each pin hole of carrier planets (Fig.2.20). The resistance of those strain gauges is 120Ω and their gage factor ($K=1.77$).

**Fig2.20:** strain gauges mounted in each pin hole of the test carrier planets

The wires from the strain gauges are connected to the acquisition system through the hollow slip. They are used in quarter bridge configuration (Fig.2.21).

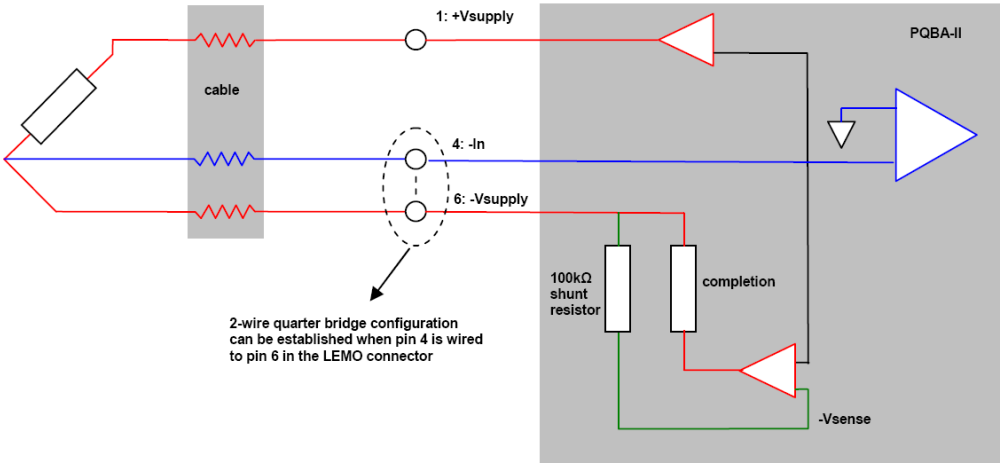


Fig.2.21: Schematic diagram of strain gauge mounting in quarter bridge mode (LMS SCADAS, 2009)

4. Excitation method

The hammer impact test is one of the most used forms of excitation because of its simplicity, low cost and portability. Figure 2.22 shows an impact hammer with a force transducer at its tip exciting the test bench (Fig.2.22).

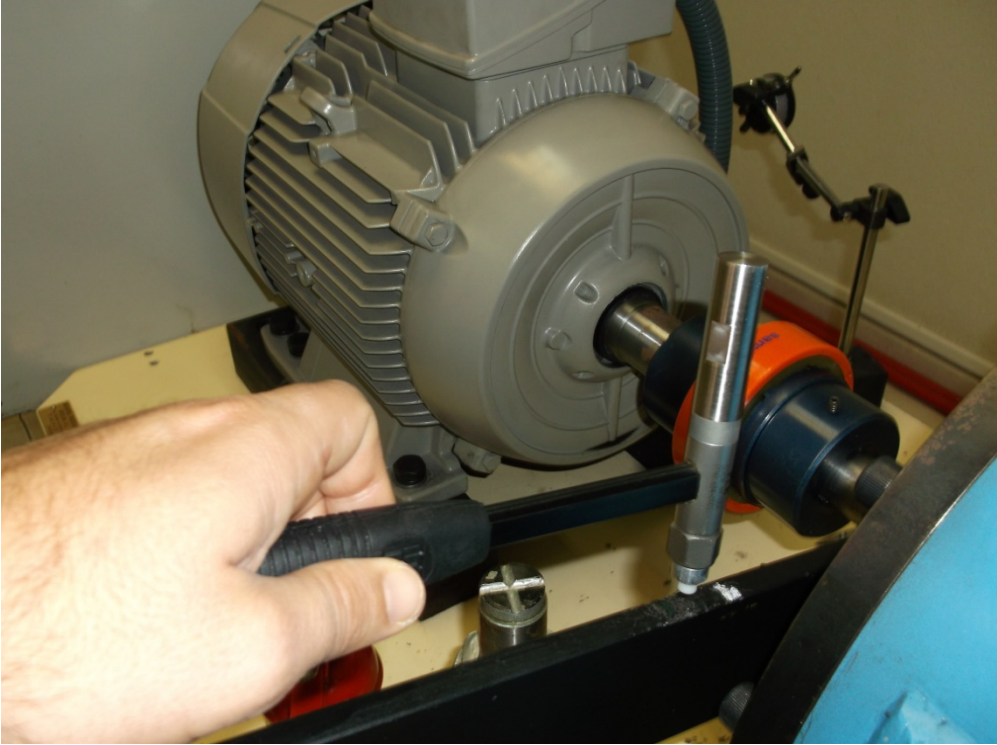


Fig.2.22: Impact test with hammer

The model of the hammer is PCB 086B03. Its sensitivity is 2,15 mV/N. A plastic or a metal tip is used to study response respectively in the low-frequencies and the high-frequencies.

5. Data analysis

5.1. Data acquisition system

The signals coming from accelerometers will be acquired by a LMS SCADAS 316 system (Fig.2.23).

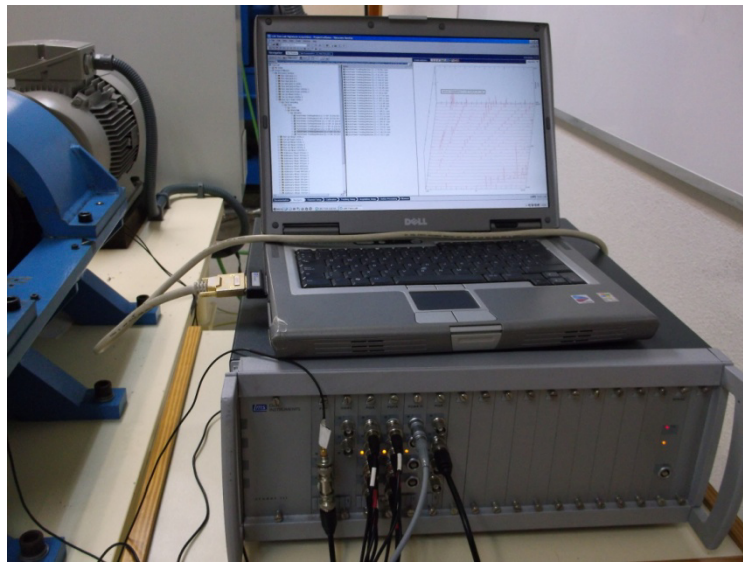


Fig.2.23: Acquisition system LMS SCADAS 316

“LMS SCADAS 316” is a high performance data acquisition system. It is connected to the computer through 1Gbit Ethernet host interface. This acquisition system is integrated with “LMS Test.Lab”, “LMS Test.Xpress” and “LMS CADA-X” software.

“LMS SCADAS 316” is composed by five different modules: four input modules and one output module. The input modules are:

- Programmable Dual Tacho module (PDT) allows order tracking acquisitions against RPM with two tachometer channel. Every tachometer can be connected to this module with an isolated BNC connector.
- Programmable Quad Amplifier module (PQA) is a basic four-channel voltage/ICP conditioning module. Each channel has its programmable input range and an analog A-weighting filter. This module has grounded a four non-isolated BNC inputs.

- Programmable Quad Floating Amplifier module (PQFA) adds a number of features to the basic PQA module. Every BNC input is isolated and has an analog programmable high-pass filter.
- Programmable Quad Bridge Amplifier module (PQBA) can support four channels of strain transducers, piezo-resistive or variable capacitor sensors. Every channel is connected by 6pole LEMO connector.

The output module is Dual Digital to Analog Converter module (DDAC). It includes two output channels with $\pm 10\text{V}$ DC as voltage and 50Ω as impedance. Output signals are ensured by digital-to-analog bit stream converters with 24-bit resolution.

5.2.Data Software

The data which is acquired with “LMS SCADAS 316” will be processed with the software “LMS Test.Lab signature acquisition” to obtain the acceleration spectra.

In fact, with this software we can use at the same time two tachometer channels used to measure the tracking parameter and twelve channels used to measure acceleration. In addition to calibration function, it can be used in stationary condition or in non stationary condition by choosing the measure mode as “stationary”, “Tracked” or “manually” in “Tracking setup”.

We define in the “Acquisition setup” of this software the “Span”, “the frequency lines” and the “resolution”. The span is the frequency range over which the measurement will be taken and which is unaffected by the cutoff filter. The frequency lines are the number of lines in the data block. The block size is two times the number of lines. The resolution is the frequency resolution of the data block. It is related to the frequency range and the number of lines in the block ($\text{Resolution} = \text{Bandwidth} / \text{Frequency lines}$). After that, we ranged the signals in the same onplet.

In the “Measure” onplet, the data is processed with the software “LMS Test.Lab signature acquisition” to obtain the acceleration spectra. Time responses were collected and averaged and later an auto-power spectrum is used to obtain frequency spectra corresponding to each averaged time history.

6. Conclusion

In this part, a back-to-back planetary test rig with purely mechanical power recirculation is presented. It allows the modification of the applied torque during the test, with the aim to reproduce non-stationary conditions.

Regarding the measurement capabilities of the test rig, several slip rings have been disposed in order to extract dynamic signals from different components of planetary gears set. In addition, the data acquisition system visualization of these signals through the software “LMS Test.Lab signature acquisition” under stationary and non-stationary conditions.

Using this test bench, the numerical model of planetary gear can be validated experimentally. It will be also possible to achieve an experimental modal analysis which is more detailed in next chapter.

Chapter 3:

Modal analysis of back-to-back planetary

Sommaire

1. Introduction	67
2. Experimental setup	67
3. Numerical model	67
4. Results	71
4.1. Natural frequencies and vibration modes	71
4.1.1. Teeth modes	73
4.1.2. Bearing modes	77
4.2. Analysis of the distribution of modal kinetic energies and modal strain energies	79
4.2.1. Teeth modes	79
4.2.2. Bearing modes	82
5. Conclusion	84

1. Introduction

In order to characterize the dynamic behaviour of the back-to-back planetary gear presented in the last chapter, experimental and numerical modal analysis techniques are achieved. Rotational and translational modal deflections are highlighted. Natural frequencies are compared to the results from lumped-parameter model. Modes are presented in the numerical studies in the low-frequency and high-frequency bands. Distributions of modal kinetic and strain energies are studied.

2. Experimental setup

An impact hammer is used to achieve the experimental modal analysis.

Four tri axial accelerometers mounted on the reaction ring, the test ring and the test carrier measure the rotational and translational vibration of each body.

The signals coming from accelerometers will be acquired by a LMS SCADAS Mobile SCM01 system and the data will be processed with the software “LMS Test.Lab Impact test” to obtain the Frequency Response Function.

3. Numerical model

The model of back to back planetary gear is based on the model developed by Lin and Parker (Lin and Parker, 1999) . The components are the ring (r), the sun (s), planets (1, 2, 3) and carrier (c) which carries the planets as shown in Fig.3.1.

The test ring and the test sun are respectively linked to the three planets of the test gear set via teeth mesh stiffness K_{rt1} , K_{rt2} , K_{rt3} and K_{st1} , K_{st2} , K_{st3} . The reaction ring and the reaction sun are respectively linked to the three planets via teeth mesh stiffness K_{rr1} , K_{rr2} , K_{rr3} and K_{sr1} , K_{sr2} , K_{sr3} . The reaction ring which has bearing stiffness K_{rrx} and K_{rry} in the x and y directions is free and its torsional stiffness is K_{rtu} whereas the test ring which has bearing stiffness K_{rtx} and K_{rty} is not exactly fixed but its torsional stiffness K_{rtu} is very high. Planets of the reaction gear set and the test gear set have bearing stiffness K_{tpix} and K_{tpiy} in the x and y directions ($i=1, 2$ or 3). The test carrier and the reaction carrier have also bearing stiffness respectively K_{ctx} , K_{cty} and K_{crx} , K_{cry} . The sun gears of both planetary gear sets are connected through a common shaft which has a torsional stiffness K_s . The carriers of both planetary gear sets are connected to each other through a hollow shaft which has a torsional stiffness K_c .

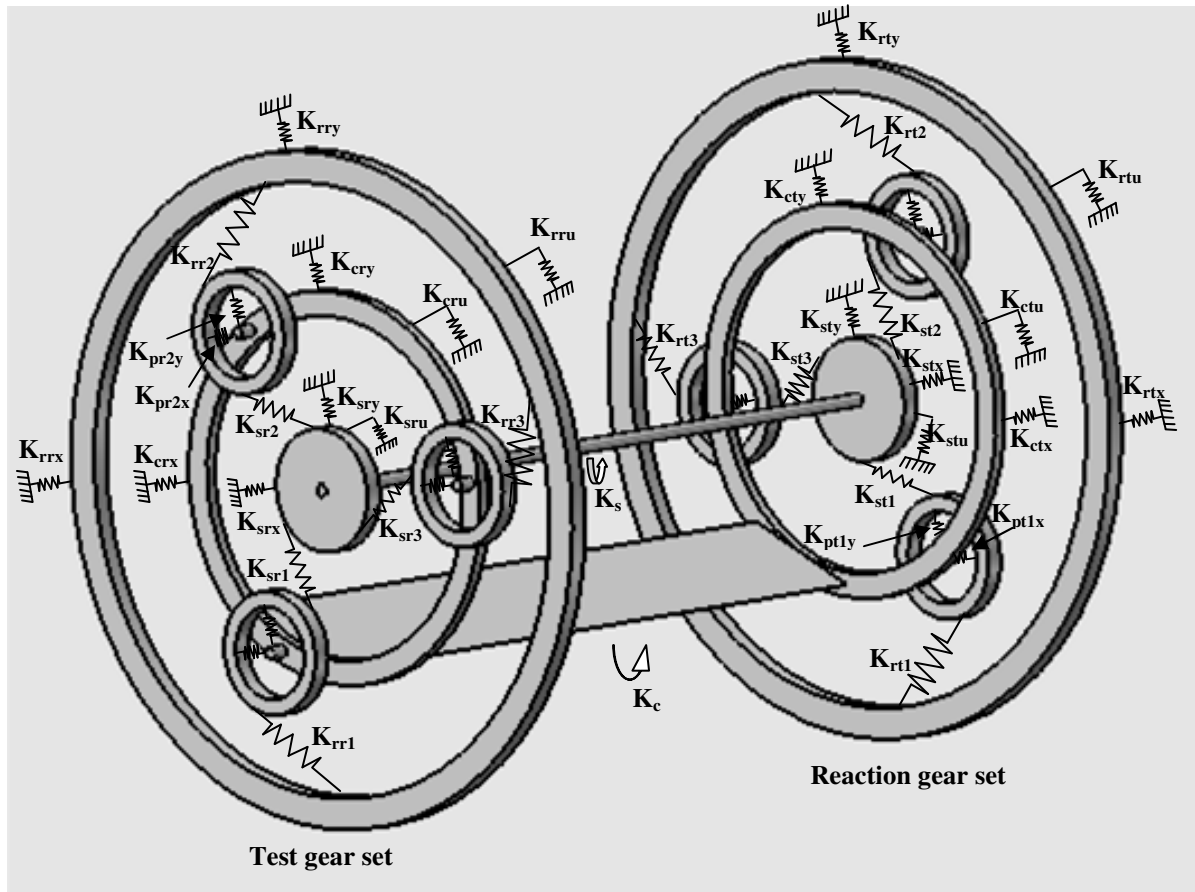


Fig.3.1: Model of planet gear

The system's equation of motion with 3 planets is:

$$M \ddot{q} + \Omega_c G \dot{q} + [K_b + K_M - \Omega_c^2 K_\Omega] q = F(t) \quad (3.1)$$

Where M is the mass matrix. K_b is the bearing stiffness matrix. G and K_Ω result from high-speed carrier. K_M is the stiffness matrix and $F(t)$ is the external force vector applied on the system. All these matrices are defined in the appendix.

The mass matrix is defined by:

$$M = \text{diag} (M_{cr}, M_{rr}, M_{sr}, M_{1r}, M_{2r}, M_{3r}, M_{ct}, M_{rt}, M_{st}, M_{1t}, M_{2t}, M_{3t}) \quad (3.2)$$

$$\text{Where : } M_{ij} = \text{diag} (m_{ij}, m_{ij}, I_{ij} / r_{ij}^2) \quad i = c, r, s, 1, 2, 3 \text{ and } j = r, t \quad (3.3)$$

$$G = \text{diag} (G_{cr}, G_{rr}, G_{sr}, G_{1r}, G_{2r}, G_{3r}, G_{ct}, G_{rt}, G_{st}, G_{1t}, G_{2t}, G_{3t}) \quad (3.4)$$

$$G_{ij} = \begin{bmatrix} 0 & -2m_{ij} & 0 \\ 2m_{ij} & 0 & 0 \\ 0 & 0 & 0 \end{bmatrix} \quad i = c, r, s, 1, 2, 3 \text{ and } j = r, t \quad (3.5)$$

$$K_\Omega = \text{diag} (K_{\Omega_r}, K_{\Omega_t}) \quad (3.6)$$

$$K_{\Omega_r} = \text{diag} (m_{cr}, m_{cr}, 0, m_{rr}, m_{rr}, 0, m_{sr}, m_{sr}, 0, m_{pr}, m_{pr}, 0, m_{pr}, m_{pr}, 0, m_{pr}, m_{pr}, 0) \quad (3.7)$$

$$K_{\Omega_t} = \text{diag} (m_{ct}, m_{ct}, 0, m_{rt}, m_{rt}, 0, m_{st}, m_{st}, 0, m_{pt}, m_{pt}, 0, m_{pt}, m_{pt}, 0, m_{pt}, m_{pt}, 0) \quad (3.8)$$

The bearing stiffness matrix :

$$K_b = \text{diag} (K_{crb}, K_{rrb}, K_{srb}, 0, 0, 0, K_{ctb}, K_{rtb}, K_{stb}, 0, 0, 0) \quad (3.9)$$

$$K_{ijb} = \text{diag} (K_{ijx}, K_{ijy}, K_{iju}) \quad i = c, r, s, 1, 2, 3 \quad \text{and} \quad j = r, t \quad (3.10)$$

$$K_m = \begin{bmatrix} K_{mr} & 0 \\ 0 & K_{mt} \end{bmatrix} + K_c \quad (3.11)$$

$$K_m = \begin{bmatrix} \sum K_{c1}^n & 0 & 0 & K_{c2}^1 & K_{c2}^2 & K_{c2}^3 \\ 0 & \sum K_{r1}^n & 0 & K_{r2}^1 & K_{r2}^2 & K_{r2}^3 \\ 0 & 0 & \sum K_{s1}^n & K_{s1}^1 & K_{s1}^2 & K_{s1}^3 \\ K_{c2}^1 & K_{r2}^1 & K_{s1}^1 & K_{pp}^1 & 0 & 0 \\ K_{c2}^2 & K_{r2}^2 & K_{s1}^2 & 0 & K_{pp}^2 & 0 \\ K_{c2}^3 & K_{r2}^3 & K_{s1}^3 & 0 & 0 & K_{pp}^3 \end{bmatrix} \quad (3.12)$$

$$K_{pp}^n = K_{c3}^n + K_{r3}^n + K_{s3}^n \quad (3.13)$$

$$K_{c1}^n = k_{pn} \begin{bmatrix} 1 & 0 & -\sin \Psi_n \\ 0 & 1 & \cos \Psi_n \\ -\sin \Psi_n & \cos \Psi_n & 1 \end{bmatrix} \quad (3.14)$$

$$K_{c2}^n = k_{pn} \begin{bmatrix} -\cos \Psi_n & \sin \Psi_n & 0 \\ -\sin \Psi_n & -\cos \Psi_n & 0 \\ 0 & -1 & 0 \end{bmatrix} \quad (3.15)$$

$$K_{c3}^n = \text{diag} (k_{pn}, k_{pn}, 0) \quad (4.16)$$

$$K_{r1}^n = k_m \begin{bmatrix} \sin^2 \Psi_m & -\cos \Psi_m \sin \Psi_m & -\sin \Psi_m \\ -\cos \Psi_m \sin \Psi_m & \cos^2 \Psi_m & \cos \Psi_m \\ -\sin \Psi_m & \cos \Psi_m & 1 \end{bmatrix} \quad (3.17)$$

$$K_{r2}^n = k_m \begin{bmatrix} -\sin \Psi_m \sin \alpha_r & \sin \Psi_m \cos \alpha_r & \sin \Psi_m \\ \cos \Psi_m \sin \alpha_r & -\cos \Psi_m \cos \alpha_r & -\cos \Psi_m \\ \sin \alpha_r & -\cos \alpha_r & -1 \end{bmatrix} \quad (3.18)$$

$$K_{r3}^n = K_m \begin{bmatrix} \sin^2 \alpha_r & -\cos \alpha_r \sin \alpha_r & -\sin \alpha_r \\ -\cos \alpha_r \sin \alpha_r & \cos^2 \alpha_r & \cos \alpha_r \\ -\sin \alpha_r & \cos \alpha_r & 1 \end{bmatrix} \quad (3.19)$$

$$K_{s1}^n = k_{sn} \begin{bmatrix} \sin^2 \Psi_{sn} & -\cos \Psi_{sn} \sin \Psi_{sn} & -\sin \Psi_{sn} \\ -\cos \Psi_{sn} \sin \Psi_{sn} & \cos^2 \Psi_{sn} & \cos \Psi_{sn} \\ -\sin \Psi_{sn} & \cos \Psi_{sn} & 1 \end{bmatrix} \quad (3.20)$$

$$K_{s2}^n = k_{sn} \begin{bmatrix} \sin \Psi_{sn} \sin \alpha_s & \sin \Psi_{sn} \cos \alpha_s & -\sin \Psi_{sn} \\ -\cos \Psi_{sn} \sin \alpha_s & -\cos \Psi_{sn} \cos \alpha_s & \cos \Psi_{sn} \\ -\sin \alpha_s & -\cos \alpha_s & 1 \end{bmatrix} \quad (3.21)$$

$$K_{s3}^n = k_{sn} \begin{bmatrix} \sin^2 \alpha_s & \cos \alpha_s \sin \alpha_s & -\sin \alpha_s \\ \cos \alpha_s \sin \alpha_s & \cos^2 \alpha_s & \cos \alpha_s \\ -\sin \alpha_s & -\cos \alpha_s & 1 \end{bmatrix} \quad (3.22)$$

$$\Psi_{sn} = \Psi_n - \alpha_s \quad (3.23)$$

$$\Psi_{rn} = \Psi_n + \alpha_r \quad (3.24)$$

The planets in the test gear set and the reaction gear set are assumed identical and equally spaced. The gyroscopic terms G and K_Ω are neglected because the electrical motor is running at low speed (200 – 1490 rpm). The equation of motion will simplify in this case to:

$$M\ddot{q} + [K_b + K_M]q = 0 \quad (3.25)$$

q is the degree of freedom vector defined as the following:

$$q = \begin{Bmatrix} q_r \\ q_t \end{Bmatrix} \quad (3.26.a)$$

$$q_r = \{x_{cr}, y_{cr}, u_{cr}, x_{rr}, y_{rr}, u_{rr}, x_{sr}, y_{sr}, u_{sr}, \zeta_{1r}, \eta_{1r}, u_{1r}, \zeta_{2r}, \eta_{2r}, u_{2r}, \zeta_{3r}, \eta_{3r}, u_{3r}\}^T \quad (3.26.b)$$

$$q_t = \{x_{ct}, y_{ct}, u_{ct}, x_{rt}, y_{rt}, u_{rt}, x_{st}, y_{st}, u_{st}, \zeta_{1t}, \eta_{1t}, u_{1t}, \zeta_{2t}, \eta_{2t}, u_{2t}, \zeta_{3t}, \eta_{3t}, u_{3t}\}^T \quad (3.26.c)$$

q_r is the degree of freedom vector in the reaction gear set (r) and q_t is the degree of freedom vector in the test gear set (t). The carrier, the ring and the sun translations x_{ij} and y_{ij} (i=c, r, s and j=r, t) and planet translations ζ_{nj} and η_{nj} (n=1, 2, 3 and j=r, t) are measured with respect to the rotational frame of reference $R = \{\vec{i}, \vec{j}, \vec{k}\}$.

The rotational coordinates are $u_{rj} = r_{rj}\theta_{rj}$ for reaction gear set $u_{tj} = r_{tj}\theta_{tj}$ and for test gear set where j=c,r,s,1,2,3. θ_{rj} and θ_{tj} are the component rotation; r_{rj} and r_{tj} are the base radius for the sun, ring and planets and the radius of the circle passing through the planets centre for the carrier.

4. Results

In this part, results from the modal analysis on the back-to-back planetary gears are presented. Experimental and numerical modes are checked and compared. The modes are classified and studied in terms of modal kinetic energies and modal strain energies for each natural frequency. Finally, effects of load changing (by adding mass) on natural frequencies and vibration modes are studied.

4.1. Natural frequencies and vibration modes

The natural frequencies and vibration modes are determined from the equation of motion (3.25) and corresponding eigen-value problem which is:

$$\omega_i^2 M \phi_i = [K_b + K_M] \phi_i \quad (3.27)$$

Where ω_i are the natural frequencies and ϕ_i are the vibration modes.

The rotational, translational and planet mode types were defined by Lin and Parker (Lin and Parker, 1999b) :

- The rotational and translational modes are vibration with natural frequencies having respectively multiplicity $m=1$ and $m=2$
- The planet modes exist only if the number of planet $N>3$ and have multiplicity $m=N-1$

In the test gear set and the reaction gear set, there are only three planets ($N=3$). So, only rotational and translational modes appear when solving the Eigen-value problem.

According to the energy distribution and component deflection, Cunliffe (Cunliffe & all 1974) and Ericson (Ericson and Parker, 2013) classified the natural frequencies into two bands. The modes of the first band are called “bearing modes” or “fixture modes”. The modes of the second band are called “tooth modes” or “gear modes”.

The distinction between fixture modes and gear modes is independent of the rotational and translational modes.

Table 3.1 shows the parameters of the model.

Reaction planetary gear set				
	Sun	Planet	Ring	Carrier
Teeth number	16	24	65	-
Mass (Kg)	0,485	1,225	28,1	3,643
Base diameter (mm)	61.38	92.08	249.38	57.55
Moment of inertia (Kg.m ²)	356.10^{-6}	2045.10^{-6}	697767.10^{-6}	21502.10^{-6}
Bearing stiffness (N/m)	$8,8.10^7$	$3,5.10^6$	$2,1.10^7$	$4,8.10^8$
Torsional stiffness (N/m)	-	-	0	-
Mesh stiffness (N/m)	$4,46.10^8$	$6,28.10^8$		
Test planetary gear set				
	Sun	Planet	Ring	Carrier
Teeth number	16	24	65	-
Mass (Kg)	0,485	1,225	28,1	3,643
Base diameter (mm)	61.38	92.08	249.38	57.55
Moment of inertia (Kg.m ²)	356.10^{-6}	2045.10^{-6}	697767.10^{-6}	21502.10^{-6}
Bearing stiffness (N/m)	$8,8.10^7$	$3,5.10^6$	$2,1.10^7$	$4,8.10^8$
Torsional stiffness (N/m)	-	-	$7,9.10^6$	-
Mesh stiffness (N/m)	$4,46.10^8$	$6,28.10^8$		
Shaft stiffness				
	Sun	Planet	Ring	Carrier
Torsional (Nm/rad)	$3,73.10^4$	-	-	$8,38.10^5$
Flexural	$4,9.10^5$	-	-	$1,1.10^7$

Table 3.1. Lumped-parameter values of reaction and test planetary gear set and shaft stiffness

The natural frequencies are identified numerically and experimentally.

Impacts were done on the arm of the free ring.

Fig.3.2 represents the Nyquist plot of the frequency response in the fix ring with hammer impact test. It shows that the response converge to zero. So, the system tends towards stability.

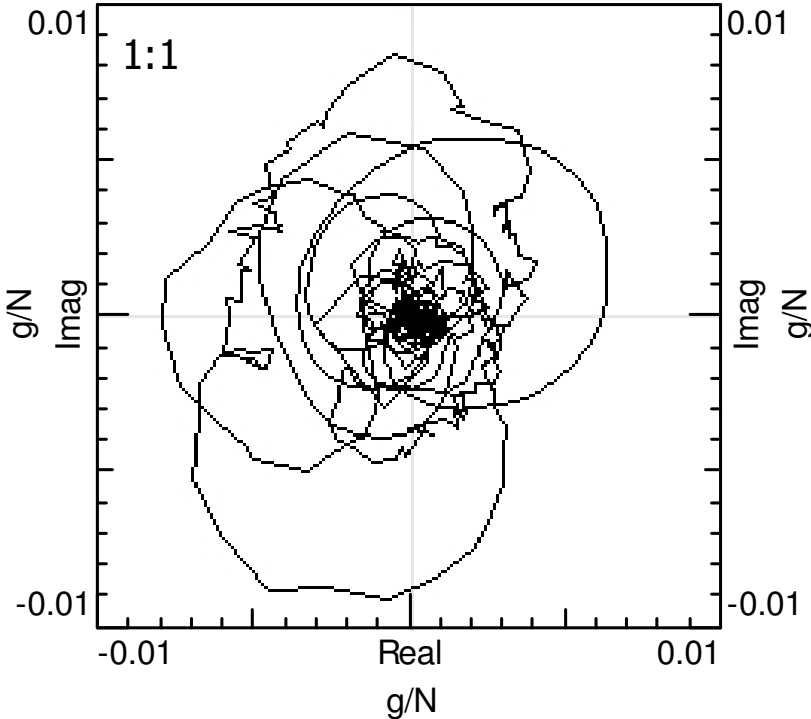


Fig.3.2: Nyquist plot of the frequency response of the fix ring

4.1.1. Teeth modes

For each test, we achieved ten impacts and the acquisition system “LMS Test.Lab Impact test” averaged the results. Fig.3.3 represents the Frequency Response Function (FRF) in the fix ring.

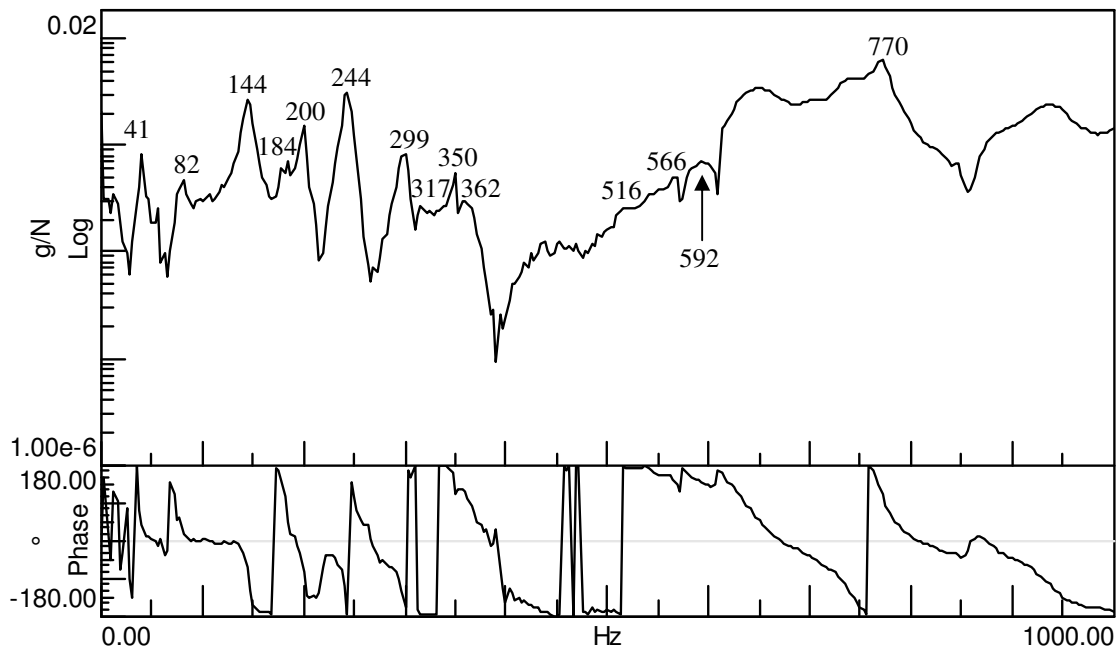


Fig.3.3: Frequency Response Function of the fix ring for low frequencies

Table 3.2 compares the natural frequencies determined from impact test experiments and numerical model and shows the multiplicity of each mode from the analytical model.

Mode	Type	Impulse exp (Hz)	Numerical model (Hz)	Multiplicity	Error (%)
1	-	41	-	-	-
2	R	82	118	1	30
3	R	144	136	1	6
4	-	182	-	-	-
5	T	200	193	2	4
6	R	244	244	1	0
7	R	-	247	1	-
8	T	299	288	2	4
9	T	317	344	2	11
10	R	350	376	1	7
11	R	362	387	1	7
12	T	516	536	2	4
13	R	566	547	1	4

14	R	592	550	1	8
15	-	770	-	-	-

Table 3.2: Natural frequencies from experiments an numerical model

Experiments show fourteen natural frequencies whereas the numerical model shows twelve natural frequencies composed of eight rotational modes and four translational modes. The natural frequencies 41Hz, 182Hz and 770Hz appear only in the impulse test whereas the natural frequency 247 Hz appears only in the numerical model. The remaining natural frequencies agree within 11% as the maximum rate. There is only one identified natural frequency where the error reaches 30% which can be explained by the fact that the adopted model in this chapter considers only 3 degrees of freedom (2 translations and 1 rotation). Obviously, it will not be possible to get low percentage error for all computed natural frequencies.

Fig.3.4 shows the modal deflection for each natural frequency of the system down to 1000Hz.

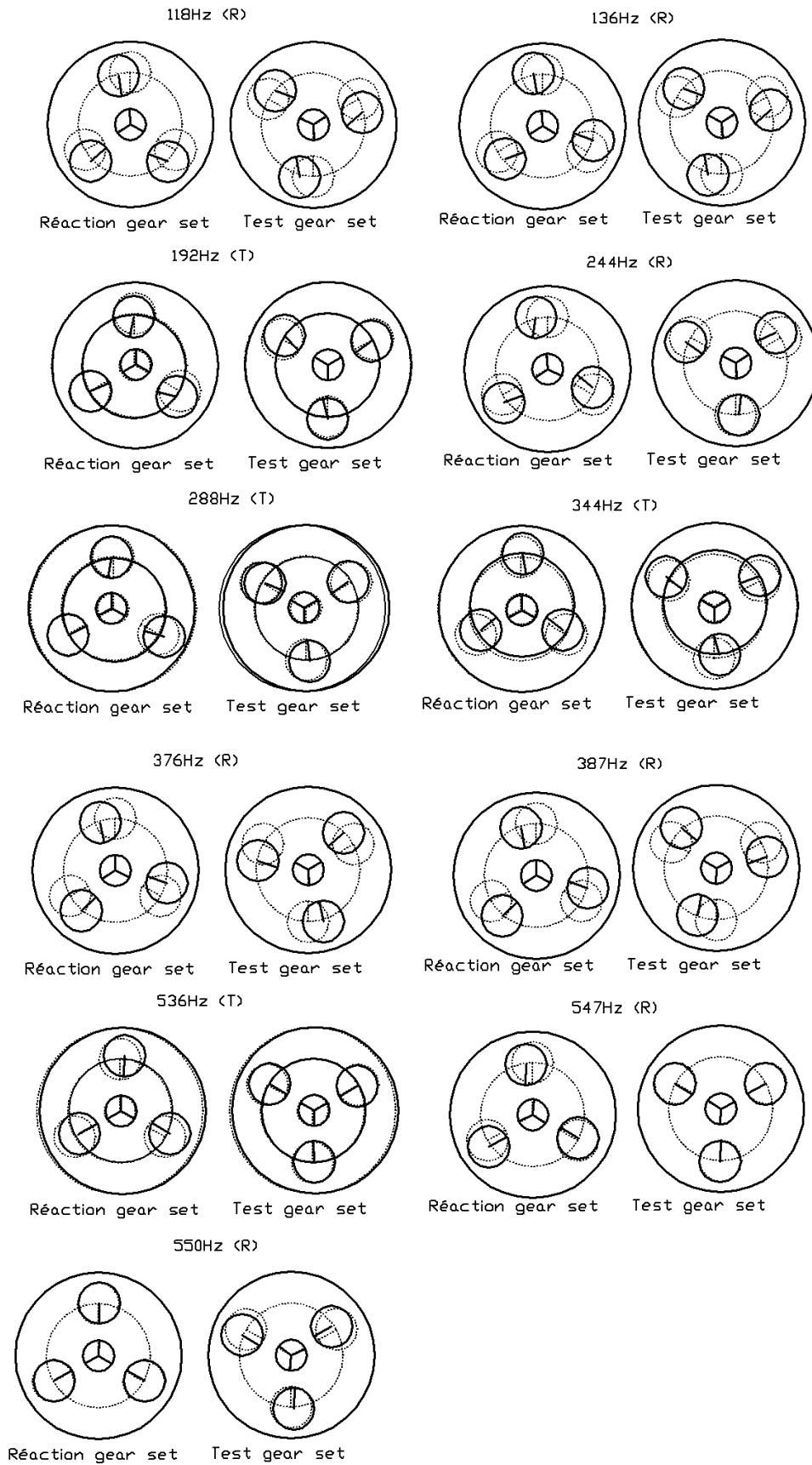


Fig. 3.4: Vibration modes in the low frequencies

It is well noticed that all planets have the same modal deflection and move in phase in the rotational modes (118Hz, 136Hz, 244Hz, 376Hz , 387Hz, 547Hz and 550Hz). Besides, the carriers, the suns and the rings on the test and the reaction gear set have pure translation in the translation modes (192Hz, 288Hz, 344Hz and 536Hz).

4.1.2. Bearing modes

Bearing modes are identified by solving Eigen-value problem and using impact test.

Fig.3.5 represents the frequency response function in the fix ring with hammer impact test.

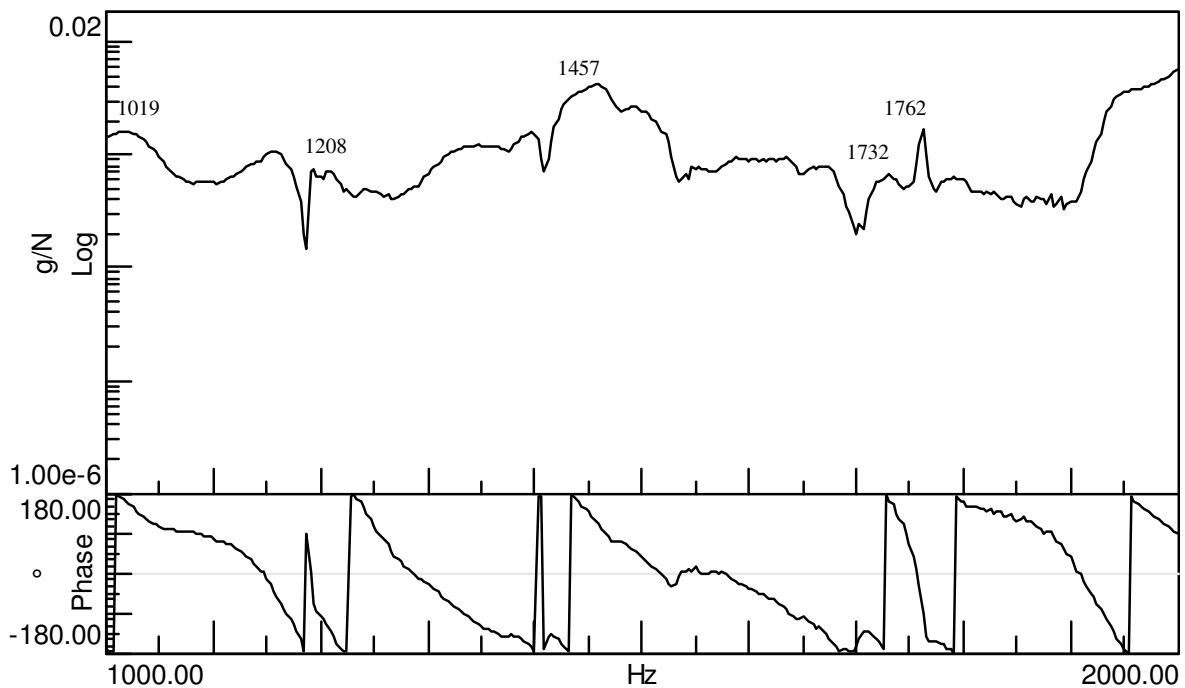


Fig.3.5: Frequency response function of the fix ring in the high frequencies

Table 3.3 compares the natural frequencies determined from impact test experiments and the numerical model in the high frequencies.

Mode	Type	Impulse exp (Hz)	Numerical model (Hz)	Multiplicity	Error (%)
16	-	1019	-	-	-
17	T	1208	1232	2	2
18	-	1457	-	-	-
19	T	1732	1847	2	7
20	T	1762	1888	2	7

Table 3.3: Natural frequencies from experiments an numerical model

Experiments show five natural frequencies whereas numerical model shows three natural frequencies associated with three translational modes. The natural frequencies 1019Hz and 1457Hz which can be due to the axial vibration appear only in the impulse test. The rest of natural frequencies agree within 7% as the maximum difference rate.

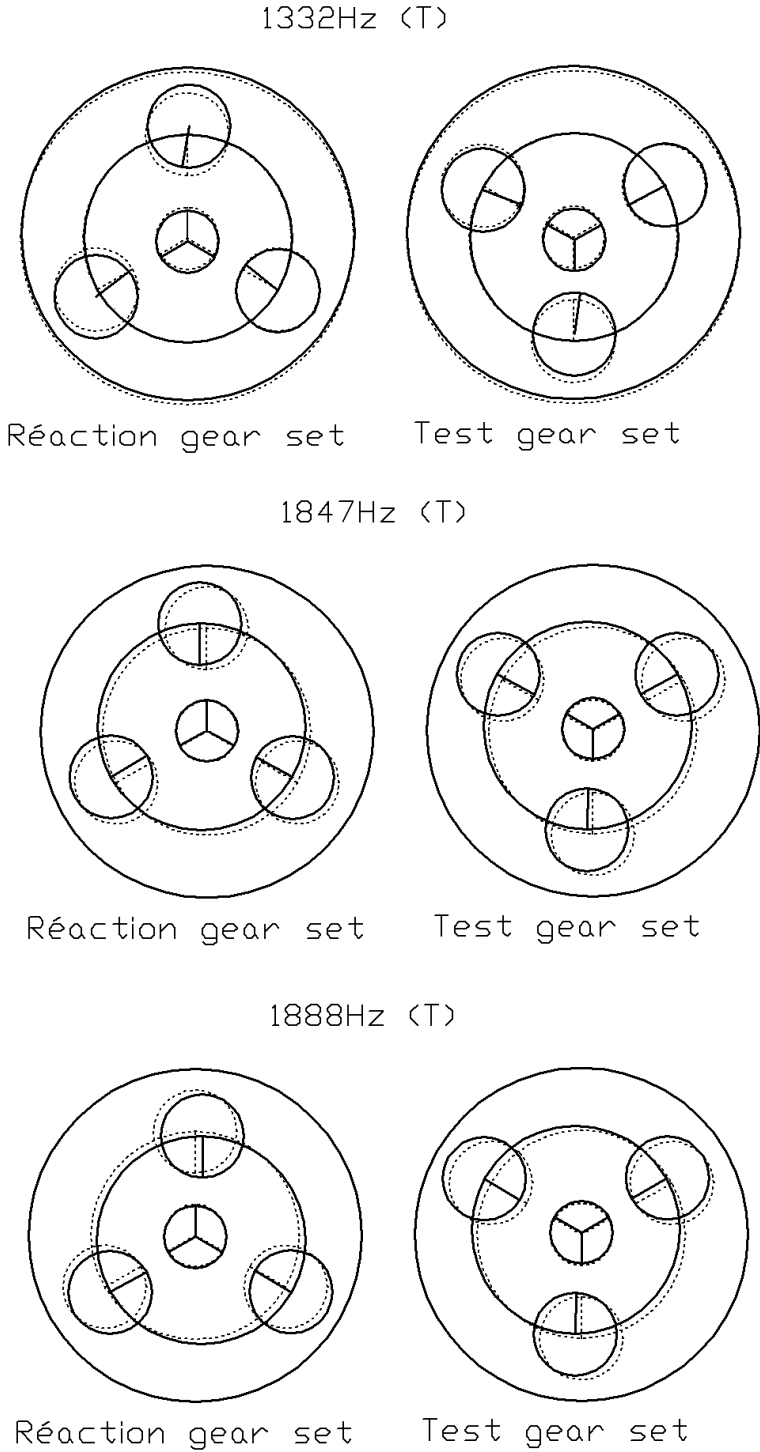


Fig.3.6: Vibration modes in the high frequencies

Fig.3.6 shows that the carriers, the suns and the rings on the test and the reaction gear set have pure translation in the translation modes (1332Hz, 1847Hz and 1888Hz).

4.2. Analysis of the distribution of modal kinetic energies and modal strain energies

Computation of the modal strain energy and the modal kinetic energy distributions gives information on bodies sought to critical speeds (which excite the natural frequencies) in terms of dominant motion and deflection.

The total modal strain energy can be written as the sum of the strain energies of rotation and translation from each component:

$$Ep_{\phi} = \frac{1}{2} \phi_i^t \tilde{K} \phi_i = \sum Ep_{\phi_{ij}} + \sum Ep_{\phi_{ijw}} + \sum (Ep_{\phi_{sin}} + Ep_{\phi_{rin}}) \quad (3.28)$$

$Ep_{\phi_{ij}}$ and $Ep_{\phi_{ijw}}$ are the modal strain energies of bearing stiffness in the rotational and translational modal deflections of the suns, carriers, rings and planets ($j=s, c, r, t, 1, 2, 3$) in the test gear set and the reaction gear set ($i=t, r$). $Ep_{\phi_{sin}}$ and $Ep_{\phi_{rin}}$ are the modal strain energies of meshing sun-planets and planets-ring meshing in the test gear set and the reaction gear set.

The modal kinetic energy can be written also as the sum of the modal kinetic energies of rotation and translation from each component of the system:

$$Ec_{\phi} = \frac{1}{2} w_i^2 \phi_i^t M \phi_i = \sum Ec_{\phi_{ij}} + \sum Ec_{\phi_{ijw}} \quad (3.29)$$

$Ec_{\phi_{ij}}$ and $Ec_{\phi_{ijw}}$ are the kinetic energies in the rotational and translational movement of the suns, carriers, rings and planets ($j=s, c, r, t, 1, 2, 3$) in the test gear set and the reaction gear set ($i=t, r$).

4.2.1. Teeth modes

Fig.3.7 shows the distribution of modal kinetic energies in the low frequencies.

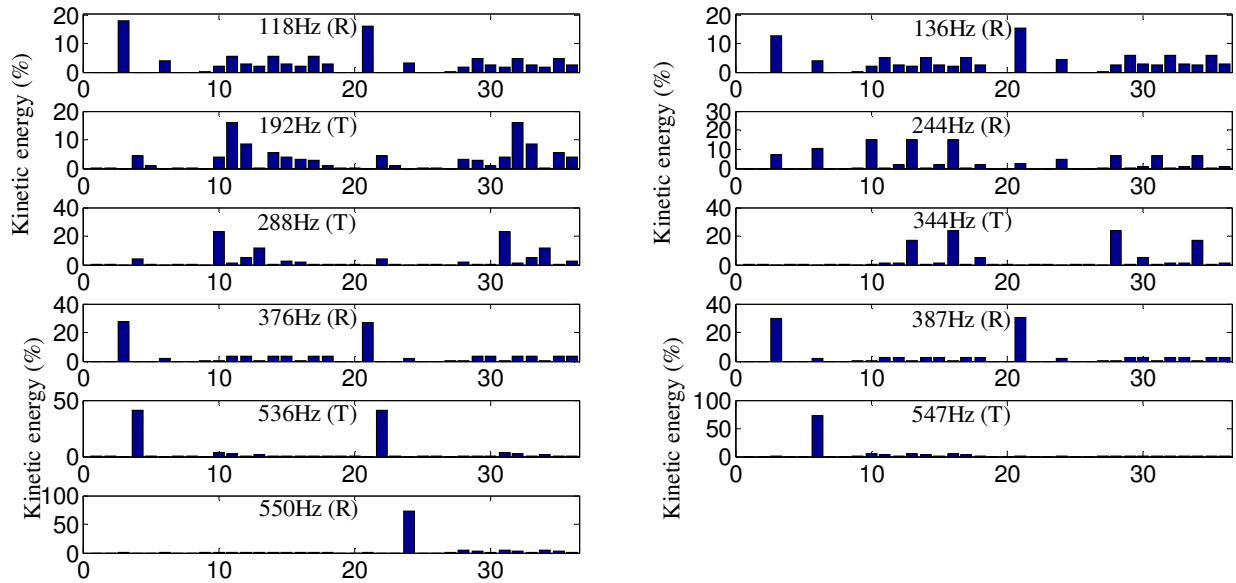


Fig.3.7: Modal kinetic energies in the low-frequencies

In X-axis is represented the contribution of each degree of freedom in the total modal kinetic energy. Details are given in table 3.4.

1-2	Translations of reaction carrier	19-20	Translations of test carrier
3	Rotation of reaction carrier	21	Rotation of test carrier
4-5	Translations of reaction ring	22-23	Translations of test ring
6	Rotation of reaction ring	24	Rotation of test ring
7-8	Translations of reaction sun	25-26	Translations of test sun
9	Rotation of reaction sun	27	Rotation of test sun
10-11	Translations of reaction planet 1	28-29	Translations of test planet 1
12	Rotation of reaction planet 1	30	Rotation of test planet 1
13-14	Translations of reaction planet 2	31-32	Translations of test planet 2
15	Rotation of reaction planet 2	33	Rotation of test planet 2
16-17	Translations of reaction planet 3	34-35	Translations of test planet 3
18	Rotation of reaction planet 3	36	Rotation of test planet 3

Table 3.4: The X-axis of kinetic energies location

The dominant motion in the translational mode 547Hz is translation of reaction ring on the X direction.

Fig.3.8 shows the distribution of modal strain energies in the low frequencies.

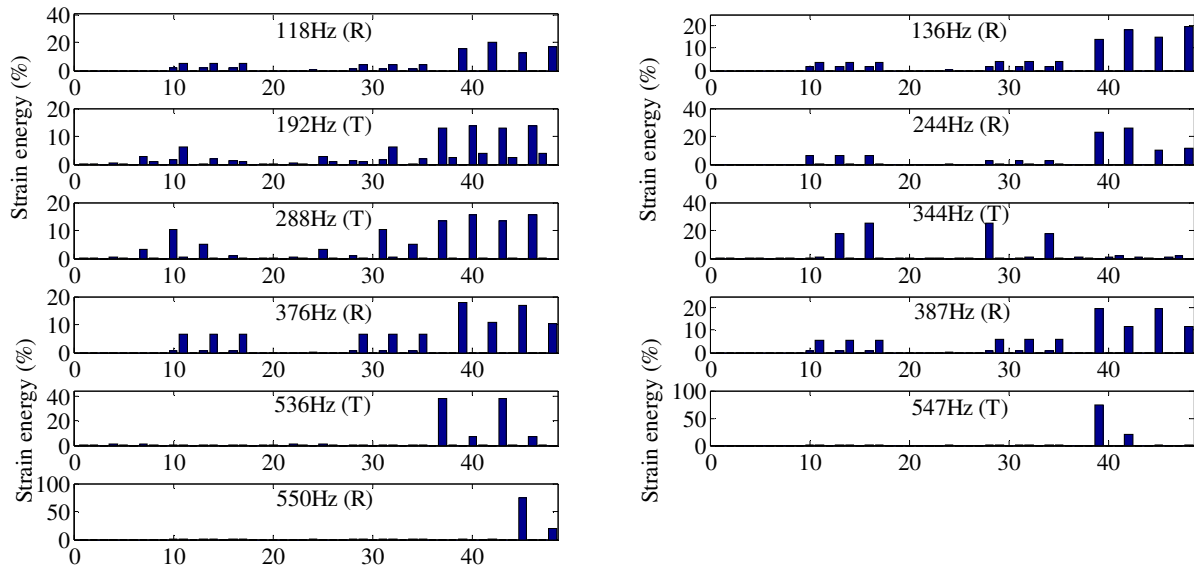


Fig.3.8: Strain energy in the low-frequencies

Where the X-axis is defined on the table 3.5:

1-3	Bearing of reaction carrier	25-27	Bearing of test sun
4-6	Bearing of reaction ring	28-30	Bearing of test planet 1
7-9	Bearing of reaction sun	31-33	Bearing of test planet 2
10-12	Bearing of reaction planet 1	34-36	Bearing of test planet 3
13-15	Bearing of reaction planet 2	37-39	Meshing reaction ring-planets
16-18	Bearing of reaction planet 3	40-42	Meshing reaction sun-planets
19-21	Bearing of test carrier	43-45	Meshing test ring-planets
22-24	Bearing of test ring	46-48	Meshing test sun-planets

Table 3.5: The X-axis of strain energies location

The dominant modal strain energy in the translational mode 547Hz is located at the meshing between reaction ring and reaction planet n°3.

Table 3.6 presents a resume of the modal dominant movement and the dominant strain energy in each low-frequency mode.

Frequencies	Modal dominant movement	Dominant strain energy
118Hz (R)	Rotation of reaction carrier	Meshing reaction sun-planet3
136Hz (R)	Rotation of test carrier	Meshing test sun-planet3
192Hz (T)	Translation of reaction planet1 (X)	Meshing reaction sun-planet1
	Translation of test planet2 (Y)	Meshing test sun-planet1
244Hz (R)	Rotation of test planet1 (X direction)	Meshing reaction sun-planet3

	Rotation of test planet2 (X direction)	
	Rotation of test planet3 (X direction)	
288Hz (T)	Translation of reaction planet1 (X)	Meshing reaction sun-planet1
	Translation of test planet2 (X)	Meshing test sun-planet1
344Hz (T)	Translation of reaction planet3 (X)	Bearing of reaction planet3 (X direction)
	Translation of test planet 1 (X)	Bearing of test planet3 (X direction)
376Hz (R)	Rotation of reaction carrier	Meshing reaction ring-planet3
387Hz (R)	Rotation of test carrier	Meshing test ring-planet3
536Hz (R)	Translation of reaction ring (X)	Meshing reaction ring-planet1
	Translation of test ring (X)	Meshing test sun-planet2
547Hz (R)	Rotation of reaction ring	Meshing reaction ring-planet3
550Hz (R)	Rotation of test ring	Meshing test ring-planet3

Table 3.6: Dominant motion and the dominant strain energy in the low-frequencies

In the teeth modes characterized fixture components deflections; significant strain energy is located in sun-planets and ring-planets meshing of the two stages. This can be explained by the fact that the stiffness of the meshing is higher than that of shafts and bearings. So, the strain energies are bigger for the components which have the higher stiffness. Also, those modes are predominantly characterized by motion of the individual planetary gear components, particularly the planet gears.

4.2.2. Bearing modes

Fig.3.9 shows the distribution of modal kinetic energies in the high frequencies. The X-axis is defined on the table 3.4.

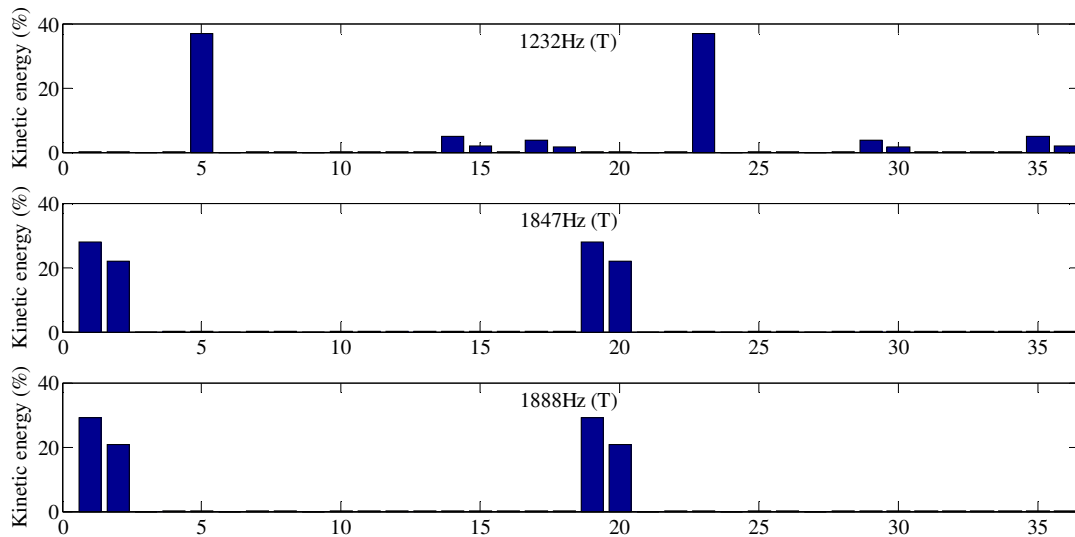


Fig.3.9: Kinetic energy in the high-frequencies

The dominant motion in the translational mode 1867Hz is the translation of the reaction sun in the Y direction.

Fig.3.10 shows the distribution of modal strain energies in the low frequencies. The X-axis is defined on the table 3.5.

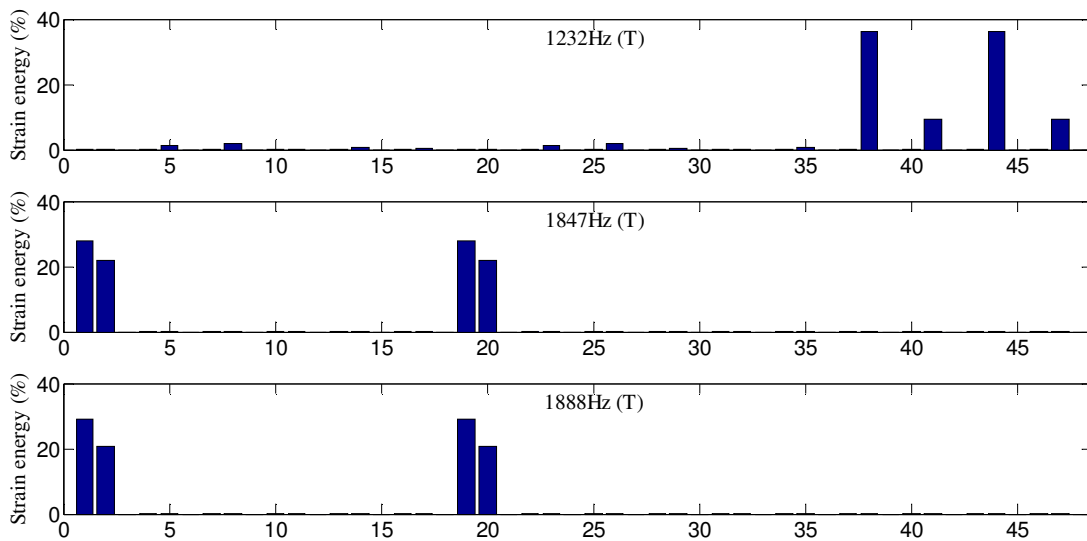


Fig.3.10: Strain energy in the high-frequencies

The dominant strain energy in the translational mode 2527Hz is the bearing of test carrier in the Y direction.

Table 3.7 presents a resume of the modal dominant movement and the dominant strain energies in each high-frequency mode.

Frequencies	Modal dominant movement	Dominant strain energy
1232Hz (T)	Translations of reaction ring (Y)	Meshing reaction ring-planet2
	Translations of test planet1 (X)	Meshing test ring-planet2
1847Hz (T)	Translations of reaction carrier (X)	Bearing of reaction carrier (X direction)
	Translations of test carrier (X)	Bearing of test carrier (X direction)
1888Hz (T)	Translations of reaction carrier (X)	Bearing of reaction carrier (X direction)
	Translations of test carrier (X)	Bearing of test carrier (X direction)

Table 3.7: Dominant motion and the dominant strain energy in the high-frequencies

Table 3.7 shows that bearing modes are characterized by the strain energies and the kinetic energies of carriers. These characterizations are confirmed at the frequencies 1847Hz and 1888Hz.

In general, the significant strain energies in the low frequencies are on the tooth of gears if the gear mesh stiffness is higher than the stiffness of shafts and bearing and the motion of gears have the higher kinetic energies. However, for the same condition, the dominant movement in the higher frequencies is the movement of carriers which have also the dominant strain energies.

5. Conclusion

In this chapter, a lumped-parameter model of back-to-back planetary gear was proposed to determine the natural frequencies, natural modes and the distribution of modal energies. The numerical results are compared to those obtained by hammer impact test.

This chapter highlights also design and modelling characteristics of back-to-back planetary gear:

In fact, only the rotational and the translational modes appear because the number of planets is three in each gear set

The impact test hammer matches the natural frequencies and forced response predicted by lumped parameter model at low-frequencies and high-frequencies. Indeed, eleven natural frequencies are confirmed in the low-frequencies and three natural frequencies are confirmed in the high-frequencies.

Two classes of modes are observed: The first is gear modes or tooth modes where the natural frequencies below 1000Hz and the significant strain energy are in the tooth meshes and the dominant motions are the movement of gears. The second is fixture modes or bearing modes where the natural frequencies above 1000Hz and the significant strain energy is in the bearing of planetary gear component. The classification of the tooth modes and the bearing modes on the low frequencies bands or on the high frequencies bands depend on the values of the mesh stiffness and the bearing and shaft stiffness.

Natural frequencies determined in this chapter are excitation sources when the system is running in stationary and non stationary conditions and they can be observed on the frequency responses.

Chapter 4:

Dynamic behaviour of back-to-back planetary gear in the non-stationary conditions

Sommaire

1. Introduction.....	87
2. Numerical model.....	87
3. Stationary conditions	90
3.1. Frequency characterization of the planetary gear.....	95
3.2. Effect of loading variation on frequency content	101
4. Variable load	105
5. Run up regime.....	108
6. Run down regime	114
7. Variable speed.....	120
8. Conclusion	123

1. Introduction

In this chapter, a numerical model of the planetary gear presented in chapter 2 is developed. Variable load effects are included to the model. Simulation of the dynamic behaviour of this transmission is presented highlighting the variable loading effects. In the second part of this chapter, variable speed effects of the run up, the run down and variable speed regimes are modelled. Simulation of the dynamic behaviour of this transmission is presented putting in evidence the non stationary effects. Finally, an extensive experimental study of the back-to-back planetary gear is conducted for validation of the mathematic model.

2. Numerical model

In this part, the model of back-to-back planetary gear test bench will be presented. A torsional model based on that of Lin and Parker (Lin and Parker, 2002) is adopted. The components are the ring (r), the sun (s), planets (1, 2, 3) and carrier (c) which carries the planets in the reaction gear set and in the test gear set as shown in Fig.4.1.

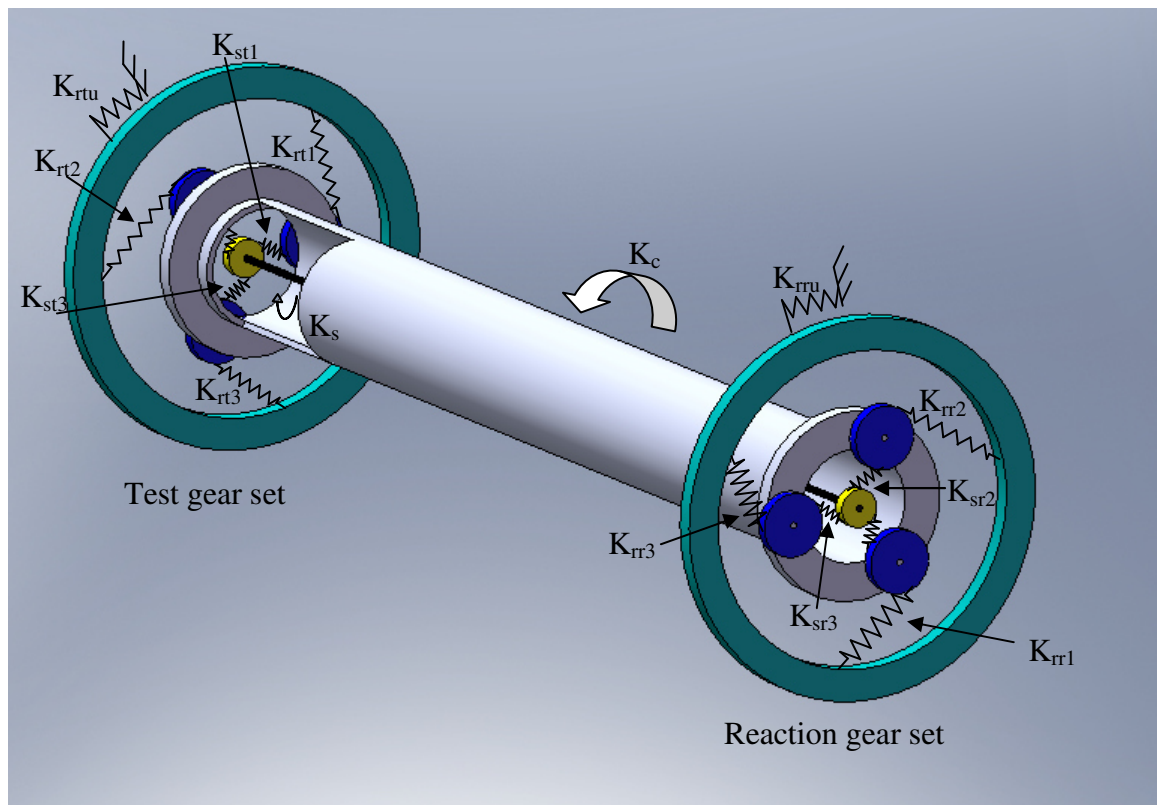


Fig.4.1: Model of planet gear

The test ring gear and the test sun are respectively linked to the three planets of the test gear set via mesh stiffness K_{rt1} , K_{rt2} , K_{rt3} and K_{st1} , K_{st2} , K_{st3} . The same modelling is adopted for the reaction gear set, the reaction ring and the reaction sun which are respectively linked to the three planets via mesh stiffness K_{rr1} , K_{rr2} , K_{rr3} and K_{sr1} , K_{sr2} , K_{sr3} . The reaction ring is free and its torsional stiffness K_{rtu} is zero whereas the test ring is not completely clamped but with high torsional stiffness K_{rtu} . The sun gears of both planetary gear sets are connected through a common shaft which has a torsional stiffness K_s . The carriers of both planetary gear sets are connected to each other through a hollow shaft which has a torsional stiffness K_c .

The parameters of the model are resumed on table 3.1 (Chapter 3).

Only rotational motions of the gear bodies are considered. The system's equation of motion for back-to-back planetary gear with 3 planets is:

$$M \ddot{q} + C \dot{q} + (K(t) + K_c)q = F(t) \quad (4.1)$$

Where M is the mass matrix:

$$M = \text{diag} \left[\frac{I_{cr}}{r_{cr}} + N.m_{pr}, \frac{I_{rr}}{r_{rr}}, \frac{I_{sr}}{r_{sr}}, \frac{I_{pr}}{r_{pr}}, \frac{I_{pr}}{r_{pr}}, \frac{I_{pr}}{r_{pr}}, \frac{I_{ct}}{r_{ct}} + N.m_{pt}, \frac{I_{rt}}{r_{rt}}, \frac{I_{st}}{r_{st}}, \frac{I_{pt}}{r_{pt}}, \frac{I_{pt}}{r_{pt}}, \frac{I_{pt}}{r_{pt}} \right] \quad (4.2)$$

$K(t)$ is the stiffness matrix:

$$K(t) = \begin{bmatrix} K_r(t) & 0 \\ 0 & K_t(t) \end{bmatrix} \quad (4.3)$$

$K_r(t)$ and $K_t(t)$ are respectively the stiffness matrix in the reaction gear set and in the test gear set:

$$K_t(t) = \begin{bmatrix} \sum_{i=1}^3 (K_{sti}(t) + K_{rti}(t)) & -\sum_{i=1}^3 K_{rti}(t) & -\sum_{i=1}^3 K_{rti}(t) & K_{rt1}(t) - K_{st1}(t) & K_{rt2}(t) - K_{st2}(t) & K_{rt3}(t) - K_{st3}(t) \\ -\sum_{i=1}^3 K_{rti}(t) & \sum_{i=1}^3 K_{rti}(t) & 0 & -K_{rt1}(t) & -K_{rt2}(t) & -K_{rt3}(t) \\ -\sum_{i=1}^3 K_{sti}(t) & 0 & \sum_{i=1}^3 K_{sti}(t) & K_{st1}(t) & K_{st2}(t) & K_{st3}(t) \\ K_{rt1}(t) - K_{st1}(t) & -K_{rt1}(t) & K_{st1}(t) & K_{st1}(t) + K_{rt1}(t) & 0 & 0 \\ K_{rt2}(t) - K_{st2}(t) & -K_{rt2}(t) & K_{st2}(t) & 0 & K_{st2}(t) + K_{rt2}(t) & 0 \\ K_{rt3}(t) - K_{st3}(t) & -K_{rt3}(t) & K_{st3}(t) & 0 & 0 & K_{st3}(t) + K_{rt3}(t) \end{bmatrix} \quad (4.4)$$

$$K_r(t) = \begin{bmatrix} \sum_{i=1}^3 (K_{sri}(t) + K_{rri}(t)) & -\sum_{i=1}^3 K_{rri}(t) & -\sum_{i=1}^3 K_{rri}(t) & K_{rr1}(t) - K_{sr1}(t) & K_{rr2}(t) - K_{sr2}(t) & K_{rr3}(t) - K_{sr3}(t) \\ -\sum_{i=1}^3 K_{rri}(t) & \sum_{i=1}^3 K_{rri}(t) & 0 & -K_{rr1}(t) & -K_{rr2}(t) & -K_{rr3}(t) \\ -\sum_{i=1}^3 K_{sri}(t) & 0 & \sum_{i=1}^3 K_{sri}(t) & K_{sr1}(t) & K_{sr2}(t) & K_{sr3}(t) \\ K_{rr1}(t) - K_{sr1}(t) & -K_{rr1}(t) & K_{sr1}(t) & K_{sr1}(t) + K_{rr1}(t) & 0 & 0 \\ K_{rr2}(t) - K_{sr2}(t) & -K_{rr2}(t) & K_{sr2}(t) & 0 & K_{sr2}(t) + K_{rr2}(t) & 0 \\ K_{rr3}(t) - K_{sr3}(t) & -K_{rr3}(t) & K_{sr3}(t) & 0 & 0 & K_{sr3}(t) + K_{rr3}(t) \end{bmatrix} \quad (4.5)$$

K_c is the coupling stiffness matrix:

$$K_c = \begin{bmatrix} k_c & 0 & 0 & 0 & 0 & 0 & -k_c & 0 & 0 & 0 & 0 & 0 \\ 0 & k_{rtu} & 0 & 0 & 0 & 0 & 0 & 0 & 0 & 0 & 0 & 0 \\ 0 & 0 & k_s & 0 & 0 & 0 & 0 & 0 & -k_s & 0 & 0 & 0 \\ 0 & 0 & 0 & 0 & 0 & 0 & 0 & 0 & 0 & 0 & 0 & 0 \\ 0 & 0 & 0 & 0 & 0 & 0 & 0 & 0 & 0 & 0 & 0 & 0 \\ 0 & 0 & 0 & 0 & 0 & 0 & 0 & 0 & 0 & 0 & 0 & 0 \\ -k_c & 0 & 0 & 0 & 0 & 0 & k_c & 0 & 0 & 0 & 0 & 0 \\ 0 & 0 & 0 & 0 & 0 & 0 & 0 & k_{rru} & 0 & 0 & 0 & 0 \\ 0 & 0 & -k_s & 0 & 0 & 0 & 0 & 0 & k_s & 0 & 0 & 0 \\ 0 & 0 & 0 & 0 & 0 & 0 & 0 & 0 & 0 & 0 & 0 & 0 \\ 0 & 0 & 0 & 0 & 0 & 0 & 0 & 0 & 0 & 0 & 0 & 0 \\ 0 & 0 & 0 & 0 & 0 & 0 & 0 & 0 & 0 & 0 & 0 & 0 \end{bmatrix} \quad (4.6)$$

$F(t)$ is the external torque vector applied on the system.

$$F(t) = \begin{bmatrix} \frac{T_{cr}}{r_{cr}}, \frac{T_{rr}}{r_{rr}}, \frac{T_{sr}}{r_{sr}}, 0, 0, 0, \frac{T_{ct}}{r_{ct}}, \frac{T_{rt}}{r_{rt}}, \frac{T_{st}}{r_{st}}, 0, 0, 0 \end{bmatrix} \quad (4.7)$$

T_{cr} , T_{rr} , T_{sr} , T_{ct} , T_{rt} and T_{st} are the external torque applied respectively in the reaction carrier, the reaction ring, the reaction sun, the test carrier, the test ring and the test sun.

C is the proportional damping matrix expressed by :

$$C = \alpha M + \beta K_c \quad (4.8)$$

Where α and β are two constants (Dhatt and Touzot, 1984).

q is the degree of freedom vector expressed by:

$$q = \{u_{cr}, u_{rr}, u_{sr}, u_{1r}, u_{2r}, u_{3r}, u_{ct}, u_{rt}, u_{st}, u_{1t}, u_{2t}, u_{3t}\}^T \quad (4.9)$$

The rotational coordinates are $u_{rj} = r_{rj}\theta_{rj}$ for reaction gear set $u_{ij} = r_{ij}\theta_{ij}$ and for test gear set where $j=c,r,s,1,2,3$. θ_{rj} and θ_{ij} are the rotational components ; r_{rj} and r_{ij} are the base radius for the sun, ring and planets and the radius of the circle passing through the planets centres for the carrier.

The resolution of the equation of motion is achieved using the step by step implicit Newmark algorithm.

3. Stationary conditions

This part present a description of the mechanisms leading to modulation sidebands of planetary gear sets due to rotation of the planet carrier.

(Inalpolat and Kahraman, 2009) achieved a classification of planetary gear based on their sideband behaviour according to spacing of planets and phasing of gear meshes.

Table 4.1 resume this classification.

N°	Case	Spacing of planets	Phasing of gear meshes
1	Equally-spaced planets and in-phase gear meshes	$\psi_i = \frac{2\pi(i-1)}{N}$	$\frac{Z_r\psi_i}{2\pi} = n$ (n :integer)
2	Equally-spaced planets and sequentially phased gear meshes	$\psi_i = \frac{2\pi(i-1)}{N}$	$\frac{Z_r\psi_i}{2\pi} \neq n$ (n :integer) $\sum_{i=1}^N Z_r\psi_i = m\pi$ (m :integer)
3	Unequally-spaced planets and in-phase gear meshes	$\psi_i \neq \frac{2\pi(i-1)}{N}$	$\frac{Z_r\psi_i}{2\pi} = n$ (n :integer)
4	Unequally-spaced planets and sequentially phased gear meshes	$\psi_i \neq \frac{2\pi(i-1)}{N}$	$\frac{Z_r\psi_i}{2\pi} \neq n$ (n :integer) $\sum_{i=1}^N Z_r\psi_i = m\pi$ (m :integer)
5	Unequally-spaced planets and arbitrarily phased gear meshes	$\psi_i \neq \frac{2\pi(i-1)}{N}$	$\frac{Z_r\psi_i}{2\pi} \neq n$ (n :integer) $\sum_{i=1}^N Z_r\psi_i \neq m\pi$ (m :integer)

Table 4.1: Classification of planetary gears

Three planets are considered for each planetary gear. The planets are positioned at angles ψ_{nj} ($n=1, 2, 3$ and $j=r, t$) within the carrier measured relatively to the rotating basis vector.

Equally-spaced planets are considered for the reaction gear set $(0, 2\pi/3, 4\pi/3)$ and for the test gear set $(\pi/3, \pi, 5\pi/3)$.

Table 4.2 present a calculation to identify the planets phase gear mesh.

i	ψ_i	$\frac{Z_r \psi_i}{2\pi}$	$Z_r \psi_i$	$\sum_{i=1}^N Z_r \psi_i$
Test gear set				
1	$\frac{\pi}{3}$	$\frac{65}{6}$	$\frac{65\pi}{3}$	$\frac{65\pi}{3} + 65\pi + \frac{325\pi}{3} = 195\pi$
2	π	$\frac{65}{2}$	65π	
3	$\frac{5\pi}{3}$	$\frac{325}{6}$	$\frac{325\pi}{3}$	
Reaction gear set				
1	0	0	0	$0 + \frac{130\pi}{3} + \frac{260\pi}{3} = 130\pi$
2	$\frac{2\pi}{3}$	$\frac{65}{3}$	$\frac{130\pi}{3}$	
3	$\frac{4\pi}{3}$	$\frac{130}{3}$	$\frac{260\pi}{3}$	

Table 4.2 : Phases classification of planetary gear of test bench

Sequentially phased gear meshes ($\frac{Z_r \psi_{nj}}{2\pi} \neq n$ and $\sum_{n=1}^N Z_r \psi_{nj} = m\pi$ where n and m are integer)

are considered for both test and reaction gears (Table 4.2).

Based on the spur gear mesh stiffness modelling developed by Fernandez (Fernandez et al, 2013), the mesh stiffness sun-planets and ring planets in both planetary gear sets are obtained by means of finite element model and an analytical approach derived from Hertzian contact theory.

The generation of the tooth profiles is based on a rack-type tool following Litvin's vector approach (Litvin and Fuentes, 2004) and the contact between profiles is Involute-Involute.

Fig.4.2 and Fig.4.3 show respectively time varying mesh stiffness sun-planets and ring-planets.

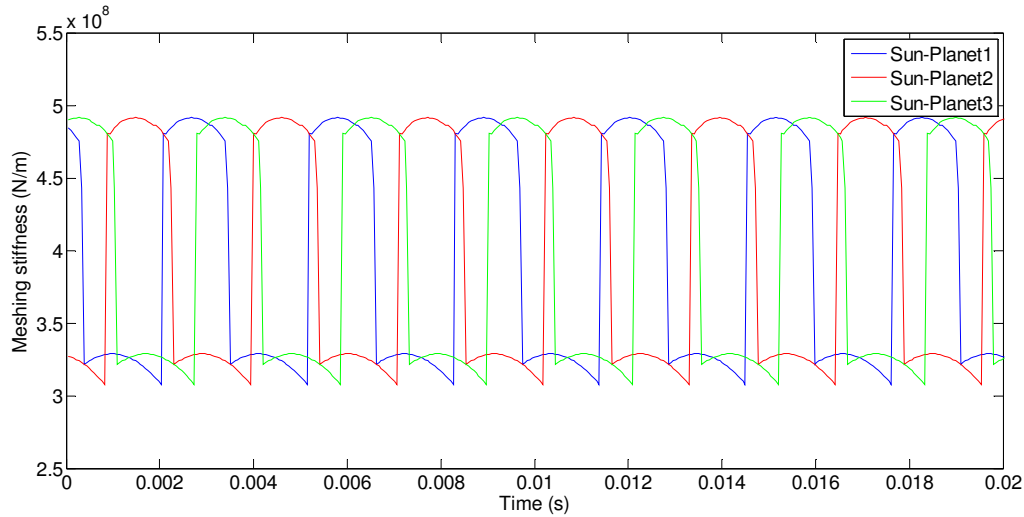


Fig.4.2: Mesh stiffness sun–planets in the test gear set

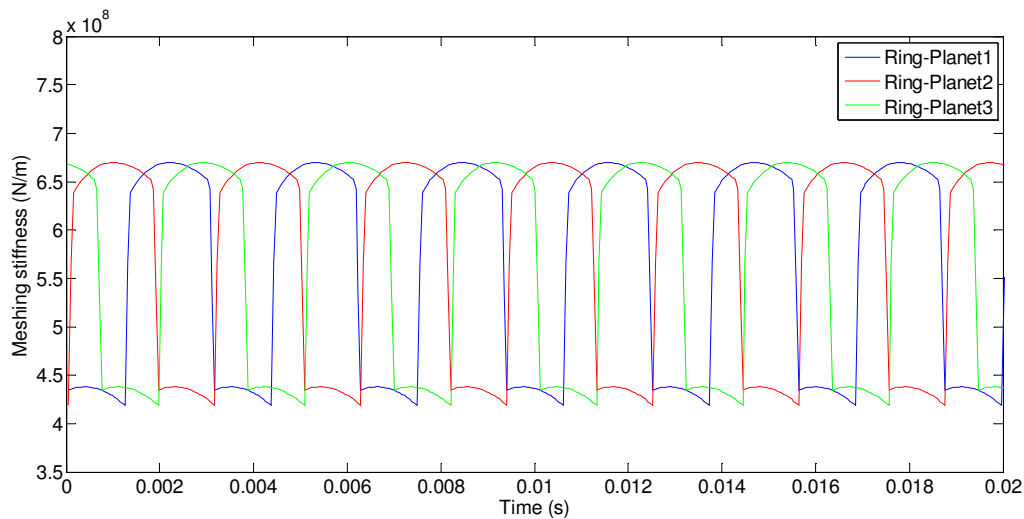


Fig.4.3: Mesh stiffness ring–planets in the test gear set

It is clearly appreciated the change in the number of pairs in contact (alternating between 1 and 2 in this case) modifying the magnitude (higher for single contact) of the mesh stiffness from figure 4.2 and figure 4.3.

For the input rotational speed of motor 1498.5 rpm, the back-to-back planetary gears is excited by mesh frequency ($f_m=320.66$ Hz) and its harmonics and the force due to the rotation of carrier which has a period $T_c=0.2027$ s and frequency $f_c=4.9$ Hz. In addition, an individual influence of each planet on the accelerometer will be assumed for a duration T_c/N ($N=3$: number of planets). So, when a planet i approach to the location of the accelerometer, its influence will increase for the first $T_c/2N$ time period, reaching its maximum when a planet i approaches the location of the accelerometer (Fig 4.4 a) and then diminishing to zero at the

end of the next $T_c/2N$ time period (Fig 4.4 b). This will be followed by the planet $n+1$ which dominates the response of the accelerometer for the next T_c/N time period, and so on (Inalpolat and Kahraman, 2009).

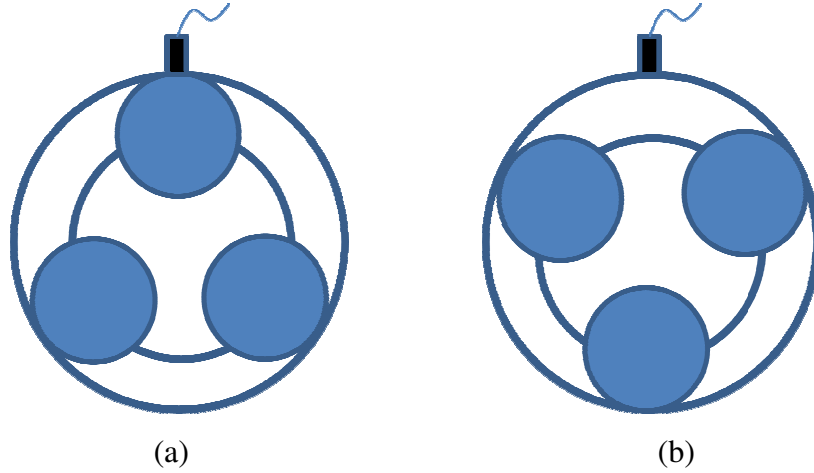


Fig.4.4: Influence of the position of planets on the accelerometer

A hanning function is used to represent this phenomenon:

$$w(t) = \frac{1}{2} \left(1 - \cos\left(\frac{2\pi Nt}{T_c}\right) \right) \quad (4.10)$$

For a planet n positioned at angle ψ_{nj} , a weighting function is defined in the perfect load sharing case as:

$$w_{nj}(t) = w\left(t - \frac{\psi_{nj}T_c}{2\pi}\right) U_{nj}(t) \quad (4.11)$$

Where $U_{nj}(t)$ is defined as:

$$U_{nj}(t) = \sum_{i=1}^{\infty} \left\{ u\left[t - \left(\frac{(i-1)N + n - 1}{N}\right)T_c\right] - u\left[t - \left(\frac{(i-1)N + n}{N}\right)T_c\right] \right\} \quad (4.12)$$

Terms $u(t-a)$ are unit step functions that ensure the influence of planet n on the accelerometer lasts only for a period of T_c/N .

The dynamic force due to the rotation of carrier will be:

$$F_j(t) = \sum_{n=1}^N w_{nj}(t) U_{nj}(t) F_{nj} \cos(Z_r \omega_c t + Z_r \psi_{nj}) \quad (4.13)$$

Where $j=r$ for the reaction ring and $j=t$ for the test ring gear. F_{nj} is the load sharing planet-ring.

Forces due to rotation of carrier on the reaction ring and the test ring gear are counter-phased. When the force on the test ring gear reaches its maximum the force on the reaction ring is around zero and vice versa. This phase opposition is explained by the fact that accelerometers of the test ring gear and of the fixed ring are fixed on the same angle whereas the difference in angular position between the planets on the test gear set and the reaction gear set is $\frac{\pi}{3}$ so, when a planet is at the location of the accelerometer on the test gear set, the accelerometer of the reaction ring is between two planets of the reaction gear set and the force due to the rotation of carrier is zero.

Figures 4.5a and 4.5b show respectively the force due to the rotation of carrier on one period of rotation of carrier on the reaction ring gear and the test ring.

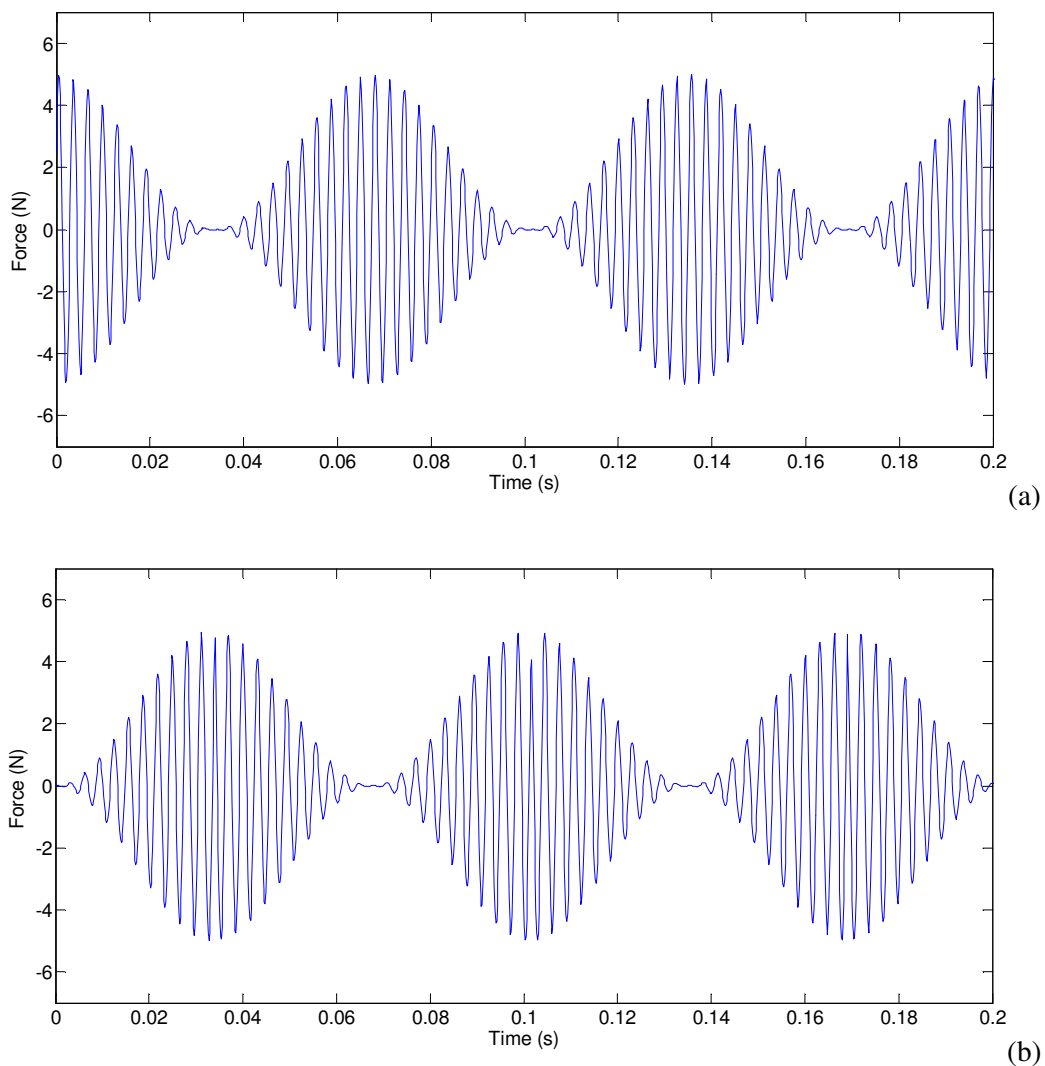


Fig.4.5: Force due to rotation of carrier in one rotational period of carrier (a) on the reaction ring and (b) on the test ring

The external force will be defined by:

$$F(t) = \begin{bmatrix} \frac{T_{cr}}{r_{cr}}, \frac{T_{rr}}{r_{rr}} + F_r(t), \frac{T_{sr}}{r_{sr}}, 0, 0, 0, \frac{T_{ct}}{r_{ct}}, \frac{T_{rt}}{r_{rt}} + F_t(t), \frac{T_{st}}{r_{st}}, 0, 0, 0 \end{bmatrix} \tag{4.14}$$

3.1. Frequency characterization of the planetary gear

First simulation is performed for a fixed speed (1498.5 rpm) and fixed external load (100 N.m on the free reaction ring). The same conditions are used for the test bench. Fig.4.6 shows acceleration on fixed ring issued from simulation and experiment on one period of rotation of carrier ($T_c=0.2027$ s).

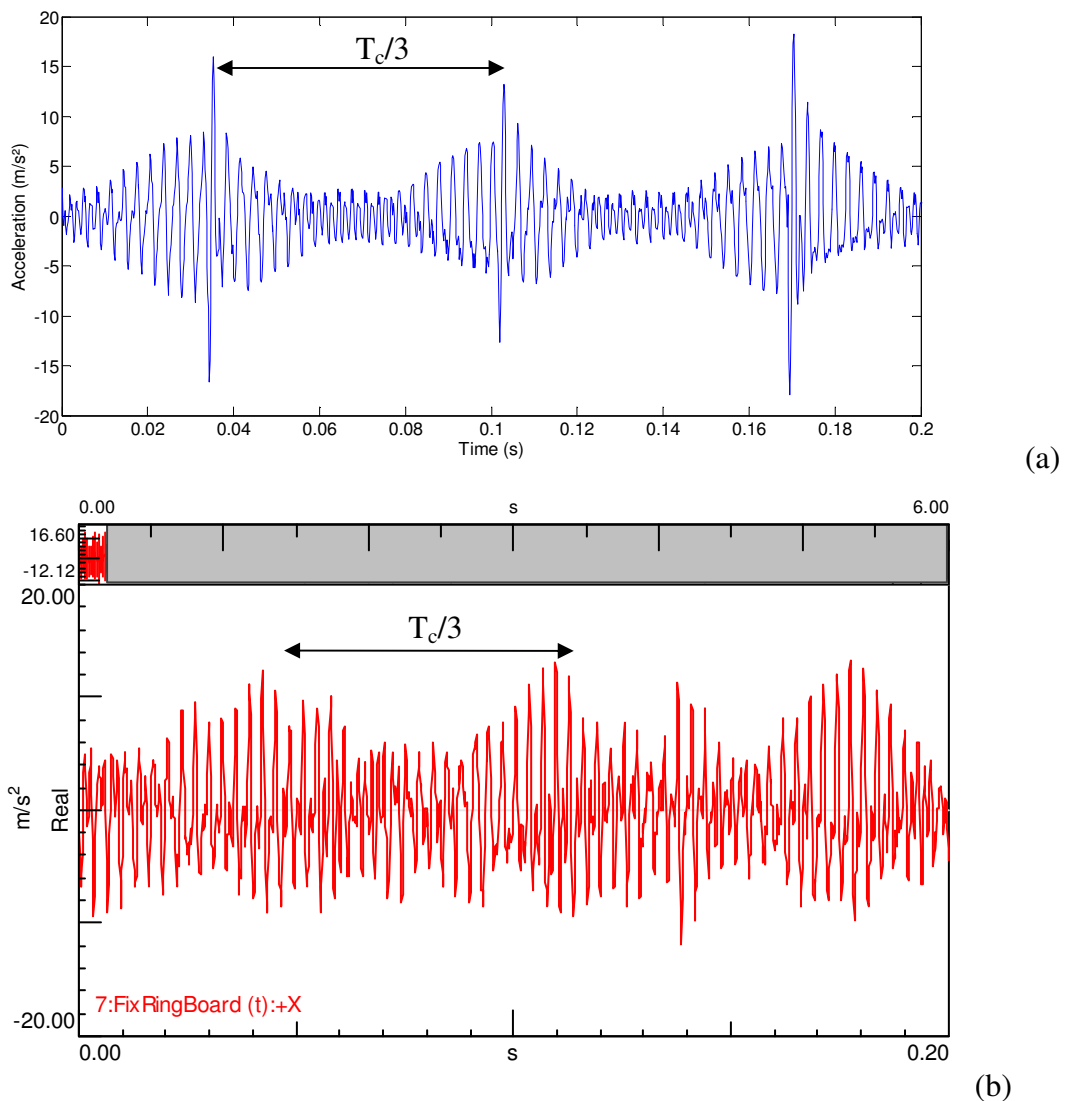


Fig.4.6: Time response of the fixed ring (a) theoretical and (b) experimental

In Fig.4.6, a clear amplitude modulation is observed as the signal repeats itself three times (Inalpolat and Kahraman, 2009). This amplitude modulation is explained by the modulation of the force due to rotation of carrier (Fig.4.5).

The spectrum of dynamic component of the fixed ring (Fig.4.6) is dominated by mesh frequency (320.66 Hz) and its harmonics. In addition, sidebands appear on these spectra on the $3.n.f_c$ (n : integer) and $m.f_c$ (m : integer).

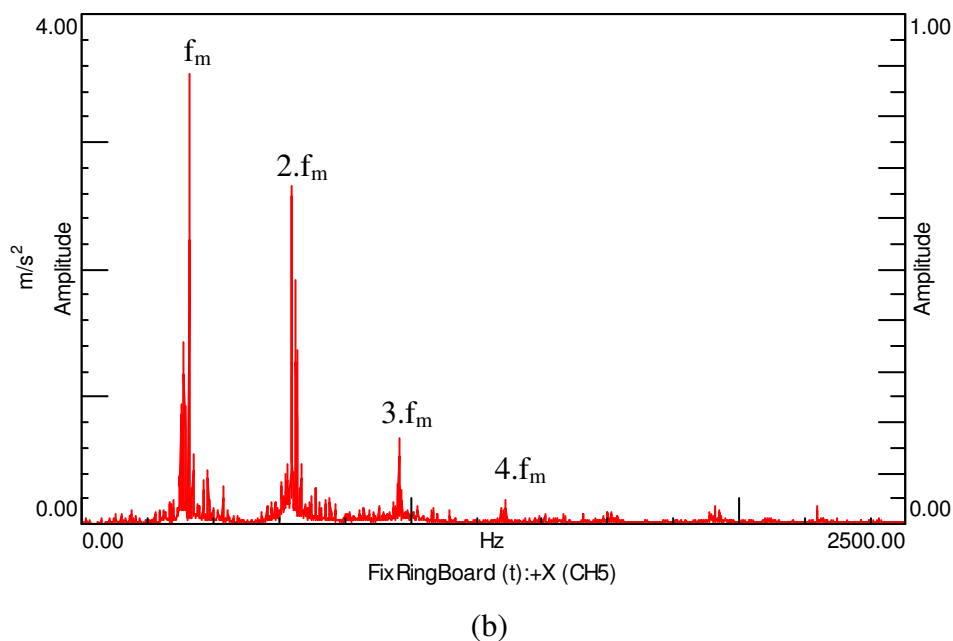
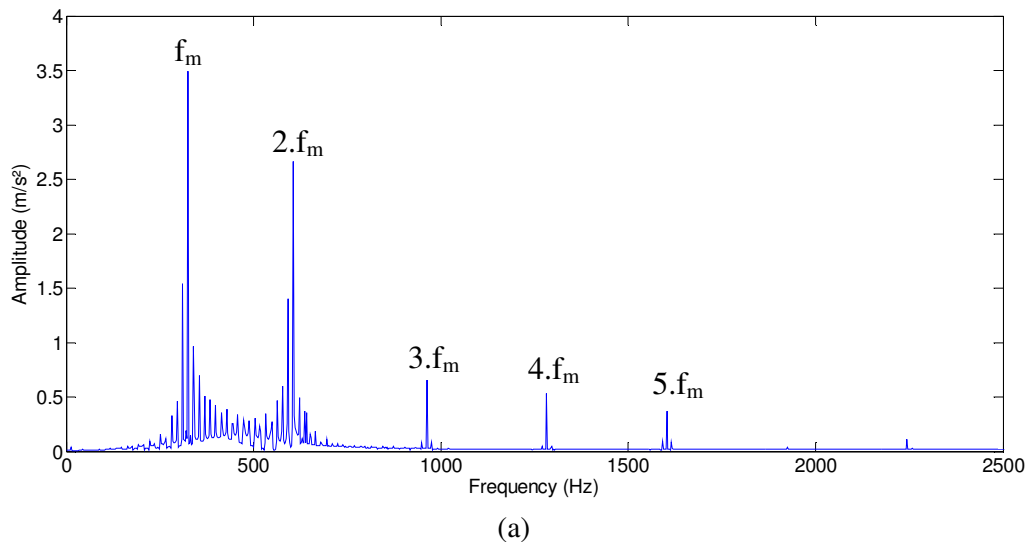


Fig.4.7: Spectra of acceleration on the fixed ring: Theoretical (a) and experimental (b)

The Fig.4.8 shows a zoom around f_m . It is clearly observed that the orders of all significant sidebands with sizable amplitudes are at $f = n.N.f_c = nx3x4.9 = nx14.7$ Hz (n : integer and $N=3$:

number of planets) in the vicinity of mesh order $f_m=320.66$ Hz. So, the frequencies with large amplitudes are 296.2 Hz, 310.9 Hz, 325.6 Hz and 340.2 Hz, 369.6 Hz and 384.3 Hz.

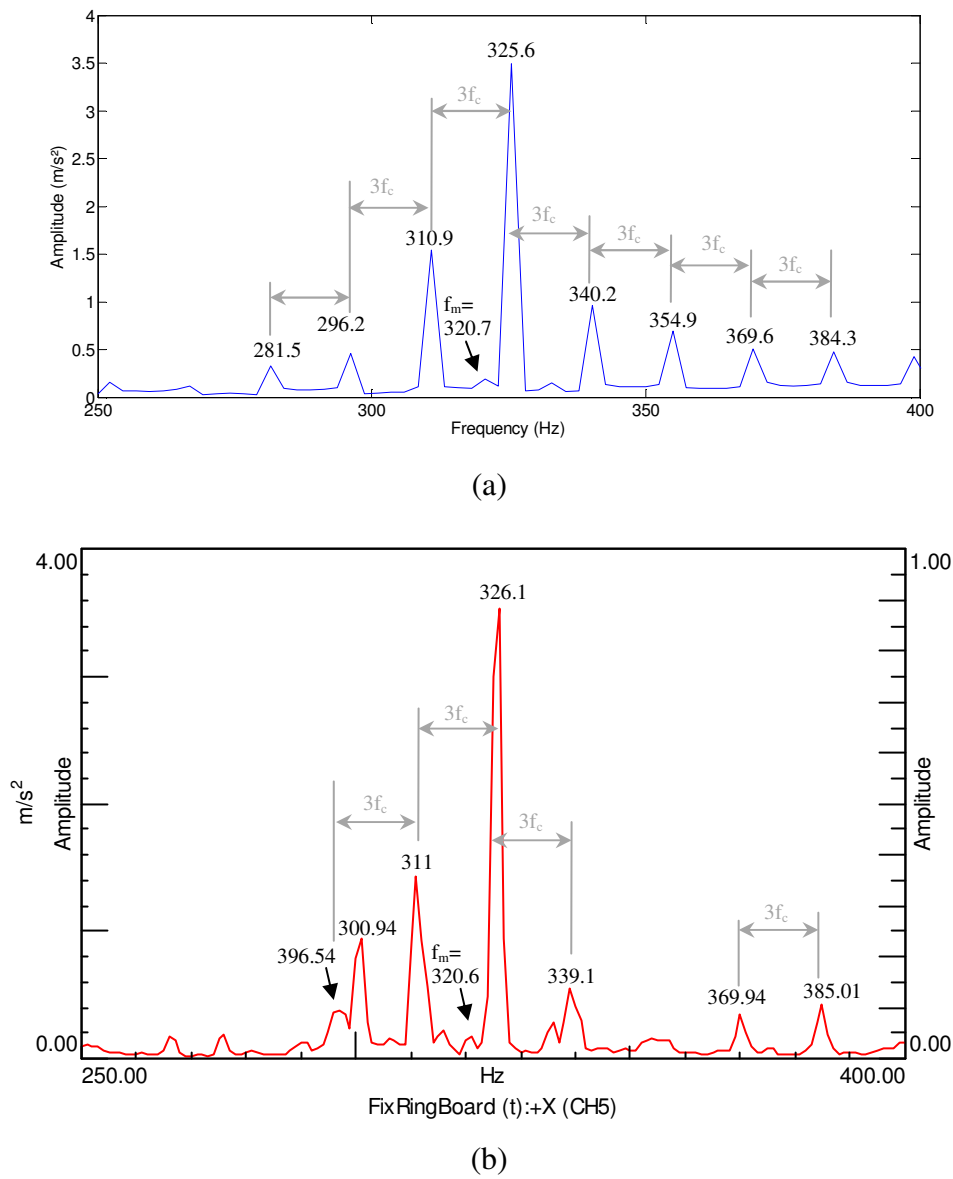


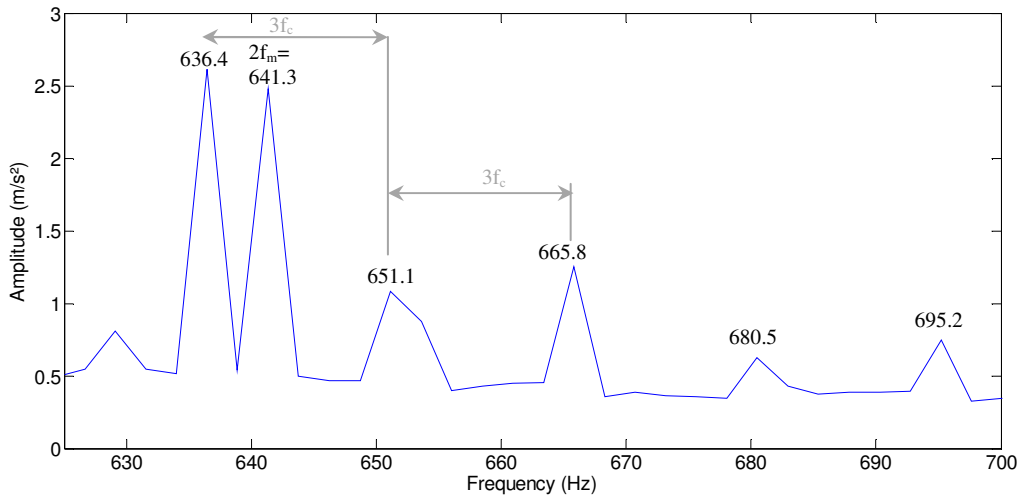
Fig.4.8: Response spectrum of the fixed ring on the first harmonic of the mesh stiffness: Theoretical (a) and experimental (b)

Also, sidebands are mostly not symmetric about $f_m = 320.66$ Hz . The harmonic order with the largest amplitude is the frequency $f_{max} = n.N.f_c = 325.6$ Hz that is the closest to $f_m = 320.66$ Hz.

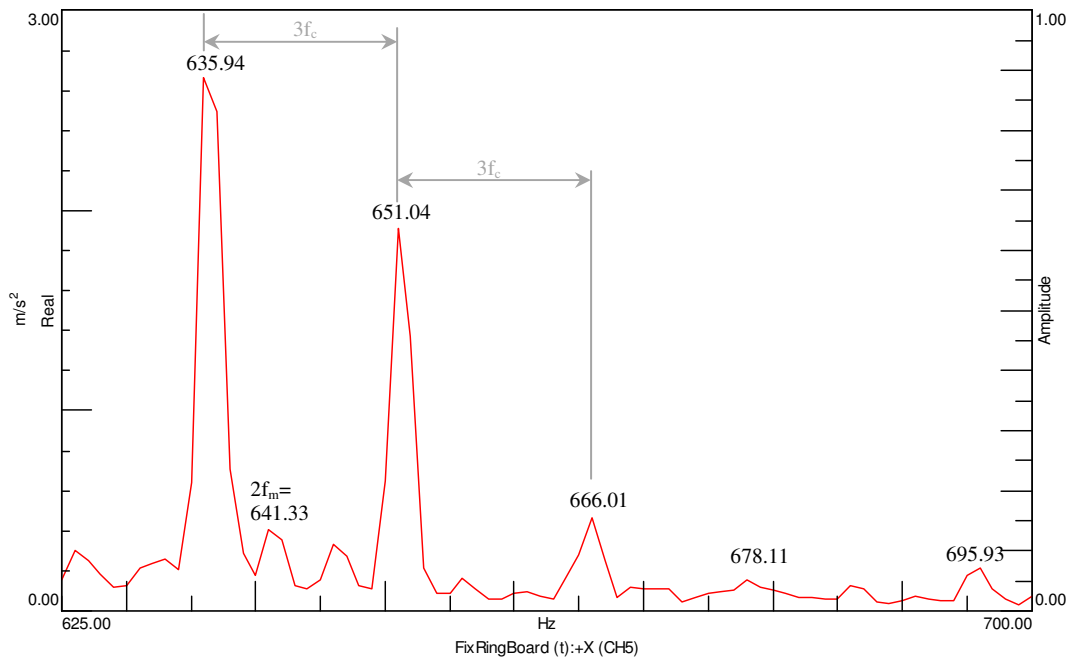
This order is satisfying the condition: $|f_{max} - f_m| \leq \frac{1}{2} N.f_c$

In fact, the actual largest component is usually at the nearest harmonic of the planet carrier speed which is a multiple of 3 (the number of planets) as explained by McFadden and Smith (McFadden and Smith, 1985). In this case, the largest response is one harmonic to the right of

the first tooth mesh frequency (Fig.4.8), and one to the left of the second harmonic (Fig.4.9), while the third harmonic is right on the max (Fig.4.10).



(a)

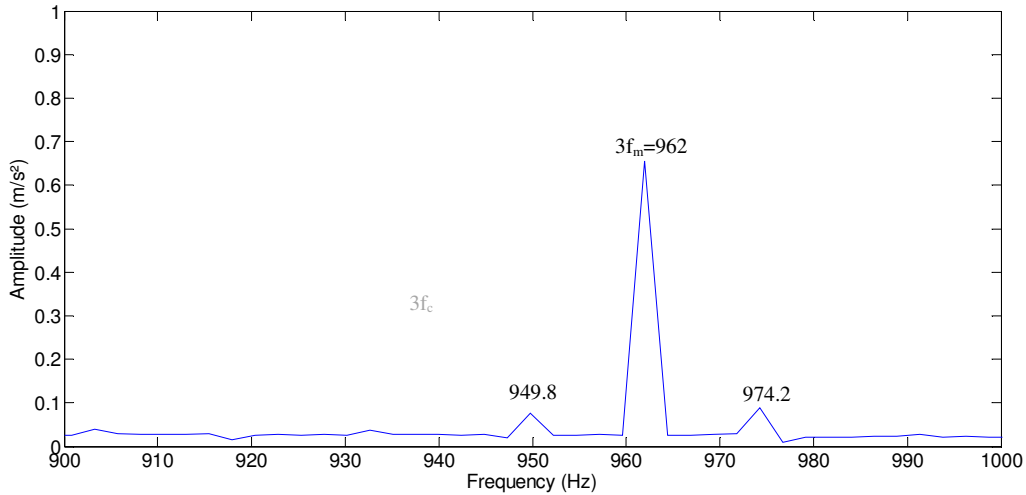


(b)

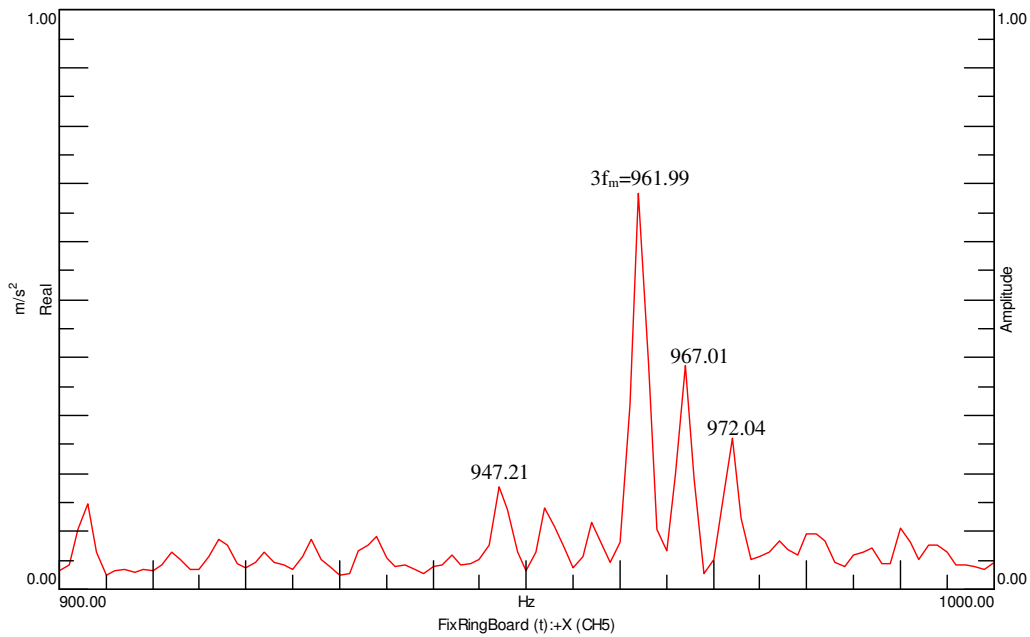
Fig.4.9: Response spectrum of the fixed ring on the second harmonic of the mesh stiffness: Theoretical (a) and experimental (b)

Fig.4.9 shows that the largest response (636.4 Hz) is one harmonic to the left of the second harmonic (641.3 Hz) of tooth mesh frequency.

Meanwhile, when the harmonic of the mesh frequency is multiple of the number of planet ($N=3$), we have $f_{max} = n \cdot N \cdot f_m$ is the most important in amplitude. Fig.5.9. shows a zoom around the third harmonic of the mesh frequency $3f_m = 962$ Hz.



(a)



(b)

Fig.4.10: Response spectrum of the fixed ring on the third harmonic of the mesh stiffness: Theoretical (a) and experimental (b)

The time response of the test carrier (Fig.4.11) shows an oscillation around 0 at mesh stiffness period. In addition, there is a clear modulation at carrier rotational period T_c .

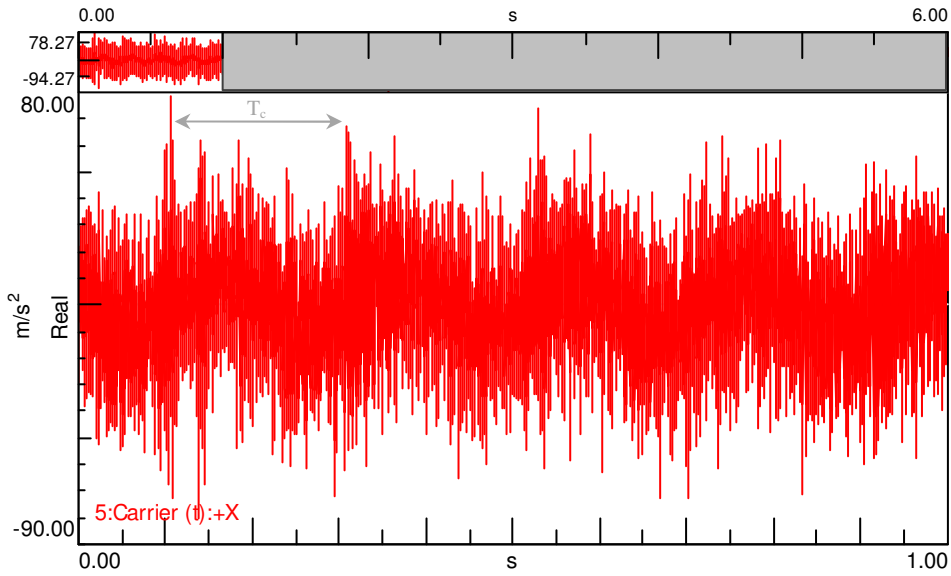


Fig.4.11: Time response of the test carrier

The spectrum shows that the test carrier is excited by the mesh frequency and its harmonics. In addition, it is observed a peak at carrier rotational frequency ($f=4.86\text{Hz}$) which can be explained by a misalignment error on shaft connecting carriers. Also, sidebands around mesh frequency and its harmonics are observed (Fig.4.12).

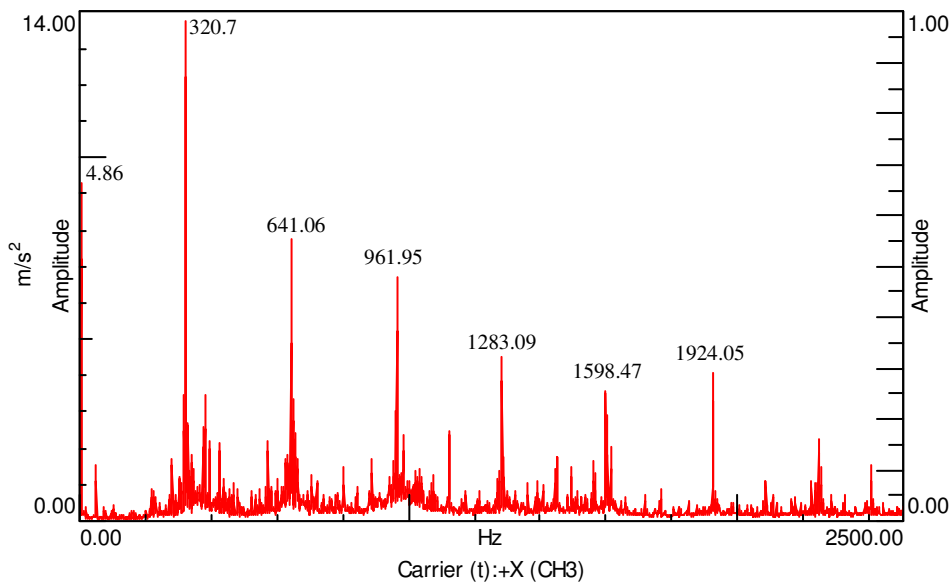


Fig.4.12: Spectra of acceleration on the test carrier

Fig.4.13 presents a zoom around $1xf_m$. It shows that the largest response is right on the mesh frequency. Also, sidebands spaced by f_c are observed.

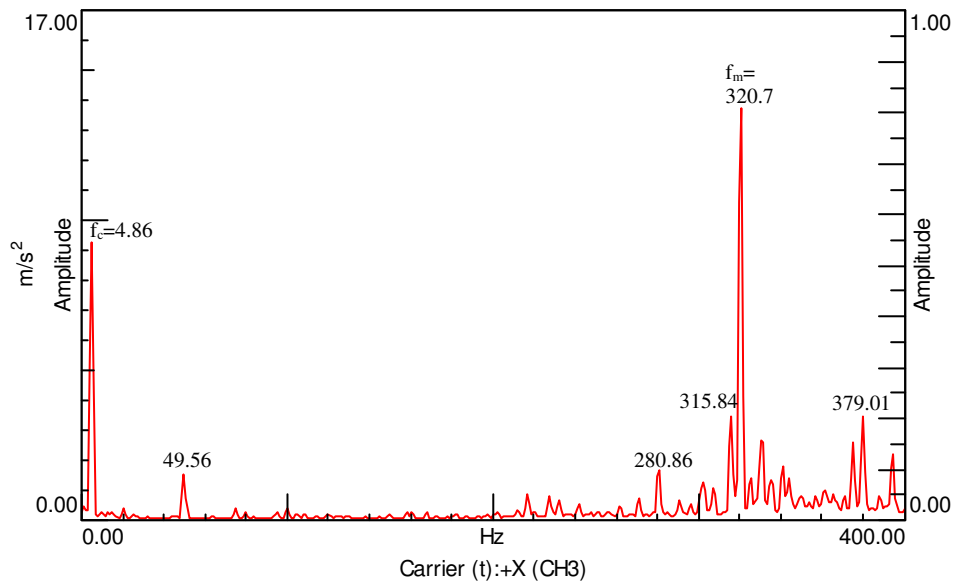


Fig.4.13: Zoom of spectra of acceleration on the test carrier

3.2. Effect of loading variation on frequency content

Simulations and experiments are achieved with different loads: 100N.m, 300N.m, 500N.m, 700N.m and 900N.m.

Based on the study of mesh stiffness in spur gear (Fernandez et al, 2013), Fig.4.14 and Fig.4.15 show respectively time varying mesh stiffness sun-planet1 and ring-planet1 corresponding to the above loads.

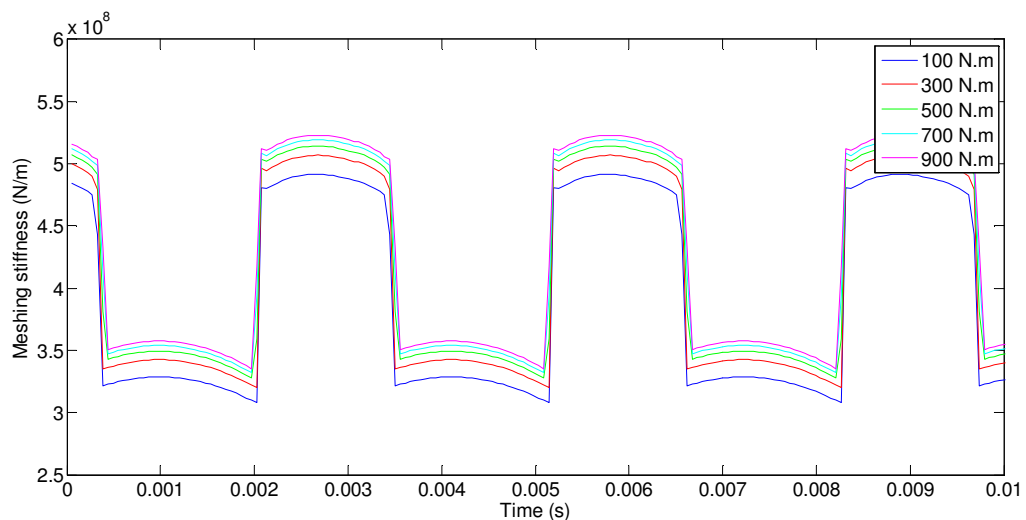


Fig.4.14: Mesh stiffness sun-planet1 in the test gear set for different loads

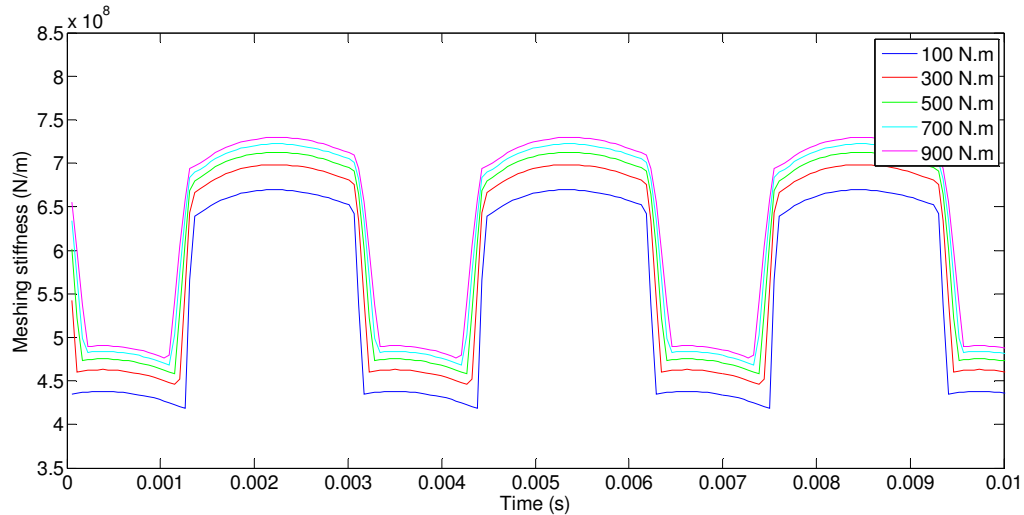


Fig.5.15: Mesh stiffness ring–planet1 in the test gear set for different loads

It is well noticed that as the torque level increases, the period of double contact increases and therefore the contact ratio. It is also possible to observe the effect of the tip rounding in the transition zone, where a sharp increase in the mesh stiffness is found. That effect is a consequence of a singularity in the local deformation as the curvature radius of the profile changes from a small value for the tip rounding to a higher one corresponding to the involute profile.

The non linear nature of the local contact model becomes evident in the shift of the stiffness curve when the torque is increased.

Fig 5.16 shows the time response of the fixed ring with different loads: 100N.m, 300N.m, 500N.m, 700N.m and 900N.m. In fact, the amplitude of the acceleration of the fixed ring decreases as the external load increases. This phenomenon can be explained by the fact that the amplitude of the mesh stiffness and period of double contact which increase with load provide more stability to the system.

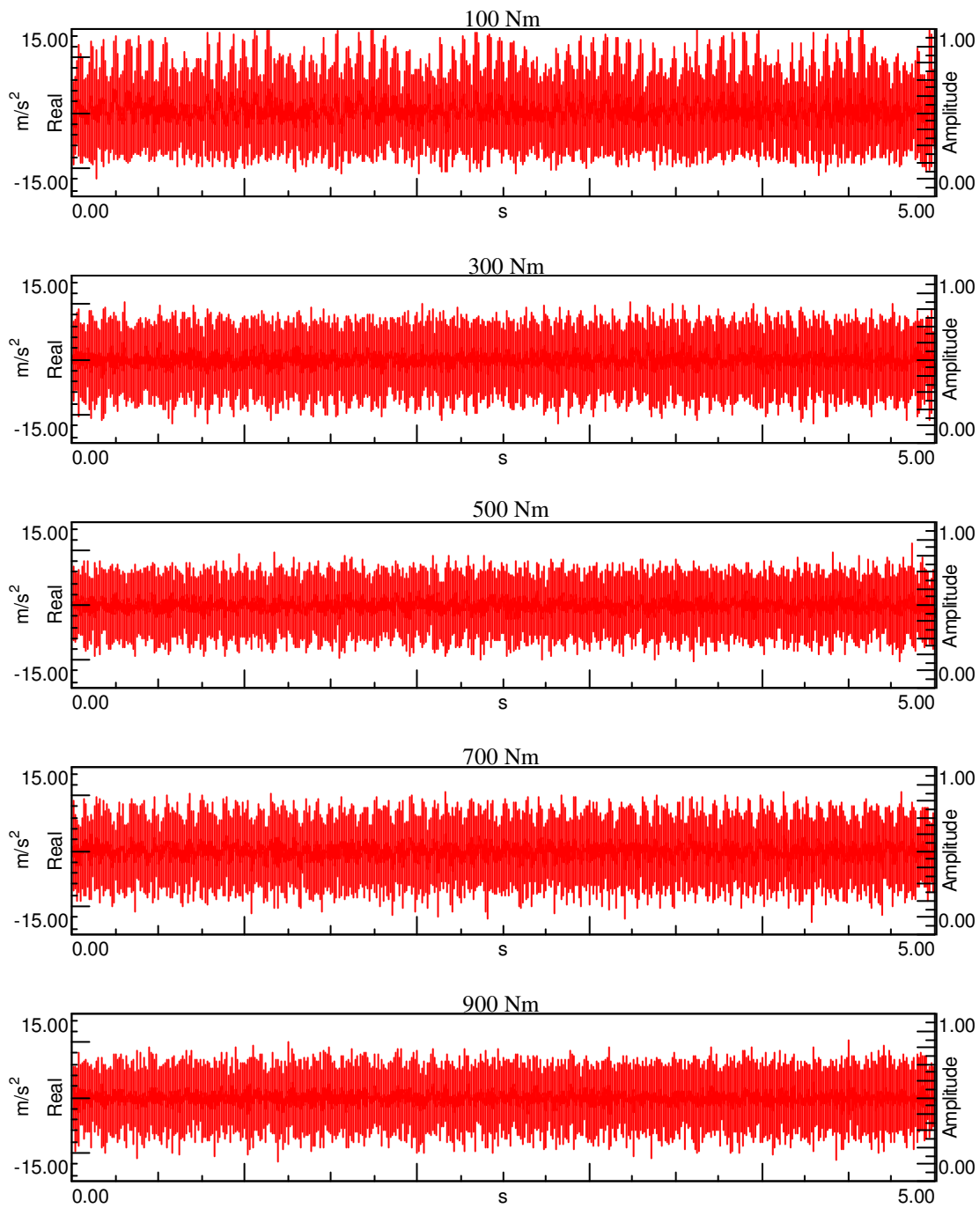
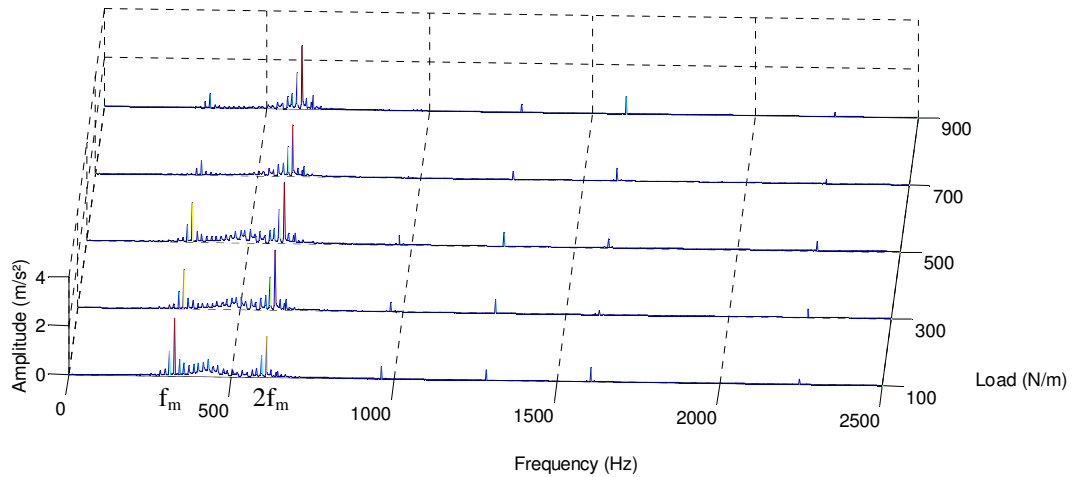
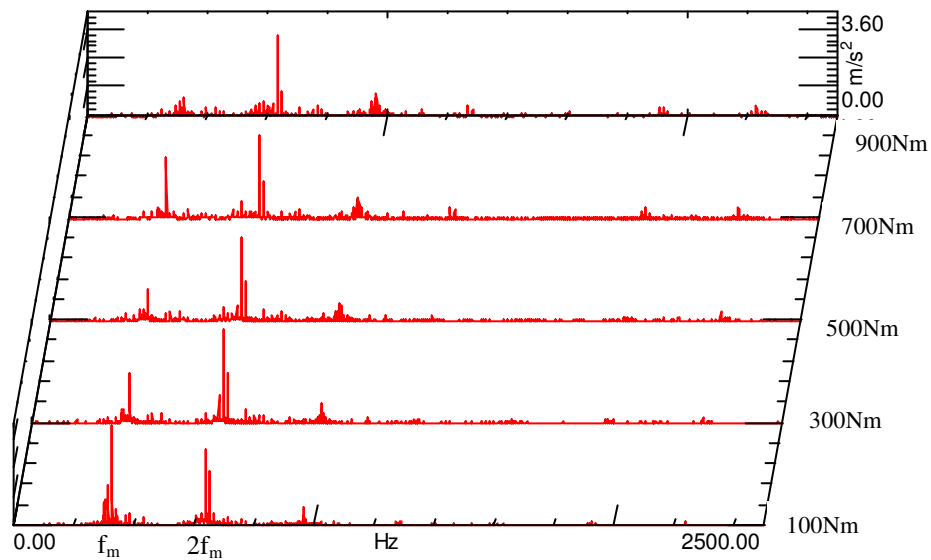


Fig.4.16: Time response of the fixed ring with different loads

Fig 4.17 shows a 3D representation spectrum of signals presented in fig 4.16.



(a)



(b)

Fig4.17: Waterfall of response spectrum of the fixed ring with different load (a) theoretical and (b) experimental

Fig4.17 shows that in each spectrum, a dominant set of harmonic amplitudes occurs in the neighbourhood of f_m and its harmonics. For the responses without load and with 100N.m of load, the dominant amplitude is in f_m . As we increase the load, the dominant amplitude changes. For the spectra of 900 Nm load, the dominant amplitude is on $2f_m$.

Mitchell (Mitchell, 1982) has recorded the vibration signature of the gearbox of a marine steam turbine generator while reducing the load from full to no load. He defined “intermediate frequencies” where an increase in amplitude was the earliest clear warning. The intermediate

frequencies are produced by resonance of the gear elements excited by a repetitive variation in the tooth spacing or related to some other phenomena.

In our case, when the torque is increased, the values of mesh forces increase for each of the contacting points through a mesh period (fig 4.14 and fig 4.15). Also, the additional external load causes a variation of the pressure angle and therefore a variation of the contact ratio. So, the period of double contact increases as the torque level increases.

In addition, the inertia and the torsional stiffness of the reaction ring gear increase as masses are added and vice-versa.

4. Variable load

An external variable load on the free ring is applied by adding and removing mass on the free ring as explained in this section. The variation of the load is presented in Fig4.18.

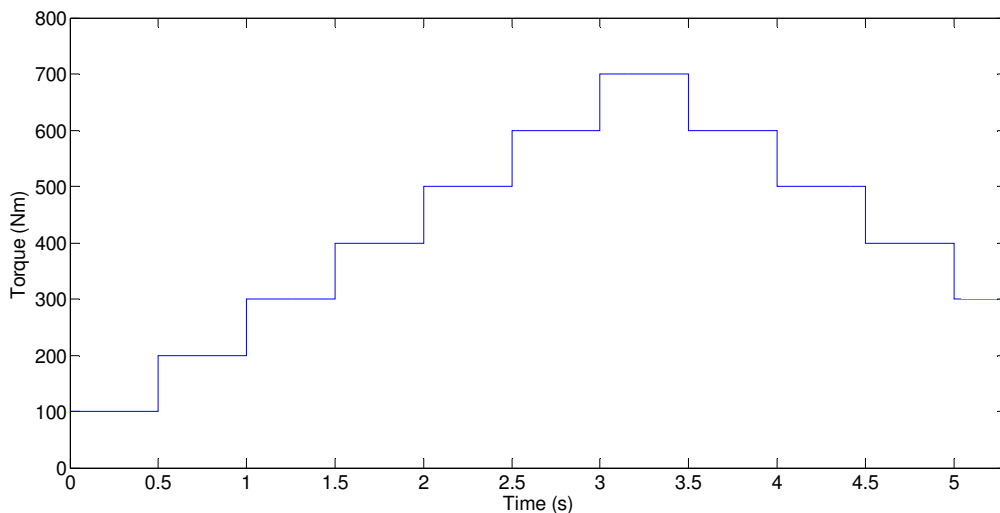


Fig4.18: The external variable torque

The variation of the external load causes a variation of the value of the meshing stiffness and a variation of the period of double contact (Fig4.19). This evolution of mesh stiffness will be injected in the developed model.

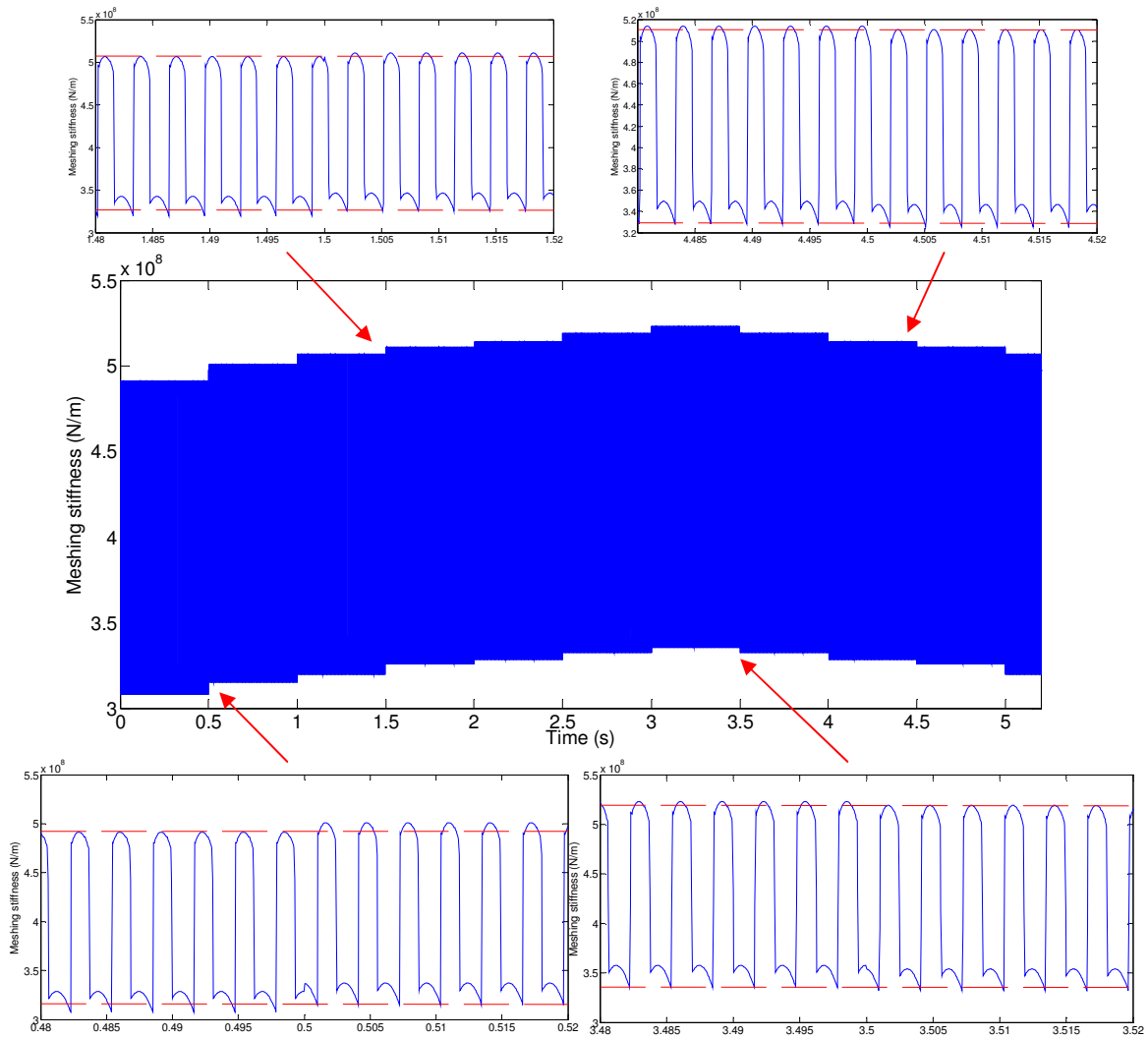


Fig4.19: Mesh stiffness sun–planet1 in the test gear set with variable load

The speed of motor is constant and is controlled by a frequency converter. The external load and the inertia of the reaction ring gear are variable.

Although the system starts with the external torque 100 N.m where the fundamental meshing frequency is the dominant (Fig4.17), the spectrum of acceleration on the fixed ring shows that the nearest harmonic of rotation of carrier to the 2nd harmonic of the meshing frequency (636.4 Hz) is the dominant (Fig4.20).

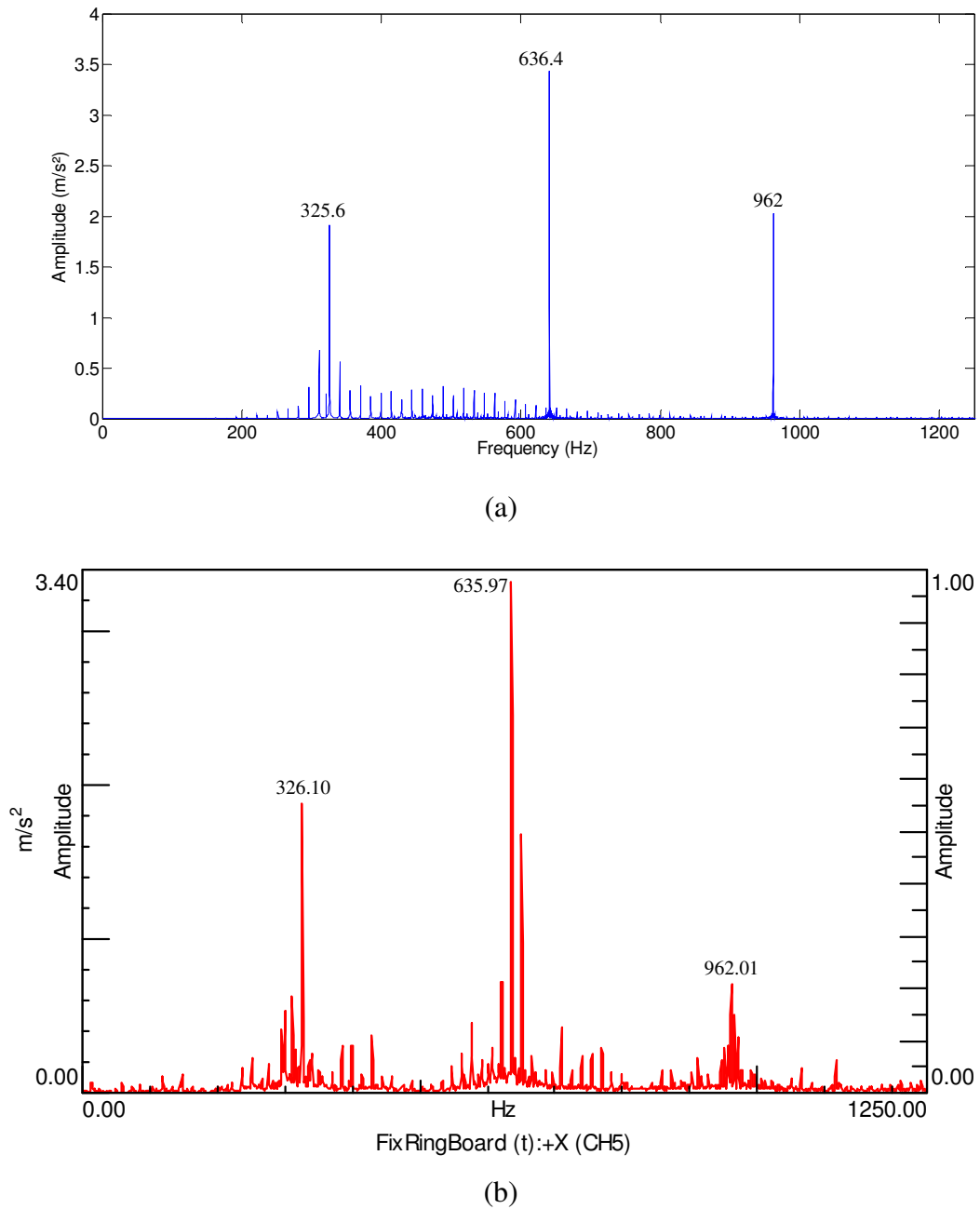


Fig4.20: Response spectrum of the fixed ring with variable load: Theoretical (a) and experimental (b)

With variable load, the dominant amplitude is on the 2nd harmonic of the mesh frequency which corresponds to intermediate frequency as shown on fig 4.17. The behaviour is similar to those of 400 Nm and it corresponds to the average.

5. Run up regime

The variation of speed during run up is controlled by the frequency converter Micromaster 440. The dynamic behaviour of the system is simulated and compared to the experimental results issued from the test ring.

Several systems are subjected to such repetitive run up and run down regimes during their exploitation. They are very critical especially when they are overloaded (Drago, 2009).

The frequency converter commands the variation of the rotational speed of motor. In fig 4.21, tach01 presents the rotational speed of carriers' shaft.

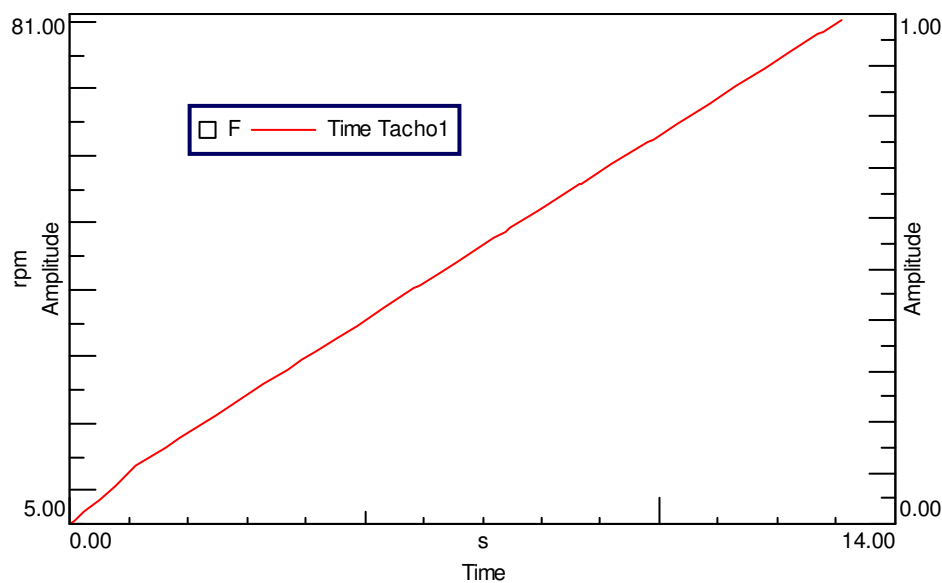


Fig 4.21: Rotational speed evolution of carriers' shaft in the run up

In order to show the evolution of the motor's torque, the torsional strain of the suns' shaft ε_T is measured. Fig4.22 shows the variation of this strain during run-up.

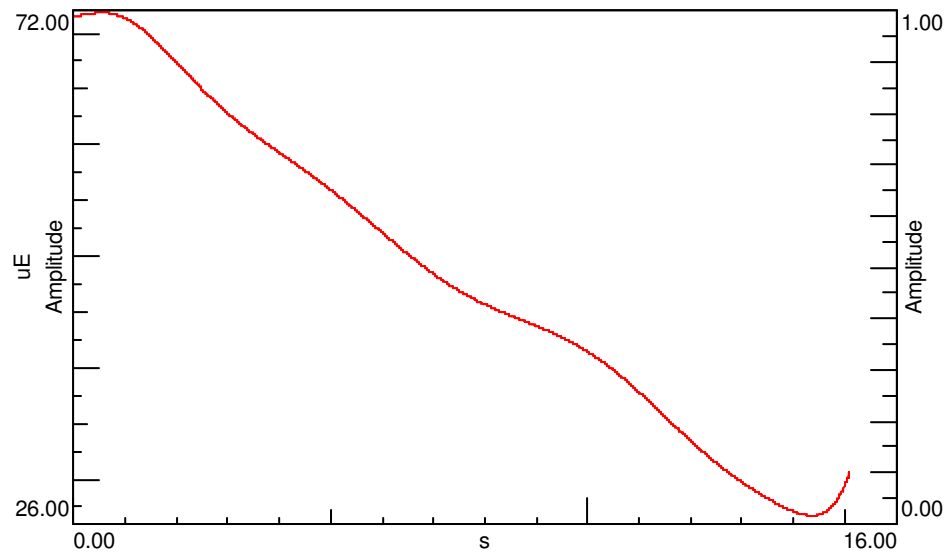


Fig 4.22: Time varying of the strain of the shaft of suns during run up

The application of Hooke's law, the torsional moment for a full bridge is written:

$$M_t = \frac{1}{2} \varepsilon_i \cdot G \cdot S_p \quad (4.15)$$

With S_p is the polar section modulus of cylindrical shaft of suns for a diameter d and G is the shear modulus, S_p can be written by:

$$S_p = \frac{\pi d^3}{16} \quad (4.16)$$

Fig4.23 shows the experimental evolution of the motor's torque measured during run up.

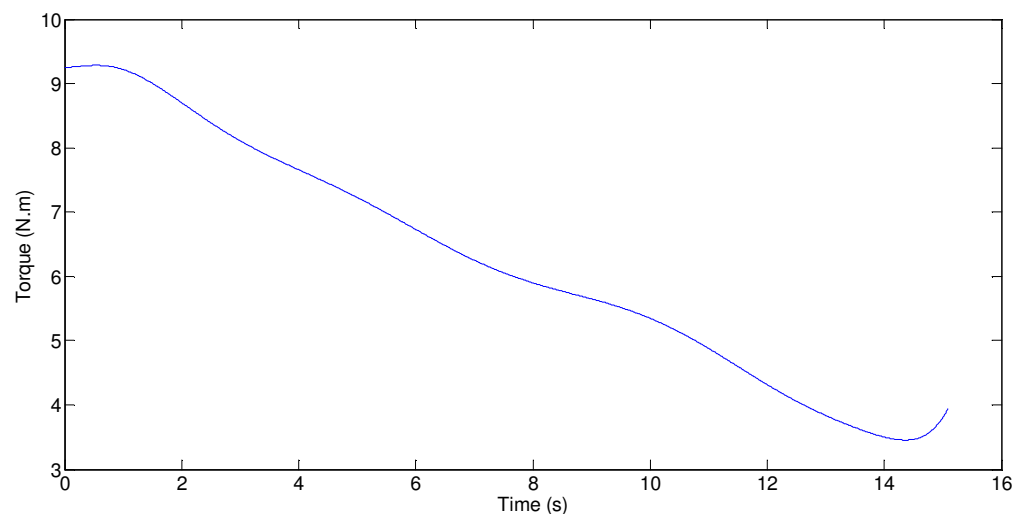


Fig4.23: Evolution of motor torque during run up

For run up regime, the period of mesh stiffness function decrease as speed increases (Khabou et al, 2011), (Viadero et al, 2014). In this part, meshes stiffness between gears are modelled as square functions. Figure 4.24 and figure 4.25 show the evolution of mesh stiffness for ring-planets and sun-planets on the test gear set during run up taking into account mesh phasing.

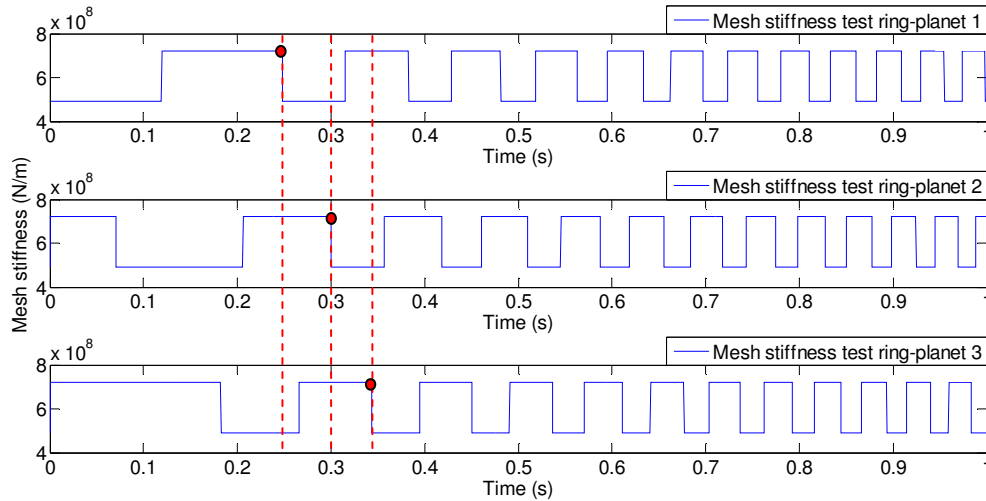


Fig 4. 24: Evolution of mesh stiffness ring-planets on the test gear set during run up.

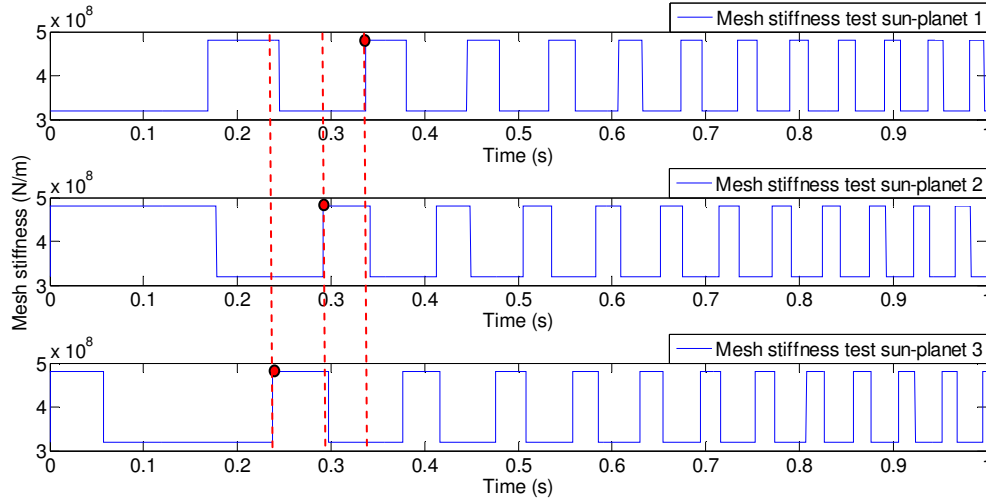
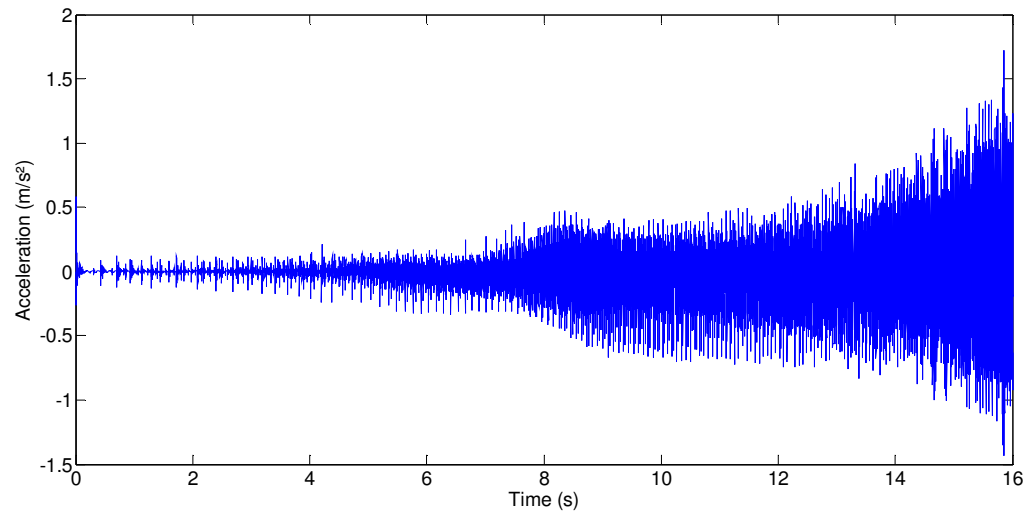
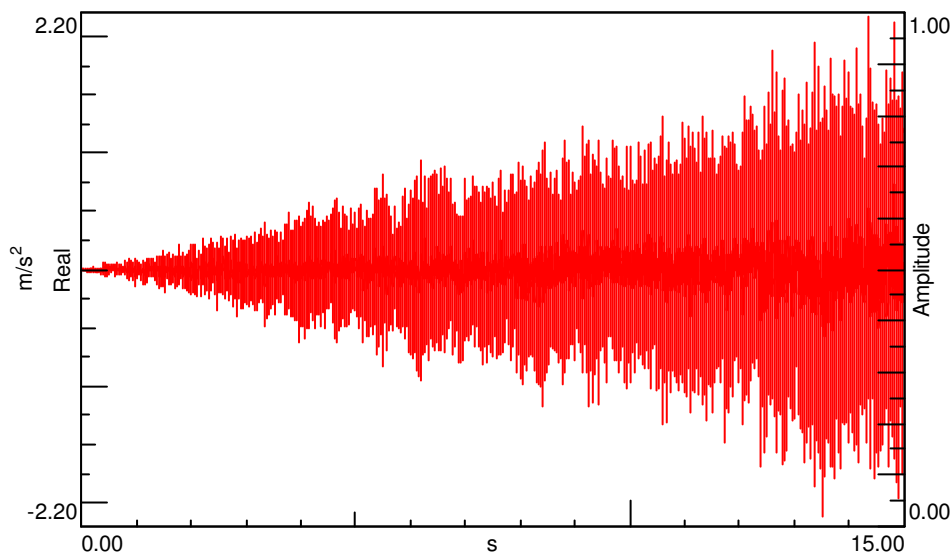


Fig 4. 25: Evolution of mesh stiffness sun-planets on the test gear set during run up.

A run up was performed according to Fig 4.21. The time response of the acceleration on the fixed ring is shown in Fig4.26. It is well observed that the vibration is increasing respectively with time. This is explained by the fact that during run up, the speed and the accelerating torque is increasing, giving rise to increased vibration.



(a)

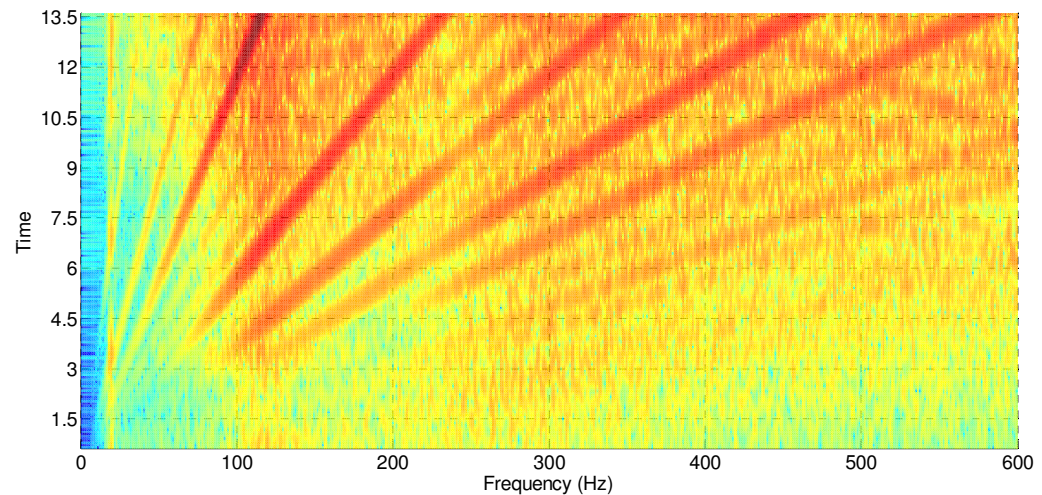


(b)

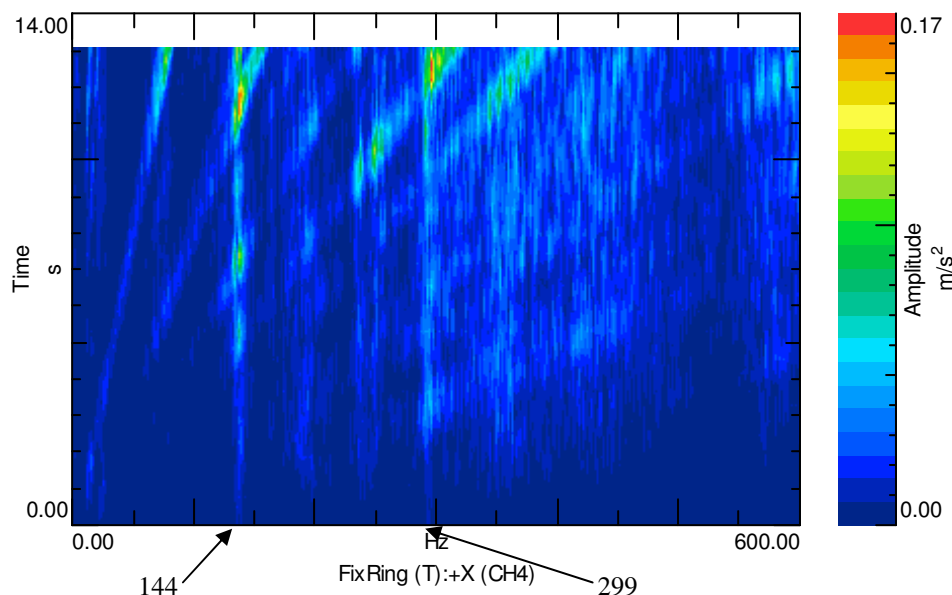
Fig4.26: Acceleration of the fixed ring: (a) simulation and (b) experimental

During the run up, the period of the meshing stiffness function which excites the system is not constant. In order to describe the evolution of the frequency content during this phase, a time-frequency map is drawn based on Short Time Fourier Transform (STFT).

Fig 4.27 shows STFT obtained from simulation and experiment for acceleration on the test ring gear. We clearly observed inclined lines showing the increase of the mesh frequency values and its harmonics. In addition, vertical lines are observed and there are particular zones where the higher amplitude corresponds to some natural frequencies of the system.



(a)



(b)

Fig 4.27: STFT on the fixed ring from simulation (a) and the experience (b)

The time response of the acceleration on the test carrier is shown in Fig 4.28. It is well observed that the vibration is increasing in time. In fact, the time signal of test carrier acceleration is modulated by a signal with a carrier rotation periodicity. For simulation, STFT plot shows two natural frequencies 25Hz and 144Hz which are excited. For experimental results, we find that natural frequencies 144Hz, 199Hz, 244Hz and 299Hz are excited.

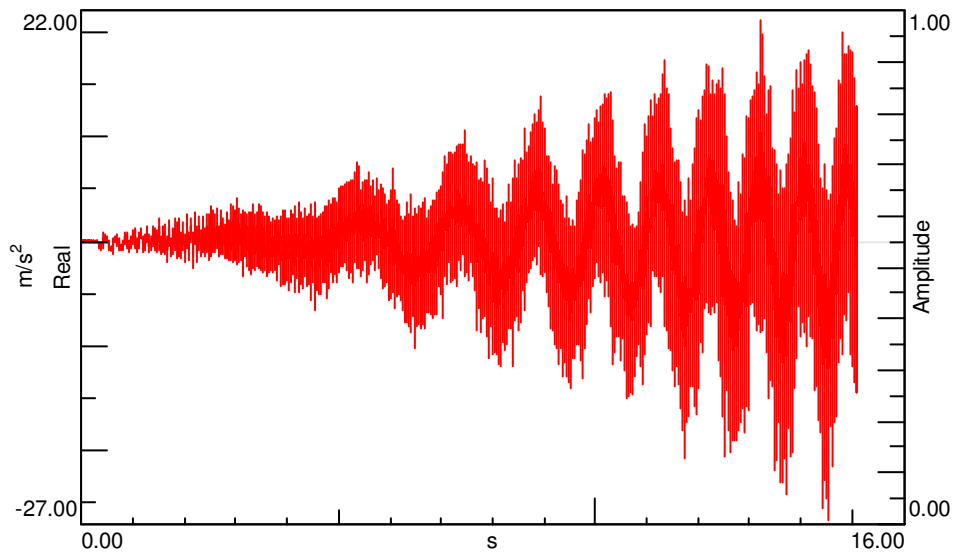


Fig 4.28: Acceleration of the test carrier during run up

STFT of signal presented in fig 4.28 is computed and presented in fig 4.29.

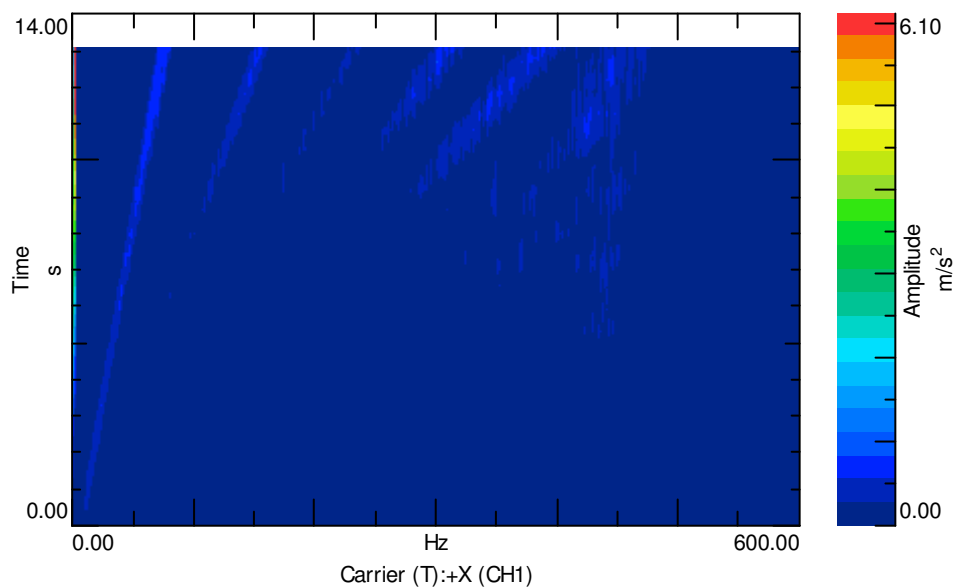


Fig 4.29: Color map of the test carrier dynamic response in the run up

We clearly observe inclined lines showing the increase of the mesh frequency value and its harmonics. In addition, an important acceleration is noticed in the low-frequencies. A zoom in 0-30Hz band is shown in Fig 4.30.

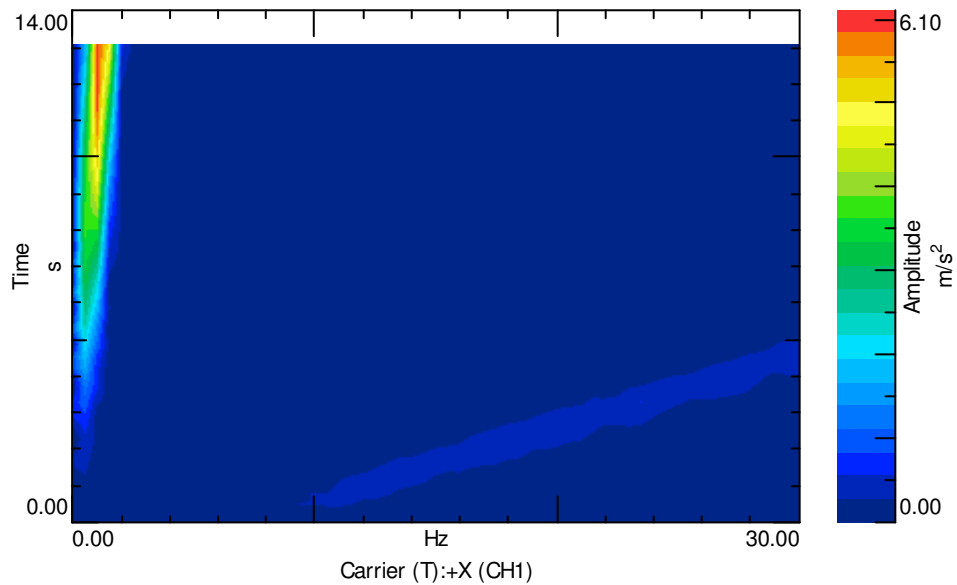


Fig4.30: Color map of the test carrier dynamic response in the run up (zoom)

Fig 4.30 shows an inclined line where the amplitude is more important. This inclined line describes the evolution of the rotation frequency of carriers and corresponds to misalignment error in the carriers' shaft.

6. Run down regime

For run down regime, the simulations and experiments are done according to the speed profile given in fig 4.31.

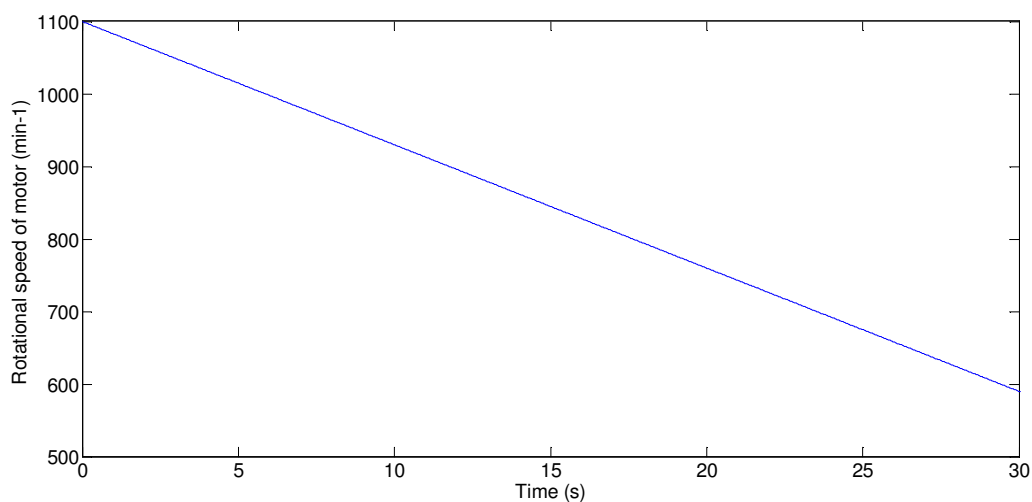


Fig 4.31: Rotational speed evolution of motor

The strain of the shaft of suns is measured in the run down. Fig 4.32 shows the time varying of this strain.

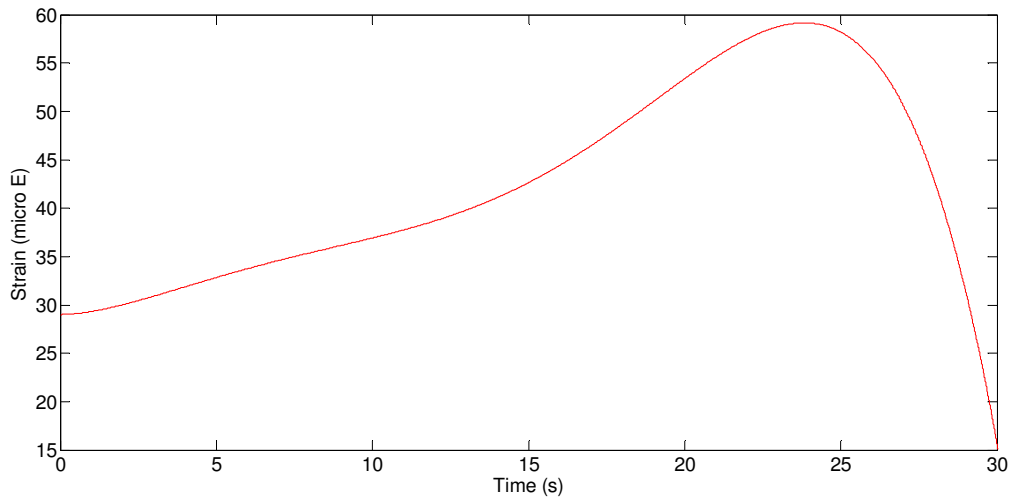


Fig 4.32: Time varying of the strain of the shaft of suns in the run down regime

Using the Hooke's law described before, the evolution of the motor's torque measured during run down will be as shown in Fig 4.33.

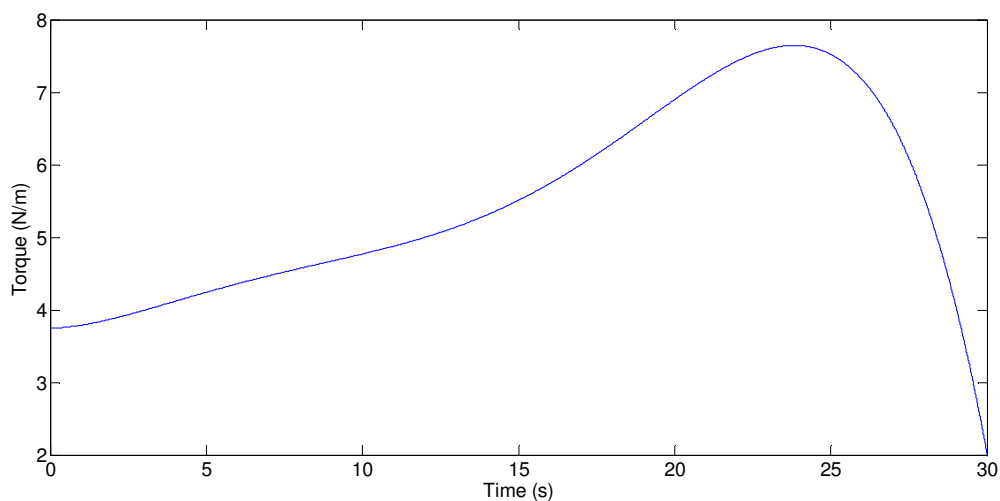
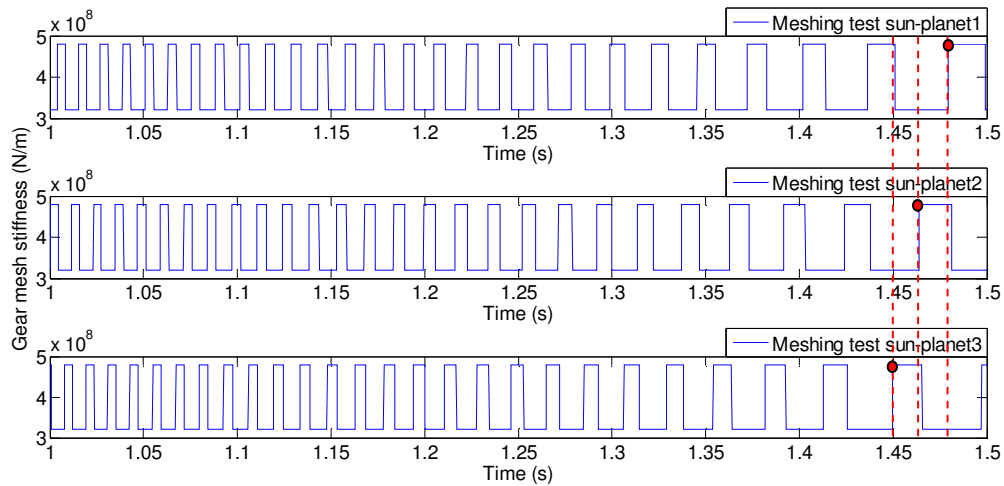
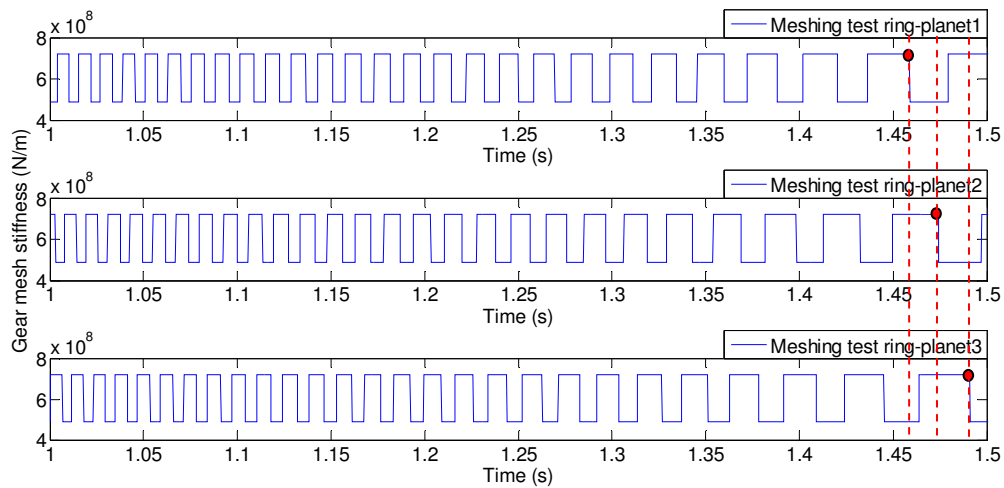


Fig4.33: Evolution of motor to during run down

During the run down regime, the period of meshing increases as the speed decrease. Figure 4.34a and figure 4.34b show the evolution of mesh stiffness for sun-planets and ring-planets on the test gear set during run down taking into account the mesh phasing.



(a)



(b)

Fig 4.34: Evolution of gear mesh stiffness for sun-planets (a) and ring-planets (b) on the test gear set during run down.

The amplitude of oscillations decreases with time during the run down. (Fig 4.35)

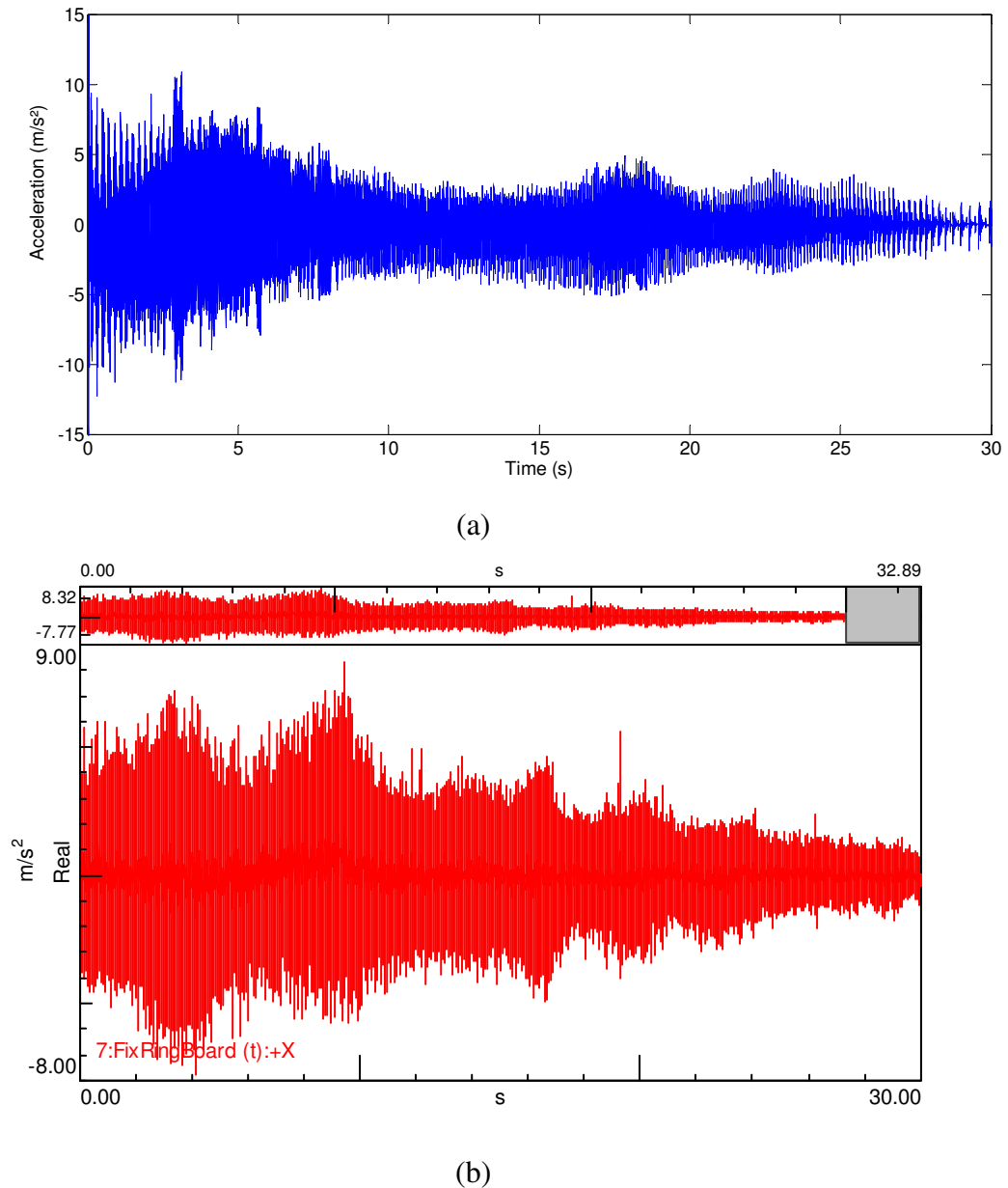
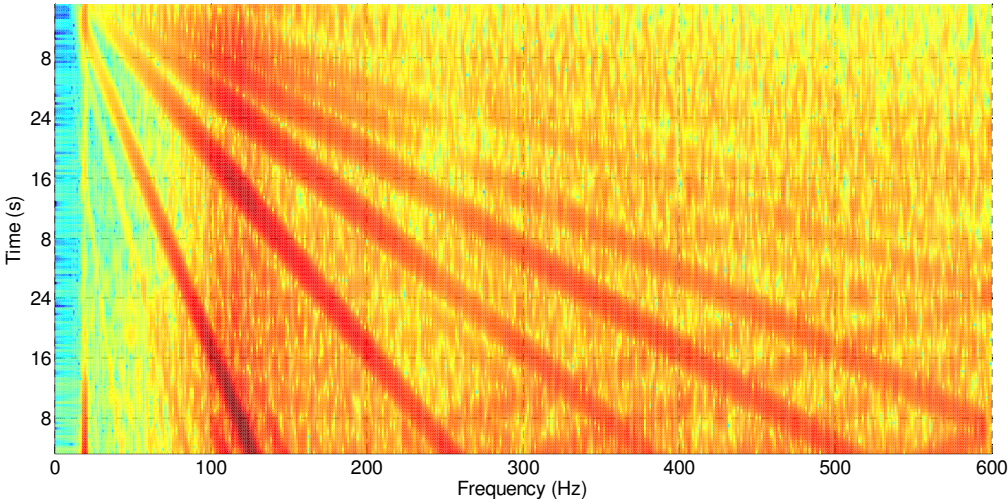
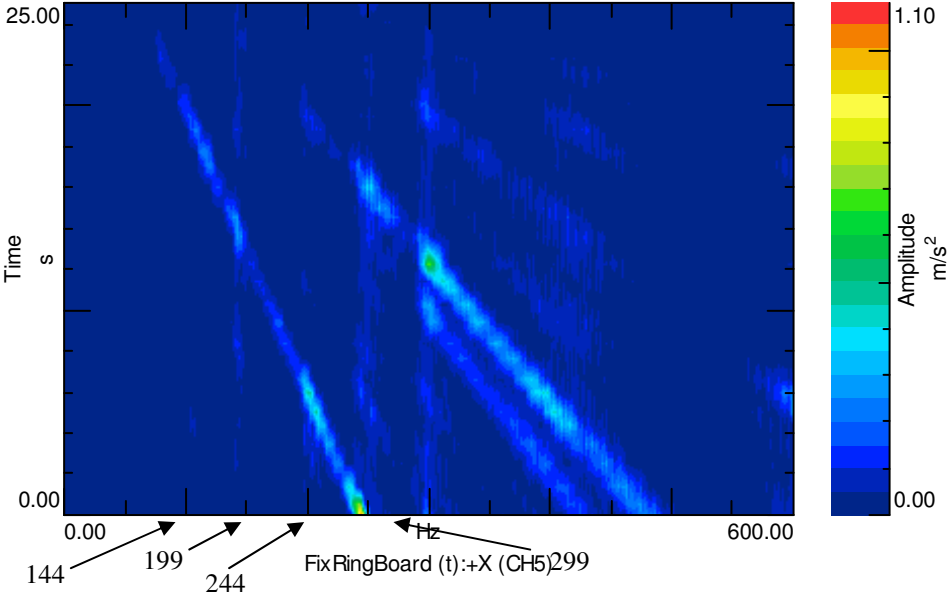


Fig 4.35: Acceleration of the fixed ring during run down: (a) simulation and (b) experimental

In the run down, the variable meshing frequency excites the system. So, inclined lines from the right to the left due to the variations of the meshing frequency and its harmonics are observed in STFT plot (Fig 4.36). In addition, natural frequencies 25Hz and 144Hz are excited in simulated STFT whereas STFT issued from experiments shows that natural frequencies 143Hz, 200Hz, 244Hz and 299Hz are excited.



(a)



(b)

Fig 4.36: STFT on the fixed ring during run down from simulation (a) and the experience (b)

The time response of the acceleration on the test carrier is shown in Fig 4.37. It is well observed that the vibration is decreasing respectively with time.

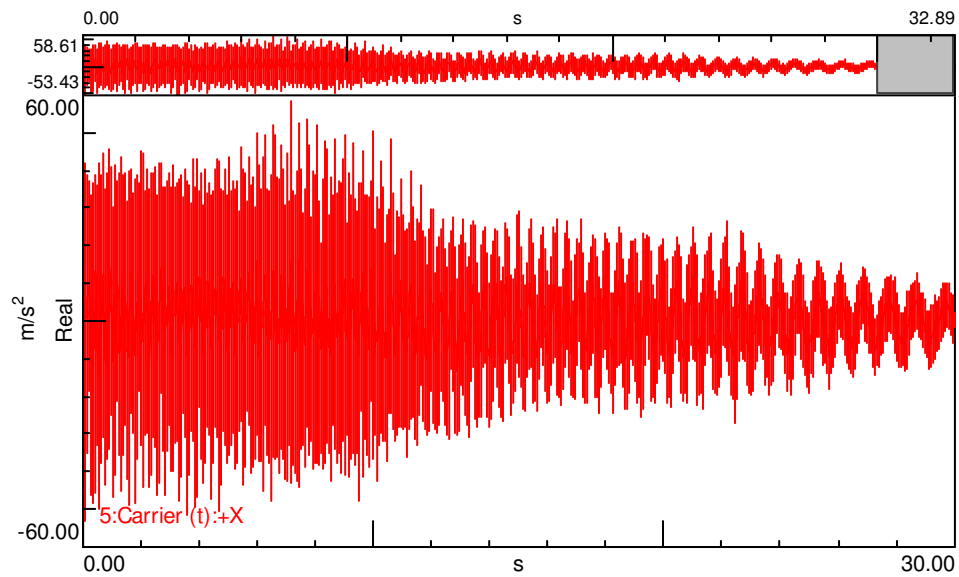


Fig 4.37: Acceleration of the test carrier during run down

Fig 4.38 shows STFT for acceleration on the test carrier.

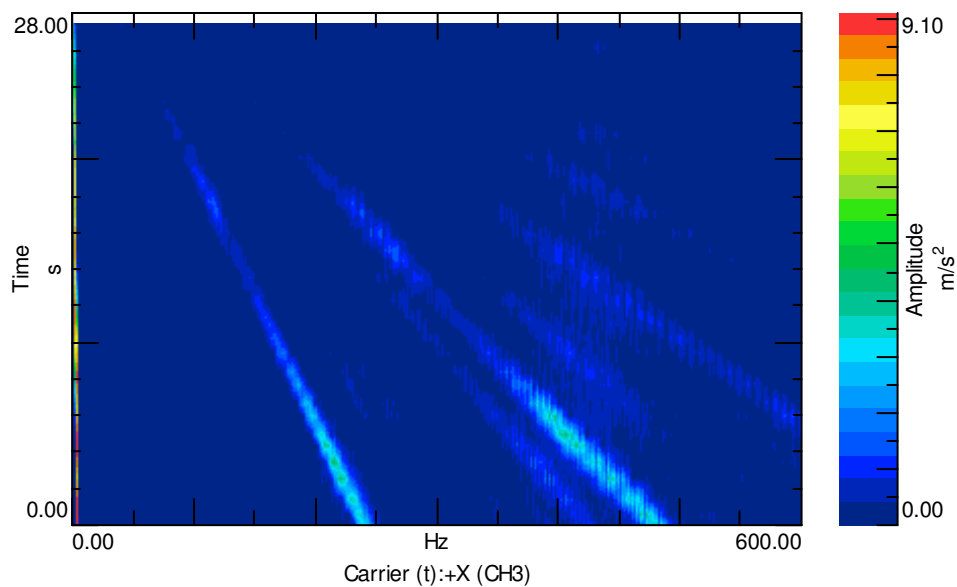


Fig 4.38: Color map of the test carrier dynamic response in the run down

We observe inclined lines showing the decrease of the meshing frequency and its harmonics on fig 4.38. In addition, an important acceleration is shown in the low-frequencies. A zoom in 0-30Hz of the band 0-30Hz is showed in Fig 4.39.

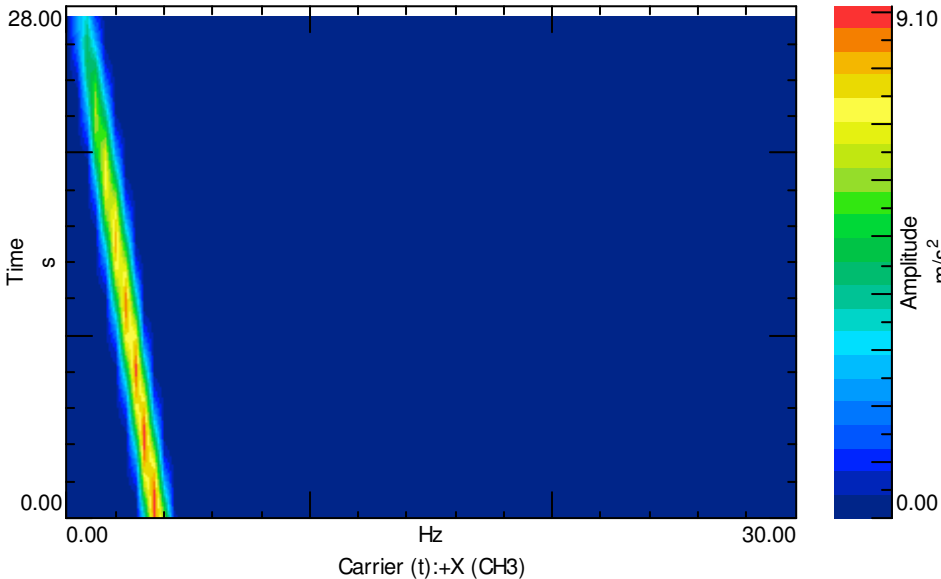


Fig 4.39: Color map of the test carrier dynamic response in the run down (zoom)

7. Variable speed

A speed variation is imposed to the driving motor simulating the variable speed generated by the variable wind velocity to the input shaft. This speed presents a balance of acceleration and deceleration until a speed reference in order to get the maximum power for the wind turbine (Arnaltes, 2014).

The driven speed which is presented in fig 4.40 creates a vibration of the gearbox modulated by this speed (Zimroz et al, 2011).

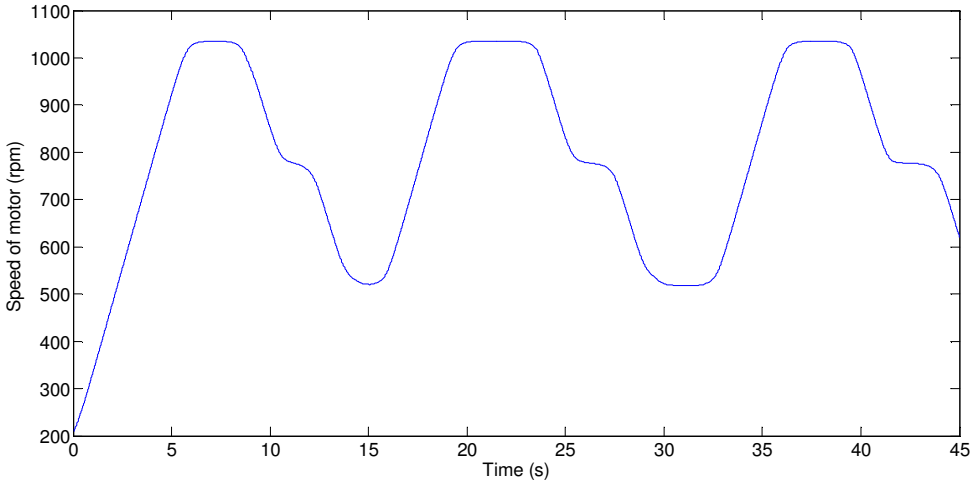
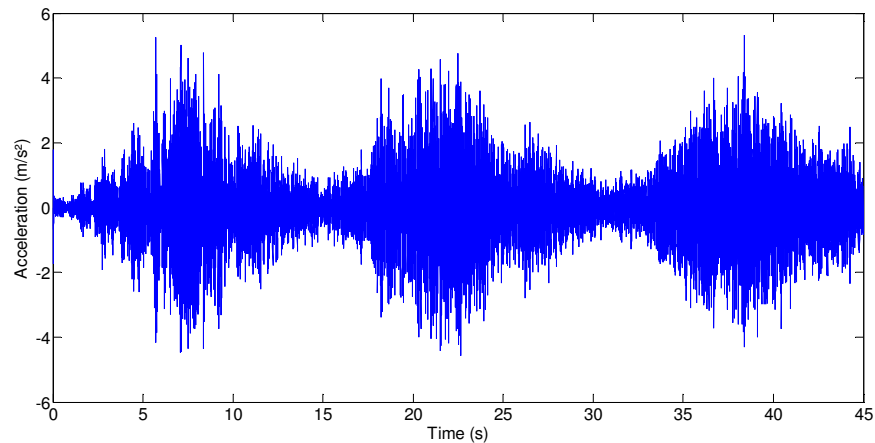


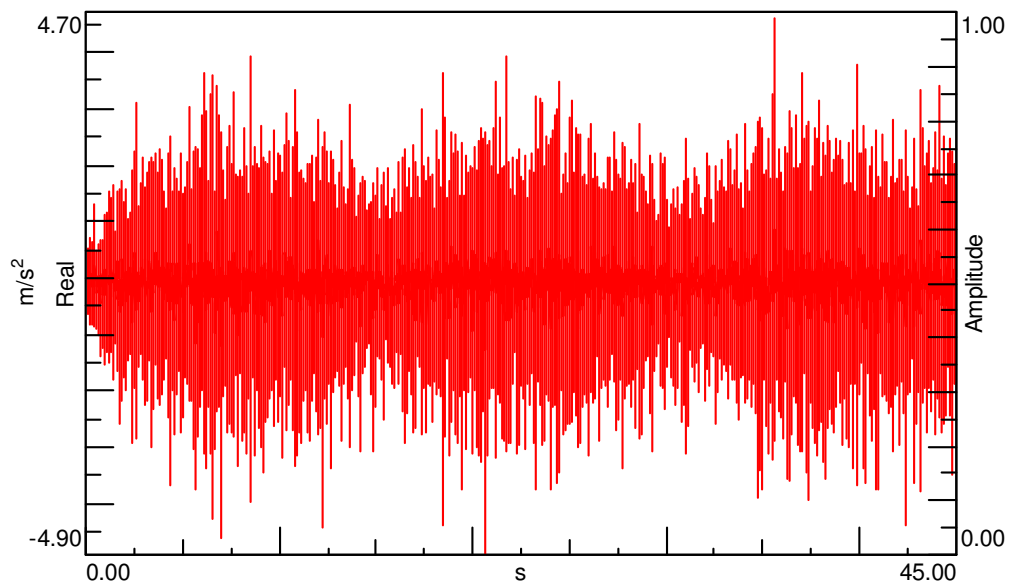
Fig 4.40: Speed of electrical motor

During the acceleration of motor, the period of mesh stiffness function decreases as we increase the speed whereas during the deceleration of motor, the period of mesh stiffness function increases as we decrease the speed.

The time response of the acceleration on the fixed ring is shown in Fig 4.41. Vibration signals are modulated by the variation of speed. Amplitude reaches its maximum values when the speed is maximum.



(a)

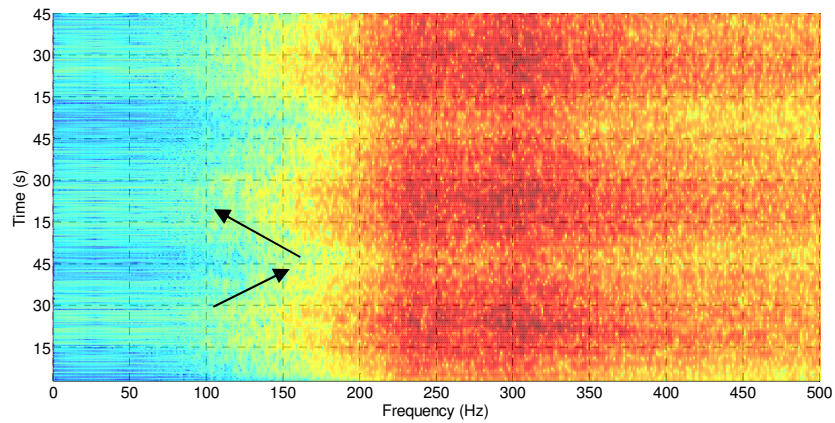


(b)

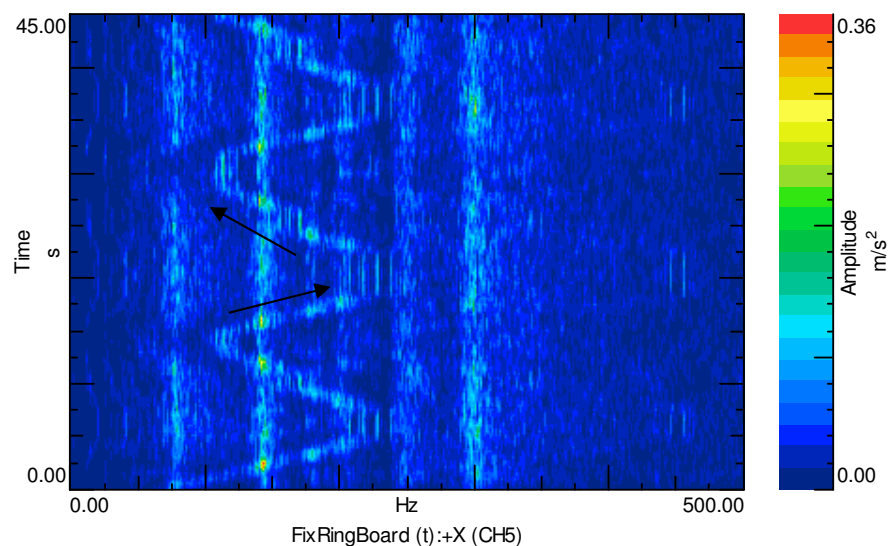
Fig4.41: Acceleration of the fixed ring (a) theoretical and (b) experimental

In fact, the meshing frequency is not constant. If we represent the Short Time Fourier Transform (STFT) of the accelerations simulated and measured on the fix ring (Fig 4.42) we can observe inclined lines from the right to the left due to the increase of the meshing

frequency (increase of speed) and its harmonics inclined lines from the left to the right due to the decrease of the meshing frequency (decrease of speed) and its harmonics.



(a)



(b)

Fig 4.42: STFT of acceleration of the test ring from the theoretical model (a) and from the experimental result (b)

In addition, the STFT present vertical lines showing the presence natural frequencies around 245Hz and 300Hz. The system is excited on the neighbourhood of the frequencies 245Hz and 300Hz in the theoretical model where the natural frequencies presented in the experimental result are on the neighbourhood of the frequencies 143Hz, 200Hz, 244Hz and 299Hz.

Variable speed condition is harmful for a gear transmission. Moreover, it is very important to characterize the dynamic behaviour since natural frequencies can be excited.

8. Conclusion

A torsional model of back to back planetary gear trains is developed in order to compute the dynamic response in stationary and non stationary operating conditions.

A first study considering stationary operations (fixed speed and load) was conducted. A theoretical and an experimental investigation of modulation sidebands of back-to-back planetary gear were highlighted. Besides, an external variable load was introduced during test on the free ring by adding masses. In this case, the values of meshing forces and the period of double contact increases as the torque level increases. Also, the inertia and the bearing stiffness of the reaction ring gear increase. The dynamic behaviour of back-to-back planetary gear changes due to the change of mass and stiffness which induced an amplification of the 2nd harmonic of the mesh frequency.

A variation of speed was imposed to the system by the driving motor. During the run up, the amplitude of acceleration of the fixed ring increased whereas it decreased during run down. In the case of a variable speed, the acceleration of the fixed ring was amplified by this variation of the speed. Short time frequency analysis was carried out in order to characterize frequency content and identify the speed variation. The STFT obtained from simulation and experiment for acceleration on the test ring gear showed inclined lines corresponding to the variation of the mesh frequency and its harmonics and vertical lines corresponding to the coincidence of some natural frequencies of the system confirming the natural frequencies obtained in chapter 3.

Chapter 5:

Load sharing and transfer path analysis

Sommaire

1. Introduction.....	125
2. Planet load sharing.....	125
2.1. Planet load sharing under stationary conditions.....	125
2.1.1. Effect of meshing phase.....	126
2.1.2. Effect of gravity of carrier.....	127
2.1.3. Effect of planet position error.....	130
2.1.4. Correlation with experimental results.....	131
2.2. Load sharing behavior during the run-up regime.....	132
3. Transfer Path Analysis.....	134
3.1. Calculation of the direct transmissibility matrix.....	134
3.2. Operational response decomposition.....	136
3.3. Experimental setup.....	137
3.4. Experimental results.....	139
3.4.1. Global and direct transmissibilities.....	139
3.4.2. Operational response reconstruction in the stationary conditions.....	142
3.4.3. Operational response reconstruction in the run-up regime.....	145
4. Conclusion.....	147

1. Introduction

Planetary gears can transmit higher power density levels because they use multiple power paths formed by each planet branches. This allows the input torque to be divided between the n planet paths, reducing the force transmitted by each gear mesh.

Under ideal conditions, each planet path carries an equal proportion of load. Nevertheless, planetary gears have inevitable manufacturing and assembly errors. So, the load is not equally shared amongst the different sun-planet and planet-ring paths, which can lead to problems in dynamic behavior and durability.

In the first part of this chapter, the effects of meshing phase, the gravity and the error position of the pin hole of planets on the load sharing behavior are studied numerically and validated experimentally in stationary conditions. The effect of speed on the load sharing behavior is studied later and the numerical results will be correlated with the experimental results. After that, the load sharing behavior is studied under the run-up regime.

The second part will be dedicated to a transfer path analysis approach termed Global Transmissibility Direct Transmissibility (GTDT): computation of the direct transmissibility from the global transmissibility is explained and the reconstruction of any degree-of-freedom is described. Then, the experimental setup and measurements are detailed. Experimental results are shown for system running under stationary conditions and non-stationary conditions.

2. Planet load sharing

The planet load sharing ratio (LSR) is defined as the ratio of the meshing torque due to sun-planet(i) and ring-planet(i) meshes of planet (i) by the meshing torque of all planets.

$$LSR_{Pi} = \frac{T_{mesh(Pi)}}{\sum_{i=1}^n T_{mesh(Pi)}} \quad (5.1)$$

2.1. Planet load sharing under stationary conditions

The effects of meshing phase, the gravity of planets carrier and the position error of planets on the load sharing behavior are studied numerically in this part and then validated experimentally through strain time histories of planets' pinhole.

2.1.1. Effect of meshing phase

For the case of equally spaced planets and in phase gear meshes (sun-planets and ring-planets), the planet load sharing factor is equal to $1/N$ (N : number of planets).

For the studied back to back planetary gear transmission, planets are equally spaced and there are sequentially phased gear meshes:

$$\frac{Z_r \psi_i}{2\pi} \neq n \quad \text{and} \quad \sum_{i=1}^N Z_r \psi_i = m\pi \quad (5.2)$$

$$\frac{Z_s \psi_i}{2\pi} \neq n \quad \text{and} \quad \sum_{i=1}^N Z_s \psi_i = m\pi \quad (5.3)$$

n and m are integer.

Using the finite element model (Fernandez Del Rincon et al 2013), Fig.5.1 and Fig.5.2 shows respectively the time evolution of the gear mesh stiffness of the contact ring-planets and sun-planets.

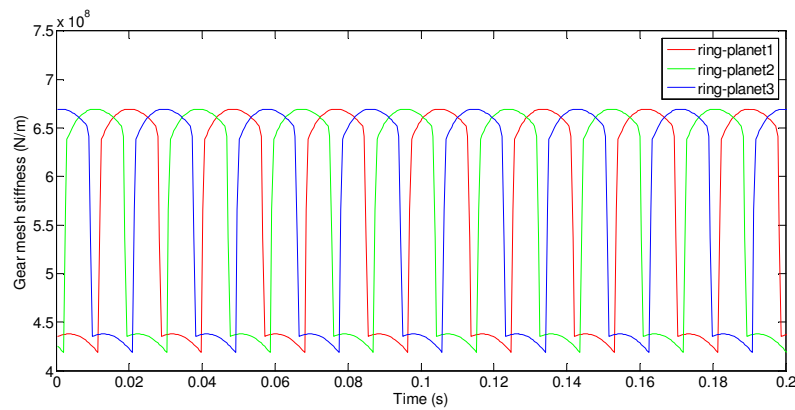


Fig.5.1: Mesh stiffness ring-planets

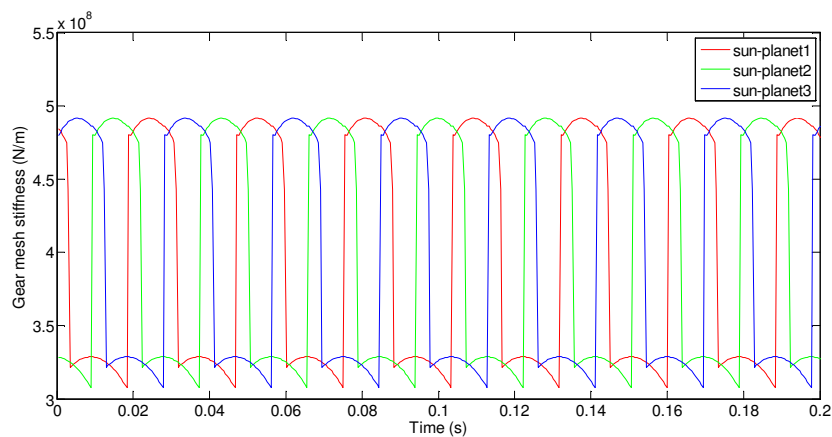


Fig.5.2: Mesh stiffness sun-planets

Fig.5.3 shows the planet load sharing ratio for the nominal position of planets (healthy system) for 100 N.m of input torque and for motor speed 165 rpm.

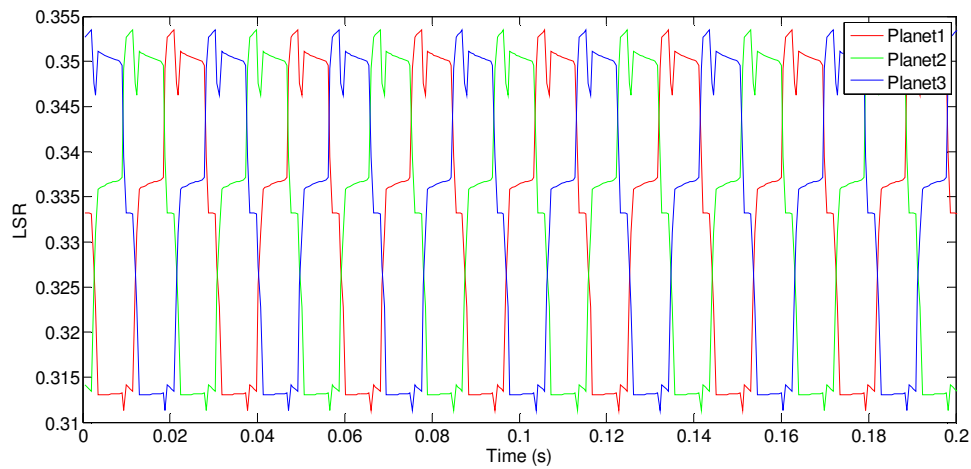


Fig.5.3: Planet load sharing ratio for the nominal position of planets

In this case, the LSR for all planets fluctuates slightly around the $1/N$ value ($N=3$: number of planets) due to variation in the number of teeth pairs in contact. The fluctuation of LSR of each planet is the same with a phase shift of $2\pi/3$. This phase is due to the fact that gear meshes sun-planets and ring-planets are sequentially phased.

2.1.2. Effect of gravity of carrier

The gravity of carriers has effect on the distances between ring-planets and sun-planets. These distances are variable during the running of gearbox. Then, the values of gear mesh stiffness decrease as the distance between gears (sun-planets and ring-planets) increase and vice versa. Fig.5.4 and Fig.5.5 show respectively the evolution of mesh stiffness ring-planets and sun-planets during one period of rotation of carrier taking into account the effect of gravity of carrier. There will be a change in the mean value of mesh stiffness. This phenomenon is periodic. The maximum value of this stiffness for contact ring planets (and sun planets) is periodically on the planet 3, then planet 2 and then planet 1.

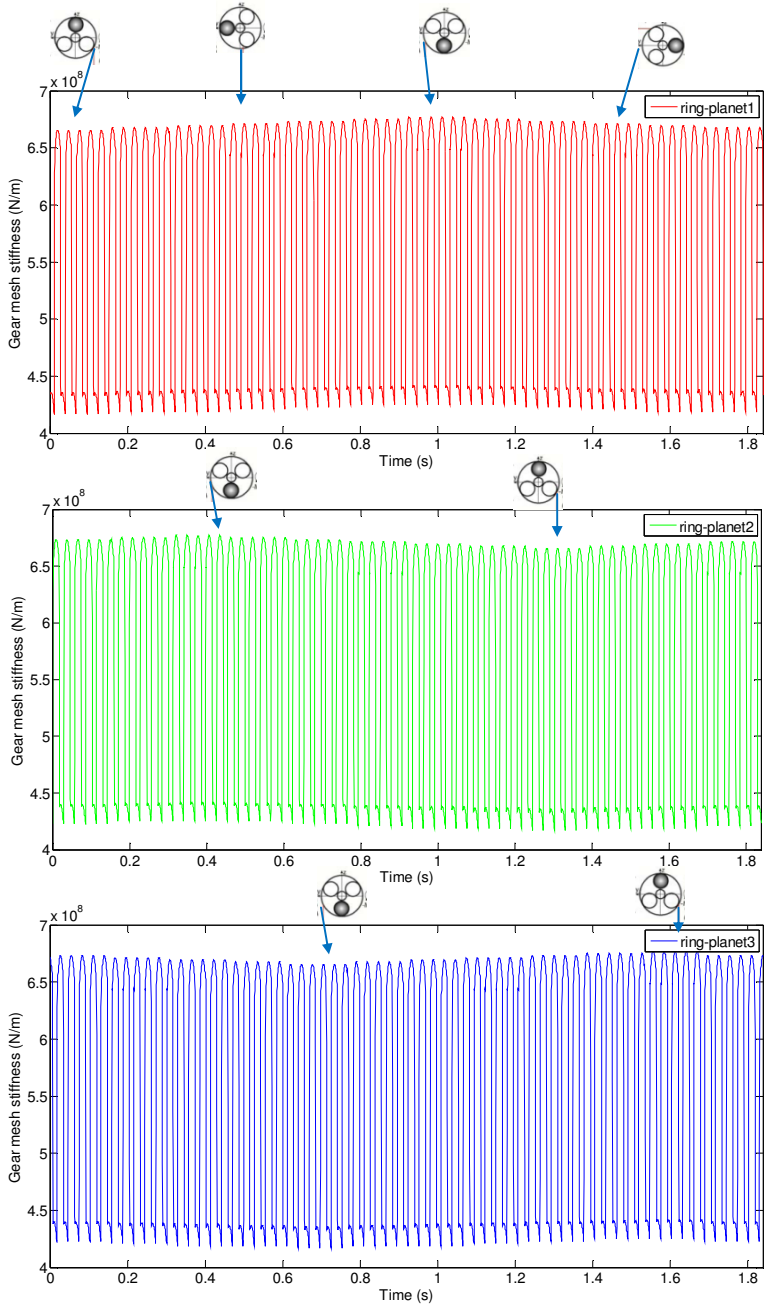


Fig.5.4: Evolution of gear mesh stiffness ring-planets with gravity effects

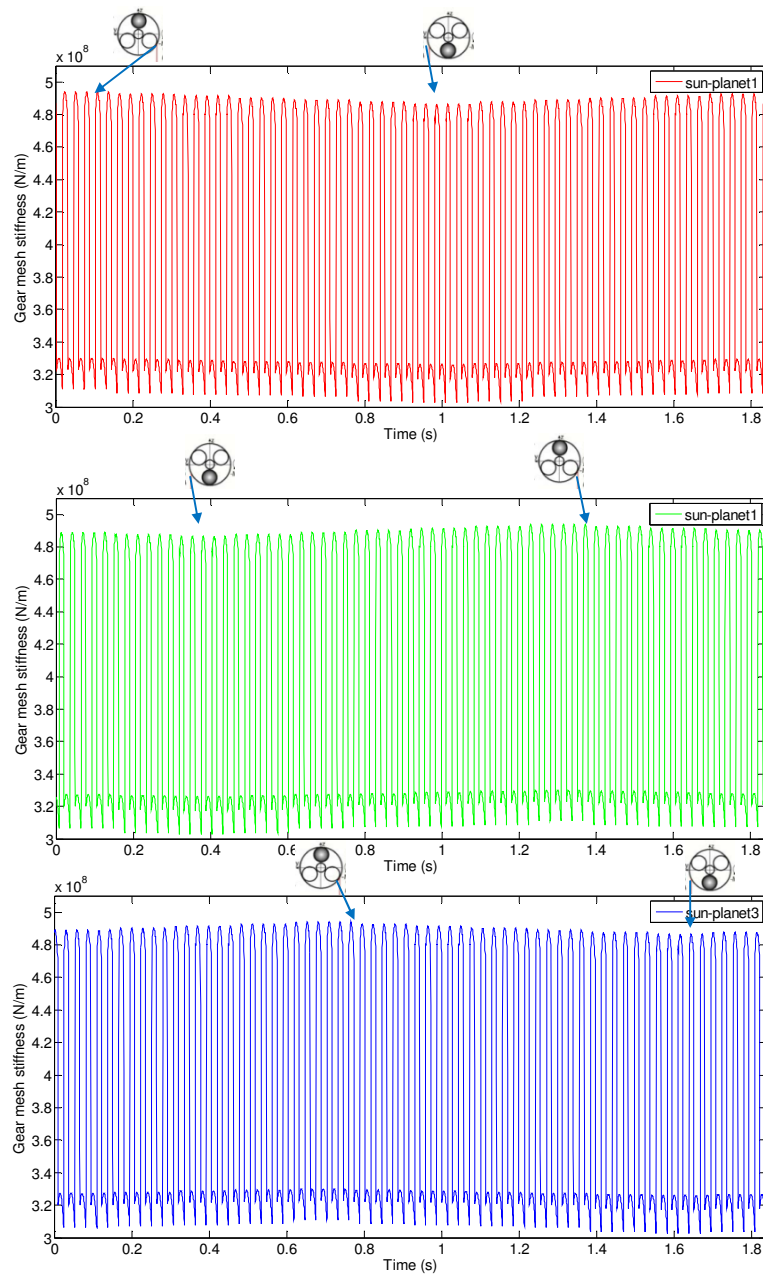


Fig.5.5: Evolution of gear mesh stiffness sun-planets with gravity effects

Fig.5.6 shows the evolution of LSR during one period of rotation of carrier. This period is shared into three periods of $T_c/3$. For each period, the LSR of each planet does not oscillate with the same amplitude. In each period, one LSR of planet dominates: LSR of planet 1 dominates in zone 1, LSR of planet 2 dominates in zone 2 and LSR of planet 3 dominates in zone 3

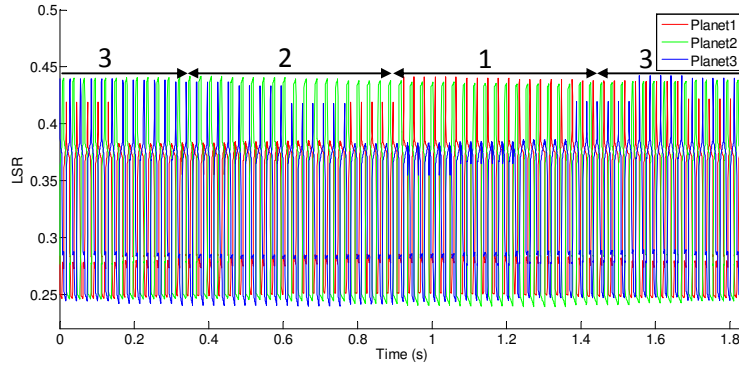


Fig.5.6: Planet load sharing ratio with gravity effects

2.1.3. Effect of planet position error

If a planet has an error “ e ” on the position of its pin hole, and all other planets are at their ideal position, then the force due to this error is given by (Singh, 2010):

$$F_e = K_{eff} . e \quad (5.4)$$

K_{eff} is the cumulative stiffness due to meshing stiffness of the contact at the sun–planet K_{ps} and planet–ring K_{pr} , and the planet bearing stiffness K_b .

K_{eff} is defined as (Ligata et al, 2009):

$$\frac{1}{K_{eff}} = \frac{1}{K_b} + \frac{1}{K_{ps} + K_{pr}} \quad (5.5)$$

Let’s consider that the test planet 1 has a tangential error “ $e_1=60\mu\text{m}$ ”, the test planet 2 has a tangential error “ $e_2=10\mu\text{m}$ ” and the test planet 3 has a tangential error “ $e_3=-60\mu\text{m}$ ”.

The LSR is shown in Fig.5.7.

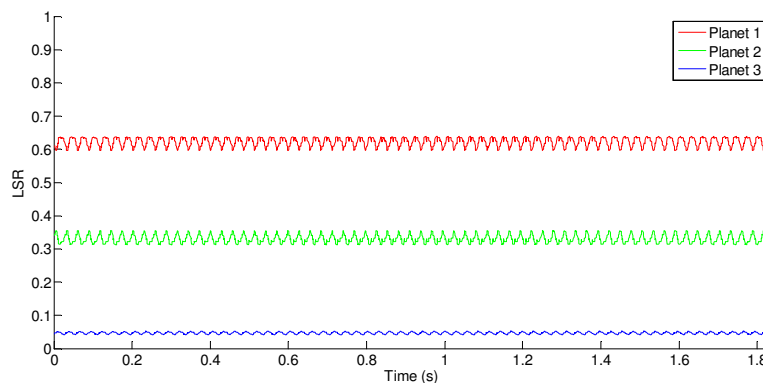


Fig.5.7: Planet load sharing ratio with planets position errors

It is clear that the position error of planets causes a substantial change of LSR when compared to the case when only gravity effect is considered. This is explained by the fact that position error of planet is in the tangential direction and the effect of gravity is in the radial direction. Bodas (Bodas and Kahraman 2004) showed that planets with tangential position error will have higher LSR. In fact, planet 1 anticipates the contact, being preloaded before planets 2 and 3 begin to transmit whereas planet 3 is preloaded after planet 2 and 1.

2.1.4. Correlation with experimental results

In order to compare the load sharing between the tests planets, three strain gauges are installed in the pin holes of each planet in the tangential direction of the test carrier (Fig. 2.20).

Strain-time histories for three planets system having errors “ $e_1=60\mu\text{m}$ ” “ $e_2=10\mu\text{m}$ ” and “ $e_3=-60\mu\text{m}$ ” are shown in Fig.5.8. Oscillations resulting of the meshing phase don't appear because the signals are smoothed. In fact, the original signals present noise due to contact on the slip ring.

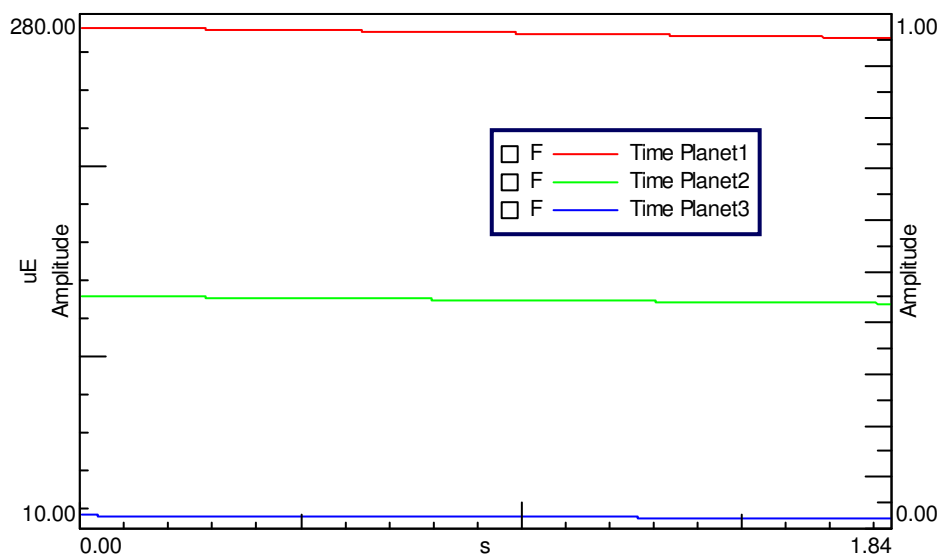


Fig.5.8: Variation of the measured planets strains for the speed motor 165 rpm

The numerical results of the load sharing ratio are compared to the measured ones (Fig. 5.9). In general, the calculated load sharing agrees with the measured data. In fact, the planet position errors have an important effect. In addition, a bend of the load sharing evolution due

to the effect of gravity of carrier is observed on the numerical and experimental results whereas the effect of meshing phase is observed only in the numerical results.

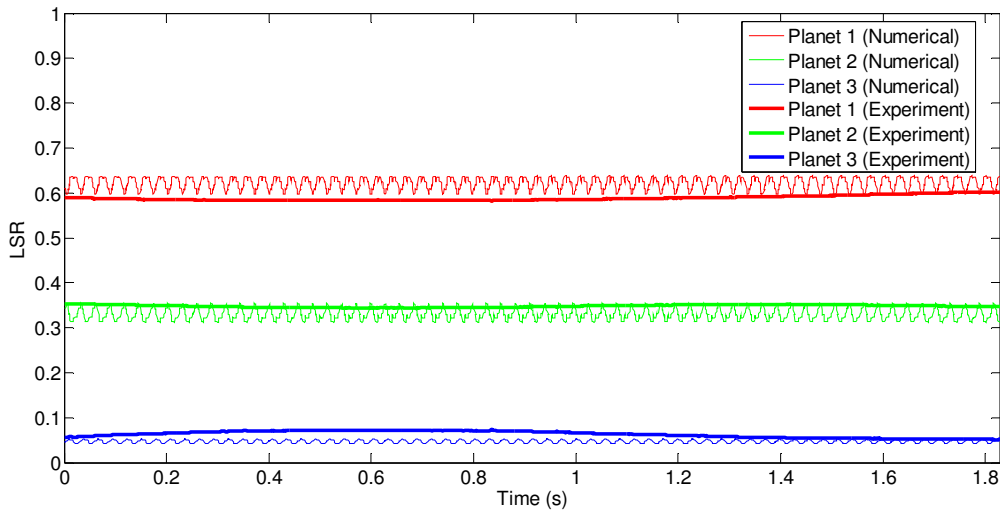


Fig.5.9: Evolution of measured and calculated LSR

2.2. Load sharing behavior during the run-up regime

A linear evolution of the motor speed is considered during run up. Fig.5.10 shows the evolution of the speed of carrier.

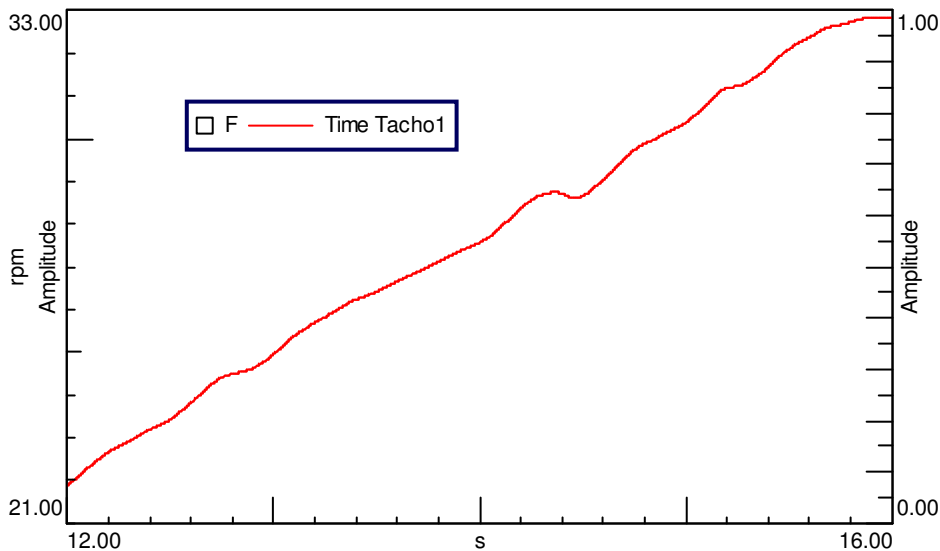


Fig.5.10: Evolution of the speed of carrier during run-up

In the following, the radial errors due to the effect of gravity are neglected compared to the tangential error of the pin position of planets. Mesh stiffness function are modeled according to the procedure detailed in section 5 of chapter 4 taking into account mesh phasing.

The LSR for all planets fluctuates around the $1/N$ value because the number of tooth pairs in contact changes. The period of fluctuation of LSR of each planet decreases in the time (Fig.5.11).

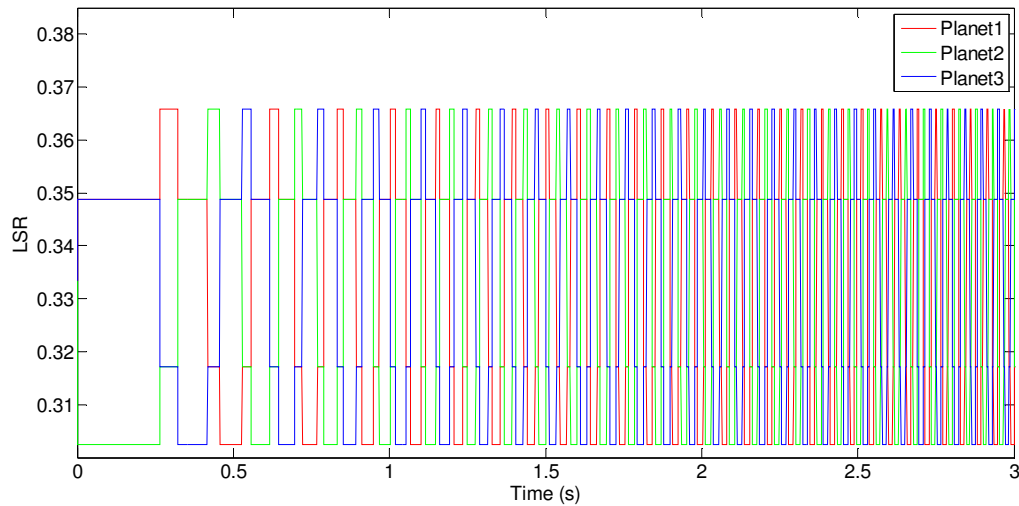


Fig.5.11: Planet load sharing ratio for the nominal position of planets during run-up

Smoothed strain-time histories for three planets system having pin position errors on planets are shown in Fig.5.12.

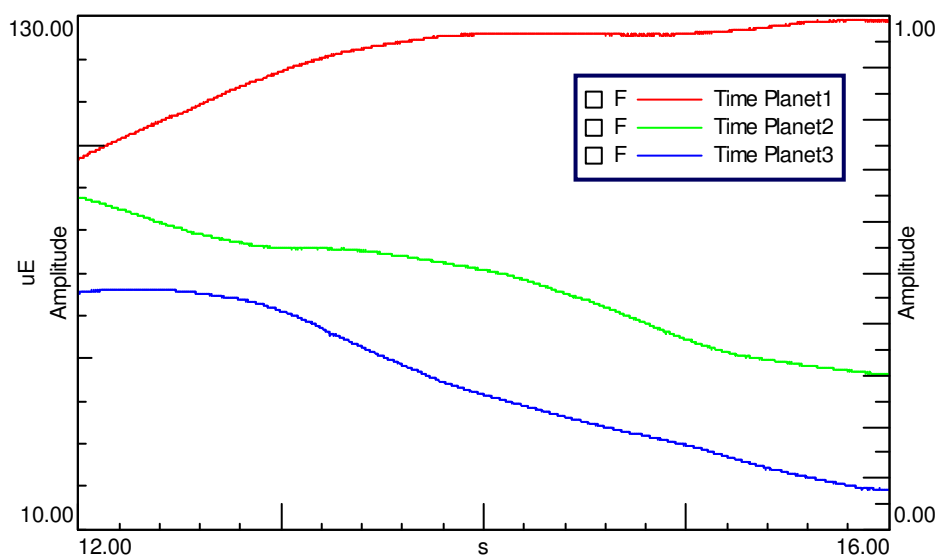


Fig.5.12: Variation of the measured planets strains during run-up

The measured LSR during run-up are shown in Fig.5.13. It is clear that planet 1 and 3 present position error which has influence on the LSR. This ratio of planet 1 increases during run up whereas the LSR of planet 2 decreases during run up.

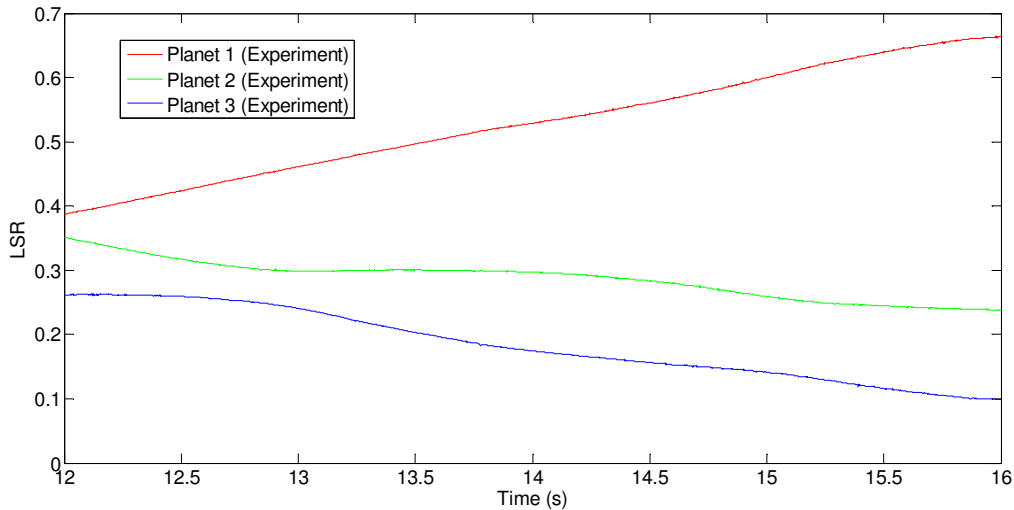


Fig.5.13: Measured planet load sharing ratio during run-up

So, the effect of the planets position error on the LSR is higher as the speed increase.

3. Transfer Path Analysis

The classical transfer path analysis allows the study of propagation of sound and vibration. This method has two limits: decoupling the active part of the system in the measurements of FRFs and the difficulties to measure the operational forces.

In order to avoid these drawbacks, another two steps strategy was developed by Magrans (Margans, 1981): the first step is the measurements of transmissibility which requires no demounting tests and the second step is the measurements of the operational responses. In contrast, the so-called direct transmissibilities obtained from the measured transmissibilities are used for the operational response contribution.

3.1. Calculation of the direct transmissibility matrix

For the case of classical TPA, the operational response at any degree-of-freedom x_i is:

$$x_i = \sum_{j=1}^{N_f} H_{ij} f_j \quad (5.6)$$

Where f_j is an external load acting the system and N_f is the number of the external loads acting the system. H_{ij} is the transfer function (FRFs).

For the GTDT reconstruction of the response of x_i :

$$x_i = \sum_{j=1, j \neq i}^{N-1} T_{ij}^D x_j + T_{ii}^D x_i^{ext} \quad (5.7)$$

The response at any degree-of-freedom x_i is decomposed into contributions from other degree-of-freedom responses and the portion of that the external load is directly acting on it ($x_i^{ext} = 0$ if no force on it). T_{ij}^D and T_{ii}^D are the direct or blocked transmissibilities.

The direct transmissibility is obtained from the global transmissibility T_{ij}^G which corresponds to the ratio between the response of the i^{th} degree-of-freedom and the response of the j^{th} degree-of-freedom when j is excited:

$$T_{ij}^G = \frac{x_j}{x_i} = \frac{H_{ij} f}{H_{ii} f} = \frac{H_{ij}}{H_{ii}} \quad (5.8)$$

The matrix form is written:

$$T^G = \text{diag} \left(\frac{1}{H_{11}}, \dots, \frac{1}{H_{nn}} \right) \times H \quad (5.9)$$

The inverse matrix of T^G is:

$$T^{G^{-1}} = H^{-1} \times \text{diag} (H_{11}, \dots, H_{nn}) = Z \times \text{diag} (H_{11}, \dots, H_{nn}) \quad (5.10)$$

The direct transmissibility corresponds to the ratio between the response of the i^{th} degree-of-freedom and the response of the j^{th} degree-of-freedom when j is excited and all remaining degree-of-freedom, except i and j , are blocked. In this case and as the system is governed by $Zx = f$, we have (Guasch, 2009), (Guasch et al., 2013):

$$\begin{bmatrix} Z_{ii} & Z_{ij} \\ Z_{ji} & Z_{jj} \end{bmatrix} \begin{Bmatrix} x_i \\ x_j \end{Bmatrix} = \begin{Bmatrix} 0 \\ 1 \end{Bmatrix} \quad (5.11)$$

From the last equation, the responses in i^{th} and j^{th} degree-of-freedom can be written:

$$x_i = \frac{Z_{ij}}{Z_{ij}Z_{ji} - Z_{ii}Z_{jj}} \quad (5.12a)$$

$$x_j = \frac{-Z_{ii}}{Z_{ij}Z_{ji} - Z_{ii}Z_{jj}} \quad (5.12b)$$

So, the direct transmissibility is defined as:

$$T_{ij}^D = \frac{x_i}{x_j} = -\frac{Z_{ij}}{Z_{ii}} \quad (5.13)$$

For the direct transmissibility T_{ii}^D , all degrees-of-freedom are blocked except the i^{th} d.o.f. From equation (5.9), we have $Z_{ii}x_i = 1$. Besides, only the i^{th} d.o.f is excited. So, $H_{ii} = x_i$.

Therefore:

$$T_{ii}^D = \frac{1}{Z_{ii}H_{ii}} \quad (5.14)$$

From equation (8.5), we can write:

$$T^{G^{-1}} \Big|_{ij} = Z_{ij}H_{ii} \quad (5.15)$$

Dividing T_{ij}^D in (8.8) by T_{ii}^D in (5.14) and taking into account to (5.15) provides:

$$\frac{T_{ij}^D}{T_{ii}^D} = -T^{G^{-1}} \Big|_{ij}, i \neq j \quad (5.16)$$

Taking $i = j$ in (5.15) and using (5.16) gives:

$$\frac{1}{T_{ii}^D} = T^{G^{-1}} \Big|_{ii} \quad (5.17)$$

From (5.16) and (5.17), we have $T_{ij}^{DE} = T_{ij}^D = -T_{ii}^D T^{G^{-1}} \Big|_{ij}, \forall i \neq j$ and

$T_{ii}^{DE} = -1 = -T_{ii}^D T^{G^{-1}} \Big|_{ii}$. Where, T^{DE} corresponds to the direct transmissibilities matrix with

its diagonal replaced by -1 values. These relations are written in the matrix form:

$$T^{DE} = -\Lambda_{TD} T^{G^{-1}} \quad (5.18)$$

Where $\Lambda_{TD} = \text{diag}(T_{11}^D, \dots, T_{mm}^D)$:

The computation of the direct transmissibility matrix involves the inversion of the measured global transmissibility (Eq (5.18)).

3.2. Operational response decomposition

The operational response at any subsystem, x_i^{ext} , is due to the act of the external force. Then, we find the overall operational response at any degree-of-freedom using the global transmissibility matrix: $x = T^G x^{ext}$

$$x^{ext} = T^{G^{-1}} x \quad (5.19)$$

As $T^{G^{-1}} = -\Lambda_{TD}^{-1} T^{DE}$, the equation (5.19) can be written:

$$-\Lambda_{TD}x^{ext} = T^{DE}x = (T^D - \Lambda_{TD} - I)x \quad (5.20)$$

Rearranging the last equation, we have a generalisation of the equation (5.7) that includes all degree-of-freedom operational decompositions using direct transmissibilities in a single expression (Guasch and Magrans, 2004) (Guasch, 2009):

$$x = (T^D - \Lambda_{TD})x + \Lambda_{TD}x^{ext} \quad (5.21)$$

3.3. Experimental setup

Twelve degree-of-freedom has been considered for back-to back planetary gear (torsional model). x is the degree of freedom vector expressed by:

$$x = \{u_{cr}, u_{rr}, u_{sr}, u_{1r}, u_{2r}, u_{3r}, u_{ct}, u_{rt}, u_{st}, u_{1t}, u_{2t}, u_{3t}\}^T \quad (5.22)$$

The rotational coordinates are $u_{rj} = r_{rj}\theta_{rj}$ for reaction gear set $u_{ij} = r_{ij}\theta_{ij}$ and for test gear set where $j=c,r,s,1,2,3$. θ_{rj} and θ_{ij} are the rotational components; r_{rj} and r_{ij} are the base radius for the sun, ring and planets and the radius of the circle passing through the planets centres for the carrier.

The global transmissibilities are measured in the first step of the GTDT. The global transmissibility is:

$$T^G = \begin{bmatrix} 1 & T_{cr,rr} & T_{cr,sr} & T_{cr,1r} & T_{cr,2r} & T_{cr,3r} & T_{cr,ct} & T_{cr,rt} & T_{cr,st} & T_{cr,1t} & T_{cr,2t} & T_{cr,3t} \\ T_{rr,cr} & 1 & T_{rr,sr} & T_{rr,1r} & T_{rr,2r} & T_{rr,3r} & T_{rr,ct} & T_{rr,rt} & T_{rr,st} & T_{rr,1t} & T_{rr,2t} & T_{rr,3t} \\ T_{sr,cr} & T_{sr,rr} & 1 & T_{sr,1r} & T_{sr,2r} & T_{sr,3r} & T_{sr,ct} & T_{sr,rt} & T_{sr,st} & T_{sr,1t} & T_{sr,2t} & T_{sr,3t} \\ T_{1r,cr} & T_{1r,rr} & T_{1r,sr} & 1 & T_{1r,2r} & T_{1r,3r} & T_{1r,ct} & T_{1r,rt} & T_{1r,st} & T_{1r,1t} & T_{1r,2t} & T_{1r,3t} \\ T_{2r,cr} & T_{2r,rr} & T_{2r,sr} & T_{2r,1r} & 1 & T_{2r,3r} & T_{2r,ct} & T_{2r,rt} & T_{2r,st} & T_{2r,1t} & T_{2r,2t} & T_{2r,3t} \\ T_{3r,cr} & T_{3r,rr} & T_{3r,sr} & T_{3r,1r} & T_{3r,2r} & 1 & T_{3r,ct} & T_{3r,rt} & T_{3r,st} & T_{3r,1t} & T_{3r,2t} & T_{3r,3t} \\ T_{ct,cr} & T_{ct,rr} & T_{ct,sr} & T_{ct,1r} & T_{ct,2r} & T_{ct,3r} & 1 & T_{ct,rt} & T_{ct,st} & T_{ct,1t} & T_{ct,2t} & T_{ct,3t} \\ T_{rt,cr} & T_{rt,rr} & T_{rt,sr} & T_{rt,1r} & T_{rt,2r} & T_{rt,3r} & T_{rt,ct} & 1 & T_{rt,st} & T_{rt,1t} & T_{rt,2t} & T_{rt,3t} \\ T_{st,cr} & T_{st,rr} & T_{st,sr} & T_{st,1r} & T_{st,2r} & T_{st,3r} & T_{st,ct} & T_{st,rt} & 1 & T_{st,1t} & T_{st,2t} & T_{st,3t} \\ T_{1t,cr} & T_{1t,rr} & T_{1t,sr} & T_{1t,1r} & T_{1t,2r} & T_{1t,3r} & T_{1t,ct} & T_{1t,rt} & T_{1t,st} & 1 & T_{1t,2t} & T_{1t,3t} \\ T_{2t,cr} & T_{2t,rr} & T_{2t,sr} & T_{2t,1r} & T_{2t,2r} & T_{2t,3r} & T_{2t,ct} & T_{2t,rt} & T_{2t,st} & T_{2t,1t} & 1 & T_{2t,3t} \\ T_{3t,cr} & T_{3t,rr} & T_{3t,sr} & T_{3t,1r} & T_{3t,2r} & T_{3t,3r} & T_{3t,ct} & T_{3t,rt} & T_{3t,st} & T_{3t,1t} & T_{3t,2t} & 1 \end{bmatrix} \quad (5.23)$$

In order to measure the global transmissibilities, tri-axial accelerometers are mounted in each component of the back-to-back planetary gear (Fig 5.14) and the transfer functions (frequency response functions, FRFs) are measured using hammer impact test.



Fig 5.14: Accelerometers mounted in components of the back-to-back planetary gear

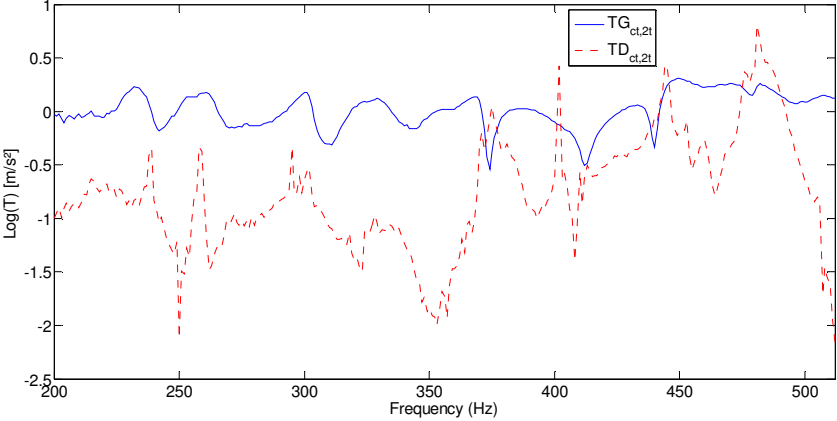
3.4. Experimental results

3.4.1. Global and direct transmissibilities

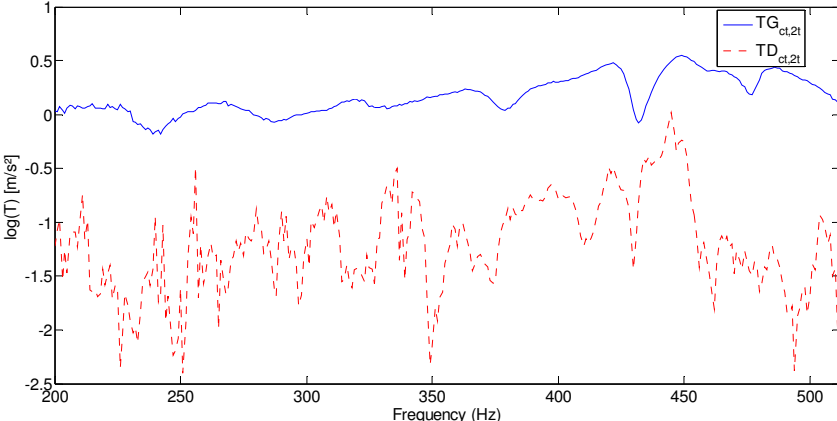
In the first step, we show some measured global transmissibilities with their direct counterparts. In figure 5.15, the logarithms of the squared module of the global and direct transmissibilities between test carrier and test planet 2 ($T_{ct,2t}^D$ and $T_{ct,2t}^G$) for two different angular positions are plotted. All these functions are different. As an example, $T_{ct,2t}^G$ stands for the ratio between the responses of the test planet 2 and the test carrier, when the test carrier is excited, whereas $T_{ct,2t}^D$ corresponds to the same ratio but keeping all the remaining system degree-of-freedom fixed.

Given that test ring is not directly connected to the reaction ring, the direct (blocked) $T_{rr,rt}^D$ should be zero and hence become minus infinity in a logarithmic plot (Maia et al., 2001) (Ribeiro et al, 2000).

However, this is not the case for the direct transmissibility $T_{rr,rt}^D$ (Figure 5.16). Also, it is clear that the direct transmissibility $T_{rr,rt}^D$ should be smaller than its respective global transmissibility $T_{rr,rt}^G$.



(a)



(b)

Figure 5.15: Global and direct transmissibilities $T_{ct,2t}^D$ and $T_{ct,2t}^G$, for position 1(a) and position 2 (b)

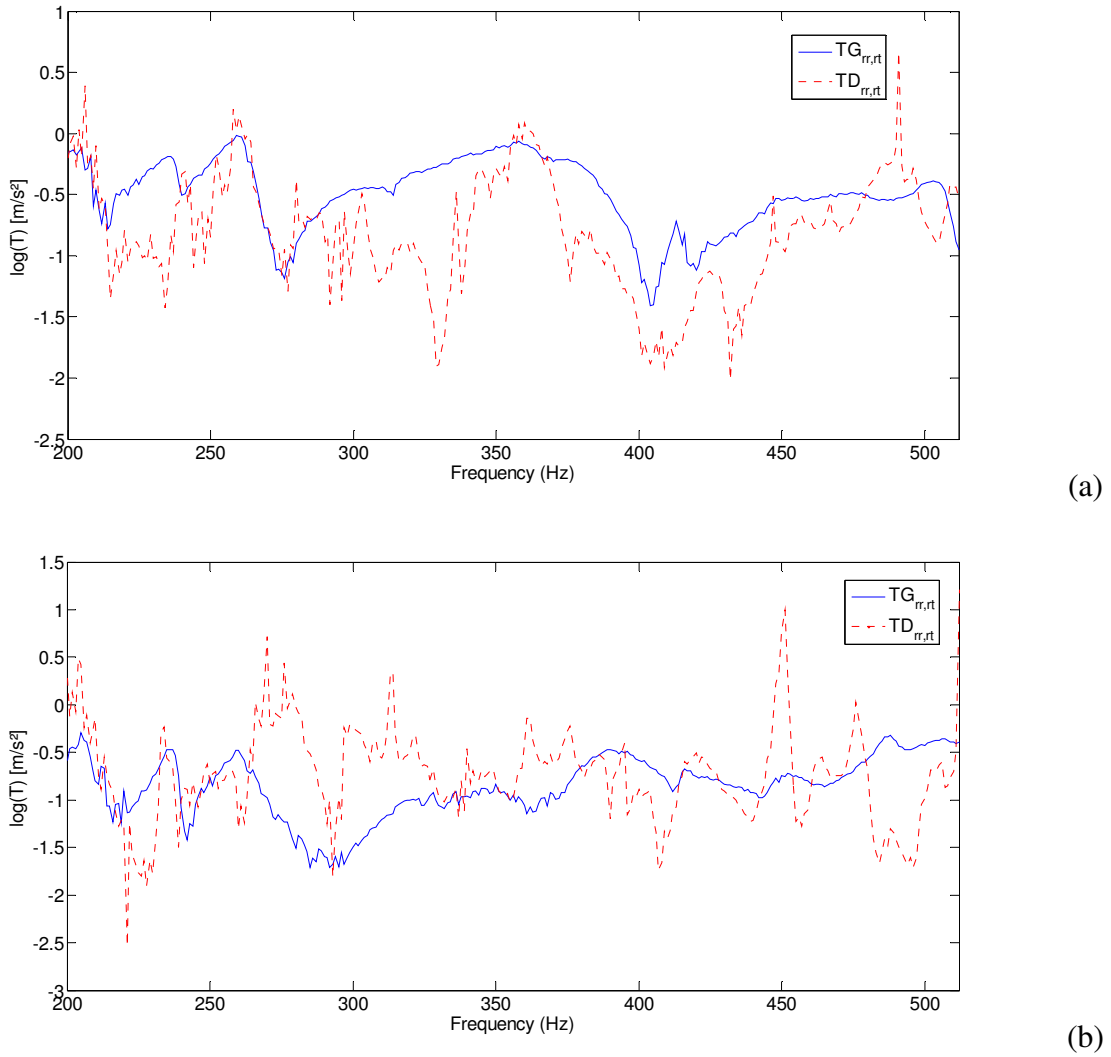


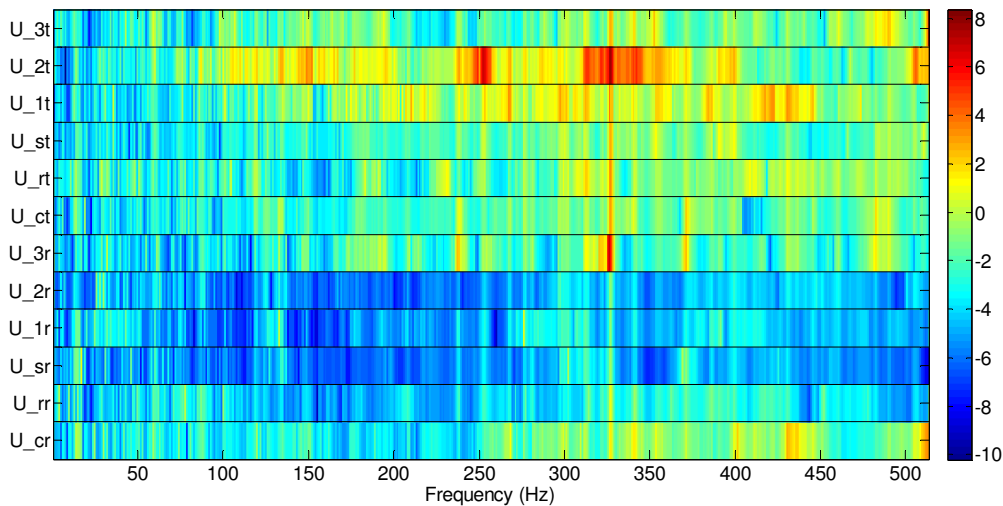
Figure 5.16: Global and direct transmissibilities $T_{rr,rt}^D$ and $T_{rr,rt}^G$, for position 1(a) and position 2 (b)

The fact that the direct transmissibility is not null, when it should, can pollute the operational response reconstruction. Neglecting the error in the reconstructed operational displacement will depend on how small the involved direct transmissibility becomes with respect to all the other direct transmissibility, and on the responses of the degree-of-freedom it connects as well.

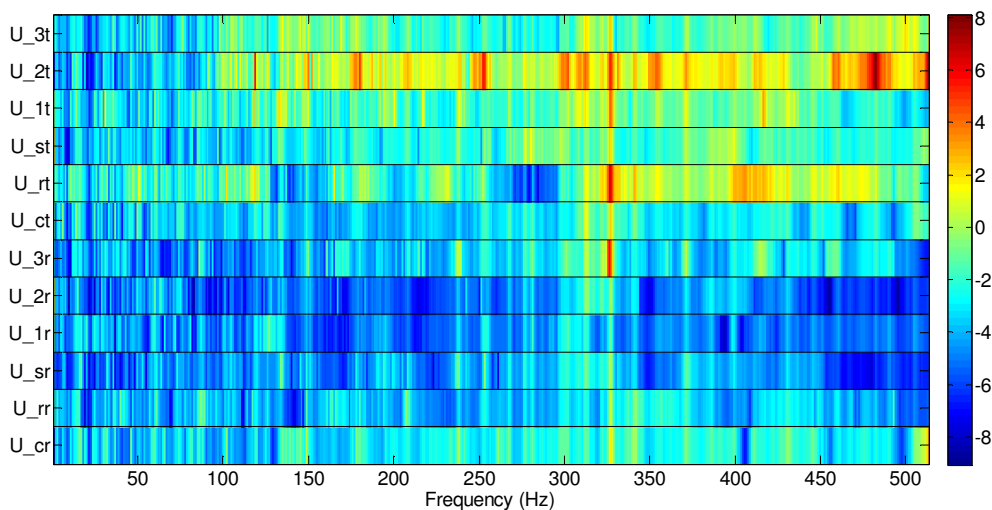
The operational response reconstruction is studied in two cases: the first is in the stationary conditions whereas the second is in non-stationary condition which is the run-up regime.

3.4.2. Operational response reconstruction in the stationary conditions

The operational situation is considered under stationary conditions where driving motor excite the system. Results correspond to partial path contribution (PPC) plots (Gajdatsy et al, 2010). Figure 5.17 shows PPC surface plot of the logarithm of the squared modulus of all reconstructed operation responses corresponding to two angular positions.



(a)



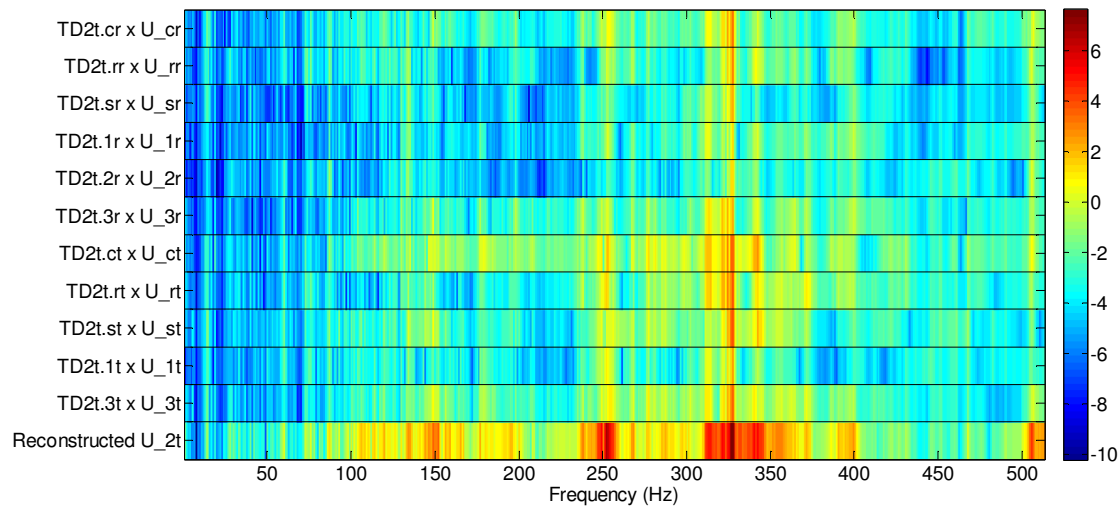
(b)

Figure 5.17: PPC surface plot of the reconstructed operation responses in stationary condition
(a) position 1 and (b) position 2

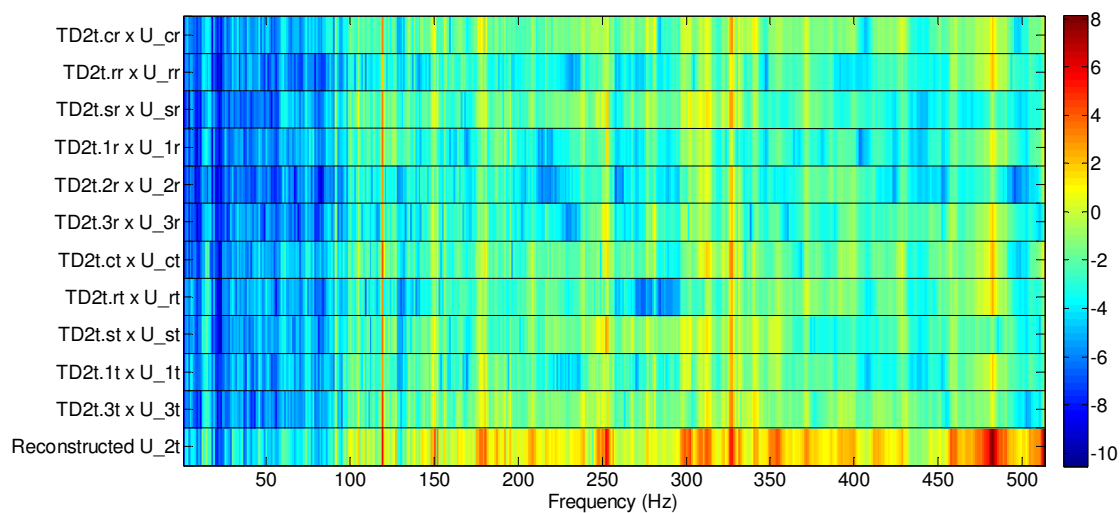
We observed on these two figures that the vibration level of all reconstructed operation responses is higher around the frequency 321Hz which correspond to the gear mesh

frequency. In addition, it is clear that the second test planet present the highest vibration level which can be explained by the fact that the test planet 2 has two pairs of teeth on contact with the sun and the ring and its transmissibility is higher in the two cases.

In order to understand better the higher vibration level of the second test planet, a decomposition of the reconstructed operational response is presented for the two cases on the figure 5.18.



(a)



(b)

Figure 5.18: PPC plot of the decomposition of reconstructed response of the 2nd test planet

We observed on this figure that the summation of all response contributions almost perfectly match the constructed response of the 2nd test planet. Also, all these responses are higher

around the gear mesh frequency (321Hz). Besides, the responses corresponding to the direct connection with this component like the test carrier, test sun ($T_{2t,ct}^D \times u_{ct}$ and $T_{2t,st}^D \times u_{st}$) present a higher vibration level.

Another meaningful PPC plot is the phase PPC plot. Figure 5.19 shows phase PPC plot of the component of the constructed response of the 2nd test planet on the first angular position at (a) 100Hz and (b) 321Hz.

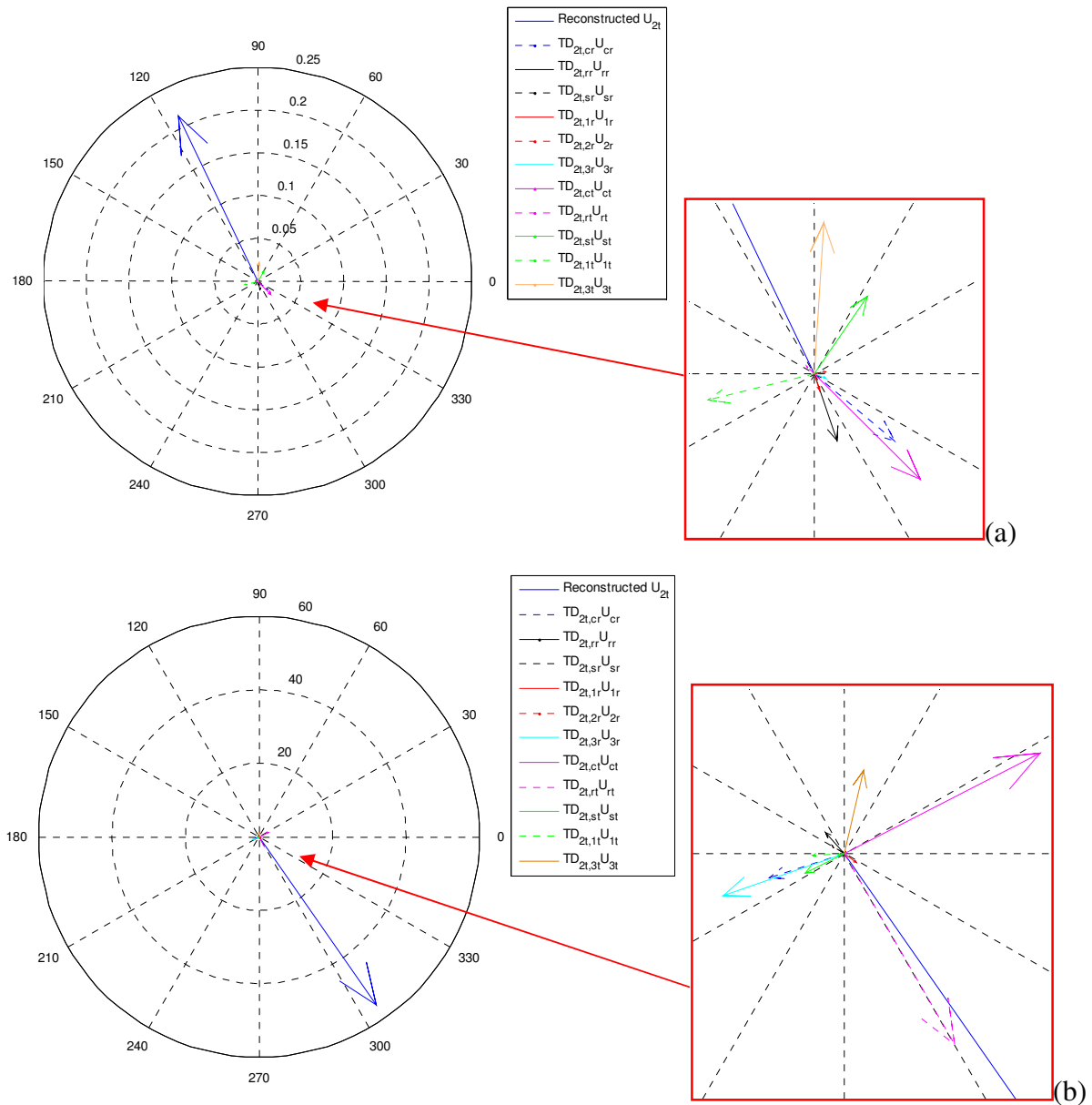


Figure 5.19: Phase PPC plot of the constructed response of the 2nd test planet at (a)100Hz, (b)321Hz

At 100Hz, contributions to the 2nd test planet should only be due to u_{rt} , u_{st} , u_{ct} , u_{1t} , u_{3t} , u_{rr} , those of u_{sr} , u_{cr} , u_{1r} , u_{2r} and u_{3r} being negligible whereas contributions to the 2nd test planet are only due to u_{rt} , u_{st} , u_{ct} , u_{1t} , u_{3t} , u_{3r} , those of u_{sr} , u_{cr} , u_{rr} , u_{1r} and u_{2r} are negligible at 321Hz.

3.4.3. Operational response reconstruction in the run-up regime

During the run-up regime, the speed of the driving motor increase linearly. (Figure 5.20).

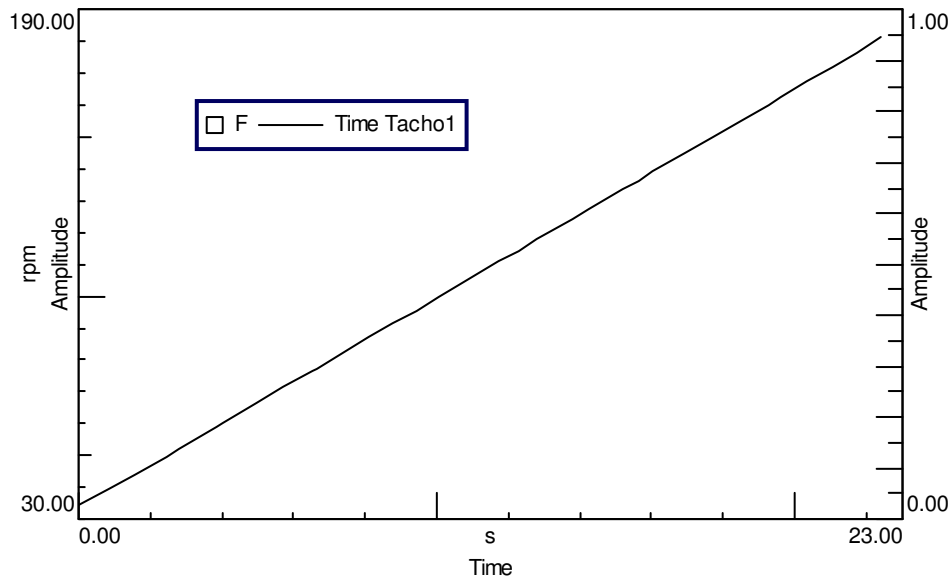


Figure 5.20: Evolution of the speed of motor during run-up regime

In this regime, the system operates in non-stationary condition and the case of the first angular position is studied. Figure 5.21, which is PPC surface plot of the reconstructed operation responses of the system in the run-up regime, shows that the second test planet present the highest vibration level which can be explained by the fact that the test planet 2 is directly connected to the test sun in which the system is excited.

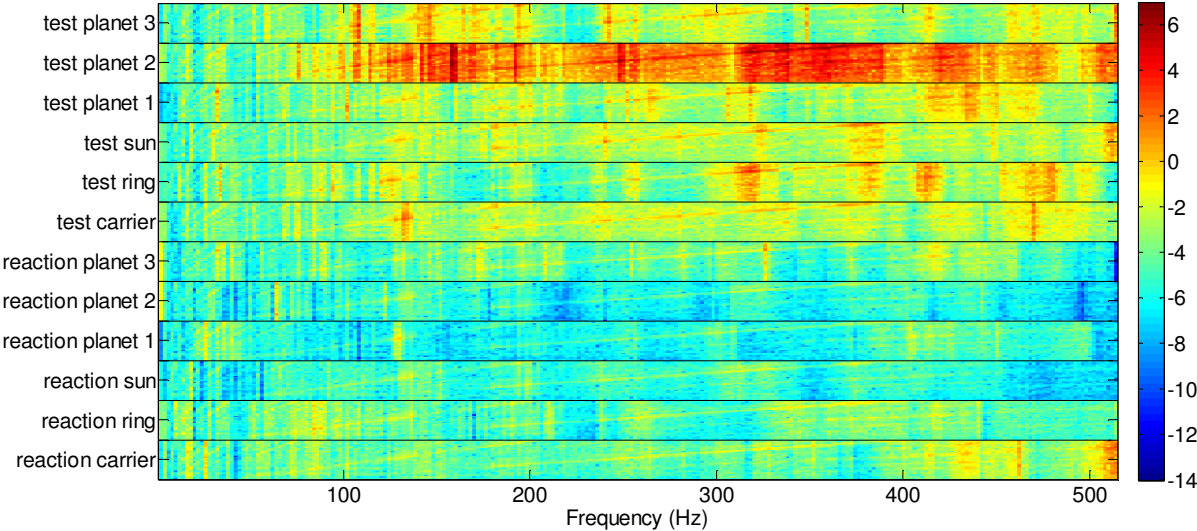


Figure 5.21: PPC surface plot of the reconstructed operation responses during the run-up

In order to understand better the behaviour of the system in the run-up regime, a zoom of the reconstructed response of the reaction ring and the second planet are respectively represented in figure 5.22 and figure 5.23.

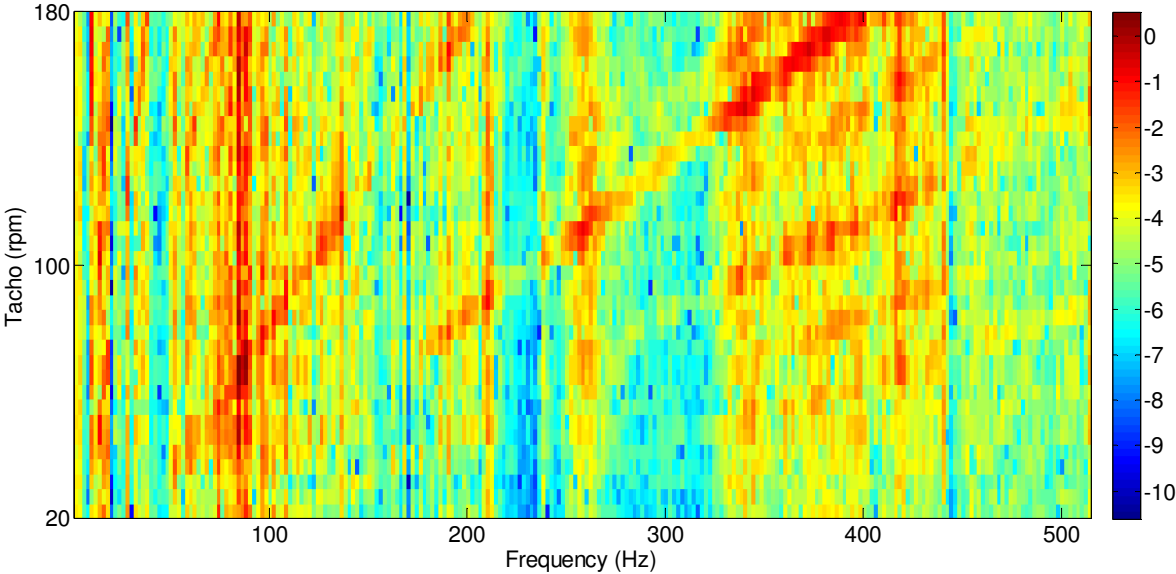


Figure 5.22: PPC surface plot of the reconstructed reaction ring response during run-up

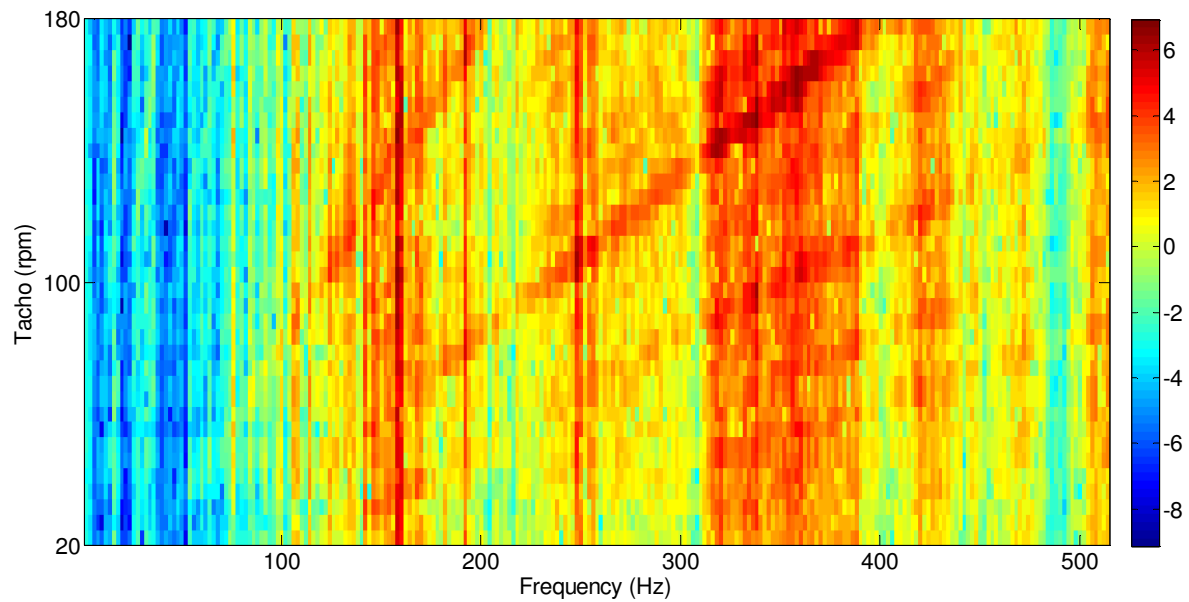


Figure 5.23: PPC surface plot of the reconstructed 2nd test planet response in run-up

In these two figures, inclined lines presented the high vibration level and are explained by the evolution of the gear mesh frequencies with the speed of motor. Besides, the vibration level of the second test planet is higher between 220 Hz and 390 Hz and is explained by the higher level of the blocked transmissibility between the second test planet and the test sun.

4. Conclusion

In this chapter, the planets load sharing behaviour is studied and correlated with thus obtained with planets measured strains on a back-to-back planetary gear test bench. Also, tests on the global transmissibility direct transmissibility (GTDT) approach to classical transfer path analysis (TPA) is performed on a system with twelve degrees of freedom composed by planetary gear set with power circulation.

The sequentially phased configuration of planets is included to the model and as results; the load sharing ratio for all planets fluctuates slightly around the $1/N$ value. The time evolution of LSR of each planet bends a little bit every $T_c/3$ by the effect of gravity of carrier. However, the planets position errors have an important effect on the LSR of each planet. The final numerical results with those three effects agree with the measured strains of planets.

The measured global transmissibility allowed to verify several issues related to the concept of direct transmissibility which allows to breakdown the response of a system degree-of-freedom

in terms of the other system degree-of-freedom and of its response to the external force acting on it.

The GTDT approach can be considered as an alternative to the more standard force TPA approach and can be applied to complex situations of practical interest like the studied system. Also, this approach involves much easier measurements, although probably, more intricate post-processing.

Contributions, conclusions and future work

1. Contributions

The main contributions of the research work presented in this thesis were the study of planetary gear transmission running under stationary and non-stationary operating conditions. The development of numerical models and experimental test on a laboratory test bench were the two approaches which have been followed to fulfill this purpose. The main investigations done through this work can be summarized as following:

- A Planetary gear test bench characterized by its mechanical power recirculation with back to back configuration was developed for experimental investigations in order to study its dynamic behavior in stationary condition and non-stationary conditions (variable load, variable speed, run up and run down regimes).
- Instrumentation, data acquisition and processing as well as motor control schemes were implemented to extract vibration signals from the test bench components to study dynamic behavior. Moreover, strain gauges have been disposed in the planet pin roots with the aim of calculate the load sharing ratio between planets.
- A36 degrees of freedom lumped parameters model of the test bench was developed in order to characterize its modal properties.
- An experimental modal analysis has been carried out with the aim of validate natural frequencies and natural modes obtained by the numerical model.

- The modal strain energy and the modal kinetic energy distributions were computed to provide information about components that can be subjected to overloads when running close to system's natural frequencies.
- A torsional model corresponding to the test bench was developed taking into account the influence of planets position on the measured vibrations. An experimental validation was also achieved.
- The effect of load value on frequency content in stationary regime (constant speed) was studied numerically and experimentally and the dominant frequency components were identified.
- The case of time varying loading conditions was tested experimentally by manual change of the masses hanging on the load arm attached to the free ring gear. The dynamic behavior in this regime was studied and experimental results were compared with those obtained by the torsional model.
- Run-up and run-down regimes were investigated through numerical and experimental studies. Time frequency analysis was carried out to characterize varying frequency content.
- A fluctuation of speed during permanent regime was simulated and tested on the bench. Time frequency analysis was also implemented to characterize this regime
- The effect of meshing phase between planets, gravity of planets carrier and planets position errors on planet load sharing was studied. The numerical results were compared with those obtained from strain measurements on planet pins.
- The effect of speed variation on load sharing was also studied in the run up regime.
- The direct transmissibilities between the components of the planetary gear test bench were computed from the frequency response function obtained by hammer impact test.
- Global Transmissibility Direct Transmissibility (GTDT) approach to the Transfer Path Analysis was performed to study the propagation of vibration in the cases of stationary condition and the run up regime.

2. Conclusions

The most relevant conclusions extracted from the presented work are summarized hereunder:

- Modal analysis done on the planetary gear model showed the presence of two classes of modes which are rotational with multiplicity 1 and translational modes with multiplicity 2. No planet modes were observed since the number of planets $N=3$ which is in agreement with previous works found in literature.
- After computing the distributions of modal kinetic energies and modal strain energies, it was shown that the modes can also be classified into gear mesh modes and bearing modes. Tooth modes are located at low frequencies and are characterized by significant strain energy in the tooth meshes and dominant motions of gears. However, bearing modes are situated rather in the high frequencies band and are characterized by significant strain energy in the bearings of planetary gear components. This investigation is of a great importance for mechanical transmissions to identify components susceptible to be damaged when running close to natural frequencies.
- In stationary conditions, when speed and load are constant, amplitude modulation was observed in the time signals with repetitive increase of vibration amplitude (three times for one period of rotation of carrier). This amplitude modulation was explained by the individual influence of the passage of each planet near the accelerometer fixed on the ring which occurs at rotational period of the carrier T_c divided by the number of planets. The spectra of vibration measurements and simulations showed non-symmetric modulating sidebands around meshing frequency f_m and its harmonics. These sidebands are multiple of $3T_c$. The highest amplitudes are observed on the right of f_m , on the left of $2f_m$. Since $3f_m$ is multiple of $3T_c$, high amplitude is observed exactly at $3f_m$. Such phenomenon should be taken into account when diagnosing planetary gears by carefully identifying the variable transmission path from planets ring meshes to measurement point.
- Several tests and simulations done with different load values showed the shift of the dominating mesh frequency harmonic from f_m to $2f_m$. This was explained by the particular procedure of load change by addition of masses on the arm fixed to the free ring causing a change to the torsional stiffness and inertia of the ring. When load is time varying during one test, spectra showed that $2f_m$ is dominating spectra.

- During run up, the evolution of the acceleration on the ring increased with time. Time-frequency map obtained from simulation and experiments for acceleration on the test ring during run up and run down operation, has shown inclined lines corresponding to the increment of the mesh frequency and its harmonics as well as vertical lines related to the system natural frequencies. So, run up and run down tests validate the modal analysis.
- During permanent regime and for an imposed speed fluctuation and fixed load, time frequency map of measured vibration showed also a fluctuation of mesh frequency and its harmonics. A cross of natural frequencies occur leading to increased vibration level. One should be aware of this behaviour; as example, for the case of wind turbine, the variability in speed may excite some natural frequencies and lead to harmful consequences.
- The fact that the planets are sequentially phased resulted in a fluctuation of the load sharing ratio for all planets around the $1/3$ value. It was also observed that the time evolution of LSR on each planet bends a little bit every $T_c/3$ by the effect of carrier gravity. Moreover, planet position errors, particularly tangential displacements, have an important effect on the LSR. The final numerical results with those three effects agree with the measured strains on planets pins.
- During run up, it was shown through experiments that in presence of planet position error, the LSR is sensitive to the increase of speed
- The reconstructed operational response of the second test planet presents the highest vibration level which can be explained by the fact the second test planet have two pairs of teeth in contact with test sun and test ring.

3. Future work

The following future lines of work are the result of a critical analysis of the work presented in this document. This proposal aims to complement, extend and continue the research work done heretofore in planetary transmissions:

- It will be interesting to extract vibration signal of sun and planets in stationary and non-stationary conditions to confirm the general dynamic behavior of the system.
- The influence of the gyroscopic effect on modes should be investigated.

- An improvement of the torque loading application on reaction ring by using dynamic shaker could help studying the effect of different load variation shapes on the dynamic behavior of the transmission. Introducing force sensors will allow measuring instantaneous applied loading torque.
- The dynamic behavior of the planetary gear transmission including defects could be studied on the available test bench. After including geometrical and/or tooth defects in the experimental setup and in the theoretical model, a characterization of the system running in non-stationary operating conditions and in presence of these defects can be done.
- The effect of floating sun on planet load sharing behavior under stationary and non-stationary conditions van also be also studied
- The propagation of vibration can be done using the operational transfer path analysis or the global transmissibility direct transmissibility obtained through operational transfer functions.

Contribuciones, conclusiones y trabajo futuro

1. Contribuciones

La principal contribución del trabajo de investigación presentado en esta tesis es el estudio de transmisiones planetarias operando en régimen estacionario y no-estacionario. Con este propósito, este estudio se ha llevado a cabo siguiendo un doble enfoque combinando el desarrollo de modelos numéricos y la realización de ensayos experimentales en un banco de ensayos de laboratorio. A continuación se presenta la relación de las principales actividades desarrolladas a lo largo de este trabajo:

- Se ha desarrollado un banco de ensayos planetario mediante la conexión de dos unidades planetarias enfrentadas (configuración back-to-back) y con recirculación mecánica de potencia con el objeto de estudiar su comportamiento dinámico en régimen estacionario y no-estacionario (carga variable, velocidad variable y operaciones de arranque y parada).
- El banco de ensayos ha sido instrumentado y se han implementado distintos procedimientos para la adquisición y procesado de datos así como para llevar a cabo el control del actuador con el fin de obtener las señales vibratorias de los distintos componentes para el estudio de su comportamiento dinámico. Además, se han dispuesto galgas extensométricas en la base de los apoyos de los planetas en el portasatélites con la finalidad de determinar el reparto de carga entre los mismos.
- Con el objetivo de caracterizar sus propiedades modales, se ha elaborado un modelo dinámico de parámetros concentrados del bando de ensayos considerando 36 grados de libertad.

- Se ha llevado a cabo el análisis modal experimental del banco de ensayos con el objetivo de validar los modos y frecuencias naturales obtenidas con el modelo numérico.
- Se han determinado la energía de deformación y la energía cinética con el propósito de obtener información en relación a los componentes que pueden estar sujetos a sobrecargas cuando el sistema opera en las proximidades de alguna de sus frecuencias de resonancia.
- Se ha elaborado un modelo del banco de ensayos considerando únicamente grados de libertad de rotación que tiene en cuenta la influencia de la posición de los planetas en el registro vibratorio medido en el anillo exterior. Dicho modelo ha sido validado experimentalmente.
- Se ha estudiado numérica y experimentalmente el efecto que la magnitud del par a transmitir tiene en el dominio de la frecuencia para condiciones de funcionamiento en régimen estacionario identificando los componentes de frecuencia más significativos.
- Se han llevado a cabo ensayos en condiciones de carga variable mediante la modificación de las masas dispuestas sobre el brazo de carga que se encuentra unido solidariamente con la corona de la caja de retorno y cuyo movimiento de rotación no está restringido. Los resultados experimentales obtenidos en estas condiciones se han comparado con los proporcionados por el modelo numérico considerando únicamente los grados de libertad de rotación.
- Se ha investigado el comportamiento de las transmisiones planetarias en regímenes de arranque y parada mediante simulaciones numéricas y registros experimentales. Se ha llevado a cabo un análisis tiempo-frecuencia para caracterizar la variación del contenido en frecuencia a lo largo de los ensayos.
-
- Se han estudiado los efectos del desfase de los ciclos de engrane entre los planetas, las cargas gravitatorias y los errores de posición sobre el reparto de la carga entre planetas. Los resultados numéricos han sido comparados con aquellos obtenidos mediante la medida de deformaciones en la base de los apoyos de los planetas.
- Adicionalmente se han analizado las consecuencias que la variación de la velocidad tiene sobre el reparto de carga entre planetas durante el régimen de arranque.

- Se han obtenido las transmisibilidades directas entre distintos componentes del banco de ensayos, a partir de las funciones de respuesta en frecuencia obtenidas mediante ensayos de impacto con martillo instrumentado.
- Se ha llevado a cabo el análisis de la trayectoria de propagación de la vibración en condiciones estacionarias y en régimen de arranque mediante la aplicación de la técnica GTDT (Global Transmissibility Direct Transmissibility).

2. Conclusions

A continuación se presentan las conclusiones más relevantes extraídas del trabajo realizado:

- El análisis modal ha permitido la identificación de modos de rotación y traslación con multiplicidad 1 y 2. No se han identificado modos vinculados con los planetas dado que el número de planetas es 3.
- La determinación de la distribución modal de energía cinética y de deformación ha permitido mostrar que los modos también pueden ser clasificados en modos relacionados con los engranajes y modos vinculados con los apoyos. Los modos de engrane aparecen en la banda de bajas frecuencias y están caracterizados por la presencia de una energía de deformación significativa en el contacto entre engranajes lo que se manifiesta en formas modales dominadas por el movimiento de los engranajes. Sin embargo, los modos relacionados con los apoyos aparecen en bandas de frecuencia más elevadas caracterizándose por energías de deformación vinculadas con los apoyos de los engranajes. Este aspecto es crucial para identificar que componentes son más susceptibles de sufrir daño cuando la transmisión opera en las proximidades de una frecuencia natural del sistema.
- Durante los ensayos en condiciones de operación estacionarias, cuando tanto la velocidad como la carga eran constantes, se ha observado la presencia de modulaciones en las señales temporales registradas con incrementos cíclicos de la amplitud (tres veces por cada rotación del porta-satélites). Esta modulación de amplitud se explica por la influencia de cada uno de los planetas al pasar por las proximidades del acelerómetro de registro localizado en la corona exterior que coincide con el periodo de rotación del porta-satélites T_c dividido por el número de planetas. El espectro resultante tanto en las simulaciones como en los registros

experimentales presenta bandas laterales distribuidas de forma asimétrica con respecto a la frecuencia de engrane f_m y sus armónicos. Las bandas laterales aparecen localizadas a múltiplos de $3T_c$ siendo de mayor amplitud aquellas situadas a la derecha del primer armónico de la frecuencia de engrane f_m , las situadas a la izquierda del segundo armónico $2f_m$Este aspecto debería ser tenido en cuenta en el diagnóstico de transmisiones planetarias identificando cuidadosamente la trayectoria de propagación de la vibración desde los planetas al punto de medida habitualmente localizado en la corona exterior.

- Se han llevado a cabo diversos ensayos y simulaciones considerando distintos valores de carga observándose un desplazamiento de la frecuencia dominante en el espectro desde el primer armónico de la frecuencia de engrane f_m al segundo $2 f_m$. Esto se explica por el procedimiento empleado en la introducción de la carga mediante la colocación de distintas masas en el brazo solidario con la corona exterior produciéndose un cambio tanto en la rigidez torsional como en la inercia del citado anillo. Cuando se introducen variaciones de carga a lo largo del tiempo se observa como el segundo armónico de la frecuencia de engrane resulta ser el más significativo en el espectro.
- La representación en un mapa tiempo frecuencia tanto de los resultados derivados de las simulaciones como de los registrados experimentalmente se observa la presencia de líneas inclinadas vinculadas a la frecuencia de engrane y sus armónicos así como líneas verticales debidas a la excitación de las frecuencias naturales del sistema. De este modo los ensayos de arranque y parada han servido para validar el análisis modal.
-
- El espaciado angular de los planetas da lugar a una fluctuación del reparto de carga de cada uno de los planetas entorno a un tercio del total. También se ha observado que la evolución temporal de LSR en cada planeta experimenta una pequeña fluctuación cada $T_c/3$ debido a las cargas gravitatorias sobre el porta-satélites. Además se ha observado que los errores de posición de los planetas tienen consecuencias importantes en el reparto de carga.
-
- La reconstrucción de la respuesta operacional correspondiente al segundo planeta (de la caja a ensayar) presenta el mayor nivel de vibración lo cual puede ser explicado por el hecho de que este posee dos dientes en contacto tanto con el sol como con el anillo.

3. Future work

A continuación se presentan las líneas de trabajo futuro que se han identificado como resultado de una evaluación crítica del trabajo presentado en este documento. Esta propuesta pretende complementar, extender y continuar la investigación llevada a cabo hasta ahora en el ámbito de las transmisiones planetarias:

- Resulta interesante extraer las señales vibratorias del sol y de los planetas en condiciones estacionarias y no estacionarias con el objeto de confirmar el comportamiento dinámico global de este tipo de sistemas.
- Es necesario investigar con mayor detalle las consecuencias que los efectos giroscópicos pueden tener en los modos de vibración resultantes.
- La mejora del dispositivo de aplicación del par exterior sobre el anillo exterior móvil mediante la utilización de un excitador electrodinámico podría ayudar en el estudio de los efectos que distintos tipos de cargas variables pueden tener en el comportamiento dinámico del sistema. La introducción de sensores de fuerza podría permitir la medida instantánea del par aplicado.
- El comportamiento dinámico de transmisiones planetarias incluyendo defectos podría ser estudiado en el banco de ensayos actualmente disponible. Es posible incluir errores y defectos de los dientes de los engranajes en el modelo experimental y en el teórico y caracterizar el comportamiento dinámico del sistema operando en régimen no estacionario y en presencia de los mismos.
- Es posible estudiar el efecto de un sol flotante en el reparto de carga entre planetas en condiciones de funcionamiento no estacionarias.
- La propagación de la vibración puede ser evaluada mediante el análisis OPA o mediante la técnica de GTDT obtenidas a partir de las funciones de transferencia registradas durante el funcionamiento del sistema.

Scientific Publications

As result of this work, two research articles are published and four communications are presented:

Articles

A1/ Journal of Theoretical and Applied Mechanics (JTAM) (Impact Factor: 0,62):

Ahmed Hammami, Alfonso Fernandez Del Rincon, Fernando Viadero Rueda, Fakher Chaari, Mohamed Haddar, Modal analysis of back-to-back planetary: experiments and correlation against lumped-parameter model, *Journal of Theoretical and Applied Mechanics*, 53, 1, pp. 125-138, Warsaw 2015

A2/ Journal of Mechanics (Impact Factor: 0,333):

Ahmed Hammami, Alfonso Fernandez Del Rincon, Fakher Chaari, Fernando Viadero Rueda, Mohamed Haddar Dynamic behaviour of back to back in run up and run down transient regimes, *Journal of Mechanics*, DOI: 10.1017/jmech.2014.95

Communications

C1/ Surveillance 7 Conference October 29th -30th, 2013 Charles France :

Ahmed Hammami, Alfonso Fernandez Del Rincon , Fernando Viadero Rueda, Fakher Chaari, Mohamed Haddar, *Dynamic behaviour of two stages planetary gearbox in non-stationary operations*

This communication is published in the web-site:

http://surveillance7.sciencesconf.org/conference/surveillance7/28_dynamic_behaviour_of_two_stages_planetary_gearbox_in_non.pdf

C2/ Mechatronic Systems Days, March 17th -19th, 2014 Mahdia-Tunisia:

Ahmed Hammami, Alfonso Fernandez Del Rincon , Fernando Viadero Rueda, Fakher Chaari, Mohamed Haddar, *Instrumentation of Back to Back Planetary Gearbox for Dynamic Behavior Investigation*

This communication is published by Springer as chapter in the book « Mechatronic Systems: Theory and Applications » pp 23-35 DOI.: 10.1007/978-3-319-07170-1_3

C3/ International Gear Conference from August 26th -28th, 2014 in Lyon, France:

Ahmed Hammami, Alfonso Fernandez Del Rincon, Fernando Viadero Rueda, Fakher Chaari, Nabih FKI, Mohamed Haddar *Back to Back Planetary gearbox: Influence of Non-stationary operating conditions*

This communication is published by ELSEVIER in book « International Gear Conference 2014 » pp 896-904.

C4/ Multiphysics Modelling and Simulation for Systems Design Conference, December 17th-19th, 2014 Sousse- Tunisia:

Ahmed Hammami, Miguel Iglesias Santamaria, Alfonso Fernandez Del Rincon, Fakher Chaari, Fernando Viadero Rueda, Mohamed Haddar, *Load Sharing Behavior in Planetary Gear Set.*

This communication is published by Springer as chapter in the book « *Multiphysics Modelling and Simulation for Systems Design and Monitoring Applied Condition Monitoring 2*», pp 459-468 DOI: 10.1007/978-3-319-14532-7_47

References

(**Abry, 1997**) Abry P., *Ondelettes et turbulences*. France Edition Nouveaux Essais, 1997.

(**Agashe, 1998**) Agashe V., *Computational Analysis of the Dynamic Response of a Planetary Gear System*, Master Thesis, Ohio State University, 1998.

(**Al-shyyab and Kahraman, 2007**) Al-shyyab A., Kahraman A., A non-linear dynamic model for planetary gear sets, *Journal of multi-body dynamics*, 221 (2007) 567-576.

(**August and Kasuba, 1986**) August R., Kasuba R., « Torsional Vibrations and Dynamic Loads in a Basic Planetary Gear System », *Journal of Vibration, Acoustics, Stress, and Reliability in Design*, vol. 108, n°3, 1986, p. 348-353.

(**Bàguski, 2010**) Bàguski B.C., *An experimental investigation of the system-level behavior of planetary gear sets*. Thesis, the Ohio State University 2010.

(**Bartelmus, 2010**) Bartelmus W., Chaari F., Zimroz R., Haddar M., *Modelling of gearbox dynamics under time-varying non stationary load for distributed fault detection and diagnosis*, *European Journal of Mechanics A/ Solids* 29 (2010) 637-646

(**Barthod et al, 2007**) Barthod M., Hayne B., Tebec J.L., J.-C. Pin J.-C., *Experimental study of dynamic and noise produced by a gearing excited by a multi-harmonic excitation*, *Applied Acoustics* 68 (2007) 982–1002

(**Bigret and Freon, 1995**) Bigret R., Freon J. L., *Diagnostic - maintenance - disponibilité des machines tournantes*, Paris, Editions Masson, 1995.

(Bodas and Kahraman, 2004) Bodas A., Kahraman A., Influence of carrier and gear manufacturing errors on static load sharing behavior of planetary gear sets, *JSME international Journal*, 47 (3) 908-915 ,2004

(Bogert et al, 1963) Bogert B.P., Healy M.J.R., Tukey J.W., The Quefreny Alanysis of Time series for Echoes: Cepstrum, Pseudo-Autocovariance, Cross-Cepstrum, and Saphe Cracking, in *Proc. of the Symp. on Time Series Analysis*, by M. Rosenblatt (Ed.),. Wiley, NY, (1963), pp. 209-243.

(Boguski, 2010) Bąguski B.C., An experimental investigation of the system-level behavior of planetary gear sets. Thesis, the Ohio State University 2010.

(Botman, 1976) Botman M., Epicyclic Gear Vibrations, *Journal of Engineering for Industry*, vol. 96, 1976, p. 811-815.

(Bu et al, 2012) Bu Z., Liu G., Wu L., Modal analyses of herringbone planetary gear train with journal bearings, *Mechanism and Machine Theory* 54 (2012) 99–115

(Cai, 1995) Cai Y., Simulation on the rotational vibration of helical gears in consideration of the tooth separation phenomenon (A new stiffness function of helical involute tooth pair). *Journal of Mechanical Design* 1995;17.

(Chaari et al, 2008) Chaari F., Baccar W., Abbes M.S., Haddar M., Effect of spalling or tooth breakage on gearmesh stiffness and dynamic response of a one-stage spur gear transmission, *European Journal of Mechanics A/Solids* 27 (2008) 691–705

(Chaari et al, 2009) Chaari F., Fakhfakh T., Haddar M., Analytical modelling of spur gear tooth crack and influence on gearmesh stiffness, *European Journal of Mechanics A/Solids* 28 (2009) 461–468

(Chaari et al, 2013) Chaari F., Abbes M. S., Viadero Rueda F., Fernandez del Rincon A., Haddar M., Analysis of planetary gear transmission in non-stationary operations, *Frontiers Mechanical Engineering*, 8 (2013) 88–94

(Chiang and Badgley, 1973) Chiang T., Badgley R. H., Reduction of Vibration and Noise Generated by Planetary Ring Gears in Helicopter Aircraft Transmission, *Journal of Engineering for Industry*, vol. 93,1973, p. 1149-1158.

(Chopra, 1995) Chopra L., Dynamics of Structures: theory and applications to earthquake engineering, Prentice Hall International Series in Civil Engineering and Engineering Mechanics, Englewood Cliffs, NJ, Prentice Hall, 1995.

(Cooley and Parker, 2012) Cooley C.G., Parker R.G., Vibration properties of high-speed planetary gears with gyroscopic effects, Journal of Vibration and Acoustics 134 (2012) 061014.

(Cooley and Parker, 2013) Cooley C.G., Parker R.G., Mechanical stability of high-speed planetary gears, International Journal of Mechanical Sciences 69 (2013) 59–71

(Cornell, 1981) Cornell R. W., Compliance and stress sensitivity of spur gear teeth, Journal of Mechanical Design, vol. 103, 1981, p. 447-459.

(Cunliffe et al, 1974) Cunliffe F., Smith J. D., Welbourn D. B., Dynamic Tooth Loads in Epicyclic Gears, Journal of Engineering for Industry, vol. 94, 1974, p. 578-584.

(De Klerk, 2010) De Klerk D., Ossipov A., Operational transfer path analysis: theory, guidelines and tire noise application, Mechanical System and Signal Processing, 24 (2010) 1950–1962.

(De Sitter et al, 2010) De Sitter G., Devriendt C., Guillaume P., Pruyt E., Operational transfer path analysis, Mechanical System and Signal Processing, 24 (2010) 416–431.

(Devriendt and Guillaume, 2007) Devriendt C., Guillaume P., The use of transmissibility measurements in out put-only modal analysis, Mechanical System and Signal Processing, 21(2007) 2689–2696.

(Devriendt et al., 2009) Devriendt C., DeSitter G., Vanlanduit S., Guillaume P., Operational modal analysis in the presence of harmonic excitations by the use of transmissibility measurements, Mechanical System and Signal Processing, 23 (2009) 621–635.

(Dhatt and Touzot, 1984) Dhatt G., Touzot G., Une présentation de la méthode des éléments finis, Paris (1984) Editions Maloine.

(Dickinson and Jenkins, 1981) Dickinson H.W., Jenkins R. “James Watt and the Steam Engine” Moorland Publishers 2nd edition 1981

(Doebelin, 2004) Doebelin E.O., Measurement systems: application and design. 2004 Mc Graw Hill Higher education (The Ohio state university: Book)

(Drago, 2009) Drago R.J., The Effect of Start-Up Load Conditions on Gearbox Performance and Life Failure Analysis, with Supporting Case Study, American Gear Manufacturers Association Fall Technical Meeting, Gear Technology, June 2009.

(El Badaoui et al, 1999) El Badaoui M., Guillet F., Daniere J., Surveillance des systèmes complexes à engrenages par l’analyse cepstrale synchrone, Traitement du Signal, vol. 16, n°5, 1999, p. 371-381.

(Ericson and Parker, 2013) Ericson T.M., Parker R.G., Planetary gear modal vibration experiments and correlation against lumped-parameter and finite element models, Journal of Sound and Vibration 332 (2013) 2350–2375

(Eritenel and Parker, 2009) Eritenel T., Parker R.G., Modal properties of three-dimensional helical planetary gears, Journal of Sound and Vibration 325 (2009) 397–420.

(Fernández et al, 2013) A. Fernández del Rincón; F. Viadero; M. Iglesias; R. Cerdá; A. de-Juan, Test Bench for the analysis of dynamic behaviour of planetary gear transmissions, The 3rd International Conference on Condition Monitoring of Machinery in Non-Stationary Operations (CMMNO 2013)

(Fernandez et al, 2013) Fernandez A., Viadero F., Iglesias M., García P., de-Juan A., Sancibrian R., A model for the study of meshing stiffness in spur gear transmissions, Mechanism and Machine Theory 61 (2013) 30–58

(Gajdatsy et al, 2010) Gajdatsy P., Janssens K., Desmet W., Van der Auweraer H., Application of the transmissibility concept in transfer path analysis. Mechanical System and Signal Processing, 24 (2010) 1963–1976.

(Genta, 2005) Genta G., Dynamics of rotating systems, Mechanical Engineering Series, Springer 2005.

(Guasch and Magrans, 2004) Guasch O., Magrans F.X., The Global Transfer Direct Transfer method applied to a finite simply supported elastic beam, *Journal of Sound and Vibration*, 276 (2004) 335–359.

(Guasch, 2009) Guasch O., Direct transfer functions and path blocking in a discrete mechanical system, *Journal of Sound and Vibration*, 321 (2009) 854–874.

(Guasch et al., 2013) Guasch O., Garcia C., Jové J., Artis P., Experimental validation of the direct transmissibility approach to classical transfer path analysis on a mechanical setup, *Mechanical System and Signal Processing*, 37 (2013) 353-369.

(Guo and Keller, 2012) Guo Y., Keller J., (2012) Combined effects of gravity, bending moment, bearing clearance, and input torque on wind turbine planetary gear load sharing, *American Gear Manufacturers Association technical paper*, 12FTM05 2012.

(Guo and Parker 2010) Guo Y., Parker R.G., Purely rotational model and vibration modes of compound planetary gears, *Mechanism and Machine Theory* 45 (2010) 365–377

(Hidaka et al, 1976a) Hidaka T., Terauchi Y., Nagamura K., « Dynamic Behavior of Planetary Gears 1st Report:Load Distribution », *Bull. JSME*, vol. 19, n° 132, 1976a, p. 690-698.

(Hidaka et al, 1976b) Hidaka T., Terauchi Y., Ishioka K., Dynamic Behavior of Planetary Gear -2nd Report, Displacement of Sun Gear and Ring Gear, *Bulletin of the JSME*, vol. 19, n° 138, 1976b, p. 1563-1570.

(Hidaka et al, 1977) Hidaka T., Terauchi Y., Nomard M., Ohsita J. I., Dynamic Behavior of Planetary Gear-3rd Report, Displacement of Ring Gear in Direction of Line of Action, *Bulletin of the JSME*, vol. 20, 1977, p. 1663-1672.

(Hidaka et al, 1979a) Hidaka T., Terauchi Y., Ishioka K., Dynamic Behavior of Planetary Gear-4th Report, Influence of the Transmitted Tooth Load on the Dynamic Increment Load , *Bulletin of the JSME*, vol. 22, n° 168, 1979a, p. 877-884.

(Hidaka et al, 1979b) Hidaka T., Terauchi Y., Nagamura K., Dynamic Behavior of Planetary Gear - 5th Report, Dynamic Increment of Torque, *Bulletin of the JSME*, vol. 22, n° 169, 1979b, p.1017-1025.

(Hidaka et al, 1979c) Hidaka T., Terauchi Y., Nagamura K., Dynamic Behavior of Planetary Gear - 6th Report, Influence of Meshing-Phase, Bulletin of the JSME, vol. 22, n° 169, 1979c, p. 1026-1033.

(Hidaka et al, 1979d) Hidaka T., Terauchi Y., Nagamura K., Dynamic Behaviour of Planetary Gear - 7th Report, Influence of the Thickness of the Ring Gear, Bulletin of the JSME, vol. 22, n° 170, 1979d, p. 1142-1149.

(Hidaka et al, 1980) Hidaka T., Terauchi Y., Fuji M., Analysis of Dynamic Tooth Load on Planetary Gear, Bulletin of the JSME, vol. 23, n° 176, 1980, p. 315-323.

(Ho and Randall, 2000) Ho H., Randall R. B., Optimisation of bearing diagnostic techniques using simulated and actual bearing fault signals, Mechanical Systems and Signal Processing (2000) 14(5), 763-788

(Hoffman, 1989) Hoffman K., An Introduction to Measurements using Strain Gages, Hottinger Baldwin Messtechnik GmbH (Book)

(Iglesias et al, 2013) Iglesias M., Fernandez A., De-Juan A., Sancibrian R., Garcia P., (2013) Planet position errors in planetary transmission: Effect on load sharing and transmission error, Frontiers Mechanical Engineering, 8(1) 80-87

(Inalpolat, 2009) Inalpolat M., A theoretical and experimental investigation of modulation sidebands of planetary gear sets. Dissertation, the Ohio State University 2009.

(Inalpolat and Kahraman, 2009) Inalpolat M, Kahraman A (2009) A theoretical and experimental investigation of modulation sidebands of planetary gear sets. Journal of Sound and Vibration 323:677–696

(ISO 6336, 2006) “Calculation of load capacity of spur and helical gear”, International Standard, 2006.

(Janssens et al, 2011) Janssens K., Gajdatsy P., Gielen L., Mas P., Britte L., Desmet W., OPAX: a new transfer path analysis method based on parametric load models, Mechanical System and Signal Processing, 25 (2011) 1321–38.

(Kahraman, 1993) Kahraman A., Planetary gear train dynamics, *Journal of Mechanical Design* 116 (1993) 713–720.

(Kahraman, 1994a) Kahraman A., Load Sharing Characteristics of Planetary Transmissions, *Mechanism and Machine Theory*, vol. 29, 1994a, p. 1151-1165.

(Kahraman, 1994b) Kahraman A., Planetary Gear Train Dynamics, *ASME Journal of Mechanical Design*, vol.116, n° 3, 1994b, p. 713-720.

(Kahraman, 1994c) Kahraman A., Natural Modes of Planetary Gear Trains, *Journal of Sound and Vibration*, vol. 173, n° 1, 1994c, p. 125-130.

(Kahraman and Blankenship, 1994a) Kahraman A., Blankenship G. W., Planet Mesh Phasing in Epicyclic Gear Sets, *Proc. Of International Gearing Conference*, Newcastle, UK, 1994, p. 99-104.

(Kahraman, 1999) Kahraman A., Static load sharing characteristics of transmission planetary gear sets: model and experiment, *Transmission and driveline subsystems symposium*, SAE paper 1999-01-1050, 1999.

(Kahraman, 2001) Kahraman A., Free torsional vibration characteristics of compound planetary gear sets, *Mechanism and Machine Theory*, vol. 36, 2001, p. 953-971.

(Kahraman and Vijayakar , 2001) Kahraman A., Vijayakar S.M., Effect of internal gear flexibility on the quasi-static behavior of a planetary gear set, *Journal of Mechanical Design* 123 (2001) 408–415.

(Khabou et al, 2011) Khabou M.T, Bouchaala N., Chaari F., Fakhfakh T., Haddar M., Study of a spur gear dynamic behavior in transient regime, *Mechanical Systems and Signal Processing* 25 (2011) 3089–3101

(Kiracofe and Parker, 2007) Kiracofe D.R., Parker R.G., Structured vibration modes of general compound planetary gear systems, *Journal of Vibration and Acoustics* 129 (2007) 1–16.

(Kohler, 1989) Kohler H., *Gear Dynamics*. British Gear Association, Décembre 1989.

(Lanchrester, 1924) Lanchrester F.W., Epicyclic gears, Proc. I. Mech. E., 1924.

(Lebold et al, 2000) Lebold M., McClintic K., Cambell R., Byington C., Maynard K., Review of vibration analysis methods for gearbox diagnostics and prognostics, Proceedings of the 54th Meeting of the Society for Machinery Failure Prevention Technology, , May 1st -4th 2000, Virginia Beach, VA, USA.

(Ligata, 2007) Ligata H. Impact of system-level factors on planetary gear set behaviour. Dissertation, the Ohio State University 2007.

(Ligata et al, 2008) Ligata H, Kahraman A, Singh A, An Experimental Study of the Influence of Manufacturing Errors on the Planetary Gear Stresses and Planet Load Sharing. Journal of Mechanical Design, 130 (2008) -041701:1-9

(Ligata et al, 2009) Ligata H., Kahraman A., Singh A., (2009), A closed-form planet load sharing formulation for planetary gear sets using a translational analogy, Journal of Mechanical Design 131:021007.

(Lin and Parker, 1999a) Lin J., Parker R.G., Analytical characterization of the unique properties of planetary gear free vibration, Journal of Vibration and Acoustics 121 (1999) 316–321.

(Lin and Parker, 1999b) Lin J., Parker R. G., Sensitivity of Planetary Gear Natural Frequencies and Vibration Modes to Model Parameters, Journal of Sound and Vibration, vol. 228, n°11, 1999, p. 109-128.

(Lin and Parker, 2000a) Lin J., Parker R. G., Parametric Instabilities in Planetary Gears under Mesh Stiffness Variations, Journal of Vibration and Acoustics, vol. 249, n° 1, 2000, 129-146.

(Lin and Parker, 2000b) Lin J., Parker R.G., Structured vibration characteristics of planetary gears with unequally spaced planets, Journal of Sound and Vibration 233 (2000) 921–928.

(Lin and Parker, 2002) Lin J., Parker R. G., Mesh Stiffness Variation Instabilities in Two-Stage Gear Systems, Journal of Vibration and Acoustics, vol. 124, 2002, p. 68-76.

(Litvin and Fuentes, 2004) Litvin F.L., Fuentes A., Gear geometry and applied theory, 2nd ed. Cambridge University Press, Cambridge, 2004.

(LMS SCADAS, 2009) LMS SCADAS manuel, 2009.

(Maatar, 1995) Maatar M., Contribution à l'analyse du comportement dynamique de réducteurs à engrenages simple étage. Influence des écarts de forme et des défauts de montage, Thèse de doctorat, Institut National des Sciences Appliquées de Lyon, 1995.

(Maia et al., 2001) Maia N.M.M., Silva J.M.M., Ribeiro A.M.R., The transmissibility concept in multi-degree-of-freedom systems, Mechanical System and Signal Processing, 15 (2001) 129–137.

(Margans, 1981) Margans F.X., Method of measuring transmission paths, Journal of Sound and Vibration, 74 (3) 321-330

(Maynard, 1999) Maynard K. P., « Interstitial processing: the application of noise processing gear fault detection», Proceedings of the international conference on Condition monitoring, 12 Avril 1999, University of Wales Swansea, UK, p. 77-86

(McFadden and Smith, 1985) McFadden P.D. and Smith J.D., An explanation for the asymmetry of the modulation sidebands about the tooth meshing frequency in epicyclic gear vibration, Proceedings of the Institution of Mechanical Engineers 199 C1 (1985)65-70.

(Miller, 1999) Miller A. J., A new wavelet basis For the decomposition of gear motion error signals and its application to gearbox diagnostics, PhD Thesis, University of Pennsylvania, 1999.

(Mitchell, 1982) Mitchell J. S., Continuous monitoring systems for high speed gearing, Proceedings of the eleventh turbomachinery symposium (1982) 157-164

(Muskhelishvili, 1975) Muskhelishvili, N.L., 1975. Some Basic Problems of the Mathematical Theory of Elasticity, second English ed. P. Noordhoff Limited, The Netherlands.

(Nakada and Utagawa, 1956) Nakada T., Utagawa M., Dynamic loads acused by the varying elasticity of mating gear teeth, Proceeding of the 6th Japan National Congress on Applied Mechanics, 1956, p. 493-497.

(Özguven and Houser, 1988) Özguven H. N., Houser D. R., Mathematical models used in gear dynamics – A review, Journal of Sound and Vibration, vol. 121, n° 3, 1988, p. 383-411

(Parker, 2000) Parker R. G., A Physical Explanation for the Effectiveness of Planet Phasing to Suppress Planetary Gear Vibration », Journal of Sound and Vibration, vol. 236, n° 4, 2000, p. 561-573.

(Parker et al, 2000) Parker R. G., Agashe V., Vijayakar S. M., « Dynamic Response of a Planetary Gear System Using a Finite Element/Contact Mechanics Model », ASME Journal of Mechanical Design, vol. 122, 2000, p. 305-311.

(Parker and Wu 2010) Parker R.G., Wu X., Vibration modes of planetary gears with unequally spaced planets and an elastic ring gear, Journal of Sound and Vibration 329 (2010) 2265–2275.

(Plunt, 2005) Plunt J., finding and fixing vehicle NVH problems with transfer path analysis, Sound and vibration (2005) 12-16.

(Rakhit, 1997) Rakhit A. K., « Improved Epicyclic Gearbox for Reduced and Controllable Subsynchronous Vibrations in Gas Turbogenerator Applications », Journal of Engineering for Gas Turbines and Power, vol. 119, n° 3, 1997, p. 640-646.

(Randall, 1977) Randall R. B., Cepstrum analysis and gearbox fault diagnosis, Edition 1. Bruel and Kjaer Application note, 1977.

(Randall, 1980) Randall R. B., Cepstrum analysis and gear box Fault diagnosis. Edition 2, Bruel and Kjaer Application note, 1980.

(Randall et al, 2011) Randall R.B., Antoni J. and Chobsaard S., The relationship between spectral correlation and envelope analysis in the diagnostics of bearing faults and other cyclostationary machine signals, Mechanical Systems and Signal Processing, **15** (5), 945–962.

(Randall, 2011) Randall R. B., *Vibration-based condition monitoring*, 2011 John Wiley & Sons, Ltd

(Randall, 2013) Randall R. B., *A History of Cepstrum Analysis and its Application to Mechanical Problems*, Surveillance 7 conference (Charles 29th and 30th October 2013) France

(Rayleigh, 1877) Rayleigh L., “*Theory of Sound*”, 1954th edition, Dover Publications, New York, 1877

(Ribeiro et al, 2000) Ribeiro AMR, Silva JMM, Maia NMM, On the generalization of the transmissibility concept. *Mechanical System and Signal Processing*, (2000) 29–35.

(Roozen and Leclère, 2013) Roozen N.B., Leclère Q., On the use of artificial excitation in operational transfer path analysis, *Applied Acoustics*, 74 (2013) 1167-1174.

(Saada and Vex, 1995) Saada A., Vex P., An Extended Model for the Analysis of the Dynamics of Planetary Trains », *ASME Journal of Mechanical Design*, vol. 117, 1995, p. 241-247.

(Sainsot et al, 2004) Sainsot, P., Vex, P., Duverger, O., 2004. Contribution of gear body to tooth deflections – A new bidimensional analytical Formula. *ASME Journal of Mechanical Design* 126, 748–752.

(Schon, 2005) Schon P.P., Unconditionally convergent time domain adaptive and time-frequency techniques for epicyclic gearbox vibration. Thesis. The University of Pretoria 2005.

(Shin and Jeon, 1993) Shin Y. S., Jeon J. J., « Pseudo Wigner-Ville time frequency distribution and its application to machinery condition monitoring », *Journal of Shock and Vibration*, vol. 1, 1993, p. 65.

(Shing, 1994) Shing T. K., Dynamics and control of geared servomechanisms with backlash and friction consideration, PHD thesis, Harvard University and Industry, 1994.

(Singh, 2005) Singh A., (2005), Application of a system level model to study the planetary load sharing behavior, *Journal of Mechanical Design*, 127: 469-476.

(Singh et al, 2008) Singh A., Kahraman A., Ligata H., Internal gear strains and load sharing in planetary transmissions: model and experiments, *Journal of Mechanical Design* 130 (2008) 072602.

(Singh, 2010) Singh A., (2010), Load sharing behavior in epicyclic gears: Physical explanation and generalized formulation, *Mechanism and Machine Theory* 45: 511–530

(Sika and Velex, 2008) Sika G., Velex P., Instability analysis in oscillators with velocity-modulated time-varying stiffness-Applications to gears submitted to engine speed fluctuations, *Journal of Sound and Vibration* 318 (2008) 166–175

(Sondkar and Kahraman, 2013) Sondkar P., Kahraman A., A dynamic model of a double-helical planetary gear set, *Mechanism and Machine Theory* 70 (2013) 157–174.

(Sweeney, 1994) Sweeney P.J, Transmission error measurement and analysis, Tesis Doctoral, The University of New South Wales, New South Wales, (1994)

(Tanna and Lim, 2004) Tanna R.P., Lim T.C., Modal frequency deviations in stimulating ring gear modes using smooth ring solutions, *Journal of Sound and Vibration* 269 (2004) 1099–1110

(Timoshenko and Baud, 1926) Timoshenko S., Baud R. V., « The strength of gear teeth », *Mechanical Engineering*, 1926, p. 1105-1109.

(Toda and Botman, 1979) Toda A., Botman M., « Planet Indexing in Planetary Gears for Minimum Vibration », ASME Design Engineering Technical Conference, St. Louis, 1979.

(Velex, 1988) Velex P., Contribution à l'analyse du comportement dynamique des engrenages à axes parallèles. PhD thesis, Inst. Nat. Des sciences appliquées de Lyon, 1988.

(Velex et al, 1994) Velex P., Randrianarivo L., Pichon V., Wittman R., Dynamic behavior of epicyclic trains: experimental and numerical analyses, *Proceedings of the International Gearing Conference*, Newcastle (1994) 265–269.

(Viadero et al, 2014) Viadero F., Fernández A., Iglesias M., de-Juan A., Liaño E., Serna M.A., Non-stationary dynamic analysis of a wind turbine power drivetrain: Offshore considerations, *Applied Acoustics* 77 (2014) 204–211

(Wang et al, 2001) Wang W.Q., Ismail F., Golnaraghi M.F., Assessment of gear damage monitoring techniques using vibration measurements, *Mechanical Systems and Signal Processing* (2001) 15(5), 905-922.

(Weber, 1949) Weber C., The deformation of loaded gears and the effect on their load-carrying capacity, Department of scientific and industrial research, sponsored research (Germany), n° 3, London, 1949.

(Wright, 2005) Wright D., Design and analysis of machine Elements, Class note, Department of mechanical and materials engineering, University of Western Australia, 2005.

(Wu and Parker, 2008) Wu X., Parker R.G., Modal properties of planetary gears with an elastic continuum ring gear, *Journal of Applied Mechanics* 75 (2008) 1–10.

(Yang and sun, 1985) Yang D.C.H., Sun Z.S., A rotary model for spur gear dynamics. *ASME Journal of Mechanisms, Transmissions, and Automation in Design* 107 (1985) 529–535.

(Zimroz et al, 2011) Zimroz R. , Urbanek J., Barszcz T., Bartelmus W., Millioz F., Martin N., Measurement of instantaneous shaft speed by advanced vibration signal processing – Application to wind turbine gearbox, *Metrology and Measurement Systems*, Vol. XVIII (2011), No. 4, pp. 701-712